Theoretical studies
of fluid membrane mechanics

Dissertation
zur Erlangung des Grades
"Doktor der Naturwissenschaften"
am Fachbereich Physik, Mathematik
und Informatik
der Johannes Gutenberg-Universität
in Mainz

Martin Michael Müller
geboren in Trier

Mainz
Oktober 2007

Tag der mündlichen Prüfung: 28. November 2007

Für meine Familie

Zusammenfassung

Biologische Membranen sind Fettmolekül-Doppelschichten, die sich wie zweidimensionale Flüssigkeiten verhalten. Die Energie einer solchen fluiden Oberfläche kann häufig mit Hilfe eines Hamiltonians beschrieben werden, der invariant unter Reparametrisierungen der Oberfläche ist und nur von ihrer Geometrie abhängt. Beiträge innerer Freiheitsgrade und der Umgebung können in den Formalismus mit einbezogen werden.

Dieser Ansatz wird in der vorliegenden Arbeit dazu verwendet, die Mechanik fluider Membranen und ähnlicher Oberflächen zu untersuchen. Spannungen und Drehmomente in der Oberfläche lassen sich durch kovariante Tensoren ausdrücken. Diese können dann z. B. dazu verwendet werden, die Gleichgewichtsposition der Kontaktlinie zu bestimmen, an der sich zwei aneinander haftende Oberflächen voneinander trennen. Mit Ausnahme von Kapillarphänomenen ist die Oberflächenenergie nicht nur abhängig von Translationen der Kontaktlinie, sondern auch von Änderungen in der Steigung oder sogar Krümmung. Die sich ergebenden Randbedingungen entsprechen den Gleichgewichtsbedingungen an Kräfte und Drehmomente, falls sich die Kontaktlinie frei bewegen kann. Wenn eine der Oberflächen starr ist, muss die Variation lokal dieser Fläche folgen. Spannungen und Drehmomente tragen dann zu einer einzigen Gleichgewichtsbedingung bei; ihre Beiträge können nicht mehr einzeln identifiziert werden.

Um *quantitative* Aussagen über das Verhalten einer fluiden Oberfläche zu machen, müssen ihre elastischen Eigenschaften bekannt sein. Der "Nanotrommel"-Versuchsaufbau ermöglicht es, Membraneigenschaften lokal zu untersuchen: Er besteht aus einer porenüberspannenden Membran, die während des Experiments durch die Spitze eines Rasterkraftmikroskops in die Pore gedrückt wird. Der lineare Verlauf der resultierenden Kraft-Abstands-Kurven kann mit Hilfe der in dieser Arbeit entwickelten Theorie reproduziert werden, wenn der Einfluss von Adhäsion zwischen Spitze und Membran vernachlässigt wird. Bezieht man diesen Effekt in die Rechnungen mit ein, ändert sich das Resultat erheblich: Kraft-Abstands-Kurven sind nicht länger linear, Hysterese und nichtverschwindende Trennkräfte treten auf. Die Voraussagen der Rechnungen könnten in zukünftigen Experimenten dazu verwendet werden, Parameter wie die Biegesteifigkeit der Membran mit einer Auflösung im Nanometerbereich zu bestimmen.

Wenn die Materialeigenschaften bekannt sind, können Probleme der Membranmechanik genauer betrachtet werden. Oberflächenvermittelte Wechselwirkungen sind in diesem Zusammenhang ein interessantes Beispiel. Mit Hilfe des oben erwähnten Spannungstensors können analytische Ausdrücke für die krümmungsvermittelte Kraft zwischen zwei Teilchen, die z. B. Proteine repräsentieren, hergeleitet werden. Zusätzlich wird das Gleichgewicht der Kräfte und Drehmomente genutzt, um mehrere Bedingungen an die Geometrie der Membran abzuleiten. Für den Fall zweier unendlich langer Zylinder auf der Membran werden diese Bedingungen zusammen mit Profilberechnungen kombiniert, um quantitative Aussagen über die Wechselwirkung zu treffen.

Theorie und Experiment stoßen an ihre Grenzen, wenn es darum geht, die Relevanz von krümmungsvermittelten Wechselwirkungen in der biologischen Zelle korrekt zu beurteilen. In einem solchen Fall bieten Computersimulationen einen alternativen Ansatz: Die hier präsentierten Simulationen sagen voraus, dass Proteine zusammenfinden und Membranbläschen (Vesikel) bilden können, sobald jedes der Proteine eine Mindestkrümmung in der Membran induziert. Der Radius der Vesikel hängt dabei stark von der lokal aufgeprägten Krümmung ab. Das Resultat der Simulationen wird in dieser Arbeit durch ein approximatives theoretisches Modell qualitativ bestätigt.

Summary

Biological membranes consist of a bilayer of lipid molecules which behaves like a two-dimensional fluid. The energy associated with such a fluid surface is often completely described by a reparametrization-invariant Hamiltonian which only depends on the surface geometry. Internal degrees of freedom and sometimes even bulk contributions are readily included.

Within this framework, the mechanics of fluid membranes and similar surfaces is studied. One can write stresses and torques on the surface in terms of covariant tensors. These can be used to determine the equilibrium position of the contact line between two adhering surfaces or different domains on one surface in a completely systematic way. With the exception of capillary phenomena, the surface energy is sensitive not only to boundary translations but may also correspond to changes in slope or even curvature. The resulting boundary conditions express the balance of stresses and torques if the contact line is free to move. At a rigid substrate, however, the variation has to follow the local substrate shape; stresses and torques enter a single balance equation and cannot be disentangled. To make *quantitative* predictions about the behavior of a fluid surface, its elastic properties have to be known. The "nanodrum" setup offers a direct way to probe membrane properties locally: it consists of a pore-spanning lipid bilayer membrane which is poked with the tip of an atomic force microscope (AFM). The linear behavior of the resulting force-distance curves is reproduced in the theory if one neglects the influence of adhesion between AFM tip and membrane. Including it in the model via an adhesion balance changes the situation significantly: force-distance curves cease to be linear, hysteresis and nonzero detachment forces can show up. These rich characteristics may offer a possibility to uniquely deduce membrane parameters such as the bending rigidity on the nano-scale in future experiments.

Once the material parameters are known, problems of membrane mechanics can be addressed in full detail. One particularly interesting problem in this context involves interface-mediated interactions. Analytical expressions for the curvature-mediated force between two membrane-bound particles such as proteins can be obtained with the help of the stress tensor. Additionally, torque and force balance yield several analytical conditions on the membrane geometry. To see how these rather abstract analytical expressions can be applied, the shape of the membrane is determined exactly for the case of two infinitely long cylinders adhering to the membrane.

When asking for the relevance of curvature-mediated interactions in the biological cell, experiment and theory both encounter difficulties. Computer simulations then offer an alternative approach with their unique ability to identify and separate individual contributions to the phenomenon or process of interest. The presented simulations predict that once a minimal local bending is realized, the effect robustly drives protein cluster formation and subsequent transformation into vesicles with radii that correlate with the local curvature imprint. This is confirmed qualitatively by an approximate theoretical model.

List of Publications

Chapter 3:

M. Deserno, M. M. Müller, and J. Guven. "Contact lines for fluid surface adhesion" *Physical Review E* **76**(1), 011605 (2007).

Chapter 4:

S. Steltenkamp, M. M. Müller, M. Deserno, C. Hennesthal, C. Steinem, and A. Janshoff. "Mechanical Properties of Pore-Spanning Lipid Bilayers Probed by Atomic Force Microscopy" *Biophysical Journal* **91**(1), 217–226 (2006).

D. Norouzi, M. M. Müller, and M. Deserno. "How to determine local elastic properties of lipid bilayer membranes from atomic-force-microscope measurements: A theoretical analysis" *Physical Review E* **74**(6), 061914 (2006).

Chapter 5:

M. M. Müller, M. Deserno, and J. Guven. "Interface mediated interactions between particles: A geometrical approach" *Physical Review E* **72**(6), 061407 (2005).

M. M. Müller, M. Deserno, and J. Guven. "Balancing torques in membrane-mediated interactions: Exact results and numerical illustrations" *Physical Review E* **76**(1), 011921 (2007).

M. M. Müller, M. Deserno, and J. Guven. "Surfaces stresses of bulk origin" *in preparation* (2007).

B. J. Reynwar, G. Illya, V. A. Harmandaris, M. M. Müller, K. Kremer, and M. Deserno. "Aggregation and vesiculation of membrane proteins by curvature-mediated interactions" *Nature* **447**(7143), 461–464 (2007).

Further Publication:

J. Guven and M. M. Müller. "How paper folds: bending with local constraints" *submitted to Journal of Physics A* (2007).

Contents

Contents

Introduction

Lipid bilayer membranes constitute one of the most fundamental components of all living cells. Apart from their obvious structural task in organizing distinct biochemical compartments, their contributions to essential functions such as protein organization, sorting, or signaling play an important role in nature [AJL$^+$02, LBM$^+$04].

Many of these tasks such as exo- or endocytosis [Mar01], the formation of vesicles [Rob97, MG05, Ant06], or the interaction with the cytoskeleton [LH92] significantly exceed mere passive separation or solubilization of proteins. Instead, they rely heavily on mechanical membrane properties and can be studied using the mathematical toolbox of theoretical physics. Various key questions are of an essentially geometrical nature: what is the shape adopted by a membrane subjected to some specified boundary conditions [Sei97]? How are forces and torques transmitted through the membrane [CG02b, Guv04, LM06, Koz06]? Which interactions does this imply [GBP93, KPDN95, WKH98, KNO98, DFG98, KRS99, MM02, BBR02, BF03, Wei03, DOD06]?

To answer questions such as these, a differential geometric description of the membrane has proven advantageous. On length scales much larger than its thickness the membrane can be described as a two-dimensional fluid surface with an energy that depends entirely on surface invariants (see Chap. 1). Consequently, stresses and torques in the membrane are expressible in terms of the local surface geometry as well. It is possible to introduce the concept of a stress tensor – well known from three-dimensional elasticity theory – to problems involving the mechanics of membranes in particular and surfaces in general (see Chap. 2).

By resisting the temptation to use some specialized parametrization and rather choose a covariant description, many problems lead to remarkably simple geometric relations, which are not at all obvious or even recognizable in a parametrized language. Examples include boundary conditions at triple-lines of contacting surfaces (see Chap. 3) or interactions between membrane-bound particles (see Chap. 5).

Even if the surrounding space is included in the theoretical picture, the mechanical surface response continues to be driven by its geometry. Hence, a geometric stress tensor is no less useful. The task is rather to couple it to potential off-surfaces stresses such as a pressure difference across the surface. There are a variety of methods how this may be done and we will discuss some of these in Chaps. 2 and 5.

Knowing the connection between stresses and geometric surface properties, however, is not a substitute for solving the relevant field equation if one wants to determine the actual shape of the membrane. Unfortunately, this equation is a nonlinear partial differential equation of fourth order which typically has to be solved numerically. In Chaps. 4 and 5 this will be done for problems obeying a rotational or translational symmetry. For more complicated situations tailored computer simulations offer an alternative approach.

Combining analytical theory, numerical calculations and computer simulations indeed seems to be the ideal way to study the mechanics of membranes theoretically. Where one approach meets its limitations the other one can step into the breach offering a more complete view of the relevant problems. Before discussing these, however, let us start with an overview of the main characters. A detailed description will occur later in the text, especially in the first chapter.

Dramatis Personae
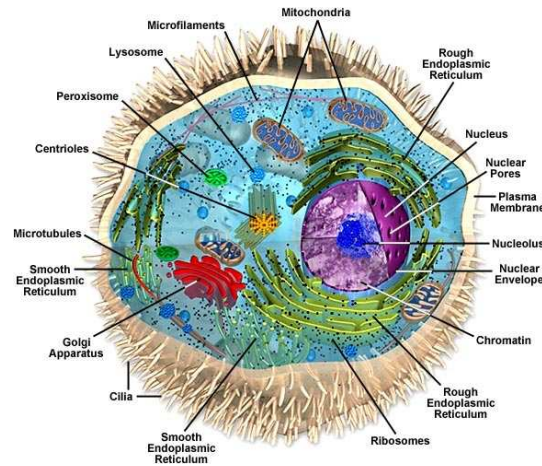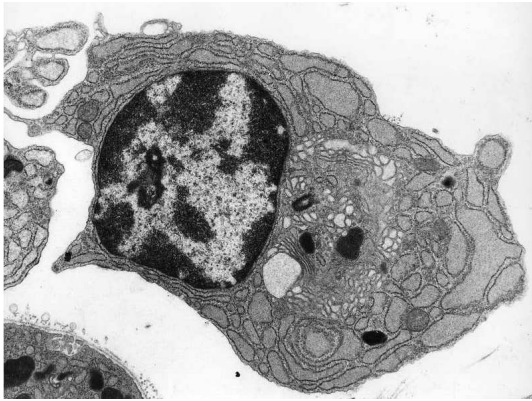
The cell
left: Electron micrograph of a plasma cell, a type of white blood cell that secretes antibodies. Only a single membrane (the plasma membrane) surrounds the cell, but the interior contains many membrane-limited compartments, or organelles *(from [CM93] with courtesy of P. Cross)*;   *right:* Schematic sketch of an animal (eukaryotic) cell *(from http://micro.magnet.fsu.edu/cells/animalcell.html)*.
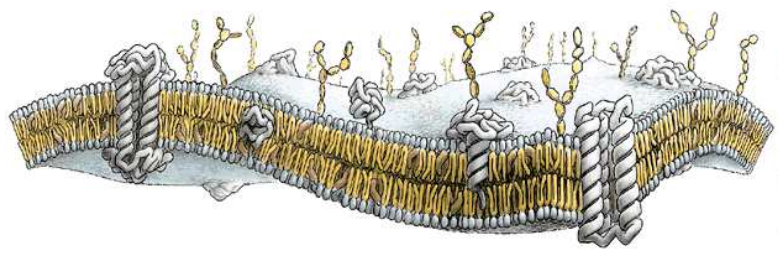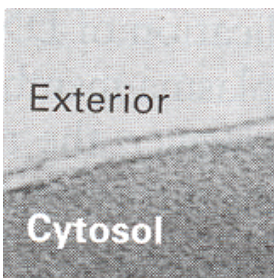
The biological fluid membrane
left: Electron micrograph of a thin section through the membrane of a red blood cell *(from [LBM$^+$04])*;   *right:* Sketch of the membrane. It consists of a lipid bilayer to which different kinds of macromolecules (*e. g.* proteins) are bound *(from [GK96, Fig. 4.15 on p.99]; copyright, W. W. Norton and Co.)*.
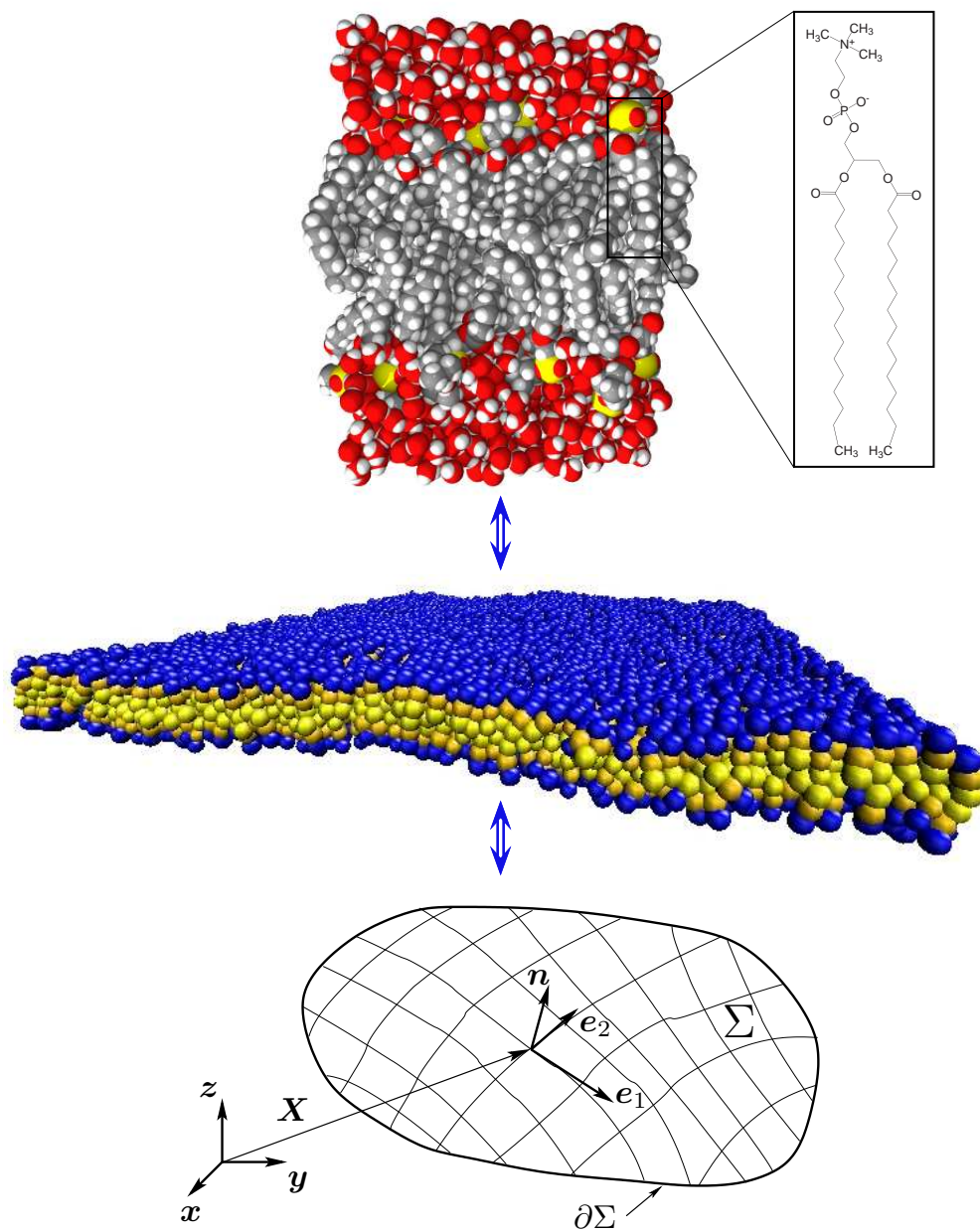
Model membranes (DPPC bilayer)
To model the membrane theoretically, different levels of resolution can be chosen. In all-atom computer simulations *(above)* every atom is represented by one bead. In coarse-grained simulations *(middle)* groups of atoms are combined; their interactions can even be tuned such that the surrounding water does not have to be simulated explicitly. Treating the membrane analytically as a two-dimensional surface is possible on length scales much larger than the membrane's thickness *(below)*.
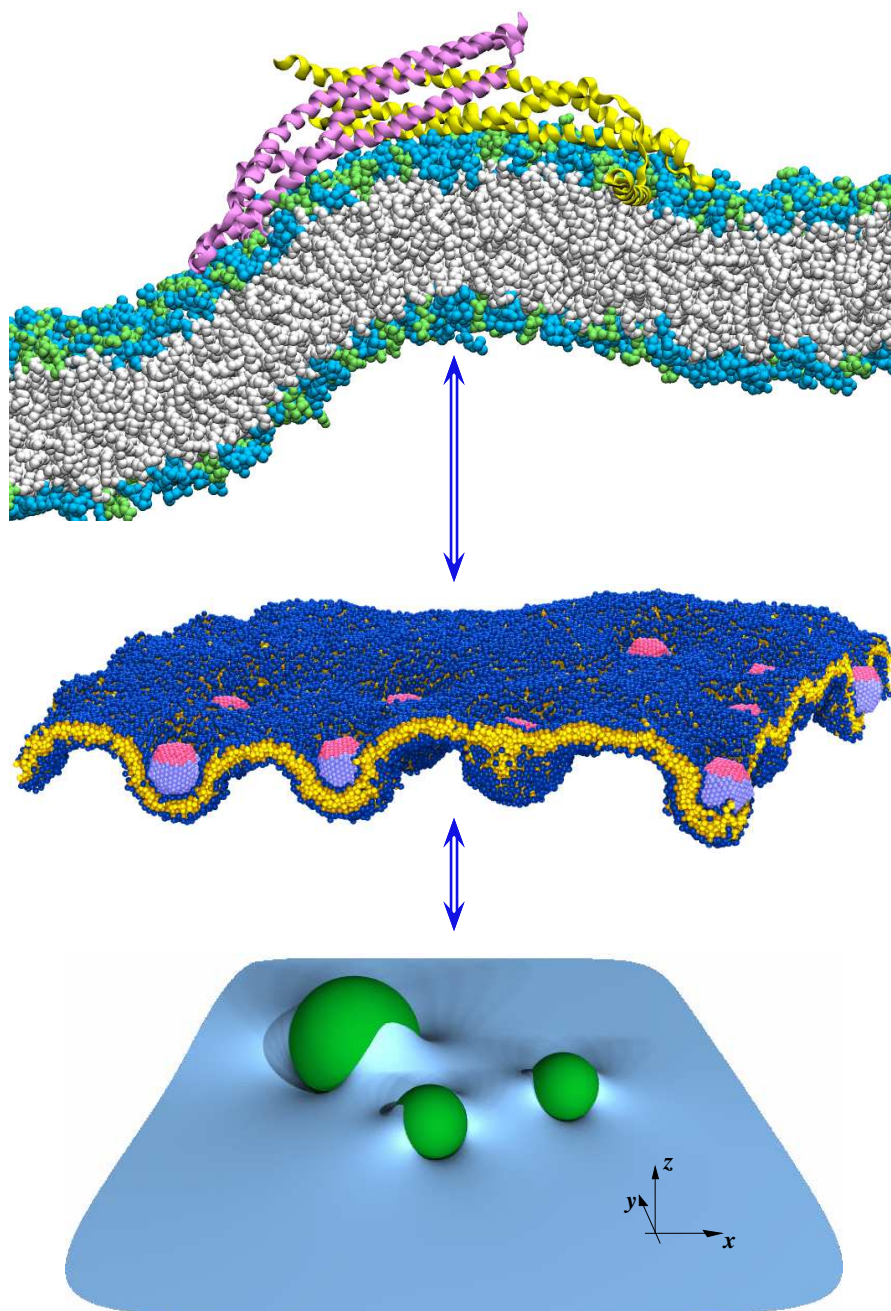
Proteins in membranes
Proteins can be included into the theoretical model on all levels of resolution. For example, the BAR domain *(above)* can deform the lipid bilayer locally *(with courtesy of P. Blood)*. On larger length scales such an effect can be modeled using hard spheres that adhere to the membrane *(middle and below)*.

1 The biological membrane – a fluid surface

1.1 Biological membranes

Biological membranes consist of a bilayer of lipid molecules in which proteins are embedded. At physiological conditions this bilayer behaves like a two-dimensional fluid, with individual molecules able to diffuse rapidly in it.

Each cell is surrounded by a closed membrane, the plasma membrane, which physically separates the extracellular environment from the cell's interior. Bacteria and archae possess just this single membrane, whereas animal and plant cells also contain internal membrane-limited subcompartments, the organelles. The nucleus, for example, stores the genetic information, the mitochondria are the power plants of the cell, and the endoplasmic reticulum is the factory where protein molecules are synthesized [LBM+04, AJL+02].[1]

To cope with the different tasks in which membranes are involved as a crucial part, a membrane's molecular composition is highly inhomogeneous. Despite that they all have a common basic structure: the lipid bilayer.

1.1.1 The lipid bilayer

Lipid molecules are the basic building blocks of the membrane. They are *amphiphiles*, that is they consist of two different parts: a *hydrophilic* (*i. e.*, "water-loving") head and a *hydrophobic* (*i. e.*, "water-fearing") tail. The hydrophobic tail is typically formed by two hydrocarbon chains originating from various fatty acids. One of them is often unsaturated. This means that at least one double bond exists between two of the carbon atoms (see Table 1.1). The fatty acids are attached via ester or amide covalent bonds to a linker group like glycerol which also binds to the hydrophilic head group. In phospho- or glycolipids, the most abundant lipids in the cell, this head group consists of a simple phosphate or sugar group, respectively, and another group such as choline (see Table 1.2).

In an aqueous environment the hydrophobic carbon tails of the lipid disturb the hydrogen bonds that exist between the water molecules close to it. These can only

---

[1] Cells that have a nucleus and other organelles are also called *eukaryotic cells*.

substance	*#C*	*#db*	*chemical structure*
laurate	12	0	$CH_3-(CH_2)_{10}-COO^-$
myristate	14	0	$CH_3-(CH_2)_{12}-COO^-$
palmitate	16	0	$CH_3-(CH_2)_{14}-COO^-$
stearate	18	0	$CH_3-(CH_2)_{16}-COO^-$
arachidate	20	0	$CH_3-(CH_2)_{18}-COO^-$
oleate	18	1	$CH_3-(CH_2)_7-CH=CH-(CH_2)_7-COO^-$
linoleate	18	2	$CH_3-(CH_2)_4-(CH=CH-CH_2)_2-(CH_2)_6-COO^-$
γ-linolenate	18	3	$CH_3-(CH_2)_4-(CH=CH-CH_2)_3-(CH_2)_3-COO^-$
arachidonate	20	4	$CH_3-(CH_2)_4-(CH=CH-CH_2)_4-(CH_2)_2-COO^-$

Table 1.1: Common biological fatty acid anions [GKD$^+$04, A3.8]. The number of carbon atoms (#C) is even because biological fatty acids are synthesized by concatenation of C_2 units. Note also that the fatty acid anions can be further divided into saturated (no double bond (db)) and unsaturated (one or more double bonds) ions.

be maintained if the water sacrifices a part of its entropy. This phenomenon is called the *hydrophobic effect* [Tan91] and is the main reason why the hydrophobic part of an amphiphile tries to avoid water. The hydrophilic part, however, can form hydrogen bonds with the water and therefore likes to stay in it.

The "schizophrenic" nature of the amphiphiles causes them to aggregate spontaneously above a certain critical concentration. At that concentration which is called the *critical micelle concentration* (cmc) it becomes energetically more favorable for them to sacrifice some of their entropy and self-assemble into a condensed structure, thereby shielding their hydrophobic parts from the water. The morphology of the aggregate depends on the nature of the amphiphile, (*i. e.*, the size of the head group and the hydrophobic tail), but also on the solution conditions (*i. e.*, salt concentration, pH or temperature) [Isr92]. Typical structures that result are spherical or cylindrical micelles, bilayers and vesicles (see Fig. 1.1).

Most of the lipid molecules in cells form bilayers, a fact already discovered in 1925 [GG25]. The bilayer of a biological membrane is approximately 5 nm thick and contains typically on the order of one hundred different lipids. The lipid fractions vary between organisms, cells, different organelles within the cell, and even between the two sides of the bilayer. Still, some common features can be identified that are essential for biological function [LBM$^+$04, AJL$^+$02, GKD$^+$04]:

- The hydrophobic core of the bilayer acts as a *barrier* to the passage of most water-soluble molecules. In consequence, a small number of molecular chan-

substance	*chemical structure*	*type*
lysophospha-tidylcholine (lysolecithin)		lyso-phospholipid
phosphatidyl-ethanolamine (PE)		glycero-phospholipid
phosphatidyl-choline (PC)		
digalactosyl-diglyceride (DGDG)		glycero-glycolipid
sphingomyelin		sphingo-phospholipid
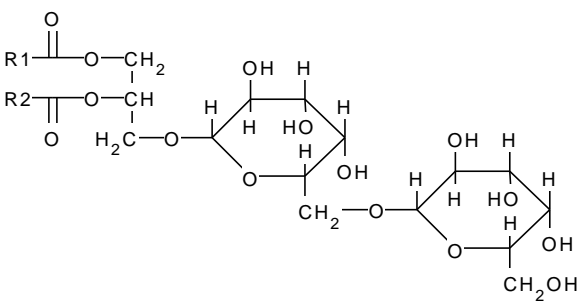
Table 1.2: Examples of membrane lipids. R1 and R2 correspond to hydrocarbon chains of fatty acids (see Table 1.1) [GKD$^+$04, A3.8f] *(from [Mül04])*.
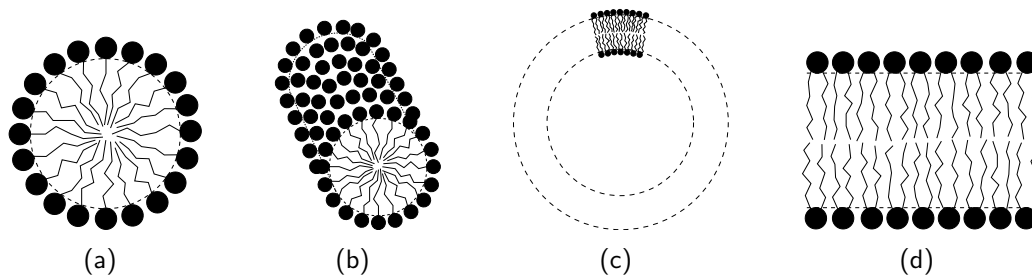
Figure 1.1: Typical structures that result from self-assembly: (a) spherical micelle, (b) cylindrical micelle, (c) flexible bilayer/vesicle, and (d) planar bilayer. The black circles are the hydrophilic heads, the chains the hydrophobic tails of the amphiphiles.

nels and pumps can strictly regulate the exchange of chemicals between the two sides of the membrane.[2]

- The cmc is very low (10^{-6}-10^{-10} M for bilayer-forming lipids as opposed to 10^{-2}-10^{-5} M for micelle-forming amphiphiles). The bilayer is therefore very *stable*: even though the exterior aqueous environment can vary widely in ionic strength and pH, the bilayer has the strength to retain its characteristic architecture.

- The biological bilayer behaves as a *two-dimensional fluid* at physiological temperatures. The lipids can diffuse freely within each leaflet of the bilayer.[3]

Below a critical transition temperature T_m the bilayer loses its fluidity and becomes a gel-like solid. Mismatches between the cross-sectional areas of lipid head and lipid tail group lead to tilted or interdigitated chains and rippled surfaces [LS95, Chap. 5].
The value of T_m depends, for instance, on the degree of saturation of the fatty acid chains in the bilayer. In unsaturated fatty acids the chains are kinked and cannot pack closely. Lipids with unsaturated fatty acids thus form bilayers with a lower transition temperature than lipids with saturated fatty acids. For example, a pure DPPC (1,2-dipalmitoyl-phosphatidylcholine) bilayer has a transition temperature of $(41.3 \pm 1.8)\,°C$, whereas DOPC with one cis double bond in every chain (see Fig. 1.2(a)) is fluid above $(-18.3 \pm 3.6)\,°C$ [KC98].[4] The same rule holds for synthetic membrane lipids. Under ambient conditions a DOTAP bilayer is already

---

[2] An alternative way of material transport through the membrane will be discussed in the next section and in Chap. 5.

[3] A membrane lipid can diffuse the length of a typical bacterial cell ($1\,\mu$m) in only one second, the length of a typical animal cell in about 20 seconds.

[4] The double bond cannot rotate. If the groups that are connected to it are oriented in the same direction the molecule is referred to as cis, while when they point in opposing directions it is referred to as trans.

(a) cis-DOPC (1,2-dioleoyl-phosphatidyl-choline)

(b) DOTAP (1,2-dioleoyl-3-trimethyl-ammonium-propane chloride)

(c) DODAB (N,N-dimethyl-N,N-dioctadecylammonium bromide)
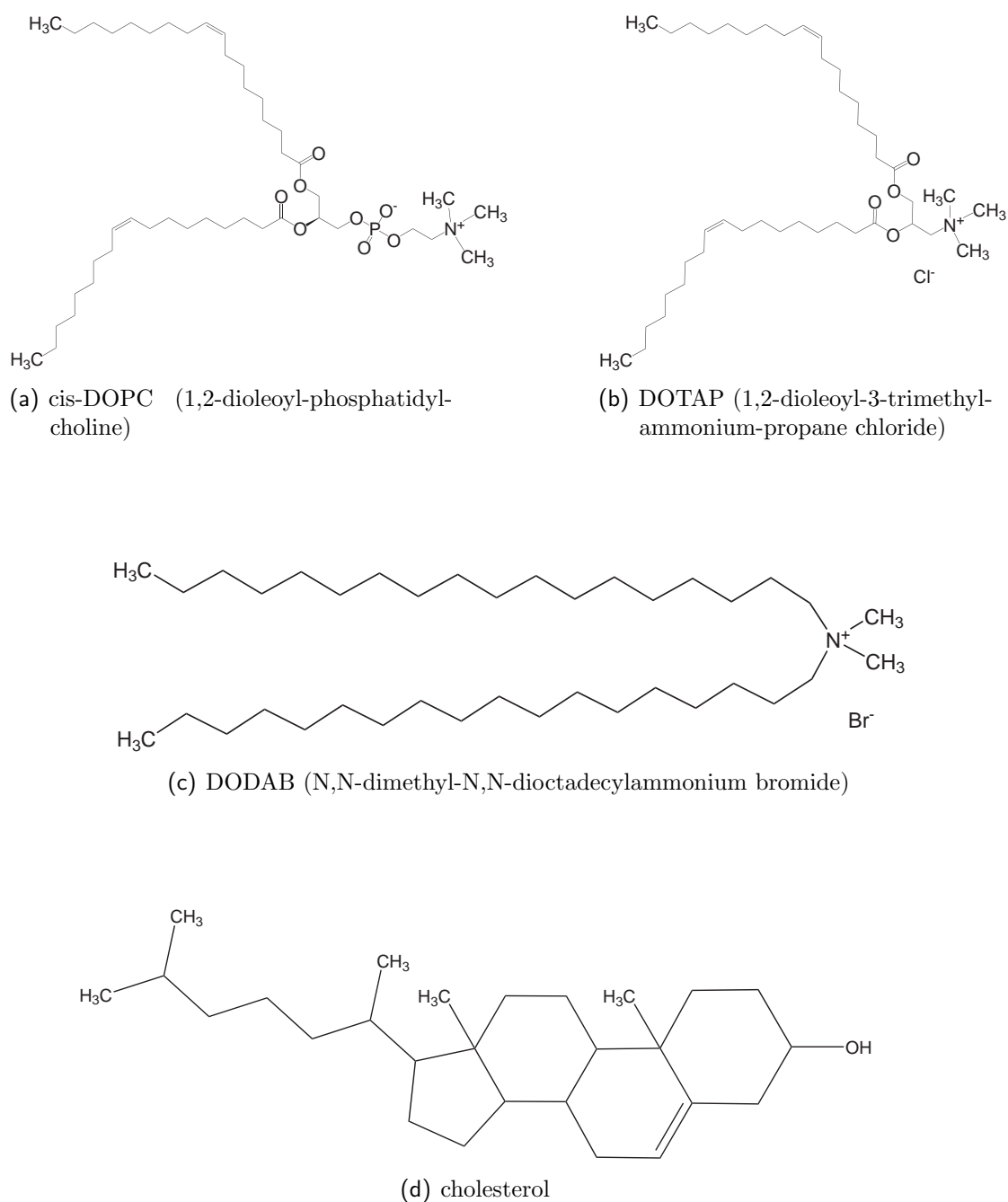
(d) cholesterol

Figure 1.2: Examples of lipids with different effect on the bilayer fluidity: DOPC (a) and DOTAP (b) bilayers are fluid under ambient conditions, DODAB (c) forms a gel-like bilayer. Cholesterol (d) tends to make fluid lipid bilayers less fluid.

fluid whereas DODAB is still in the gel phase (see Fig. 1.2(b) and 1.2(c)). We will come back to that point in Chap. 4 where these lipids will be used in an experiment in which the elastic properties of bilayers are investigated.

The fluidity of the bilayer also depends on the length of the hydrocarbon tails it contains. A shorter chain length reduces the tendency of the tails to interact with each other, so that the bilayer remains fluid at lower temperatures.

Both effects, degree of saturation and chain length of the fatty acid tails, are exploited in nature. Under thermal stress (arising from, say, an abnormal decrease in temperature) many organisms such as bacteria or yeasts actively adjust the fatty acid composition of their membrane to maintain its fluidity [TJI98].

Eukaryotic cell membranes additionally contain cholesterol for these purposes. Cholesterol consists of a rigid and relatively planar steroid skeleton with a single hydroxyl group as the hydrophilic part (see Fig. 1.2(d)). It cannot form a bilayer unless it is mixed with other lipids. By decreasing the mobility of the hydrocarbon chains it tends to make fluid lipid bilayers less fluid. At the high concentration found in most eukaryotic plasma membranes, it also prevents the hydrocarbon chains from coming together and crystallizing thereby inhibiting the fluid-gel phase transition [LBM$^+$04, AJL$^+$02]. Ten years ago, it has been proposed that both cholesterol and sphingolipids accumulate in the plasma membrane to form tiny domains of a diameter of a few tens of a nanometer [SI97, BL97, BL98]. These "lipid rafts" are supposed to help organizing certain proteins which are important for biological functions such as cell signaling.

Experiments with synthetic vesicles made from cholesterol, sphingomyelin and a phospholipid like POPC have shown a variety of phases, phase transitions, and coexistence regimes [DBV$^+$01, VK05]. Typically, such a mixture can phase-separate into *micrometer-sized* liquid ordered (L_o) domains which are rich in sphingomyelin and cholesterol and liquid disordered (L_d) domains of similar size. Whether rafts exist in living cells or not, however, remains the subject of lively debate [Mun03, Nic05, Han06] as it is much harder to search for domains of *nanometer size*, especially in vivo. In Chap. 4 an experimental setup will be presented that reaches the necessary spatial resolution. It may thus offer a possibility to search for lipid rafts in the near future.

1.1.2 Membrane proteins

Although the lipid bilayer provides the basic structure of the membrane, proteins perform most of its biological functions. They serve as ion channels and specific receptors, for example, or catalyze membrane-associated reactions, such as the synthesis of adenosine 5'-triphosphate (ATP), the principal carrier of chemical energy in cells.

Proteins are macromolecules that consist of amino acids joined together by peptide bonds (see Fig. 1.3). One can distinguish four levels of organization in their
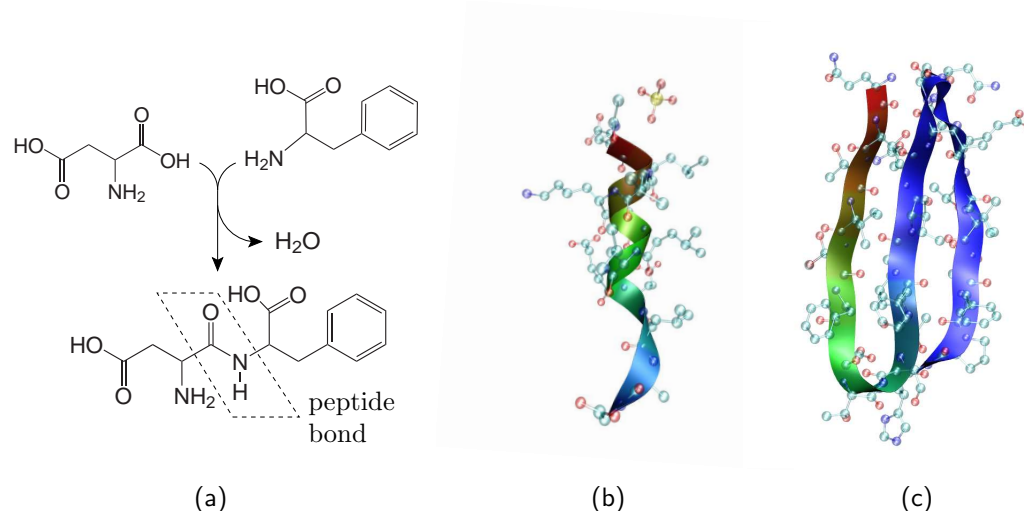
Figure 1.3: (a) Amino acids can connect to each other via a peptide bond. Two important secondary structures are (b) the α helix and (c) the β sheet.

structure. The linear sequence of amino acids is called the primary structure. It is composed of 20 different types of amino acids and is encoded in the genome of the cell. Individual amino acid residues on a protein may attract or repel one another. Localized parts of the peptide chain can thus fold into three-dimensional structures like α helices or β sheets (see again Fig. 1.3). These arrangements are referred to as secondary structures. Their degree of hydrophobicity depends on the character of the side chains of the amino acids involved. The tertiary structure describes the full three-dimensional organization of the chain. The protein can, however, be formed as a complex of more than one polypeptide chain. For instance, hemoglobin, the oxygen carrier of the blood, consists of four subunits. The complete structure is then designated as the quaternary structure [LBM+04, AJL+02].

Proteins can be bound to membranes in different ways: (*i*) *integral membrane proteins*, also called transmembrane proteins, span the lipid bilayer. They contain one or more hydrophobic domains that are inserted into the core of the bilayer as well as hydrophilic domains that extend into the aqueous medium on both sides. (*ii*) *Lipid-anchored membrane proteins* are bound covalently to one or more lipid molecules. The hydrophobic tail of the attached lipid is embedded in one leaflet of the membrane. The polypeptide chain itself does not enter the bilayer. (*iii*) *Peripheral membrane proteins* do not interact with the fatty acid chains of the bilayer. Instead they are only bound indirectly by interactions with integral membrane proteins or directly by interactions with the lipid head groups. How a protein associates with the membrane depends on its biological function. Only transmembrane proteins can function on both sides of the bilayer or transport

molecules across it. By contrast, many proteins that function on only one side of the bilayer are often lipid-anchored or peripheral proteins.

Because the bilayer is fluid, all types of proteins can move laterally in the membrane and interact with one another. In Chap. 5 we will discuss membrane remodeling as one example where proteins aggregate to act cooperatively. Such processes are, for instance, important in endocytosis in which material is ingested by invagination of the plasma membrane and subsequent internalization in a membrane-bound vesicle.

However, living cells have found ways to immobilize specific membrane proteins. In the previous section we have already discussed lipid rafts as one example. Beside that, the interaction with the *cytoskeleton* restricts the mobility of proteins as well. The cytoskeleton provides structural support for the eukaryotic cell. It consists of a network of filaments build up from proteins such as actin or tubulin and permits directed movements of organelles and the cell itself.[5] Some proteins in the plasma membrane can link permanently to the cytoskeleton leaving them completely immobile in the membrane. Other proteins, though still mobile, are slowed down in the presence of the cytoskeleton.

We will not go further into the biological details here. The interested reader is referred once more to Refs. [LBM+04, AJL+02]. The rest of this introductory chapter will instead present a physical description of the biological membrane and similar fluid surfaces which will ultimately enable us to consider interesting problems of fluid membrane or – more generally – fluid surface mechanics.

1.2 The energy associated with fluid surfaces

> *The energy associated with a fluid surface is often completely described by a reparametrization-invariant Hamiltonian that only depends on the surface geometry. Internal degrees of freedom and sometimes even bulk contributions are readily included.*

In order to choose the correct physical description of the membrane it first has to be clear how much detail is needed to answer the questions of interest. To model the exact conformation of a protein embedded in the membrane, for example, computer simulations are the right tool to use [Lea01].

In this thesis, however, the membrane will be considered from a *mesoscopic* point of view.[6] This is applicable when the lateral extension and the size of all deformations of interest are much larger than its width. The lipid bilayer can then be modeled as a two-dimensional surface embedded in three-dimensional Euclidean

---

[5] For active transport you of course additionally need some kind of engine and fuel. In the cell these are provided by special motor proteins and ATP, respectively.

[6] Only in Sec. 5.3.2 molecular dynamics simulations will be used to study the interactions of a number of proteins bound to the membrane.
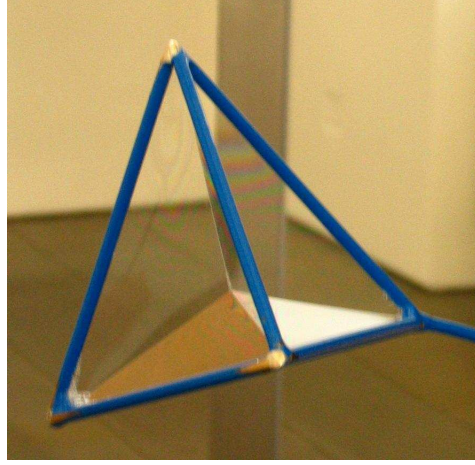
Figure 1.4: A soap film spanning a tetrahedral frame *(from [Mül04])*.

space $\mathbb{R}^3$. Proteins or other entities that can bind to the membrane (*e. g.* viruses) are represented by solid particles that impose deformations in the surface.

To predict the behavior of the membrane under deformations such as these, one has to know how its energy changes. Let us therefore study possible contributions to the energy of a fluid surface and discuss their relevance for the case of the membrane.

1.2.1 Surface tension and curvature energy

Surface tension

When surfaces occur in physical systems, the energy associated with them is often completely described by a Hamiltonian that only depends on the surface geometry. The easiest and the best known examples involve capillary phenomena [RW02, dGBWQ03], in which the energy of a liquid-fluid interface is simply given by the surface integral over a constant surface tension σ.[7] The resulting Hamiltonian is therefore:

$$H = \int_\Sigma \mathrm{d}A \, \sigma \, , \tag{1.1}$$

where Σ is the surface domain and $\mathrm{d}A$ the infinitesimal area element.

Hamiltonian (1.1) is not only relevant for interfaces between pure phases (such as, for instance, water and water vapor) but also describes the behavior of soap

---

[7] We will only consider interfaces in their ground states. Thermal fluctuations around these states or dynamical phenomena will not be taken into account. This implies that we do not need to worry about entropic contributions to the free energy (for a general discussion in the case of capillary phenomena, see again Ref. [RW02]).

films (see Fig. 1.4) [Ise92]. Soap films consist of a $5\,\mathrm{nm}$ - $20\,\mu\mathrm{m}$ thin layer of water between two monolayers composed of amphiphilic soap ions (such as the fatty acid anions, see Table 1.1). These ions can move laterally in the film exactly as the lipids in the membrane.

The fluidity of the surface implies that it cannot resist shear stresses. Hence, static shear is not a deformation which costs the surface any energy; in fact, it cannot even be defined. As we will restrict our considerations to fluid surfaces this property holds generally throughout this work.

Helfrich Hamiltonian

A bending deformation in the direction normal to the interface, however, *can* contribute to the total energy of a fluid surface. In a harmonic expansion the energy due to any deformation of the interface is proportional to the square of the deformation (remember Hooke's law). In the particular case of bending, one has to consider quadratic expressions of the curvature. At every point a surface has two principal curvatures k_1 and k_2, which are the eigenvalues of the local curvature tensor K^b_a. The corresponding eigenvectors define two orthogonal principal directions (see App. A.1). One therefore has to include two independent terms in the expression for the energy that depend on a quadratic combination of the two curvatures and are furthermore invariant scalars. One convenient choice is a combination of the Gaussian curvature $K_\mathrm{G} = k_1 k_2$ and the squared trace $K^2 = (k_1 + k_2)^2$ of the curvature tensor K_{ab}. Including surface tension the complete Hamiltonian is then according to Helfrich [Hel73]:

$$H = \int_\Sigma \mathrm{d}A \left[\sigma + \frac{\kappa}{2}(K - K_0)^2 + \bar{\kappa} K_\mathrm{G} \right] . \tag{1.2}$$

where κ and $\bar{\kappa}$ are proportionality constants called *bending rigidity* and *saddle-splay modulus*, respectively. The constant K_0 is the spontaneous curvature. Its value determines how much the surface prefers to be bent in its minimal energy state. The term involving the Gaussian curvature can be written as the sum of a topological constant and a line integral over the boundary of the surface (see App. A.3). The implications of this turn out to be subtle and will be discussed in more detail in Technical Point 2.3 on page 38.

A series of experimental and theoretical studies has shown that the energy associated with the membrane is mainly dominated by bending (see, for instance, Refs. [BL75, FMM$^+$89, DS95, LS95, Sei97, CDBN05]). The reason for this is that it is the softest mode: characteristically, weak bending is a deformation which costs significantly less energy than, for instance, stretching.

On length scales much larger than the bilayer thickness the Hamiltonian (1.2) is suitable to describe a fluid membrane.[8] For typical phospholipid membranes, κ

---

[8] It should be mentioned that the Hamiltonian (1.2) is also valid for other interfaces such as

is of the order of a few tens of $k_{\mathrm{B}}T$, where $k_{\mathrm{B}}T$ is the thermal energy [SL95]. Furthermore, membranes exhibit tensions σ in a broad range from 0 up to about 10 mN/m [MH01]. At even higher values they rupture. The Gaussian bending rigidity $\bar{\kappa}$ is rather difficult to measure. Its value is usually negative and also smaller than that of κ in the same system [GKD$^+$04, A3.24].[9]

General curvature Hamiltonians

The fact that curvature (a "generalized strain") enters quadratically in the Hamiltonian (1.2) classifies this form of the bending energy as "linear curvature elasticity" (even though the resulting field equations that describe the shape of the surface are highly nonlinear as we will see in Sec. 2.2.2). However, for sufficiently strong bending higher than quadratic terms will generally contribute to the energy density, giving rise to genuinely nonlinear curvature elasticity [GH96].

A general expression including all these terms is given by [Mül04]:

$$H_\Sigma[\boldsymbol{X}] = \int_\Sigma \mathrm{d}A\,\mathcal{H}(g_{ab}, K_{ab}, \nabla_a K_{bc}, \ldots)\,, \qquad a, b, \in \{1, 2\}\,, \qquad (1.3)$$

where the Hamiltonian density $\mathcal{H}$ depends exclusively on surface scalars constructed using the metric g_{ab}, the extrinsic curvature tensor K_{ab}, or its covariant derivatives $\nabla_a K_{bc}$, etc.

Note in particular that Hamiltonian (1.3) is invariant under surface reparametrizations. In order to describe the surface in a parametrization-free way, a covariant differential geometric language will be used. The notation is essentially standard and is summarized briefly in Technical Point 1.1.

1.2.2 Internal degrees of freedom

So far the discussion was restricted to Hamiltonians which are exclusively constructed from the geometry of the underlying surface. However, the surface itself may possess internal degrees of freedom which can couple to each other and, more interestingly, also to the geometry. The simplest example would be a *scalar field* ϕ on the membrane, which could describe a local variation in surface tension or lipid composition. In that case the Hamiltonian

$$H_\phi[\boldsymbol{X}, \phi] = \int_\Sigma \mathrm{d}A\,\left[\frac{\lambda_\phi}{2}(\nabla_a \phi)(\nabla^a \phi) + V(\phi) + \beta_\phi K \phi\right] \qquad (1.4)$$

---

those containing block copolymers.

[9] In Sec. 3.5 we will discuss an experimental setup with which the *difference* of the saddle-splay moduli of two different lipid domains on a vesicle can be measured.

─── **Technical Point 1.1:** *Differential geometry* ───

This Technical Point presents the basic notions of the differential geometry of two-dimensional surfaces. A comprehensive summary can be found in App. A.

A surface Σ is described locally by its position $\boldsymbol{X}(\xi^1, \xi^2) \in \mathbb{R}^3$, where the ξ^a ($a \in \{1,2\}$) are a suitable set of local coordinates on the surface. The tangent vectors of Σ, $\boldsymbol{e}_a = \partial \boldsymbol{X}/\partial \xi^a = \partial_a \boldsymbol{X}$ ($a, b \in \{1,2\}$), form a local coordinate frame; together with the extrinsic unit normal vector, $\boldsymbol{n} = \boldsymbol{e}_1 \times \boldsymbol{e}_2/|\boldsymbol{e}_1 \times \boldsymbol{e}_2|$, they define two geometrical tensors on the surface: the metric $g_{ab} = \boldsymbol{e}_a \cdot \boldsymbol{e}_b$ and the extrinsic curvature $K_{ab} = \boldsymbol{e}_a \cdot \partial_b \boldsymbol{n}$.
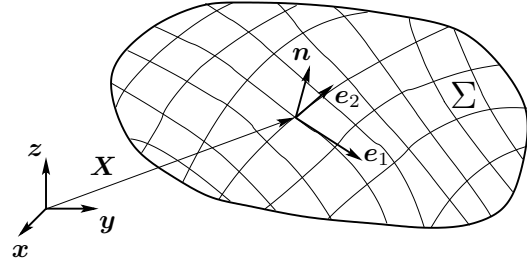
The symbol ∇_a is the metric-compatible covariant derivative. The trace of the extrinsic curvature tensor will be denoted by $K = K^a_a = K_{ab}g^{ab}$, which for a sphere of radius r with outward pointing normal vector is positive and has the value $K = 2/r$. The determinant $K_{\mathrm{G}} = \det(K^b_a)$ is the Gaussian curvature. It can be written as half the Ricci scalar curvature $\mathcal{R} = g^{ac}g^{bd}R_{abcd}$, the double-contraction of the Riemann tensor. This link between intrinsic and extrinsic curvatures is a consequence of the (doubly contracted) Gauss-Codazzi equation $\mathcal{R} = K^2 - K_{ab}K^{ab}$ ($= 2K_{\mathrm{G}}$). As usual, indices are lowered or raised with the metric or its inverse, respectively, and a repeated index a (one up, one down) implies a summation over $a = 1, 2$. More background on differential geometry can, for instance, be found in Refs. [Car76, Spi76, Kre91].

─────────

has to be added to the geometric Hamiltonian (1.3) [CG04].[10] The symbols λ_ϕ and β_ϕ denote coupling constants. The last term represents an interaction between the membrane curvature K and the field ϕ, whereas $V(\phi)$ is a scalar potential depending on the value of ϕ. This case will not be discussed further here.

Instead, let us look a little more closely at the case of an additional *tangential surface vector field* m^a (see Fig. 1.5). Such a field has been introduced to describe the *tilt* degrees of freedom of the molecules within a lipid bilayer to accommodate the fact that the average orientation $\hat{\boldsymbol{m}}$ of the lipids themselves need not coincide with the local bilayer normal $\boldsymbol{n}$ (see, for instance, Refs. [HP88, ML91, ML93, NP92, NP93, SSN96, HK00, MBS99, Fou99, May00, BKIM03, KZK04]).

How can such a tilt be excited? In Sec. 1.1.2 it was mentioned that proteins

───────

[10] As mentioned in Technical Point 1.1 the sum convention is used throughout this work: if an index occurs twice in a product, once as super- and once as subscript, one has to sum over this index from 1 to 2 even though no explicit summation sign is present.
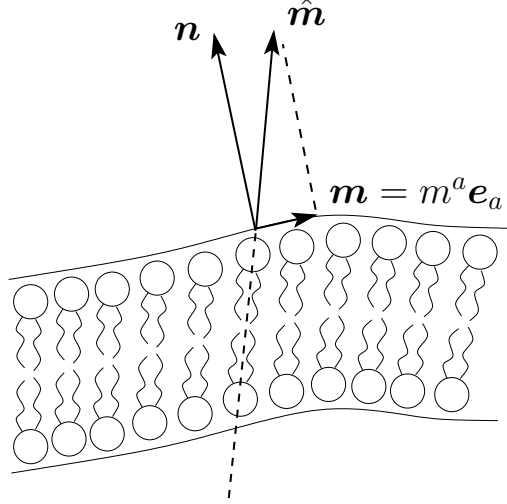
Figure 1.5: Lipid tilt. The unit vectors $\boldsymbol{n}$ and $\hat{\boldsymbol{m}}$ denote the local bilayer normal and average orientation of the lipids themselves. The values for m^a $(a \in \{1, 2\})$ can be obtained by projecting $\hat{\boldsymbol{m}}$ onto the tangent plane of the bilayer.

can span the entire membrane. These transmembrane proteins are not necessarily shaped like a straight cylinder but can also vary in thickness over the width of the membrane looking, for instance, like a truncated cone. Such a *membrane inclusion* distorts the lipid order close to it leading to a non-vanishing field m^a.[11]

In the presence of a field m^a many additional terms for the energy emerge (for a systematic classification see Refs. [NP92, NP93]). However, the aim here is not to treat the most general case. Instead, let us focus on a simple representative example to illustrate how easily the present formalism generalizes to treat such situations.

If one defines the properly symmetrized covariant tilt-strain tensors M^{ab} and F^{ab} according to

$$M^{ab} = \frac{1}{2}\big(\nabla^a m^b + \nabla^b m^a\big) \; , \tag{1.5a}$$

$$F^{ab} = \nabla^a m^b - \nabla^b m^a \; , \tag{1.5b}$$

one can construct (in the spirit of a harmonic theory) a Hamiltonian H_m from four quadratic invariants:

$$H_\mathrm{m}[\boldsymbol{X}, m^a] = \int_\Sigma \mathrm{d}A \left[\frac{1}{2}\lambda_\mathrm{m} M^2 + \mu_\mathrm{m} M_{ab} M^{ab} + \frac{1}{4}\nu_\mathrm{m} F_{ab} F^{ab} + V(m^2)\right] \; , \tag{1.6}$$

---

[11] Note that membrane inclusions can also excite a change in membrane thickness if their hydrophobic domain is much larger or smaller than the hydrophobic core of the bilayer [Kil98]. This *hydrophobic mismatch*, however, will not be treated here.

where $M = g_{ab}M^{ab} = \nabla_a m^a$ is the tilt divergence. The first two terms coincide with the lowest order intrinsic terms identified by Nelson and Powers [NP92, NP93], provided one restricts to unit vectors m^a.[12] These terms are multiplied by new elastic constants λ_{m} and μ_{m}, playing the analogous role to Lamé-coefficients.[13] If $m^2 \neq 1$, a third term (also absent in usual elasticity theory [LL86]) occurs, the quadratic scalar constructed from the antisymmetrized tilt gradient; its structure is completely analogous to the Lagrangian in electromagnetism [LL00]. Finally, if the magnitude of m^a is not fixed, one may also add a potential V depending on the square $m^2 = m_a m^a$ of the vector field m^a. Without loss of generality one can assume that $V(0) = 0$ because any nonvanishing constant is more appropriately absorbed into the surface tension σ. If $V(x)$ is minimal for $x = 0$, then $m^a \equiv 0$ will minimize the energy, but depending on physical conditions V may favor nonzero values of $|m^a|$. In this case the lipids can acquire a spontaneous tilt below the main phase transition temperature of lipid bilayers (*cf.* Sec. 1.1.1).

1.2.3 Bulk energies

Surfaces do not live in vacuum. They are embedded in the surrounding space which often provides for additional contributions to the total energy. In this section we will discuss two examples, a global pressure difference and a gravitational field.

Global pressure difference

In an aqueous environment any *open* patch of membrane costs a large amount of energy because at the edge the hydrophobic core of the bilayer is in direct contact with the water. Therefore, free membrane patches usually do not exist in the cell. They close to form vesicles (see Fig. 1.1(c)).
If the volume V is fixed to a constant V_0, a term $-P(V - V_0)$ has to be added to the energy functional H of the free surface:

$$H_P = H - P(V - V_0) \, , \tag{1.7}$$

where the pressure difference P is the Lagrange multiplier for the enclosed volume. A similar term may also be used to fix the pressure difference between the two

---

[12] Using the commutation relations for covariant derivatives (A.19) and (A.20) it is easy to see that $(\nabla_a m^b)(\nabla_b m^a) = (\nabla_a m^a)^2 - \frac{1}{2}\mathcal{R}m^2$. If $m^2 = 1$, the Gauss-Bonnet-theorem renders the last term a boundary contribution (see App. A.3), and it is then easy to see that the λ_{m}- and μ_{m}-terms in Eqn. (1.6) are sufficient.

[13] In order for the Hamiltonian density (1.6) to be positive definite in the strain gradient $\nabla^a m^b$, it is necessary that $\mu_{\mathrm{m}} > 0$ and $\lambda_{\mathrm{m}} + \mu_{\mathrm{m}} > 0$. The latter differs from the "usual" condition $\lambda_{\mathrm{m}} + \frac{2}{3}\mu_{\mathrm{m}} > 0$ found in Ref. [LL86] because in the surface case one only has two-dimensional tensors. The positivity of the *antisymmetric* term requires $\nu_{\mathrm{m}} < 0$ since the square of an antisymmetric matrix has negative eigenvalues.

sides of the surface:

$$H_P = H - PV \; . \tag{1.8}$$

Both ensembles (constant volume vs. constant pressure) yield the same ground states for the shape of the surface. Questions of stability depend on which of the two variables is fixed: a surface shape found to be stable under constant V is not necessarily stable under constant P. In Technical Point 2.5 on page 44 we will discuss this point for one example where the surface is a closed soap film (*i. e.*, a soap bubble).

With the help of Gauss' Theorem the volume V can be written as an integral over the enclosing surface ∂V:

$$V = \int_V \mathrm{d}V' \, \frac{\nabla \cdot \boldsymbol{X}}{3} = \frac{1}{3} \int_{\partial V} \mathrm{d}A \, \boldsymbol{n} \cdot \boldsymbol{X} \; , \tag{1.9}$$

where $\boldsymbol{n}$ is the unit vector normal to the surface and $\boldsymbol{X}$ the position of the surface in $\mathbb{R}^3$ as before. This allows us to express Hamiltonian (1.8) as a surface integral:

$$H_P = H - \frac{1}{3} P \int_{\Sigma} \mathrm{d}A \, \boldsymbol{n} \cdot \boldsymbol{X} \; . \tag{1.10}$$

Gravity

Another energy contribution from the bulk may stem from gravity. On the size of a typical cell membrane ($\lesssim 1\,\mu\mathrm{m}$) the gravitational field can be neglected. For fluid surfaces on larger length scales, however, it becomes relevant as we will see in the following chapters.

As an example consider a liquid-fluid interface Σ in a homogeneous (downwards pointing) gravitational field of acceleration g (see Fig. 1.6). Gravity will make sure that in equilibrium the heavier of the two fluid phases will be below the lighter one. Furthermore, any deformation of the interface will increase the potential energy of the system, *e. g.* by lifting or lowering the heavier phase. This total potential energy can be written as

$$E_{\mathrm{pot}} = g \int_{\mathrm{all \; fluid}} \mathrm{d}V \, \rho(\boldsymbol{X}) h(\boldsymbol{X}) \; , \tag{1.11}$$

where $\rho(\boldsymbol{X})$ is the local density and $h(\boldsymbol{X})$ is the height above some arbitrary horizontal reference plane which fixes the zero-point of the potential energy.

In the following let us assume that both phases are incompressible. Hence, the density in each phase will not depend on the position. Up to a constant one may thus equivalently integrate the *excess density* ρ of the heavier phase over the volume V_{hp} occupied by the heavier phase:

$$E_{\mathrm{pot}} = \rho g \int_{V_{\mathrm{hp}}} \mathrm{d}V \, h(\boldsymbol{X}) \; . \tag{1.12}$$
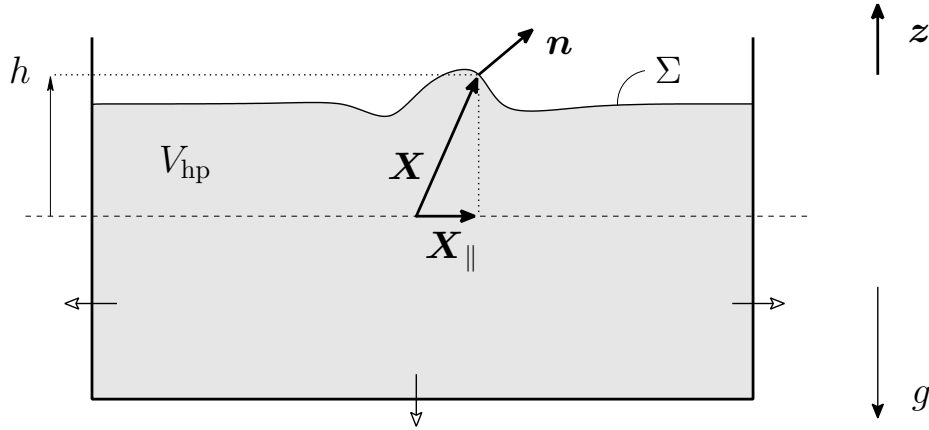
Figure 1.6: Liquid-fluid interface in a homogeneous gravitational field.

The volume integral can then be split into an area integral over the reference plane times a height integral perpendicular to it; the latter can be done explicitly:

$$E_{\text{pot}} = \rho g \int \mathrm{d}A_{\parallel} \int_0^{h(\boldsymbol{X}_{\parallel})} \mathrm{d}z\, z = \frac{1}{2}\rho g \int \mathrm{d}A_{\parallel}\, h(\boldsymbol{X}_{\parallel})^2 \,, \qquad (1.13)$$

where $h(\boldsymbol{X}_{\parallel})$ is now written as a function of the coordinates $\boldsymbol{X}_{\parallel}$ of the reference plane.[14] This energy depends of course on the embedding of the interface into exterior space which is indeed a physical requirement. However, the way it is written it also depends on the *parametrization* of that surface, and this is something one would like to avoid if possible.

In order to achieve that, any reference to some arbitrary base plane has to be eliminated. This could be done if one was able to rewrite the integrand in the volume integral (1.12) as a pure divergence. Using Gauss' Theorem again it would then be possible to express it as a surface integral over the actual surface of the heavier phase rather than some arbitrary reference plane.

Indeed, if $\boldsymbol{z}$ is the upward direction, then

$$h = \boldsymbol{X} \cdot \boldsymbol{z} = \frac{1}{2}\boldsymbol{\nabla} \cdot \left(X^2 \boldsymbol{z}\right) \,, \qquad (1.14)$$

and thus the potential energy can also be written as

$$E_{\text{pot}} = \frac{1}{2}\rho g \int_{V_{\text{hp}}} \mathrm{d}V\, \boldsymbol{\nabla} \cdot (X^2 \boldsymbol{z}) = \frac{1}{2}\rho g \int_{\partial V_{\text{hp}}} \mathrm{d}A\, (\boldsymbol{n} \cdot \boldsymbol{z})\, X^2 \,, \qquad (1.15)$$

---

[14] The surface parametrization that is chosen here is also called *Monge parametrization*. It is applicable as long as the surface has no overhangs (see App. A.4.1).

where the surface integral now runs over the *complete* surface of the lower phase. This expression is essentially parametrization-free; in particular, it does no longer make reference to some arbitrary base plane. Notice, however, that the vertical sides of the fluid volume do not contribute to this integral (since there $\boldsymbol{z} \perp \boldsymbol{n}$) while the lower (horizontal) surface gives a contribution which does not change if the upper free surface is modified. Hence, the only nontrivial contribution to the energy stems from the *upper surface integral* over the fluid-liquid interface Σ in Eqn. (1.15).

To obtain the full Hamiltonian H_G, the potential energy has to be added to all other terms that contribute to the surface energy. In the case of a liquid-fluid interface a tension will enter.[15] Additionally, one has to take into account that the volume of the liquid is constant. One thus obtains the Hamiltonian:

$$H_G = \int_\Sigma \mathrm{d}A \, \sigma - P(V - V_0) + E_{\mathrm{pot}} \, . \tag{1.16}$$

Gravity will serve as an interesting and instructive but still manageable example for how non-constant bulk stresses act on surfaces. We therefore include it in our discussion, even though it is seldomly important for the length scales prevailing at biological membranes.

However, the main focus in this work will be on the fluid membrane. As we now know the energies that determine its physics, questions of membrane mechanics can be addressed, for instance, by examining the effects of forces and torques on its shape.

---

[15] In general of course, Hamiltonian (1.3) and possibly terms that reflect internal degrees of freedom have to be inserted.

2 Surface Mechanics

In Sec. 1.1 we have seen that membranes in cells are not isolated free objects. They experience a variety of external forces and torques. For example, proteins adhere to them and impose deformations, actin filaments of the cytoskeleton push and pull at them, pressure differences between the inner and outer sides may even cause their rupture. Furthermore, lipid rafts have a higher rigidity than their surroundings, or certain mechanosensitive membrane channels open and close gated by the tension of the membrane.

All these examples show that the mechanical properties of membranes are vital for the functioning of biological cells. A first step to understand these properties is to determine what *shape* the membrane adopts if it is subjected to some specific boundary conditions. Given the shape, *forces* and *torques* can be determined which are imprinted in the geometry of the membrane.

2.1 Stresses and torques in fluid surfaces

The equilibrium shape of a surface is governed by a nonlinear partial differential equation, the "shape equation". Stresses and torques in the surface are fully encoded in its geometry and described by divergence-free tensors.

In the following, the basic equations which govern the behavior of the membrane are derived. To keep the approach sufficiently general, we first consider the generic case of a surface Σ whose energetics can be described by the reparametrization invariant Hamiltonian (1.3)

$$H_\Sigma[\boldsymbol{X}] = \int_\Sigma \mathrm{d}A\ \mathcal{H}(g_{ab}, K_{ab}, \nabla_a K_{bc}, \dots)\ . \tag{2.1}$$

2.1.1 First variation and Euler-Lagrange equations

To determine the equilibrium (*i. e.*, energy minimizing) shape of the surface, the functional (2.1) has to be minimized with respect to deformations of Σ. These deformations are described by a change in the embedding functions $\boldsymbol{X} \to \boldsymbol{X} + \delta\boldsymbol{X}$. The response of the Hamiltonian can be written as [CG02b, Mül04]:

$$\delta H_\Sigma = \int_\Sigma \mathrm{d}A\ \mathcal{E}(\mathcal{H})\, \boldsymbol{n} \cdot \delta\boldsymbol{X} + \int_\Sigma \mathrm{d}A\ \nabla_a Q^a\ . \tag{2.2}$$

The bulk part of this variation is a surface integral over the Euler-Lagrange derivative $\mathcal{E}(\mathcal{H})$ times the normal projection of the surface variation $\delta \boldsymbol{X}$. Its vanishing determines the equilibrium shape of the interface. Hence, $\mathcal{E} = 0$ is also called the "shape equation". The second term of the variation is a surface integral over a divergence and can thus be recast as a boundary integral using the divergence theorem [Fra03]. It originates from tangential variations[1] as well as the derivatives of normal variations.

The straightforward way to determine $\mathcal{E}$ and Q^a explicitly is to track the course of the deformation on $\boldsymbol{X}$ through g_{ab}, $\sqrt{g}$, K_{ab}, and any appearing covariant derivatives. This turns out to be rather tedious as g_{ab}, K_{ab}, ... indirectly depend on $\boldsymbol{X}$ via the structural relationships (see App. A.1)

$$
\begin{align}
g_{ab} &= \boldsymbol{e}_a \cdot \boldsymbol{e}_b \qquad\qquad \text{and} \tag{2.3a}\\
K_{ab} &= \boldsymbol{e}_a \cdot \partial_b \boldsymbol{n} = \boldsymbol{e}_a \cdot \nabla_b \boldsymbol{n} \,, \tag{2.3b}
\end{align}
$$

with

$$
\begin{align}
\boldsymbol{e}_a &= \partial \boldsymbol{X}/\partial \xi^a = \partial_a \boldsymbol{X} = \nabla_a \boldsymbol{X} \,, \tag{2.4a}\\
\boldsymbol{e}_a \cdot \boldsymbol{n} &= 0 \,, \tag{2.4b}\\
\boldsymbol{n}^2 &= 1 \,. \tag{2.4c}
\end{align}
$$

Alternatively, one can treat g_{ab}, K_{ab}, $\boldsymbol{e}_a$ and $\boldsymbol{n}$ as *independent* variables, enforcing the structural relations (2.3) and (2.4) using Lagrange multiplier functions as was first pointed out by Guven [Guv04]. One thus introduces the new functional $H_c[g_{ab}, K_{ab}, \ldots, \boldsymbol{X}, \boldsymbol{e}_a, \boldsymbol{n}, \lambda^{ab}, \Lambda^{ab}, \boldsymbol{f}^a, \lambda_\perp^a, \lambda_n]$ given by

$$
\begin{align}
H_c &= H[g_{ab}, K_{ab}, \nabla_a K_{bc}, \ldots] + \int_\Sigma \mathrm{d}A \, [\lambda^{ab}(g_{ab} - \boldsymbol{e}_a \cdot \boldsymbol{e}_b) + \Lambda^{ab}(K_{ab} - \boldsymbol{e}_a \cdot \nabla_b \boldsymbol{n})] \notag\\
&+ \int_\Sigma \mathrm{d}A \, [\boldsymbol{f}^a \cdot (\boldsymbol{e}_a - \nabla_a \boldsymbol{X}) + \lambda_\perp^a (\boldsymbol{e}_a \cdot \boldsymbol{n}) + \lambda_n (\boldsymbol{n}^2 - 1)] \,. \tag{2.5}
\end{align}
$$

The original Hamiltonian H is now treated as a function of the *independent* variables g_{ab}, K_{ab} and their covariant derivatives; λ^{ab}, Λ^{ab}, $\boldsymbol{f}^a$, $\lambda_\perp^a$ and λ_n are Lagrange multiplier functions fixing the constraints (2.3) and (2.4). The introduction of auxiliary variables greatly simplifies the variational problem, because now we do not have to track explicitly how the deformation $\delta \boldsymbol{X}$ propagates through to g_{ab} and K_{ab}. As we will see in the following, this approach also provides a very simple and direct derivation of the shape equation in which the multiplier $\boldsymbol{f}^a$, which pins the tangent vectors to the surface, can be identified as the surface stress tensor.

---

[1] Away from the boundary, a tangential variation can be identified with a reparametrization of the surface. It always results in a pure divergence which is why it does not enter the shape equation [CG02b].

The Euler-Lagrange equations for $\boldsymbol{X}$, $\boldsymbol{e}_a$, $\boldsymbol{n}$, g_{ab}, and K_{ab}, respectively, are given by

$$\nabla_a \boldsymbol{f}^a = 0 \, , \tag{2.6a}$$

$$\boldsymbol{f}^a = (\Lambda^{ac} K_c^{\ b} + 2\lambda^{ab})\boldsymbol{e}_b - \lambda_\perp^a \boldsymbol{n} \, , \tag{2.6b}$$

$$0 = (\nabla_b \Lambda^{ab} + \lambda_\perp^a)\boldsymbol{e}_a + (2\lambda_n - \Lambda^{ab} K_{ab})\boldsymbol{n} \, , \tag{2.6c}$$

$$\lambda^{ab} = \tfrac{1}{2} T^{ab} \, , \tag{2.6d}$$

$$\Lambda^{ab} = -\mathcal{H}^{ab} \, . \tag{2.6e}$$

Note that the Weingarten equations (A.39) $\nabla_a \boldsymbol{n} = K_a^{\ b} \boldsymbol{e}_b$ have been used in Eqn. (2.6b), the Gauss equations (A.41) $\nabla_a \boldsymbol{e}_b = -K_{ab}\boldsymbol{n}$ in Eqn. (2.6c). We have also defined

$$\mathcal{H}^{ab} := \frac{\delta \mathcal{H}}{\delta K_{ab}} \quad \text{and} \tag{2.7a}$$

$$T^{ab} := -\frac{2}{\sqrt{g}} \frac{\delta(\sqrt{g}\mathcal{H})}{\delta g_{ab}} \, . \tag{2.7b}$$

The manifestly symmetric tensor T^{ab} is the intrinsic stress tensor associated with the metric g_{ab}. If $\mathcal{H}$ does not depend on derivatives of K_{ab}, the functional derivatives in (2.7) reduce to ordinary ones.

Equation (2.6a) reveals the existence of a conservation law for the multiplier $\boldsymbol{f}^a$. Using the other equations (2.6c), (2.6d), and (2.6e), it is straightforward to eliminate the Lagrange multipliers on the right hand side of Eqn. (2.6b) to obtain an explicit expression for $\boldsymbol{f}^a$ in terms of the original geometrical variables. From Eqn. (2.6c) we find $\lambda_\perp^a = -\nabla_b \Lambda^{ab}$ because $\boldsymbol{e}_a$ and $\boldsymbol{n}$ are linearly independent; the Eqns. (2.6d) and (2.6e) determine λ^{ab} and Λ^{ab}. Thus Eqn. (2.6b) can be recast as

$$\boxed{\boldsymbol{f}^a = (T^{ab} - \mathcal{H}^{ac} K_c^{\ b})\boldsymbol{e}_b - (\nabla_b \mathcal{H}^{ab})\boldsymbol{n} \, .} \tag{2.8}$$

Once the Hamiltonian density has been specified, Eqn. (2.8) determines the conserved multiplier $\boldsymbol{f}^a$ completely in terms of the geometry (see App. B.2 where several examples are treated).

The Hamiltonian (2.5) involves covariant derivatives of $\boldsymbol{X}$, $\boldsymbol{n}$, and possibly K_{ab}. To isolate the Euler-Lagrange equations (2.6), these derivatives have to be removed via integration by parts. The resulting total derivatives must not be neglected, however, as they contribute to the boundary integral of the variation (2.2). An additional term due to the variation with respect to g_{ab} may appear as well because $\nabla_a K_{bc}$ depends on the metric indirectly via the Christoffel symbols.[2,3]

---

[2] Note that this is not true for $\nabla_a \boldsymbol{X}$ and $\nabla_a \boldsymbol{n}$ as both can be written as partial derivatives.

[3] For instance, the covariant derivative of a scalar ϕ is given by $\nabla_a \phi = \partial_a \phi$ while for the

Collecting all terms together one obtains an expression for the boundary part of the variation (2.2):

$$Q^a = -\boldsymbol{f}^a \cdot \delta \boldsymbol{X} \ + \ \mathcal{H}^{ab} \boldsymbol{e}_b \cdot \delta \boldsymbol{n} \ + \ \mathcal{G}^{abc} \delta g_{bc} \ + \ \mathcal{K}^{abc} \delta K_{bc} \ . \tag{2.9}$$

This equation defines the tensors $\mathcal{G}^{abc}$ and $\mathcal{K}^{abc}$ as the boundary contributions belonging to the variation with respect to the metric and the extrinsic curvature tensor, respectively. If $\mathcal{H}$ is just a function of g_{ab} and K_{ab}, $\mathcal{G}^{abc}$ and $\mathcal{K}^{abc}$ are equal to zero. If only first derivatives of K_{ab} appear in $\mathcal{H}$, these tensors will be functions and can be written as (see App. B.2.2)

$$\mathcal{K}^{abc} \ = \ \frac{\partial \mathcal{H}}{\partial (\nabla_a K_{bc})} \quad \text{and} \tag{2.10a}$$

$$\mathcal{G}^{abc} \ = \ -\left(\mathcal{K}^{acd} K_d^b + \mathcal{K}^{cad} K_d^b - \mathcal{K}^{cbd} K_d^a \right) \ . \tag{2.10b}$$

In general, if derivatives of order higher than first occur in the Hamiltonian, $\mathcal{G}^{abc}$ and $\mathcal{K}^{abc}$ will be differential operators acting on g_{ab} and K_{ab} respectively.

Now let us suppose that $\delta \boldsymbol{X} = \delta \boldsymbol{a} \in \mathbb{R}^3$ is just an arbitrary constant translation that of course leaves the Hamiltonian invariant, even if the surface is *not* in equilibrium. In this case, the first variation (2.2) can be written as[4]

$$\begin{aligned} \delta H_\Sigma \ &= \ \int_\Sigma \mathrm{d}A \ \mathcal{E}(\mathcal{H}) \, \boldsymbol{n} \cdot \delta \boldsymbol{a} - \int_\Sigma \mathrm{d}A \ \nabla_a (\boldsymbol{f}^a \cdot \delta \boldsymbol{a}) \\ &= \ \delta \boldsymbol{a} \cdot \int_\Sigma \mathrm{d}A \ \left[\mathcal{E}(\mathcal{H}) \, \boldsymbol{n} - \nabla_a \boldsymbol{f}^a \right] \overset{!}{=} 0 \ . \end{aligned} \tag{2.11}$$

The integral must be equal to zero because $\delta \boldsymbol{a}$ can be arbitrarily chosen. Moreover, the integrand vanishes pointwise because Σ may be arbitrarily chosen as well. Thus,

$$\nabla_a \boldsymbol{f}^a = \mathcal{E}(\mathcal{H}) \boldsymbol{n} \ . \tag{2.12}$$

If the surface is a true equilibrium surface, which implies that it is stationary with respect to *arbitrary* variations, the shape equation $\mathcal{E} = 0$ also holds and we recover the conservation law (2.6a) for $\boldsymbol{f}^a$.[5]

Finally, Eqn. (2.8) permits us to write $\mathcal{E}(\mathcal{H})$ completely in terms of the surface geometry: projecting Eqn. (2.12) onto the surface normal $\boldsymbol{n}$ and using the Gauss equations (A.41) once more, we obtain the remarkably succinct result

$$\boxed{\boldsymbol{n} \cdot \nabla_a \boldsymbol{f}^a = \mathcal{E}(\mathcal{H}) = -K_{ab} T^{ab} + (K_{ac} K_b^c - \nabla_a \nabla_b) \mathcal{H}^{ab}} \ . \tag{2.13}$$

---

contravariant tensor field K_{bc} one has $\nabla_a K_{bc} = \partial_a K_{bc} - \Gamma_{ab}{}^d K_{dc} - \Gamma_{ac}{}^d K_{bd}$, where $\Gamma_{ab}{}^c$ is the Christoffel symbol of the second kind, defined by $\Gamma_{ab}{}^c = \frac{1}{2} g^{cd} (\partial_a g_{bd} + \partial_b g_{da} - \partial_d g_{ab})$ (see page 168 in App. A.1).

[4] The variations $\delta \boldsymbol{n}$, δg_{ab}, and δK_{ab} vanish in this case.

[5] For unconstrained surfaces $\mathcal{E}(\mathcal{H}) = 0$ is indeed the shape equation. However, further constraints such as a global pressure difference imply additional terms as we will see in Sec. 2.3.
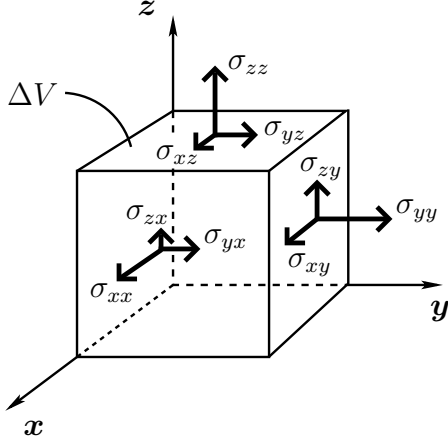
In classical elasticity theory the divergence of the stress tensor $\boldsymbol{\sigma}$ at any point in a strained material equals the external force density if the whole body is in equilibrium [LL86]. Or equivalently, the stress tensor contracted with the normal vector of a local fictitious area element yields the *force per unit area* transmitted through this area element. For a small cubic part ΔV of an arbitrarily shaped body in Euclidean space $\mathbb{R}^3$ the components of the total external force can thus be written as ($i \in \{x, y, z\}$)

$$\boldsymbol{F}_i^{\Delta V} = \sum_{j=x}^{z} \int_{\Delta V} \mathrm{d}V \, \partial_j \sigma_{ij} = \sum_{j=x}^{z} \oint_{\partial \Delta V} \mathrm{d}A_j \, \sigma_{ij} \, ,$$

where, for example σ_{xy} is the force in x-direction acting on the unit area perpendicular to the y axis (see sketch). The divergence theorem was used in the second step and ∂_j is the partial derivative with respect to j.

Comparing this with Eqn. (2.14) we see that $\boldsymbol{f}^a$ is indeed the surface analog of the stress tensor: its divergence integrated over the surface yields a force. In fact, analogous to the 3D case, this integral can be rewritten as a boundary integral over the contraction of $\boldsymbol{f}^a$ with the normal vector of the local line element (see Eqns. (2.15) and (2.16)).

2.1.2 Surface stress and surface torque tensor

Identification of the stress tensor

A closer inspection of the translational variation (2.11) reveals that the conservation law (2.6a) for the vector $\boldsymbol{f}^a$ is simply a consequence of Noether's theorem: a continuous symmetry (= translational invariance) implies an associated conserved current (= $\boldsymbol{f}^a$) on shell (*i. e.*, in equilibrium). To identify this current, consider the variation (2.11) for $\mathcal{E}(\mathcal{H}) = 0$:

$$\delta H_\Sigma = -\delta \boldsymbol{a} \cdot \int_\Sigma \mathrm{d}A \, \nabla_a \boldsymbol{f}^a \, . \tag{2.14}$$

The change in energy is given by the negative product of an infinitesimal translation times an integral. Thus, the integral is a force. From this follows that the divergence of $\boldsymbol{f}^a$ must be a force density. The vector $\boldsymbol{f}^a$ encodes the stresses in the surface. If we compare it with the stress tensor $\boldsymbol{\sigma}$ of a body in three-dimensional
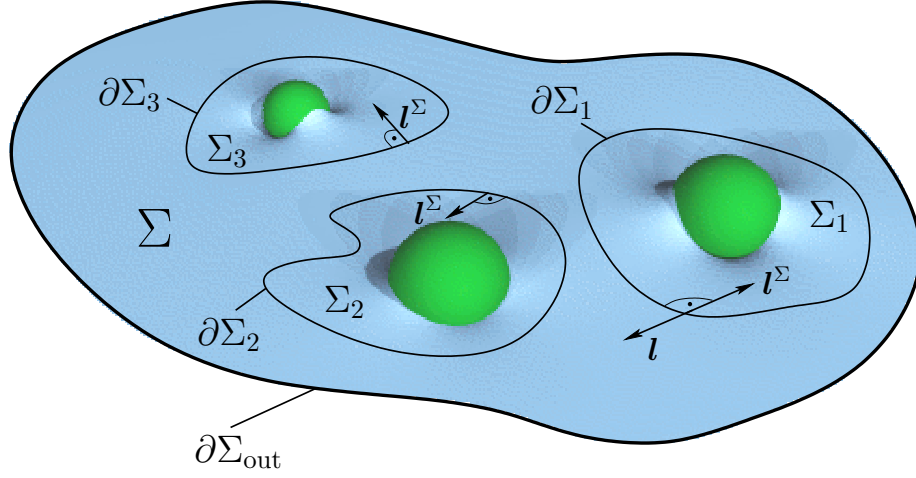
Figure 2.1: Surface patch Σ with 3 disjoint boundary components $\partial\Sigma_i$ and an outer limiting boundary $\partial\Sigma_{\text{out}}$.

Euclidean space, it becomes obvious that $\boldsymbol{f}^a$ must be the *surface stress tensor* (see Technical Point 2.1).

This identification is correct for a surface which is free to equilibrate in every point. But does $\boldsymbol{f}^a$ still encode all of the surface stresses if external forces are acting on the surface? To answer that question we have to discuss a more complicated situation: consider a region of surface bounded by an outer limiting curve $\partial\Sigma_{\text{out}}$ and suppose that the bulk of this surface is in equilibrium with N particles that are attached to it (see Fig. 2.1). We now choose a curve around each of the particles, labeling these curves $\partial\Sigma_i, i = 1, \ldots, N$. The outer curve $\partial\Sigma_{\text{out}}$ together with all $\partial\Sigma_i$ encloses the surface patch Σ. Considering this patch first allows us to use variation (2.2) to identify the stress tensor as no particles are attached to Σ and every point on it is free to equilibrate.

If one of the boundaries $\partial\Sigma_i$ is translated infinitesimally by $\delta\boldsymbol{a}$, the boundary variation of the Hamiltonian (2.1) is equal to

$$\delta H^{(i)}_\Sigma \overset{(2.2)}{=} -\delta\boldsymbol{a} \cdot \oint_{\partial\Sigma_i} \mathrm{d}s\, l^\Sigma_a \boldsymbol{f}^a = -\delta\boldsymbol{a} \cdot \boldsymbol{F}^{(i)}_{\Sigma,\text{ext}} \, , \tag{2.15}$$

where the divergence theorem was used to convert the surface integral into a boundary integral. The vector $\boldsymbol{l}^\Sigma = l^\Sigma_a \boldsymbol{e}^a$ is the unit vector which is normal to $\partial\Sigma_i$ and points out of the surface Σ; by construction it is tangential to Σ (see Fig. 2.1 and App. A.2). The variable s measures the arc length along $\partial\Sigma_i$.

In Eqn. (2.15), the boundary integral is identified as the external force $\boldsymbol{F}^{(i)}_{\Sigma,\text{ext}}$ acting on Σ via its boundary $\partial\Sigma_i$. The external force $\boldsymbol{F}^{(i)}_{\text{ext}}$ *on the surface patch Σ_i is then*

simply given by $-\boldsymbol{F}_{\Sigma,\text{ext}}^{(i)}$ due to force balance. Notice that this argument does not require us to assume that the Euler-Lagrange equation is satisfied on Σ_i. Thus, *even if* external forces are acting, the conserved current $\boldsymbol{f}^a$ correctly encodes the stresses in the surface at all points not externally acted upon.

The conservation law (2.6a) for $\boldsymbol{f}^a$ in fact allows us to deform the contour of integration $\partial\Sigma_i$ to our advantage when asking for the external force $\boldsymbol{F}_{\text{ext}}^{(i)}$. As long as we do not cross any further sources of stress, the value of the integral in Eqn. (2.15) will remain the same. In Chap. 5 this fact will be exploited in the context of interface-mediated interactions.

To simplify notation, we will restrict our considerations to the patch $\partial\Sigma_1$ without loss of generality and write $\boldsymbol{F}_{\text{ext}} := \boldsymbol{F}_{\text{ext}}^{(1)}$, with

$$\boldsymbol{F}_{\text{ext}} = \oint_{\partial\Sigma_1} \mathrm{d}s \, l_a \boldsymbol{f}^a \;, \tag{2.16}$$

where $\boldsymbol{l} = l_a \boldsymbol{e}^a = -\boldsymbol{l}^\Sigma$.

It proves instructive to look at the tangential and normal projection of the stress tensor by defining the tensors f^{ab} and f^a such that [CG02b, Guv04]

$$\boldsymbol{f}^a = f^{ab}\boldsymbol{e}_b + f^a \boldsymbol{n} \;. \tag{2.17}$$

Using the equations of Gauss (A.41) and Weingarten (A.39) again, Eqn. (2.12) can then be cast in the form

$$\nabla_a f^a = K_{ab} f^{ab} + \mathcal{E} \;, \tag{2.18a}$$
$$\nabla_a f^{ab} = -K_a^b f^a \;. \tag{2.18b}$$

Tangential stress acts as a source of normal stress – and vice versa. Both conditions hold irrespective of whether the Euler-Lagrange derivative $\mathcal{E}$ actually vanishes. In fact, Eqn. (2.18a) shows that the shape equation $\mathcal{E} = 0$ is equivalent to $\nabla_a f^a = K_{ab} f^{ab}$, while Eqn. (2.18b) merely provides consistency conditions on the stress components that reflect the reparametrization invariance of the Hamiltonian. In Table 2.1 the stress tensor and the Euler-Lagrange derivative for several simple Hamiltonians are summarized (for the calculations see App. B.2).

Analogous to translational invariance, the rotational invariance of H implies the existence of another conserved tensor $\boldsymbol{m}^a$ which, as will be demonstrated in the next section, can be identified as the torque tensor.

Identification of the torque tensor

Once again consider the surface in Fig. 2.1: under a constant infinitesimal rotation $\delta\boldsymbol{\beta}$ of one of the boundaries $\partial\Sigma_i$, the position and normal vectors change according

$\mathcal{H}$	$\mathcal{E}$	f^{ab}	f^a
1	K	$-g^{ab}$	0
$\mathcal{R}$	0	0	0
K^n	$\left(\frac{1}{n}K^2 - K_{ab}K^{ab} - \Delta\right)nK^{n-1}$	$(nK^{ab}-Kg^{ab})K^{n-1}$	$-n\,\nabla^a K^{n-1}$
K^2	$K(K^2-2K_{ab}K^{ab})-2\Delta K$	$(2K^{ab}-Kg^{ab})K$	$-2\nabla_a K$
$K_{ab}K^{ab}$	,,	,,	,,
$\frac{1}{2}(\nabla K)^2 \equiv \frac12\cdot(\nabla_c K)(\nabla^c K)$	$(\Delta + K^2 - \mathcal{R})\Delta K - K^{ab}\cdot[(\nabla_a K)(\nabla_b K) - \frac12 g_{ab}(\nabla K)^2]$	$(\nabla^a K)(\nabla^b K) - \frac12 g^{ab}\cdot(\nabla K)^2 - K^{ab}\Delta K$	$\nabla^a\Delta K$

Table 2.1: Euler-Lagrange derivative $\mathcal{E}(\mathcal{H}) = -K_{ab}f^{ab} + \nabla_a f^a$ and the components of the stress tensor $\boldsymbol{f}^a = f^{ab}\boldsymbol{e}_b + f^a\boldsymbol{n}$ for several simple scalar surface Hamiltonian densities $\mathcal{H}$. Notice that K^2 and $K^{ab}K_{ab}$ yield identical $\mathcal{E}$ and $\boldsymbol{f}^a$ (see App. B.2.1).

to $\delta\boldsymbol{X} = \delta\boldsymbol{\beta}\times\boldsymbol{X}$ and $\delta\boldsymbol{n} = \delta\boldsymbol{\beta}\times\boldsymbol{n}$. In this case, the boundary variation of the Hamiltonian (2.1) is given by

$$\delta H_\Sigma^{(i)} \overset{(2.2)}{=} -\delta\boldsymbol{\beta}\cdot\oint_{\partial\Sigma_i}\mathrm{d}s\, l_a^\Sigma\left[\boldsymbol{X}\times\boldsymbol{f}^a + \mathcal{H}^{ab}\boldsymbol{e}_b\times\boldsymbol{n}\right]$$

$$= -\delta\boldsymbol{\beta}\cdot\oint_{\partial\Sigma_i}\mathrm{d}s\, l_a^\Sigma\boldsymbol{m}^a = -\delta\boldsymbol{\beta}\cdot\boldsymbol{M}_{\Sigma,\mathrm{ext}}^{(i)}\,, \tag{2.19}$$

where the surface integral was converted into a boundary integral on the first line. The vector $\boldsymbol{l}^\Sigma = l_a^\Sigma\boldsymbol{e}^a$ is defined as above and s again measures the arc length along $\partial\Sigma_i$.

In Eqn. (2.19), the boundary integral is nothing but the external torque $\boldsymbol{M}_{\Sigma,\mathrm{ext}}^{(i)}$ acting on Σ via its boundary $\partial\Sigma_i$: the corresponding change in energy is given by (minus) the scalar product of $\boldsymbol{M}_{\Sigma,\mathrm{ext}}^{(i)}$ with the infinitesimal rotation angle $\delta\boldsymbol{\beta}$. The external torque $\boldsymbol{M}_{\mathrm{ext}}^{(i)}$ *on the surface patch* Σ_i is then simply given by $-\boldsymbol{M}_{\Sigma,\mathrm{ext}}^{(i)}$ due to torque balance. Again, this argument does not require us to assume that the Euler-Lagrange equation is satisfied on Σ_i.

In total analogy to the force, we will consider patch $\partial\Sigma_1$ without loss of generality and write $\boldsymbol{M}_{\mathrm{ext}} := \boldsymbol{M}_{\mathrm{ext}}^{(1)}$, with

$$\boldsymbol{M}_{\mathrm{ext}} = \oint_{\partial\Sigma_1}\mathrm{d}s\, l_a\boldsymbol{m}^a\,, \tag{2.20}$$

where $\boldsymbol{l} = -\boldsymbol{l}^\Sigma$ again (see Fig. 2.1). The surface tensor

$$\boxed{\boldsymbol{m}^a = \boldsymbol{X} \times \boldsymbol{f}^a + \mathcal{H}^{ab} \boldsymbol{e}_b \times \boldsymbol{n}} \qquad (2.21)$$

is the covariantly conserved torque tensor. It consists of two parts: a contribution due to the couple of the stress tensor $\boldsymbol{f}^a$ about the origin as well as an intrinsic contribution proportional to $\mathcal{H}^{ab}$ which originates only from curvature terms. The value of the former does depend on the choice of origin while the latter is independent of this choice. The divergence of $\boldsymbol{m}^a$, is indeed zero in mechanical equilibrium as required by Noether's theorem:

$$
\begin{aligned}
\nabla_a \boldsymbol{m}^a \overset{(2.4a, A.39, A.41)}{=} \quad & \boldsymbol{e}_a \times \boldsymbol{f}^a + \boldsymbol{X} \times (\nabla_a \boldsymbol{f}^a) + (\nabla_a \mathcal{H}^{ab}) \boldsymbol{e}_b \times \boldsymbol{n} + \mathcal{H}^{ab} \boldsymbol{e}_b \times K_a^c \boldsymbol{e}_c \\
\overset{(2.6a, 2.8)}{=} \quad & (T^{ab} - \mathcal{H}^{ac} K_c^b) \boldsymbol{e}_a \times \boldsymbol{e}_b - (\nabla_b \mathcal{H}^{ab}) \boldsymbol{e}_a \times \boldsymbol{n} + (\nabla_a \mathcal{H}^{ab}) \boldsymbol{e}_b \times \boldsymbol{n} \\
& + \mathcal{H}^{ab} K_a^c \boldsymbol{e}_b \times \boldsymbol{e}_c \\
= \quad & 0 \, , \qquad\qquad\qquad\qquad\qquad\qquad\qquad\qquad (2.22)
\end{aligned}
$$

where we have exploited the symmetry of T^{ab} and $\mathcal{H}^{ab}$.

The occurrence of curvature terms in the Hamiltonian is ultimately due to the fact that the physical surface is not infinitely thin but has an inhomogeneous force distribution along its transverse direction [LM06]. If one captures this internal structure in the strictly two-dimensional Hamiltonian (2.1), the curvature terms give rise to an intrinsic torque density and a non-vanishing normal component of the stress tensor.

Note that the torque tensor, like the stress tensor, depends only on geometric properties of the surface (modulo a contribution that is due to a shift of the origin). It is thus always possible in principle to determine the forces and torques operating on a patch of surface from a knowledge of the shape of the surface alone. The snag is to determine the correct shape.

2.2 The fluid membrane

The stress tensor of a Helfrich membrane depends on local curvatures and gradients of curvature. It has a nonvanishing normal component and does not contain the saddle-splay modulus $\bar{\kappa}$. A tilt degree of freedom adds further tangential terms to the stress tensor.

Our treatment so far has been entirely general: the only properties of the Hamiltonian we have used are reparametrization, translational, and rotational invariance. In the following, we will specialize the expressions for stress tensor, torque tensor and shape equation to Hamiltonians which are relevant for describing the mechanics of fluid membranes.

2.2.1 Surface tension

It is instructive to have a look at the simplest case of surface tension first before considering the entire Helfrich Hamiltonian (1.2). For the constant Hamiltonian density

$$\mathcal{H}_{\text{capillary}} = \sigma \tag{2.23}$$

we get: $\mathcal{H}^{ab} \overset{(2.7a)}{=} \delta\mathcal{H}/\delta K_{ab} = 0$ and $T^{ab} \overset{(2.7b)}{=} -2\sigma(\sqrt{g})^{-1}\delta\sqrt{g}/\delta g_{ab} \overset{(\text{B.4})}{=} -\sigma g^{ab}$. Thus, the stress tensor is given by

$$\boldsymbol{f}^a \overset{(2.8)}{=} -\sigma \boldsymbol{e}^a \ . \tag{2.24}$$

The force transmitted across a fictitious line element is normal to this line, independent of its direction, tangential to the surface, and equal in magnitude to the value of the surface tension. This simple case has guided our intuition of how to think about tensions and stresses in surfaces, but it is far too special: in general, surface stresses are not shear-free nor isotropic nor tangential nor constant as we will see in the following example.

Inserting expression (2.24) for $\boldsymbol{f}^a$ into Eqn. (2.21), one obtains for the torque tensor

$$\boldsymbol{m}^a \overset{(2.21)}{=} -\sigma\big(\boldsymbol{X} \times \boldsymbol{e}^a\big) \ . \tag{2.25}$$

The intrinsic torque vanishes; the torque on a surface patch Σ_1 is given by

$$\boldsymbol{M}_{\text{ext}} = -\sigma \oint_{\partial\Sigma_1} \mathrm{d}s \, \big(\boldsymbol{X} \times \boldsymbol{l}\big) \ . \tag{2.26}$$

It is simple to interpret this expression: the tangential stress $-\sigma\boldsymbol{l}$ provides a torque per unit length at every point of the contour $\partial\Sigma_1$. The line integral along $\partial\Sigma_1$ yields the total external torque on the surface patch.

From Eqns. (2.18a) and (2.24), one obtains for the shape equation:

$$K = 0 \ . \tag{2.27}$$

Thus, surfaces that extremize their area have vanishing mean curvature K. Such surfaces are also called *minimal surfaces*. One simple example is the catenoid (see Technical Point 2.2). In fact, it is the only surface of revolution which solves Eqn. (2.27) besides the plane [Kre91].

2.2.2 The Helfrich membrane

The energetics of a fluid membrane without internal degrees of freedom can be described by the Hamiltonian density

$$\mathcal{H} = \mathcal{H}_{\text{capillary}} + \mathcal{H}_{\text{bend}} \ , \tag{2.28}$$

Technical Point 2.2: *The catenoid - a surface of zero mean curvature*

A soap film which is suspended between two parallel coaxial circular rings of equal radius a can be described by the function [dGBWQ03]

$$\rho(h) = b \cosh \frac{h-c}{b} \ ,$$

where ρ is the radial distance from the symmetry axis and h is its height (see sketch down right).[§] The parameter b is the radius at the waist of the film whereas c determines its shift along the h axis. A surface from this two-parameter family of surfaces is called a *catenoid*.

Soap film spanning two
rings.
*(Mathematikum Gießen/
photo: Rolf K. Wegst)*

If the two rings are a distance d apart, the boundary value problem to solve is

$$a = b \cosh \frac{d}{2b} \ .$$

For $d \leq d_{\mathrm{crit}} \simeq 1.325a$ two solutions exist, one with a minimum, the other with a maximum surface area. If $d/a > 1.055$, the surface becomes metastable as its area is now larger than the combined area of two soap films which separately cover the two rings [Ise92][Arf85, Example 17.2.2]. As soon as d exceeds d_{crit} a connecting solution no longer exists—the soap film collapses.

[§] This is only true in equilibrium. In the photo (top right) dynamical effects play a role as well.

---

where

$$\mathcal{H}_{\mathrm{bend}} = \frac{1}{2}\kappa(K - K_0)^2 + \frac{1}{2}\bar{\kappa}\mathcal{R} \ . \tag{2.29}$$

Compared to Sec. 1.2.1 we have rewritten the Gaussian curvature in terms of the Ricci scalar $\mathcal{R} \overset{\text{(A.51c)}}{=} 2K_{\mathrm{G}}$. This allows us to apply expression (B.9) for the stress tensor of the general curvature Hamiltonian density $\mathcal{H}(K, \mathcal{R})$ to the special case of the Helfrich membrane (see App. B.2.1). Inserting (2.28) yields[6]

$$\boldsymbol{f}^a = \left\{ \kappa(K - K_0)\Big[K^{ab} - \frac{1}{2}(K - K_0)g^{ab} \Big] - \sigma g^{ab} \right\} \boldsymbol{e}_b - \kappa(\nabla^a K)\,\boldsymbol{n} \ . \tag{2.30}$$

In contrast to the capillary case, the surface stress tensor is not isotropic nor tangential nor constant. The local curvatures contribute additional tangential

---

[6] One can also read off the relevant expressions from Table 2.1.

stresses, while the gradient of the curvature creates a new normal stress; the saddle-splay modulus $\bar{\kappa}$, however, does not enter $\boldsymbol{f}^a$.

To determine the external force on the membrane patch Σ_1, we first simplify the contraction of $\boldsymbol{f}^a$ and $\boldsymbol{l}$:

$$
l_a \boldsymbol{f}^a \overset{\text{(A.56a)}}{=} \left\{ \kappa(K - K_0)\left[(K_\perp l^b + K_{\perp\parallel} t^b) - \frac{1}{2}(K - K_0)l^b\right] - \sigma l^b \right\} \boldsymbol{e}_b - \kappa(\nabla_\perp K)\,\boldsymbol{n}
$$

$$
= \left\{ \kappa(K - K_0)\left[K_\perp - \frac{1}{2}(K - K_0)\right] - \sigma \right\} \boldsymbol{l} + \kappa K_{\perp\parallel}(K - K_0)\,\boldsymbol{t}
$$

$$
- \kappa(\nabla_\perp K)\,\boldsymbol{n} \ . \tag{2.31}
$$

In expression (2.31) the unit tangent vector $\boldsymbol{t} = t^a \boldsymbol{e}_a = \boldsymbol{n} \times \boldsymbol{l}$ is introduced: it points along the integration contour $\partial\Sigma_1$ and is perpendicular to $\boldsymbol{l}$ and $\boldsymbol{n}$. The symbol $\nabla_\perp = l_a\nabla^a$ denotes the directional derivative along the vector $\boldsymbol{l}$. The projections of the extrinsic curvature onto the orthonormal basis of tangent vectors $\{\boldsymbol{l}, \boldsymbol{t}\}$ are given by $K_\perp = l^a l^b K_{ab}$, $K_\parallel = t^a t^b K_{ab}$, and $K_{\perp\parallel} = l^a t^b K_{ab}$ (see also App. A.2). Since the trace K of the extrinsic curvature tensor can be written as $K = K_\perp + K_\parallel$, expression (2.31) can be further simplified and inserted into Eqn. (2.16) afterwards to calculate the external force on Σ_1

$$
\boldsymbol{F}_{\text{ext}} = \oint_{\partial\Sigma_1} \mathrm{d}s \left\{ \left[\frac{\kappa}{2}\left[K_\perp^2 - (K_\parallel - K_0)^2\right] - \sigma\right] \boldsymbol{l} + \kappa K_{\perp\parallel}(K - K_0)\,\boldsymbol{t} - \kappa(\nabla_\perp K)\,\boldsymbol{n} \right\} \ . \tag{2.32}
$$

Knowing the stress tensor, the well-known shape equation of the Helfrich Hamiltonian can be easily obtained from Eqn. (2.18a) (see, for instance, Refs. [ZcH89, Sei97, CG02b]):

$$
-\Delta K + \frac{1}{2}(K - K_0)\left[(K - K_0)K - 2K_{ab}K^{ab}\right] + \lambda^{-2}K = 0 \ , \tag{2.33}
$$

where we introduced the characteristic length

$$
\lambda := \sqrt{\frac{\kappa}{\sigma}} \ , \tag{2.34}
$$

separating short length scales over which bending energy dominates from the large ones over which tension does.

Remarks:

- Eqn. (2.33) has to be solved to determine the shape of a membrane under certain boundary conditions. Unfortunately, this equation is a partial non-linear differential equation of fourth order in the embedding functions $\boldsymbol{X}$; as such, it can only be solved analytically in exceptional cases.

- In Chaps. 4 and 5 we will focus on an up-down symmetric fluid membrane for which the spontaneous curvature K_0 vanishes[7] and solve the shape equation numerically for special cases (see also App. C) .

- Instead of trying to solve the shape equation one may also exploit that forces and torques can be expressed in terms of the local surface geometry. In Chap. 5 we will see that this fact enables one to gain a host of exact nonlinear results, *e. g.* the sign of the force between two membrane-bound particles.

- The Helfrich Hamiltonian density (2.28) involves the Gaussian curvature K_{G}. However, this term neither contributes to the stress tensor nor to the shape equation. To see whether it is relevant for torques, let us determine the torque tensor $\boldsymbol{m}^a$ of the fluid membrane and subsequently calculate the external torque $\boldsymbol{M}_{\mathrm{ext}}$ on the membrane patch Σ_1.

The derivative of the density (2.28) with respect to K_{ab} is (see also Table B.1)

$$\mathcal{H}^{ab} = \kappa(K - K_0)\,g^{ab} + \bar{\kappa}(Kg^{ab} - K^{ab})\ . \tag{2.35}$$

Thus, the intrinsic torque does not vanish and, using the expression for $\boldsymbol{f}^a$ from Eqn. (2.30) again, the torque tensor can be written as

$$\boldsymbol{m}^a \overset{(2.21)}{=} \boldsymbol{X} \times \boldsymbol{f}^a + \Big[\kappa(K - K_0)\,g^{ab} + \bar{\kappa}(Kg^{ab} - K^{ab})\Big]\big(\boldsymbol{e}_b \times \boldsymbol{n}\big)\ . \tag{2.36}$$

Inserting this result into Eqn. (2.20) yields the external torque

$$
\begin{aligned}
\boldsymbol{M}_{\mathrm{ext}} \;=\; & \oint_{\partial\Sigma_1} \mathrm{d}s\,\bigg\{\Big[\frac{\kappa}{2}\big[K_\perp^2 - (K_\parallel - K_0)^2\big] - \sigma\Big]\big(\boldsymbol{X} \times \boldsymbol{l}\big) \\
& + \kappa K_{\perp\parallel}(K - K_0)\big(\boldsymbol{X} \times \boldsymbol{t}\big) - \kappa(\nabla_\perp K)\big(\boldsymbol{X} \times \boldsymbol{n}\big) \\
& - \kappa(K - K_0)\boldsymbol{t}\bigg\}\ ,
\end{aligned}
\tag{2.37}
$$

on the membrane patch Σ_1. The intrinsic part of the torque tensor adds a contribution to the integrand in Eqn. (2.37), which is proportional to the curvature $(K - K_0)$ and tangential to the contour of integration. If K is constant on $\partial\Sigma_1$, the intrinsic part of the torque tensor does not contribute to $\boldsymbol{M}_{\mathrm{ext}}$ at all. This is because the integral of $\boldsymbol{t} = \nabla_\parallel \boldsymbol{X}$ vanishes along any closed contour.

Remarkably, the term $\boldsymbol{M}_{\mathrm{ext}}^{\bar{\kappa}} = \int_{\partial\Sigma_1} \mathrm{d}s\,l_a \boldsymbol{m}_{\bar{\kappa}}^a$ originating from the Gaussian curvature vanishes (see Technical Point 2.3 for the details). This implies that torques on membrane patches do not depend on the last term of the Hamiltonian density (2.28) involving the Gaussian curvature K_{G}. As shape and stresses are also independent of the term, we can neglect it in the following except for Chap. 3: there, *local* conditions *at the boundary* will be discussed in which that term may become important (see Sec. 3.5).

---

[7] Stress tensor, torque tensor, and shape equation for the up-down symmetric membrane can be obtained by simply inserting $K_0 = 0$ into the corresponding expressions from this section.

──── **Technical Point 2.3:** *Contribution of the Gaussian curvature* ────

By virtue of the Gauss-Bonnet theorem the surface integral of the last term of Hamiltonian density (2.29) can be written as a sum of a topological constant and a line integral over the geodesic curvature at the boundary of the membrane (see App. A.3). It does not contribute to the membrane stress tensor (2.30) and does not enter the shape equation (2.33). In spite of that, it gives a contribution $\boldsymbol{m}_{\bar{\kappa}}^a$ to the torque tensor (2.36).

In Sec. 3.5 we will discuss an example where this term becomes important. Its contribution $\boldsymbol{M}_{\text{ext}}^{\bar{\kappa}}$ to the external torque, however, vanishes. The reason is that its integrand can be written as a derivative with respect to the arc length s:

$$l_a \boldsymbol{m}_{\bar{\kappa}}^a \overset{(2.36)}{=} l_a \Big[\bar{\kappa}(K g^{ab} - K^{ab}) \Big] (\boldsymbol{e}_b \times \boldsymbol{n}) \overset{(\text{A.57a})}{=} -\bar{\kappa}(K_{\parallel}\boldsymbol{t} + K_{\perp\parallel}\boldsymbol{l}) \overset{(\text{A.57b})}{=} -\bar{\kappa}\nabla_{\parallel}\boldsymbol{n} \, ,$$

where $K = K_\perp + K_\parallel$ was used and the symbol $\nabla_\parallel = t_a \nabla^a$ denotes the directional derivative along $\boldsymbol{t}$, *i.e.* the derivative with respect to the arc length s (see App. A.2). Integrating $\nabla_\parallel \boldsymbol{n}$ over the closed contour $\partial \Sigma_1$ yields zero and thus $\boldsymbol{M}_{\text{ext}}^{\bar{\kappa}} = 0$, even if an external torque is acting.

2.2.3 Lipid tilt

To take an additional tilt degree of freedom into account, we add the Hamiltonian density

$$\mathcal{H}_{\text{m}} = \frac{1}{2}\lambda_{\text{m}}M^2 + \mu_{\text{m}}M_{ab}M^{ab} + \frac{1}{4}\nu_{\text{m}}F_{ab}F^{ab} + V(m^2) \tag{2.38}$$

to the density (2.28) of the Helfrich Hamiltonian (see Sec. 1.2.2). Now, $\mathcal{H}$ additionally depends on m^a and $\nabla_a m^b$. A close inspection of the calculations in Sec. 2.1.1 reveals that the tilt degree of freedom adds further terms to the stress tensor and the Euler-Lagrange equation (see below). The structure of the equations, however, stays the same.

As the choice for $\mathcal{H}_{\text{m}}$ is purely intrinsic, Eqn. (2.8) shows that the corresponding material stress $\boldsymbol{f}_{\text{m}}^a$ is also purely intrinsic, therefore tangential, and given by $\boldsymbol{f}_{\text{m}}^a = T_{\text{m}}^{ab}\boldsymbol{e}_b$, where $T_{\text{m}}^{ab} = -2\sqrt{g}^{-1}\delta(\sqrt{g}\mathcal{H}_{\text{m}})/\delta g_{ab}$ is the metric material stress. The surface tensors $\mathcal{H}^{ab}$ and $\mathcal{K}^{abc}$ remain unchanged; yet, $\mathcal{G}^{abc}$ collects a contribution as $\nabla_a m^b$ depends on the metric via the Christoffel symbol (see Table B.1 and calculations in App. B.2.3).

Performing the functional variation (see again App. B.2.3) we find that

$$
\begin{aligned}
T_{\mathrm{m}}^{ab} &= \frac{1}{2}\Big[\lambda_{\mathrm{m}}\big(M^2 + 2m^c\nabla_c M\big) + \nu_{\mathrm{m}}\big(\varepsilon_{cd}\nabla^c m^d\big)^2\Big]g^{ab} \\
&\quad + \mu_{\mathrm{m}}\Big[-M_{cd}M^{cd}g^{ab} + 2MM^{ab} + 2m^c\nabla_c M^{ab} \\
&\qquad\quad - (\nabla_c m^a)(\nabla^c m^b) + (\nabla^a m_c)(\nabla^b m^c)\Big] \\
&\quad - V(m^2)g^{ab} - 2V'(m^2)m^a m^b \,, \tag{2.39}
\end{aligned}
$$

where $\varepsilon_{ab} = \boldsymbol{n}\cdot(\boldsymbol{e}_a\times\boldsymbol{e}_b)$ is the antisymmetric epsilon-tensor (see App. A.1). Notice that the metric stress tensor is *quadratic* in the tilt-strain, not linear. Unlike the stress tensor in elasticity theory, this tensor is not obtained as the derivative of the energy with respect to the strain but rather with respect to the *metric*, which leaves it quadratic in the strain. The formal analogy alluded to in Sec. 1.2.2 is therefore not complete.

External force and torque on a membrane patch Σ_1 follow directly

$$
\boldsymbol{F}_{\mathrm{m,\,ext}} = \oint_{\partial\Sigma_1} \mathrm{d}s\, l_a T_{\mathrm{m}}^{ab}\boldsymbol{e}_b \quad \text{and} \tag{2.40a}
$$

$$
\boldsymbol{M}_{\mathrm{m,\,ext}} = \oint_{\partial\Sigma_1} \mathrm{d}s\, l_a T_{\mathrm{m}}^{ab}(\boldsymbol{X}\times\boldsymbol{e}_b) \,, \tag{2.40b}
$$

where T_{m}^{ab} is given by Eqn. (2.39). Note that the additional contribution to the torque is purely extrinsic.

Adding the material stress T_{m}^{ab} to the tangential *geometric* stress f^{ab}, we find with the help of Eqns. (2.18) the equilibrium conditions

$$
0 = K_{ab}T_{\mathrm{m}}^{ab} + \mathcal{E} \,, \tag{2.41a}
$$

$$
\nabla_a T_{\mathrm{m}}^{ab} = 0 \,. \tag{2.41b}
$$

The first of these equations shows how the material degrees of freedom "add" to the geometric Euler-Lagrange derivative $\mathcal{E}$; this is the modified shape equation. The second equation – which before provided consistency conditions on the geometrical stresses – tells us that the material stress tensor is conserved. The equilibrium of the material degrees of freedom involves the vanishing of the Euler-Lagrange derivative with respect to the field m^a, which is given by

$$
\mathcal{E}_{\mathrm{m}\,a} = \frac{\delta H_{\mathrm{m}}}{\delta m^a} = -\lambda_{\mathrm{m}}\nabla_a\nabla_b m^b - (\mu_{\mathrm{m}} + \nu_{\mathrm{m}})\nabla_b\nabla_a m^b - (\mu_{\mathrm{m}} - \nu_{\mathrm{m}})\Delta m_a + 2V'(m^2)m_a \,. \tag{2.42}
$$

In general, the equilibrium condition $\mathcal{E}_{\mathrm{m}\,a} \equiv 0$ implies Eqn. (2.41b). For a single vector field m^a the converse also holds so that Eqn. (2.41b) may be used in place

━━━ **Technical Point 2.4:** *Axisymmetric solution of the tilt shape equation* ━

For flat membranes, the Euler-Lagrange equation (2.42) reduces to

$$(\lambda_{\mathrm{m}} + \mu_{\mathrm{m}})\boldsymbol{\nabla}\boldsymbol{\nabla} \cdot \boldsymbol{m} + \mu_{\mathrm{m}}\boldsymbol{\nabla}^2\boldsymbol{m} - 2V'\boldsymbol{m} = 0 \ , \tag{2.I}$$

where $\boldsymbol{m}$ is the 2D tilt vector in the membrane plane. The symbol $\boldsymbol{\nabla}$ denotes the two-dimensional nabla operator in the plane. Focusing on a cylindrically symmetric membrane inclusion which excites the tilt, the situation acquires axisymmetry. For small values of tilt, we can expand the potential as

$$V(m^2) = \frac{1}{2}tm^2 + \frac{1}{4}um^4 + \cdots \tag{2.II}$$

In the untilted phase we can terminate this expression after the first term (since then $t > 0$).

If we now write $\boldsymbol{m}(\boldsymbol{\rho}) = m(\rho)\boldsymbol{e}_\rho$ and restrict to the untilted membrane phase, Eqn. (2.I) reduces to a simple Bessel equation (see Technical Point 4.1 on page 85)

$$x^2 m'' + x m' - (x^2 + 1)m = 0 \ ,$$

where $x = \rho/\ell_{\mathrm{m}}$, ℓ_{m} is the length defined in Eqn. (2.45), and the prime denotes a derivative with respect to x. The solution is

$$m(\rho) = m_0 \frac{\mathrm{K}_1(\rho/\ell_{\mathrm{m}})}{\mathrm{K}_1(\rho_0/\ell_{\mathrm{m}})} \ , \tag{2.III}$$

where ρ_0 is the radius of the inclusion, m_0 the value of the tilt at this point, and K_n a modified Bessel function of the second kind (see again Technical Point 4.1) [AS70]. Thus, the tilt decays essentially exponentially with a decay length of ℓ_{m}.

───

of the equilibrium condition.[8]

Lipid tilt order, described by the Hamiltonian density (2.38), influences the shape of the membrane, even though $\mathcal{H}_{\mathrm{m}}$ does not contain an explicit coupling of m^a to the extrinsic curvature. Solving the coupled system of differential equations (2.41) poses a formidable task, clearly exceeding the already substantial one for the undecorated shape equation alone. If we assume for a moment that the energy density stems exclusively from lipid tilt (as described by $\mathcal{H}_{\mathrm{m}}$), the membrane itself remains flat and the tilt shape equation can be solved analytically for special

───────────

[8] The converse is not always true. Had we considered two vector fields instead of one, m_1^a and m_2^a say, the corresponding Euler-Lagrange equations $\mathcal{E}_{\mathrm{m}_1 a} \equiv 0$, and $\mathcal{E}_{\mathrm{m}_2 a} \equiv 0$ would not follow from the conservation law. The two sets of Euler-Lagrange equations are required to determine the equilibrium. The conservation law alone is not enough.

cases (see Technical Point 2.4). This is not a self-consistent approximation, but should give a good description in the limit in which the tilt moduli λ_{m} and μ_{m} are significantly "softer" than the bending modulus.

In equilibrium, we not only have $\mathcal{E}_{\mathrm{m}\,a} \equiv 0$, but also $\nabla^a \mathcal{E}_{\mathrm{m}\,a} = 0$. Using the commutation relations for covariant derivatives (A.19, A.20) and exploiting that for 2D surfaces the Riemann tensor is given by $R_{abcd} \overset{(\mathrm{A.51a})}{=} \frac{1}{2}\mathcal{R}(g_{ac}g_{bd} - g_{ad}g_{bc})$ it is then easy to see that the tilt also satisfies the following equation on the surface:[9]

$$(\lambda_{\mathrm{m}} + 2\mu_{\mathrm{m}})\Delta M + \mu_{\mathrm{m}}\nabla^a(\mathcal{R}m_a) - 2\big[2V''m^2 + V'M\big] \; = \; 0 \; . \tag{2.43}$$

Notice that ν_{m} has dropped out of this equation, which follows from the fact that F^{ab} is invariant under $U(1)$ gauge transformations.[10] If we again restrict to a flat membrane in the untilted phase, $\mathcal{R} \equiv 0$ and $V(m^2) = \frac{1}{2}tm^2$ (see Technical Point 2.4); Eqn. (2.43) simplifies to a Helmholtz equation for the tilt divergence:[11]

$$\big[(\lambda_{\mathrm{m}} + 2\mu_{\mathrm{m}})\Delta - t\big]M \; = \; 0 \; , \tag{2.44}$$

showing that in lowest order any nonzero M is essentially exponentially damped with a decay length of ℓ_{m} (see again Technical Point 2.4), where

$$\ell_{\mathrm{m}} = \sqrt{\frac{\lambda_{\mathrm{m}} + 2\mu_{\mathrm{m}}}{t}} \; . \tag{2.45}$$

This result is confirmed qualitatively by coarse-grained computer simulations [Ill07] (see Fig. 2.2 for a typical snapshot of the simulation).

Note that even though the system of Euler-Lagrange equations (2.41) is quite formidable, it still enjoys one nice nontrivial property: the material equation (2.41b) is purely intrinsic. This is the case because the material stress is tangential, which itself derives from the fact that the material Hamiltonian is intrinsic. If we were to add a coupling between tilt and extrinsic curvature, such as the chiral term $\varepsilon_{ac}K_b^c m^a m^b$, this decoupling would no longer hold.

---

[9] This is very dry stuff, I know. As a reward for those that fought their way up to this point without falling asleep: the first five readers that discover this footnote are very welcome to pick up a bottle of champagne from the author.

[10] The Euler-Lagrange derivative of the F^{ab} contribution in Eqn. (2.38) is easily seen to be $\mathcal{E}_{\nu\,a} = \nabla^b F_{ab}$. Furthermore, due to its asymmetry F^{ab} is invariant under gauge transformations $m^a \rightarrow m^a + \nabla^a\Lambda$ with some arbitrary gauge function Λ. Performing an infinitesimal transformation, we get

$$\delta_\Lambda \frac{1}{4}\int \mathrm{d}A\, F_{ab}F^{ab} = -\int \mathrm{d}A\,(\nabla^a\mathcal{E}_{\nu\,a})\Lambda \; .$$

Since Λ was arbitrary, $\nabla^a\mathcal{E}_{\nu\,a}$ must vanish identically. In the corresponding electrodynamic situation $\mathcal{E}_{\nu\,a}$ is proportional to the 4-current [LL00]; there, the same gauge invariance is responsible for charge conservation.

[11] If $t < 0$ gets us into the tilted phase, the expansion (2.II) has to be taken one order higher, leaving instead a nonlinear Ginzburg-Landau equation to be solved.
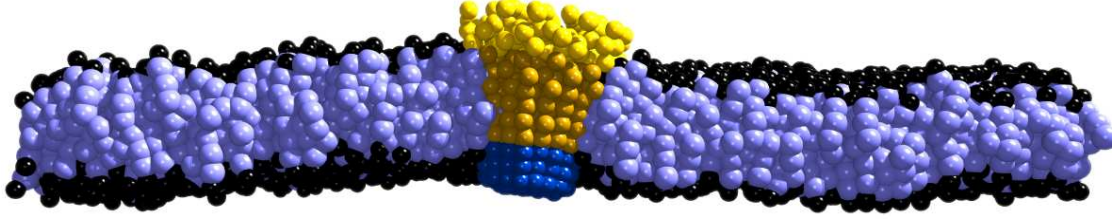
Figure 2.2: Computer simulation of a cylindrically symmetric inclusion in a membrane (snapshot). The inclusion excites a lipid tilt whose time average is found to decay roughly exponentially for increasing lateral distance from the inclusion center [Ill07]. The membrane is modeled in a similar manner to that described in Technical Point 5.8 on page 156, differing only in the number of tail beads.

2.3 Stresses from the surrounding space

The surroundings of a surface often provide additional sources of stress. In the case of a global pressure difference the bulk stress can be rewritten as an effective surface stress. For a locally varying stress field, however, this is generally not possible.

In this section we will see that the conservation law for $\boldsymbol{f}^a$ ceases to hold in its simple version (2.6a) if the surrounding space is taken into account. Rather than having a divergence-free stress tensor with a few localized sources of stress (such as the Maxwell stress of the electrostatic field in the presence of point charges), one now has a continuous source of stress. However, even in complicated examples the mechanical surface response continues to be driven by its geometry and thus a geometric stress tensor is still useful. The task is rather to couple it to off-surface stresses. In the following, we will discuss how this can be done for the two examples from Sec. 1.2.3.

2.3.1 Global pressure difference

Let us first look again at a surface with a global pressure difference between its two sides. In this case a term $-PV$ has to be included in the free energy functional (see Sec. 1.2.3). If we use the auxiliary variables approach from Sec. 2.1.1 [Mül04], the new functional is given by

$$H_{\mathrm{c},P} = \tilde{H}_{\mathrm{c}} - PV \stackrel{(1.9)}{=} \tilde{H}_{\mathrm{c}} - \frac{1}{3}P \int \mathrm{d}A\, \boldsymbol{n} \cdot \boldsymbol{X} \;. \tag{2.46}$$

Note that the original Lagrange multiplier functions $\boldsymbol{f}^a, \ldots$ of H_{c} from Eqn. (2.5) have to be replaced by $\tilde{\boldsymbol{f}}^a, \ldots$ in $\tilde{H}_{\mathrm{c}}$ because the additional term in the functional

also induces changes in the other multipliers: looking at the Euler-Lagrange equations (2.6), we observe that Eqns. (2.6b) for $\boldsymbol{e}_a$ and (2.6e) for K_{ab} are as before; the others, however, change slightly:

$$\nabla_a \tilde{\boldsymbol{f}}^a \;=\; \frac{1}{3} P \, \boldsymbol{n} \;, \tag{2.47a}$$

$$\tilde{\boldsymbol{f}}^a \;=\; (\tilde{\Lambda}^{ac} K_c^b + 2\tilde{\lambda}^{ab})\boldsymbol{e}_b - \tilde{\lambda}_\perp^a \, \boldsymbol{n} \;, \tag{2.47b}$$

$$0 \;=\; \left(\nabla_b \tilde{\Lambda}^{ab} + \tilde{\lambda}_\perp^a - \frac{1}{3} P \, \boldsymbol{X} \cdot \boldsymbol{e}^a \right) \boldsymbol{e}_a$$
$$+ \left(2\tilde{\lambda}_n - \tilde{\Lambda}^{ab} K_{ab} - \frac{1}{3} P \, \boldsymbol{X} \cdot \boldsymbol{n} \right) \boldsymbol{n} \;, \tag{2.47c}$$

$$\tilde{\lambda}^{ab} \;=\; \frac{1}{2} T^{ab} + \frac{1}{6} P(\boldsymbol{X} \cdot \boldsymbol{n}) g^{ab} \;, \tag{2.47d}$$

$$\tilde{\Lambda}^{ab} \;=\; \Lambda^{ab} = -\mathcal{H}^{ab} \;, \tag{2.47e}$$

where T^{ab} and $\mathcal{H}^{ab}$ remain defined as in Eqns. (2.7). The Lagrange multiplier function $\tilde{\Lambda}^{ab}$ is the only one that is equal to its counterpart Λ^{ab}. In Eqn. (2.47d) we inserted the derivative of $\sqrt{g}$ with respect to the metric (see Eqn. (B.4)); in Eqn. (2.47c) we made use of completeness $\boldsymbol{X} = (\boldsymbol{X} \cdot \boldsymbol{e}^a)\boldsymbol{e}_a + (\boldsymbol{X} \cdot \boldsymbol{n})\boldsymbol{n}$.

Combining Eqns. (2.47) in the same way as Eqns. (2.6) above results in the following expression for the multiplier $\tilde{\boldsymbol{f}}^a$:

$$\tilde{\boldsymbol{f}}^a \;=\; \left[T^{ab} - \mathcal{H}^{ac} K_c^b + \frac{1}{3} P(\boldsymbol{X} \cdot \boldsymbol{n}) g^{ab} \right] \boldsymbol{e}_b - \left[\nabla_b \mathcal{H}^{ab} + \frac{1}{3} P(\boldsymbol{X} \cdot \boldsymbol{e}^a) \right] \boldsymbol{n}$$
$$=\; \boldsymbol{f}^a - \frac{2}{3} P \boldsymbol{J}^a \;, \tag{2.48}$$

where $\boldsymbol{f}^a$ is the original stress tensor (2.8) and where we have introduced the *Jemal tensor*

$$\boldsymbol{J}^a = \frac{1}{2} \left[(\boldsymbol{X} \cdot \boldsymbol{e}^a)\boldsymbol{n} - (\boldsymbol{X} \cdot \boldsymbol{n})\boldsymbol{e}^a \right] = \frac{1}{2} \boldsymbol{X} \times (\boldsymbol{n} \times \boldsymbol{e}^a) \;. \tag{2.49}$$

Its distinctive property is that its divergence equals the normal vector [Guv06]

$$\boldsymbol{n} = \nabla_a \boldsymbol{J}^a \;. \tag{2.50}$$

Applying this identity allows Eqn. (2.47a) to be rewritten as

$$\nabla_a \boldsymbol{f}^a = P \, \boldsymbol{n} \;. \tag{2.51}$$

Thus, pressure acts as a source of (continuous) normal stress which has to be balanced by geometrical stresses.[12] A comparison with Eqn. (2.12) reveals that

---

[12] Note that the tensor Q^a, which collects all terms of the boundary part of the variation (see Eqn. (2.9)), obtains an additional term as well. Using the Jemal tensor this term can be written as $\frac{2}{3} P \boldsymbol{J}^a \cdot \delta \boldsymbol{X}$. A closed free surface, however, does not have a boundary; thus, all boundary terms can be discarded in this case.

Technical Point 2.5: *The sphere - a surface of constant mean curvature*

The sphere is a surface of constant mean curvature. Specializing Eqn. (2.52) to this case yields the well-known expression for the Laplace pressure of a spherical bubble of radius a

$$P = \frac{2\sigma}{a} \; . \qquad\qquad (2.\text{IV})$$

Consider the bubble in the constant volume and the constant pressure ensemble, respectively (see Sec. 1.2.3): if the volume V_0 is fixed, the Lagrange multiplier P adjusts to $P = 2\sigma[3V_0/(4\pi)]^{-3}$; the bubble is stable. In the constant pressure ensemble this is not the case: to balance a small decrease of the radius due to a fluctuation, the pressure has to increase according to Eqn. (2.IV). Because it is constant, however, surface tension will contract the bubble; it thus is unstable. This simple example already shows that questions of stability depend on the ensemble even though the equilibrium shapes are the same.

---

the shape equation is now given by $\mathcal{E} = P$. For a soap film, with surface tension σ, this, for instance, reduces to the well-known Young-Laplace law [LL87]:

$$\sigma K = P \; . \qquad\qquad (2.52)$$

Surfaces that solve this equation are called "constant mean curvature surfaces". A simple example is the sphere (see Technical Point 2.5). It is the only closed surface of genus 0 in $\mathbb{R}^3$ which has a constant mean curvature.[13]

The geometric stress tensor $\boldsymbol{f}^a$ is no longer divergence-free. But one can define a new *effective* stress tensor $\breve{\boldsymbol{f}}^a$ which *is* divergence-free by including the right hand side of Eqn. (2.51) in $\boldsymbol{f}^a$ [Guv06]. Using the Jemal tensor (2.49) again, we obtain

$$\breve{\boldsymbol{f}}^a := \boldsymbol{f}^a - P\boldsymbol{J}^a \; . \qquad\qquad (2.53)$$

The external force on a surface patch Σ_1 is now given by

$$\boldsymbol{F}_{\text{ext}} = \int_{\Sigma_1} \mathrm{d}A \; \nabla_a \breve{\boldsymbol{f}}^a = \oint_{\partial\Sigma_1} \mathrm{d}s \; l_a \breve{\boldsymbol{f}}^a \; . \qquad\qquad (2.54)$$

The effective stress tensor $\breve{\boldsymbol{f}}^a$ possesses a surprising feature which needs some further explanation: it is *not* translationally invariant. Due to the explicit $\boldsymbol{X}$

---

[13] Another closed constant mean curvature surface in $\mathbb{R}^3$ is the Wente-torus which, however, self-intersects and has genus 1 [Wen86]. If the constraint on closure is relaxed, many other examples can be found such as the nodoid [LFL01] or the unduloid [Del41].

dependence of $\boldsymbol{J}^a$, a constant translation $\boldsymbol{X} \rightarrow \boldsymbol{X} + \boldsymbol{a}$ will add a term proportional to $\boldsymbol{J}_0^a = \boldsymbol{a} \times (\boldsymbol{n} \times \boldsymbol{e}^a)$ to $\breve{\boldsymbol{f}}^a$. However, a change of origin should have no physical significance on the external force, *i. e.*, the value of the integral in Eqn. (2.54) must not change in this case. Indeed, the divergence of $\boldsymbol{J}_0^a$ vanishes in every point; the *null stress* $\boldsymbol{J}_0^a$ does not contribute to the force [Guv06].

The value of the effective stress tensor $\breve{\boldsymbol{f}}^a$ at a point, however, is not fixed. The reason for this lies in the inherent ambiguity in the definition of any divergence-free effective stress; one can always add a null stress $\boldsymbol{f}_0^a$ for which $\nabla_a \boldsymbol{f}_0^a = 0$. Nevertheless, $\breve{\boldsymbol{f}}^a$ is useful especially if one is interested in forces as we will see in Chap. 5.

Due to the global pressure difference P, the divergence of the geometric torque tensor $\boldsymbol{m}^a$ picks up an additional term as well [CG02b]:

$$\nabla_a \boldsymbol{m}^a \overset{(2.22,\,2.51)}{=} P \boldsymbol{X} \times \boldsymbol{n} \; . \tag{2.55}$$

Analogous to Eqn. (2.53) one can define a divergence-free torque tensor

$$\breve{\boldsymbol{m}}^a := \boldsymbol{m}^a - \frac{2}{3} P \boldsymbol{X} \times \boldsymbol{J}^a = \boldsymbol{X} \times \tilde{\boldsymbol{f}}^a + \mathcal{H}^{ab} \boldsymbol{e}_b \times \boldsymbol{n} \; , \tag{2.56}$$

which can be used to express the external torque on the surface patch Σ_1 as a line integral over its boundary $\partial \Sigma_1$

$$\boldsymbol{M}_{\text{ext}} = \oint_{\partial \Sigma_1} \mathrm{d}s \, l_a \breve{\boldsymbol{m}}^a \; . \tag{2.57}$$

Again, an effective tensor such as $\breve{\boldsymbol{m}}^a$ is only defined up to null stresses. In the calculation of the external torque, however, these stresses do not contribute.

2.3.2 Gravity

What happens with stress and torque tensor if the source of stress is not constant but varies spatially? To study an illustrative example, let us focus on an interface in a gravitational field as introduced in Sec. 1.2.3. Using the framework of auxiliary variables again one can define the functional (compare Eqns. (2.5) and (2.46))

$$H_{\text{c},G} = H_{\text{c},P} + E_{\text{pot}} = \tilde{H}_\text{c} - \frac{1}{3} P \int \mathrm{d}A \, (\boldsymbol{n} \cdot \boldsymbol{X}) + \frac{1}{2} g \rho \int \mathrm{d}A \, (\boldsymbol{n} \cdot \boldsymbol{z}) X^2 \; . \tag{2.58}$$

As in the previous section, the additional term in the functional induces changes in the multipliers. The Euler-Lagrange equations for $\boldsymbol{X}$, $\boldsymbol{e}_a$, $\boldsymbol{n}$, g_{ab} and K_{ab} are

now given by

$$\nabla_a \tilde{\boldsymbol{f}}^a = \frac{1}{3} P \boldsymbol{n} - \rho g (\boldsymbol{n} \cdot \boldsymbol{z}) \boldsymbol{X} \;, \tag{2.59a}$$

$$\tilde{\boldsymbol{f}}^a = (\tilde{\Lambda}^{ac} K_c^{\;b} + 2\tilde{\lambda}^{ab}) \boldsymbol{e}_b - \tilde{\lambda}_\perp^a \boldsymbol{n} \;, \tag{2.59b}$$

$$0 = \left[\nabla_b \tilde{\Lambda}^{ab} + \tilde{\lambda}_\perp^a - \frac{1}{3} P \, \boldsymbol{X} \cdot \boldsymbol{e}^a + \frac{1}{2} \rho g X^2 (\boldsymbol{z} \cdot \boldsymbol{e}^a) \right] \boldsymbol{e}_a$$

$$\qquad + \left[2\tilde{\lambda}_n - \tilde{\Lambda}^{ab} K_{ab} - \frac{1}{3} P \, \boldsymbol{X} \cdot \boldsymbol{n} + \frac{1}{2} \rho g X^2 (\boldsymbol{z} \cdot \boldsymbol{n}) \right] \boldsymbol{n} \;, \tag{2.59c}$$

$$\tilde{\lambda}^{ab} = \frac{1}{2} T^{ab} + \frac{1}{6} P (\boldsymbol{X} \cdot \boldsymbol{n}) g^{ab} - \frac{1}{4} \rho g (\boldsymbol{n} \cdot \boldsymbol{z}) X^2 g^{ab} \;, \tag{2.59d}$$

$$\tilde{\Lambda}^{ab} = \Lambda^{ab} = -\mathcal{H}^{ab} \;, \tag{2.59e}$$

where Eqn. (B.4) and completeness were used again. Combining these equations we obtain the expression

$$\tilde{\boldsymbol{f}}^a = \boldsymbol{f}^a - \frac{1}{2} \rho g X^2 \Big[(\boldsymbol{z} \cdot \boldsymbol{n}) \boldsymbol{e}^a - (\boldsymbol{z} \cdot \boldsymbol{e}^a) \boldsymbol{n} \Big] - \frac{2}{3} P \boldsymbol{J}^a \;, \tag{2.60}$$

for the multiplier $\tilde{\boldsymbol{f}}^a$. Together with Eqn. (2.59a) this yields the divergence of the geometric stress tensor $\boldsymbol{f}^a$

$$\nabla_a \boldsymbol{f}^a = \rho g (\boldsymbol{X} \cdot \boldsymbol{e}_a) \Big[(\boldsymbol{z} \cdot \boldsymbol{n}) \boldsymbol{e}^a - (\boldsymbol{z} \cdot \boldsymbol{e}^a) \boldsymbol{n} \Big] - \rho g (\boldsymbol{n} \cdot \boldsymbol{z}) \boldsymbol{X} + P \boldsymbol{n}$$

$$= -\rho g \Big[(\boldsymbol{X} \cdot \boldsymbol{n}) (\boldsymbol{z} \cdot \boldsymbol{n}) + (\boldsymbol{X} \cdot \boldsymbol{e}_a) (\boldsymbol{z} \cdot \boldsymbol{e}^a) \Big] \boldsymbol{n} + P \boldsymbol{n}$$

$$= [P - \rho g (\boldsymbol{X} \cdot \boldsymbol{z})] \boldsymbol{n} \;, \tag{2.61}$$

where completeness was exploited twice.
With gravity included, one thus obtains

$$\nabla_a \boldsymbol{f}^a = (P - \rho g h) \, \boldsymbol{n} \;, \tag{2.62}$$

where $h = \boldsymbol{X} \cdot \boldsymbol{z}$ is the height above the reference plane at which the potential energy is fixed to zero (see Sec. 1.2.3). The shape equation $\mathcal{E} = P - \rho g h$ seems to depend on the gauge. We have, however, not yet determined the pressure P.

For this let us assume that the variation is localized so that the interface is asymptotically flat (see Fig. 2.3). When the surface is varied one either has to keep the volume constant or has to add (or extract) material depending on the ensemble. In the latter case one can think of a reservoir at constant pressure which provides the material. If it lies at the height of the reference plane, the added or extracted material has no potential energy. However, the reservoir has to work against the hydrostatic pressure $\rho g h_0$, where h_0 is the distance between the reference and the
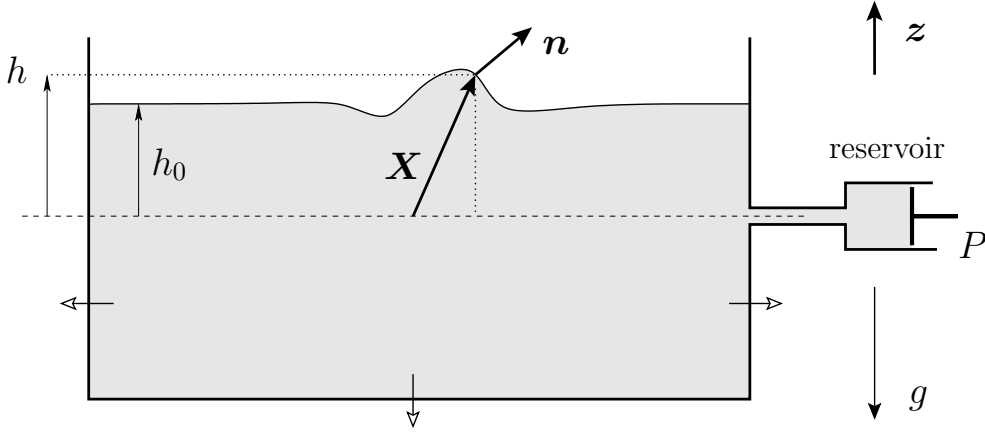
Figure 2.3: Interface in a homogeneous gravitational field. In the constant pressure ensemble a reservoir has to provide material when the surface is varied.

asymptotic plane (see again Fig. 2.3).[14] Thus, $P = \rho g h_0$, and Eqn. (2.62) reads[15]

$$\nabla_a \boldsymbol{f}^a = -\rho g (h - h_0) \, \boldsymbol{n} \; . \tag{2.63}$$

If the volume is kept constant, P can be obtained with the following argument: no forces act at the asymptotic plane far from the deformation. The divergence of the stress tensor thus has to be zero there. Inserting this into Eqn. (2.62) yields $P = \rho g h_0$ again which reproduces the result from before.

Eqn. (2.63) does not depend on the gauge but only on differences between the height of the interface and the height of the asymptotic plane. In the following, h_0 will be set to zero, *i. e.*, the asymptotic plane is equivalent to the reference plane. If we specialize to a liquid-fluid interface where tension is the only *surface* energy contribution, Eqn. (2.63) reads:

$$\sigma K = -\rho g h \; . \tag{2.64}$$

The curvature K is a linear function of the height. The corresponding proportionality constant has the dimension LENGTH^{-2}. Using it one can construct a characteristic length scale of the system

$$\ell = \sqrt{\frac{\sigma}{\rho g}} \; , \tag{2.65}$$

---

[14] In principle, we can place the reservoir at any other height as well. The provided material then enters the system with a nonvanishing potential energy. Its effect on the change of the total energy, however, is canceled as the hydrostatic pressure against which it has to work changes accordingly. To disentangle both effects, we put the reservoir at the height of the reference plane.

[15] Note that P is not a global pressure difference now but fixed by the choice of the reference plane.

which is also called the *capillary length*.[16] For liquid-fluid interfaces, gravity is only relevant on length scales much larger than ℓ [Mül04].

Returning to the case of the general surface Hamiltonian (2.1) one can ask whether the right hand side of Eqn. (2.63) can be cast as a divergence. Unfortunately, this is not possible. Thus, one cannot rewrite $\boldsymbol{f}^a$ as an effective surface stress tensor in analogy to the pressure case. Consequently, forces acting on the surface are no longer pure boundary integrals: under a constant translation $\delta\boldsymbol{X} = \delta\boldsymbol{a}$ the variation δH_G of the Hamiltonian (1.16) is directly connected to the external force $\boldsymbol{F}_{\text{ext}}$ that acts on a surface patch Σ_1

$$
\begin{aligned}
\delta H_G &= -\delta\boldsymbol{a} \cdot \boldsymbol{F}_{\text{ext}} = -\delta\boldsymbol{a} \cdot \left[\int_{\Sigma_1} \mathrm{d}A \left(\nabla_a \boldsymbol{f}^a + \rho g h \boldsymbol{n} \right) \right] \\
&= -\delta\boldsymbol{a} \cdot \left[\oint_{\partial\Sigma_1} \mathrm{d}s\, l_a \boldsymbol{f}^a + \rho\, g \int_{\Sigma_1} \mathrm{d}A\, h\, \boldsymbol{n} \right] .
\end{aligned}
\tag{2.66}
$$

Compared to the expressions (2.16) and (2.54) from the previous sections the force is now not only given by a boundary integral alone but comprises an additional area integral over the stresses from gravity.[17]

This prevents us from deforming the contour of integration without changing the value of the force. One may, however, analyze both terms of the force separately. In Chap. 5 we will come back to this point.

---

[16] For instance, an air-water interface under ambient conditions has $\ell \simeq 2.6\,\text{mm}$.

[17] An analogous statement is true for the external torque as the divergence of the torque tensor is now given by

$$
\nabla_a \boldsymbol{m}^a = -\rho g h (\boldsymbol{X} \times \boldsymbol{n}) .
$$

3 Boundary conditions at contact lines

In the two previous chapters we have seen that the energetics of a fluid surface is often completely described by a Hamiltonian that depends only on its geometry. External forces and torques are imprinted in the shape of the surface and can be written in terms of integrals over geometric stress and torque tensors.

One possible source of these stresses is the surrounding space. However, this is not the full picture: the surface may be in contact with a solid substrate or another fluid surface, it may even consist of different domains. This gives rise to additional external torques and stresses which are transmitted along the line of contact.

In equilibrium, the location of that contact line adjusts locally in order to minimize the overall energy. This implies boundary conditions which depend on the characteristic surface deformation energies. In this chapter the geometrical framework introduced so far will be used to derive these conditions in a completely systematic and parametrization-free way, generalizing and strongly simplifying the analysis previously given in Ref. [CG02a]. Adhesion to a rigid substrate, adhesion between two fluid surfaces, and a surface consisting of two different domains will be treated. To illustrate the general results, several examples will be presented which involve both curvature and curvature gradients. Some of these have previously been studied using different techniques, others are new.

3.1 The Young-Dupré equation

The boundary condition at the three-phase line between a liquid drop and a solid to which it adheres is given by the Young-Dupré equation. It expresses a tangential force balance.

Water droplets or lipid membrane vesicles may rest on a substrate, and this generally influences their shape quite strongly. For instance, water droplets on hydrophilic surfaces (*e. g.* clean glass) resemble flat contact lenses, while on very hydrophobic surfaces (*e. g.* teflon®) they are almost completely spherical (see Fig. 3.1). When gravity can be neglected,[1] the shape equation (2.52) dictates a constant mean curvature surface in both cases (in fact, a spherical cap, compare

---

[1] This is true for droplets small compared to the capillary length (see previous section).
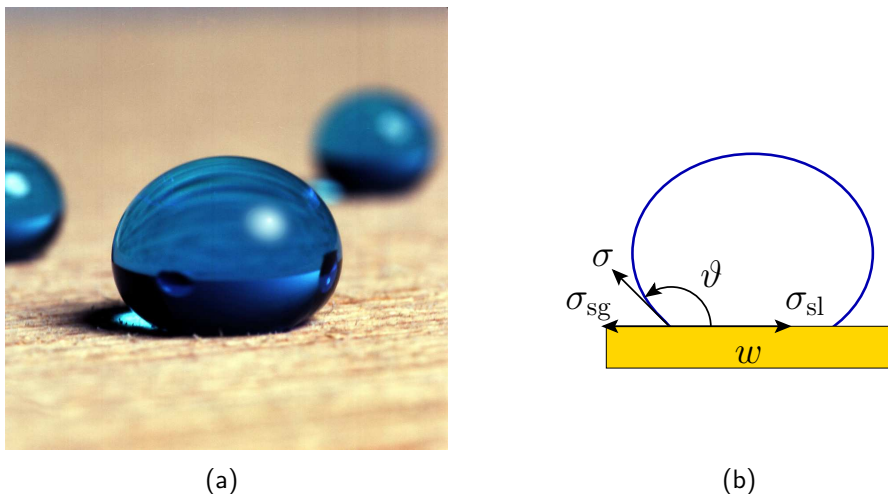
Figure 3.1: (a) picture of a drop of water adhering to a solid hydrophobic substrate (impregnated wood) *(from BASF Aktiengesellschaft)* and (b) schematic sketch of the geometry. The drop is not completely spherical. Its size must therefore be larger than the capillary length ℓ which is approximately $2.6\,\mathrm{mm}$ for an air-water interface.

Technical Point 2.5), but the *contact angle* ϑ at the three-phase line where water and substrate meet is different for the two different substrates.

In most cases the spatial extension of the surface being studied exceeds the range of the interaction between it and the substrate by a large amount. For instance, van der Waals forces, hydrophobic interactions, or (screened) electrostatic forces typically extend over several nanometers, while the extensions of vesicles or droplets can be microns or even millimeters. Under these conditions the interaction is well approximated by a *contact energy*, i. e., an *energy per unit area*, w, liberated when the surface makes contact with the substrate. It is this adhesion energy, together with the energy parameters characterizing the contacting surfaces, which determine the boundary conditions holding at the contact line. In the case of capillary phenomena, for example, the ratio between adhesion energy w and surface tension σ determines the contact angle ϑ between liquid and substrate (see Fig. 3.1(b)): by requiring that the tangential projections of the three tension σ, σ_{sg}, and σ_{sl} balance,[2] and after using the obvious energetic relation $w = \sigma + \sigma_{\mathrm{sg}} - \sigma_{\mathrm{sl}}$, one

---

[2] The symbol σ_{sg} denotes the tension of the solid-gas interface and the symbol σ_{sl} the tension of the solid-liquid interface.

arrives at the well-known Young-Dupré equation [RW02, dGBWQ03][3]

$$w = \sigma \left(1 + \cos\vartheta\right) . \tag{3.1}$$

This "standard" derivation of the equation involves a balance of tangential forces at the contact line. Yet, despite its very intuitive nature, the requirement of surface stress balance does not yield the correct condition for more complicated surface Hamiltonians, *even* if the concept of surface stress is generalized along the lines discussed in Chap. 2. Higher order Hamiltonians give rise to additional energy contributions when the contact line is varied. These contributions can be accounted for in a systematic and parametrization-free way, and without assuming any additional symmetries (such as axisymmetry or translational symmetry along the contact line) as we will see in the following.

3.2 Geometry and energy

> *Surface properties such as the curvature can be written in terms of an orthonormal vector basis adapted to the line of contact. The energy of the system is given by the sum over the reparametrization invariant surface Hamiltonian and an adhesion or line energy.*

By "contact line" $\mathcal{C}$ we will either denote the curve along which the surface detaches from the substrate or the separating boundary between two surface domains. Its local direction is given by the tangent vector $\boldsymbol{t} = t^a \boldsymbol{e}_a$, which is tangential to $\mathcal{C}$ and all existing surfaces: the surface Σ itself and, if Σ is adhering to a substrate, the substrate surface $\underline{\Sigma}$ (see Fig. 3.2). Here and in what follows (with the exception of Sec. 3.4.2) we will underline quantities referring to the substrate.

Perpendicular to $\mathcal{C}$ we can define local normal vectors which are either tangential to Σ or $\underline{\Sigma}$, namely $\boldsymbol{l} = l^a \boldsymbol{e}_a$ and $\underline{\boldsymbol{l}} = \underline{l}^a \underline{\boldsymbol{e}}_a$, respectively (see again Fig. 3.2 and App. A.2). Also, we will have two surface normals $\boldsymbol{n}$ and $\underline{\boldsymbol{n}}$. If the surface contacts the substrate smoothly at a contact angle of 180°, we will have $\boldsymbol{e}_a = \underline{\boldsymbol{e}}_a$, $\boldsymbol{n} = \underline{\boldsymbol{n}}$, and $\boldsymbol{l} = \underline{\boldsymbol{l}}$ there; however, their *derivatives* perpendicular to the contact line need not coincide, since the curvatures of surface and substrate generally need not be identical. In fact, the values of perpendicular and parallel components of these curvatures (and possibly their higher derivatives) will be among the primary focus of this chapter. As before, they will be denoted by $K_\perp = l^a l^b K_{ab}$, $K_\parallel = t^a t^b K_{ab}$, and $K_{\parallel\perp} = K_{\perp\parallel} = l^a t^b K_{ab}$ (see Eqns. (A.52)). We analogously define $\underline{K}_\perp$, $\underline{K}_\parallel$, and $\underline{K}_{\perp\parallel}$.

---

[3] Notice that in the literature on "wetting" the tendency of a liquid to wet a substrate is usually not characterized by the adhesion energy w but rather by the *spreading parameter $S = w - 2\sigma$*, which measures the difference in surface energy between the dry and the wet substrate. In terms of S the Young-Dupré equation reads $S/\sigma = \cos\vartheta - 1$.
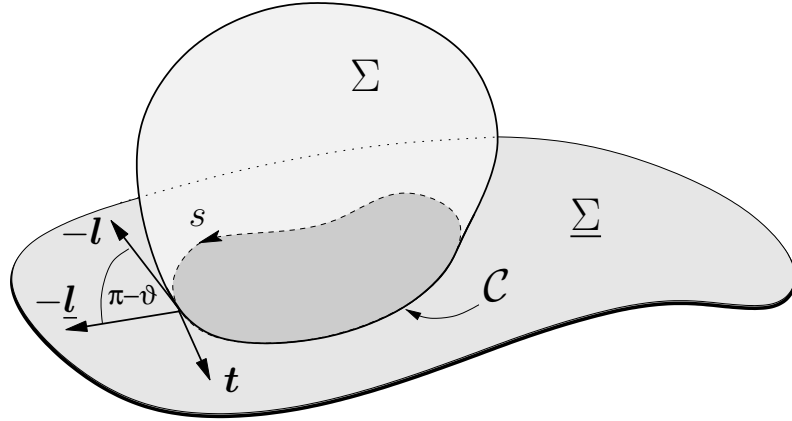
Figure 3.2: Illustration of the geometry of surface adhesion. Perpendicular to the contact line $\mathcal{C}$ two vectors exist, $\boldsymbol{l}$ and $\underline{\boldsymbol{l}}$, which are tangential to surface Σ and substrate $\underline{\Sigma}$, respectively.

We will exclusively study surfaces whose surface energy H is given by the integral (1.3)[4]

$$H = \int_{\Sigma} dA \; \mathcal{H}(g_{ab}, K_{ab}, \nabla_a K_{bc}, \ldots) \; . \tag{3.2}$$

The integral extends over the entire surface Σ. If the surface adheres to a substrate, we will assume an additional adhesion energy density

$$\mathcal{H}_{\text{adhesion}} = -w(\xi^1, \xi^2) \leq 0 \; , \tag{3.3}$$

for those parts of the surface which are in contact with it. Note that w may in general be a function of position.

We will not only study adhesion but also closed surfaces consisting of two different domains such as a two-component membrane vesicle: if the two components do not like to mix but rather form separate domains, a line tension γ arises which tries to minimize the length of the contact line between the domains. To account for that tension, a line energy will replace the adhesion energy in the Hamiltonian. It is given by

$$H_{\text{line}} = \gamma \oint_{\mathcal{C}} ds \; . \tag{3.4}$$

---

[4] A generalization to surfaces with internal degrees of freedom is straightforward but will not be done here.

3.3 Determining the boundary conditions

The form of the energy density restricts which surface property changes discontinuously across the contact line. The corresponding boundary conditions are determined by setting the energy change upon variation of the contact line to zero.

As we will see, adhesion balance between surface and substrate and line tension between different surface domains, respectively, will result in a discontinuous change of some surface property across the contact line. However, since the energy density needs to remain integrable, not all quantities can be discontinuous.

3.3.1 Continuity considerations

Capillary surfaces

Obviously, the shape itself has to be continuous. Yet, already its first derivative may display a jump, as it does in the case of capillary adhesion. The energy density is given by Eqn. (2.23)

$$\mathcal{H}_{\text{capillary}} = \sigma \ , \tag{3.5}$$

and a kink in the surface at the contact line, *i.e.* a finite contact angle, is not associated with an extra energy.

Curvature elastic surfaces

For curvature elastic surfaces the situation is different. There, the energy density of the surface is given by Eqn. (2.29):

$$\mathcal{H}_{\text{bend}} = \frac{1}{2}\kappa(K - K_0)^2 + \frac{1}{2}\bar{\kappa}\mathcal{R} \ . \tag{3.6}$$

where κ and $\bar{\kappa}$ as before are the bending modulus and the saddle-splay modulus, respectively, and K_0 describes a spontaneous curvature of the elastic surface. A kink in the surface at the contact line implies a δ-singularity in the curvature, whose square is non-integrable. Hence, the surface needs to be differentiable across the contact line, and the distinction between surface- and substrate tangents and normals drawn in Sec. 3.2 becomes unnecessary. Moreover, a quick glance at Eqns. (A.52b, A.52c) shows that both $K_{||}$ and the off-diagonal curvature $K_{\perp||}$ are expressible as a tangential derivative along the curve $\mathcal{C}$ of a quantity continuous across $\mathcal{C}$, hence both these curvatures will also be continuous. It is only the perpendicular curvature component $K_{\perp}$ which might possess a discontinuity, and indeed we will see that it does.

─── **Technical Point 3.1:** *Decomposing $\nabla_\perp K_\parallel$ and $\nabla_\perp K_{\perp\parallel}$* ───

Projecting the contracted Codazzi-Mainardi equation (A.46) onto l_a yields:

$$\nabla_b(l_a K^{ab}) - K^{ab}(\nabla_b l_a) = \nabla_\perp(K_\perp + K_\parallel) \ . \tag{3.I}$$

The first term of this equation can be rewritten as

$$
\begin{aligned}
\nabla_b(l_a K^{ab}) \quad &\overset{\text{(A.56a)}}{=} \quad \nabla_b(K_\perp l^b + K_{\perp\parallel} t^b) \\
&= \quad K_\perp(\nabla_b l^b) + K_{\perp\parallel}(\nabla_b t^b) + \nabla_\perp K_\perp + \nabla_\parallel K_{\perp\parallel} \\
&\overset{\text{(A.58b, A.58d)}}{=} \quad K_\perp \boldsymbol{t}\cdot\nabla_\parallel \boldsymbol{l} + K_{\perp\parallel}\boldsymbol{l}\cdot\nabla_\perp\boldsymbol{t} + \nabla_\perp K_\perp + \nabla_\parallel K_{\perp\parallel} \ ,
\end{aligned}
$$

where we used $\boldsymbol{t}\cdot\nabla_\parallel\boldsymbol{t} = \boldsymbol{l}\cdot\nabla_\perp\boldsymbol{l} = 0$ in the last step. The second term in Eqn. (3.I) can be simplified to

$$-K^{ab}(\nabla_b l_a) \overset{\text{(A.58b)}}{=} -K^{ab}\boldsymbol{e}_a(l_b\nabla_\perp\boldsymbol{l} + t_b\nabla_\parallel\boldsymbol{l}) \overset{\text{(A.56)}}{=} -K_{\perp\parallel}\boldsymbol{t}\cdot\nabla_\perp\boldsymbol{l} - K_\parallel\boldsymbol{t}\cdot\nabla_\parallel\boldsymbol{l} \ .$$

Collecting everything together and rewriting $-\boldsymbol{t}\cdot\nabla_\perp\boldsymbol{l} = \boldsymbol{l}\cdot\nabla_\perp\boldsymbol{t}$ we obtain Eqn. (3.8). Analogously, $\nabla_\perp K_{\perp\parallel}$ can be written as

$$\nabla_\perp K_{\perp\parallel} = \nabla_\parallel K_\perp + (K_\perp - K_\parallel)\boldsymbol{l}\cdot\nabla_\perp\boldsymbol{t} - 2K_{\perp\parallel}\boldsymbol{t}\cdot\nabla_\parallel\boldsymbol{l} \ . \tag{3.II}$$

Gradients of curvature

Finally, higher order derivatives might occur in surface Hamiltonians (compare Sec. 1.2.1). Take, for instance, the curvature-gradient term of the form

$$\mathcal{H}_\nabla = \frac{1}{2}\kappa_\nabla(\nabla_a K)(\nabla^a K) \equiv \frac{1}{2}\kappa_\nabla(\nabla K)^2 \ , \tag{3.7}$$

which in a generalized higher-curvature Hamiltonian prevents the occurrence of infinitely sharp curvature changes [GH96]. In this case it is obvious that all curvature components have to be continuous across the contact line, since otherwise again a squared δ-singularity results. Moreover, most of the first order directional derivatives are automatically continuous: the parallel ones, $\nabla_\parallel$, again differentiate quantities along $\mathcal{C}$ which are continuous across $\mathcal{C}$ and thus are themselves continuous. For the perpendicular ones it turns out that $\nabla_\perp K_\parallel$ and $\nabla_\perp K_{\perp\parallel}$ are continuous, while $\nabla_\perp K_\perp$ is not. This is intuitively reasonable, since every term involving a "$\parallel$" features at least one less derivative across the contact line and thus cannot jump. A rigorous proof is however a bit more involved. One may, for instance, proceed like this: start with the contracted Codazzi-Mainardi equation (A.46) $\nabla_b K^{ab} - \nabla^a K = 0$ and project onto l_a. By decomposing the resulting identity into

the local $(\boldsymbol{l}, \boldsymbol{t})$ frame, it can be cast in the form (see Technical Point 3.1)

$$\nabla_\perp K_{||} = \nabla_{||} K_{\perp||} + (K_\perp - K_{||}) \boldsymbol{t} \cdot \nabla_{||} \boldsymbol{l} + 2K_{\perp||} \boldsymbol{l} \cdot \nabla_\perp \boldsymbol{t} \ . \tag{3.8}$$

Since every term on the right hand side is continuous across $\mathcal{C}$ (recall that derivatives of tangent vectors are essentially curvatures), $\nabla_\perp K_{||}$ must be continuous as well. By projecting the contracted Codazzi-Mainardi equation on t_a instead, one can show that $\nabla_\perp K_{\perp||}$ is also continuous (see again Technical Point 3.1).[5]

3.3.2 Contact line variation

For an adhering surface the total energy is stationary with respect to variations of the contact line along the substrate. Such a variation contributes twofold to the Hamiltonian: assume that locally the contact line is moved such that a bit of surface unbinds from the substrate. This removes its corresponding binding energy, as well as any elastic energy associated with the constraint of conforming to the substrate, and thus gives rise to an energy change δH_{bound}. On the other hand, the unbound part of the surface acquires at the contact line a new boundary strip which implies also a change δH_{free} in its elastic energy. The boundary condition at the contact line then follows from the stationarity condition

$$\delta H_{\text{cl}} = \delta H_{\text{bound}} + \delta H_{\text{free}} = 0 \ . \tag{3.9}$$

In the case of adhesion to a rigid substrate the bound contribution involves the variation along a surface of known shape. The corresponding term is thus conceptually very different from a deformable substrate or even the free variation, because in both these cases the local shape of the surface is not known. Below we will see how these differences manifest themselves when computing the boundary terms.

For a surface consisting of two domains the variation of the contact line changes the elastic energy of each domain, giving rise to an energy change δH_{free}. Additionally, the line energy (3.4) contributes: it is proportional to the length of the contact line $\mathcal{C}$. Deforming $\mathcal{C}$ implies that its length and thus the energy change. In total, we have

$$\delta H_{\text{cl}} = \delta H_{\text{line}} + \delta H_{\text{free}} = 0 \ . \tag{3.10}$$

The bound variation

For definiteness, let the normal $\underline{\boldsymbol{l}}$ to the contact line $\mathcal{C}$ be directed *towards* the adhering portion of the surface (see Fig. 3.2 on page 52). A local infinitesimal

---

[5] Note that continuity of $\nabla_\perp K_{||}$ and $\nabla_\perp K_{\perp||}$ only holds for Hamiltonians involving gradients of curvature. For curvature elastic surfaces, $K_\perp$ is discontinuous and, consequently, $\nabla_\perp K_{||}$ and $\nabla_\perp K_{\perp||}$ as well due to Eqns. (3.8) and (3.II).

normal displacement $\varepsilon \underline{\boldsymbol{l}}$ of the contact line along a rigid substrate thus implies the following obvious change in the bound part of the surface:

$$\delta H_{\text{bound}} = -\int_{\mathcal{C}} \mathrm{d}s \, \left(\underline{\mathcal{H}} - w\right)\varepsilon(s) \, . \tag{3.11}$$

The underlining of $\mathcal{H}$ should again indicate that it is evaluated with geometric surface scalars (such as curvatures) pertaining to the *substrate*. If the substrate is flexible, the w term remains, but the change in elastic energy will instead be taken care of by an additional free boundary variation.

The free variation

The change in energy due to the addition or removal of *unbound* parts to the boundaries of the surface is identical to the boundary terms in the variation of the free surface. In Sec. 2.1.1 we have seen that for Hamiltonians *up to curvature order* these terms are given by[6,7]

$$\delta H_{\text{free}} = -\int_{\mathcal{C}} \mathrm{d}s \, l_a \Big[\boldsymbol{f}^a \cdot \delta \boldsymbol{X} + \mathcal{H}^{ab}\boldsymbol{n} \cdot \delta \boldsymbol{e}_b\Big] \, . \tag{3.12}$$

where $\boldsymbol{f}^a$ is the surface stress tensor, given by Eqn. (2.8) and $\mathcal{H}^{ab} = \delta\mathcal{H}/\delta K_{ab}$ as before. Finally, $\delta \boldsymbol{X}$ and $\delta \boldsymbol{e}_b$ denote the change of contact line position and the associated change in the slope of the tangent vectors, respectively. Notice that the second term in Eqn. (3.12) is only relevant if $\mathcal{H}^{ab} \neq 0$.

Variation of the line energy

The variation of the line energy is given by [CGS02]

$$\delta H_{\text{line}} = \gamma \oint_{\mathcal{C}} \delta \mathrm{d}s = -\gamma \oint_{\mathcal{C}} \mathrm{d}s \, (\nabla_{\parallel}\boldsymbol{t}) \cdot \delta \boldsymbol{X} = \gamma \oint_{\mathcal{C}} \mathrm{d}s \, (K_{\text{g}}\boldsymbol{l} + K_{\parallel}\,\boldsymbol{n}) \cdot \delta \boldsymbol{X} \, , \tag{3.13}$$

where $K_{\text{g}} = -\boldsymbol{l} \cdot \nabla_{\parallel}\boldsymbol{t}$ is the geodesic curvature of the contact line (see Eqn. (A.55) on page 175). The length change $\delta \mathrm{d}s$ of the line element contains a part which is tangential and a part which is normal to the surface. The corresponding prefactors can be understood by looking at a purely tangential and a purely normal variation of a circular arc of length L and radius R (see Fig. 3.3). Its length changes according to $\delta L = \frac{L}{R} \delta R$. The radius is given by the inverse of the corresponding curvature, *i. e.*, $1/K_{\text{g}}$ for the tangential variation and $1/K_{\parallel}$ for the normal one. Furthermore, δR equals $\boldsymbol{l} \cdot \delta \boldsymbol{X}$ in the former case and $\boldsymbol{n} \cdot \delta \boldsymbol{X}$ in the latter. If we generalize this result to an infinitesimal element of an arbitrary curve (where $L = \mathrm{d}s$), we exactly obtain the components of the integrand on the right hand side of Eqn. (3.13).

---

[6] For general curvature Hamiltonians $\mathcal{K}^{abc}$ and $\mathcal{G}^{abc}$ are zero (see App. B.2.1).

[7] Equation (3.12) is written slightly differently in Sec. 2.1.1. That the two forms are identical may be seen from the fact that since $\boldsymbol{e}_b \cdot \boldsymbol{n} = 0$, we have $\boldsymbol{e}_b \cdot \delta\boldsymbol{n} = -\boldsymbol{n} \cdot \delta\boldsymbol{e}_b$.

(a) $R = 1/K_{\mathrm{g}}$, $\delta R = \boldsymbol{l} \cdot \delta \boldsymbol{X}$ (b) $R = 1/K_{\|}$, $\delta R = \boldsymbol{n} \cdot \delta \boldsymbol{X}$
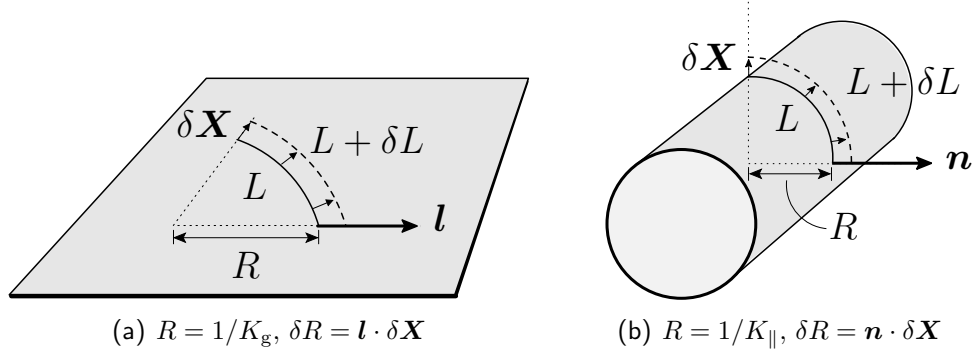
Figure 3.3: Length change δL of a circular arc due to a variation which is (a) tangential and (b) normal to the surface. In both cases the change is given by $\delta L = \frac{L}{R}\,\delta R$.

3.4 Specific examples I – Fluid surface adhesion

The boundary conditions describing adhesion between two fluid surfaces express the balance of stresses and torques. At a rigid substrate, however, this simple identification will generally fail. Stresses and torques enter a single balance condition and cannot be disentangled.

In this and the following section the above formalism will be illustrated by applying it to several important situations and surface Hamiltonians. In Sec. 3.4.1 we first treat the problem of adhesion to a rigid substrate. We will see how known results (the Young-Dupré equation and the contact curvature condition for Helfrich membranes) follow with remarkable ease and can be extended just as quickly to new Hamiltonians. In Sec. 3.4.2 we look at the boundary conditions involving adhesion to deformable substrates. Specifically, we first look at the triple line between three tension surfaces, and then study the adhesion of two vesicles. The final Sec. 3.5 will treat a vesicle with two different domains and determine the conditions at the boundary between these.

A central ingredient in all this will be the knowledge of the tensors $\mathcal{H}^{ab}$, T^{ab}, $\mathcal{K}^{abc}$, and $\mathcal{G}^{abc}$ defined in Sec. 2.1.1 and determined for specific examples in App. B (see Table B.1).

3.4.1 Adhesion to a rigid substrate

Since the variation of the contact line has to proceed along the substrate, we must have

$$\delta \boldsymbol{X} = \varepsilon \, \underline{\boldsymbol{l}} \,. \tag{3.14}$$

No component in the t direction is necessary, since for fluid surfaces this amounts to a reparametrization of $\mathcal{C}$.[8] Notice that (3.14) is nothing but the Lie derivative of $\boldsymbol{X}$ along the substrate, since $\mathcal{L}_{\varepsilon\underline{l}}\boldsymbol{X} = \varepsilon\underline{l}^a\nabla_a\boldsymbol{X} = \varepsilon\underline{l}^a\underline{\boldsymbol{e}}_a = \varepsilon\,\underline{\boldsymbol{l}}$ (see also page 169 in App. A.1). This property holds generally, and we will make use of it later.

The normal component of the change in the surface tangent vectors $\boldsymbol{e}_b$ only contributes to the variation if $\mathcal{H}^{ab} \neq 0$, *i. e.*, if curvature terms enter the Hamiltonian. We will assume that they do it in such a way that differentiability of the surfaces is implied (see Sec. 3.3.1), so that no distinction needs to be drawn between normal and tangent vectors of substrate and adhering surface. We then find

$$\boldsymbol{n}\cdot\delta\boldsymbol{e}_b = \boldsymbol{n}\cdot\nabla_b\delta\boldsymbol{X} = \varepsilon l^c\boldsymbol{n}\cdot\nabla_b\underline{\boldsymbol{e}}_c = -\varepsilon l^c\underline{K}_{bc}\;, \tag{3.15}$$

where in the last step the equations of Weingarten (A.39) have been used; this is again the Lie derivative along the substrate.[9] Notice that there still remains a distinction between *curvatures* of substrate and surface; hence, the derivative of the tangent vectors resulting from a variation *along the substrate* yields the *substrate* curvature and not the free surface curvature.

Capillary surfaces

In this case the energy density is given by Eqn. (3.5), and as we have seen in Sec. 3.3.1, we will expect a discontinuity in the slope at $\mathcal{C}$. The bound variation is

$$\delta H_{\mathrm{bound}} = -\int_{\mathcal{C}}\mathrm{d}s\,(\sigma - w)\varepsilon(s)\;. \tag{3.16}$$

For this Hamiltonian we have $\mathcal{H}^{ab} = 0$ and $\boldsymbol{f}^a = -\sigma\boldsymbol{e}^a$ (see Sec. 2.2), and therefore

$$l_a\boldsymbol{f}^a\cdot\delta\boldsymbol{X} = -\sigma l_a\boldsymbol{e}^a\cdot\varepsilon\underline{\boldsymbol{l}} = -\sigma\varepsilon\boldsymbol{l}\cdot\underline{\boldsymbol{l}} = -\sigma\varepsilon\cos(\pi - \vartheta)\;, \tag{3.17}$$

where ϑ is the angle between capillary surface and substrate – in other words, the contact angle (see Fig. 3.2). Equation (3.9) thus specializes to

$$\delta H_{\mathrm{cl}} = -\int_{\mathcal{C}}\mathrm{d}s\,\left[\sigma - w + \sigma\cos\vartheta\right]\varepsilon(s)\;. \tag{3.18}$$

Since $\varepsilon(s)$ is arbitrary, the term in square brackets must vanish – which gives the Young-Dupré equation (3.1).

---

[8] The corresponding variation does indeed not change the energy as one can also check by repeating the calculations of this section with $\delta\boldsymbol{X} = \varepsilon_{\|}\boldsymbol{t}$.

[9] This is most easily seen in the following way: $\boldsymbol{n}\cdot\delta\boldsymbol{e}_b = -\boldsymbol{e}_b\cdot\delta\boldsymbol{n} = -\boldsymbol{e}_b\cdot\mathcal{L}_{\varepsilon l}\boldsymbol{n} = -\boldsymbol{e}_b\cdot\varepsilon l^c\nabla_c\boldsymbol{n} = -\boldsymbol{e}_b\cdot\varepsilon l^c\underline{K}_c^a\boldsymbol{e}_a = -\varepsilon l^c g_{ab}\underline{K}_c^a = -\varepsilon l^c\underline{K}_{bc}$, which is exactly the right hand side of Eqn. (3.15).

Helfrich Hamiltonian

Let us now look at the energy density (3.6) which, as we have seen in the previous chapters, describes the continuum behavior of (tensionless) fluid lipid bilayers. Since K appears quadratic, the surface will now be differentiable across the contact line, as pointed out in Sec. 3.3.1.

We have seen in Sec. 2.2.2 that the intrinsic contribution $\frac{1}{2}\bar{\kappa}\mathcal{R} = \bar{\kappa}K_{\mathrm{G}}$ does not influence the shape of the membrane. It may, however, contribute to the boundary condition at the contact line depending on the case one considers. In Sec. 3.5 we will indeed discuss a case where it does.

Yet, for surface adhesion a simple argument shows that the intrinsic contribution will *not* matter for the boundary conditions. Since the contact line is varied locally, we can focus our attention on a membrane strip of finite width and *fixed edges*, covering the contact line. Due to the Gauss-Bonnet theorem (see App. A.3) the contribution of K_{G} to the energy will not change upon variation of the contact line (which lies in the middle of the strip) and must therefore not enter any condition resulting from it. For readers not convinced by this quick argument, the following derivation shows explicitly (but less elegantly) that the $\bar{\kappa}$-contributions indeed drop out.

Let us begin with the stress tensor. From Eqn. (2.31) we find (with $\sigma = 0$)

$$l_a \boldsymbol{f}^a \cdot \boldsymbol{l} \;=\; -\frac{1}{2}\kappa(K - K_0)^2 + \kappa(K - K_0)K_\perp \,, \tag{3.19a}$$

$$=\; \frac{1}{2}\kappa\big[K_\perp^2 - (K_\parallel - K_0)^2\big] \,. \tag{3.19b}$$

Notice again that this expression is independent of $\bar{\kappa}$: the Gaussian contribution in the Helfrich Hamiltonian does not create membrane stresses. Next, we look at the dependence of $\mathcal{H}$ on the extrinsic curvature. From Table B.1/Eqn. (2.35) we get

$$\mathcal{H}^{ab} = \kappa(K - K_0)g^{ab} + \bar{\kappa}(Kg^{ab} - K^{ab}) \,. \tag{3.20}$$

Here the $\bar{\kappa}$-contribution does not cancel right away. With the help of Eqns. (3.15) and (3.20) we can further calculate

$$l_a\mathcal{H}^{ab}\boldsymbol{n}\cdot\delta\boldsymbol{e}_b \;=\; \left\{-\kappa(K - K_0)\underline{K}_\perp - \bar{\kappa}\big(K_\parallel\underline{K}_\perp - K_{\perp\parallel}\underline{K}_{\perp\parallel}\big)\right\}\varepsilon$$

$$=\; -\left\{\kappa(K - K_0)\underline{K}_\perp + \frac{1}{2}\bar{\kappa}\underline{\mathcal{R}}\right\}\varepsilon \,. \tag{3.21}$$

The final step follows from the continuity conditions $\underline{K}_\parallel = K_\parallel$ and $\underline{K}_{\perp\parallel} = K_{\perp\parallel}$ from Sec. 3.3.1 and the representation (A.51c) of the Ricci scalar curvature as the Gaussian curvature determinant $\frac{1}{2}\underline{\mathcal{R}} = \underline{K}_{\mathrm{G}} = \underline{K}_\perp\underline{K}_\parallel - \underline{K}_{\perp\parallel}^2$.

Inserting Eqns. (3.19a) and (3.21) into the general expression for the free variation, Eqn. (3.12), and adding the bound variation (3.11), we arrive at the total energy

change upon contact line variation

$$
\delta H_{\mathrm{cl}} = -\int_{\mathcal{C}} \mathrm{d}s \left\{ \frac{1}{2}\kappa(\underline{K} - K_0)^2 + \frac{1}{2}\bar{\kappa}\underline{\mathcal{R}} - w \right.
$$

$$
-\frac{1}{2}\kappa(K - K_0)^2 + \kappa(K - K_0)K_\perp
$$

$$
\left. -\kappa(K - K_0)\underline{K}_\perp - \frac{1}{2}\bar{\kappa}\underline{\mathcal{R}} \right\} \varepsilon(s) \tag{3.22a}
$$

$$
= -\int_{\mathcal{C}} \mathrm{d}s \left\{ \frac{1}{2}\kappa(K_\perp - \underline{K}_\perp)^2 - w \right\} \varepsilon(s) , \tag{3.22b}
$$

where in the second step we again made use of the continuity condition $K_\parallel = \underline{K}_\parallel$. Notice that the $\bar{\kappa}$-dependence has finally canceled out completely, as we have argued above. Equation (3.22b) implies a discontinuity in the perpendicular curvature $K_\perp$ as the appropriate adhesion boundary condition:

$$
K_\perp - \underline{K}_\perp = \sqrt{\frac{2w}{\kappa}} . \tag{3.23}
$$

The correct sign after taking the square root follows from the fact that the detaching surface must not penetrate the substrate; unfortunately this depends on one's specific choice of the orientation of the surface normal vectors.

Quite remarkably, this boundary condition depends neither on the spontaneous curvature K_0 (the contribution to the Hamiltonian linear in K does not enter), nor on the local parallel curvature $K_\parallel$. It would also remain unaffected if the bilayer were under a finite tension σ. Formally, it is easily seen to cancel; physically, the reason is that the jump we would expect from the Young-Dupré equation (3.1) cannot materialize since the curvature terms in the energy density enforce differentiability of the profile at $\mathcal{C}$.

Equation (3.23) coincides with the result given previously in Ref. [CG02a]. Its axisymmetric version was first quoted in Ref. [SL90], and its specialization to a straight contact line can be found in Ref. [LL86, Sec. 12, problem 6]. We want to stress that the $\mathcal{H}^{ab}\boldsymbol{n}\cdot\delta\boldsymbol{e}_b$ term in Eqn. (3.12), which is responsible for the third line in Eqn. (3.22a), was crucial in obtaining equation (3.23). Leaving it out – *i. e.*, only treating the problem as a *stress balance* – will *not* result in the correct boundary condition, as first pointed out in Ref. [Mül04]. The only exception (treated via stress-balance in Refs. [CG02a, Fou07]) is the special case of a flat substrate, in which case $\delta\boldsymbol{e}_b \equiv 0$ and the missing contribution vanishes anyway. The deeper reason for the apparent failure of a stress-based approach is the interdependence of the variations $\delta\boldsymbol{X}$ and $\delta\boldsymbol{e}_b$, as enforced by the rigid substrate. This point will become more clear once we have studied deformable substrates in Sec. 3.4.2.

General curvature Hamiltonians

It is not difficult to extend the above analysis to the entire class of Hamiltonians which depend on intrinsic and extrinsic surface curvatures. Since (i) for two-dimensional surfaces the Ricci scalar $\mathcal{R}$ uniquely determines the Riemann tensor via $R_{abcd} = \frac{1}{2}\mathcal{R}(g_{ac}g_{bd} - g_{ad}g_{bc})$, and since ($ii$) the doubly contracted Gauss-Codazzi equation $\mathcal{R} = K^2 - K_{ab}K^{ab}$ permits the replacement of products of the extrinsic curvature tensor K_{ab} with powers of the extrinsic curvature scalar K and the Ricci scalar $\mathcal{R}$, we can without loss of generality assume that any such curvature Hamiltonian has been brought into the form

$$\mathcal{H} = \mathcal{H}(K, \mathcal{R}) . \tag{3.24}$$

According to Eqns. (B.8) the two tensors T^{ab} and $\mathcal{H}^{ab}$ are given by

$$
\begin{aligned}
T^{ab} &= -\mathcal{H}g^{ab} + 2\frac{\partial\mathcal{H}}{\partial K}K^{ab} + 2\frac{\partial\mathcal{H}}{\partial\mathcal{R}}\mathcal{R}g^{ab} , \tag{3.25a} \\
\mathcal{H}^{ab} &= \frac{\partial\mathcal{H}}{\partial K}g^{ab} + 2\frac{\partial\mathcal{H}}{\partial\mathcal{R}}(Kg^{ab} - K^{ab}) . \tag{3.25b}
\end{aligned}
$$

Before we proceed, let us look once more at the continuity requirements spelled out in Sec. 3.3.1. The question to be answered is whether or not the general Hamiltonian $\mathcal{H}$ enforces differentiability. If it does not involve the curvature at all, it is of the form (3.5) and will permit kinks. This case has been treated on page 58. However, differentiability is *not* automatically guaranteed once curvature appears. In particular, kinks are possible if $\mathcal{H}$ is *linear* in K or $\mathcal{R}$, since both curvatures involve the component $K_\perp$ across the boundary only linearly. The resulting δ-singularity is hence integrable and adds a *finite* extra contribution to the energy (and its variation) which we would need to consider separately. While such a situation can also be treated within the general framework presented in this chapter, the details are surprisingly tricky. Since it is better not to obfuscate the overall picture by devoting a disproportionate amount of space to these singular cases, we will from now on assume that differentiability holds. The reader should notice that this will be the case once a nonzero bending modulus κ is present. Indeed, for dimensional consistency it is implausible to assume that a term linear in $\mathcal{R}$ will occur without its "partner" quadratic in K. However, a Hamiltonian of the form $\sigma + \beta K$ is *not* irrelevant and occurs, for instance, if one asks what are the shapes of vesicles of given area and area difference (between outer and inner monolayer) which have maximal volume, as Svetina and Žekš have done [SŽ89]. The treatment of the adhesion balance for this case can be found in Ref. [CG02a]. Assuming differentiability from now on, we can combine the expressions (3.25) for the tensors T^{ab} and $\mathcal{H}^{ab}$ with the boundary variations in Eqns. (3.14, 3.15) and

from this readily find

$$l_a \boldsymbol{f}^a \cdot \delta \boldsymbol{X} \;=\; -\Big[\mathcal{H} - \frac{\partial \mathcal{H}}{\partial K} K_\perp - \frac{\partial \mathcal{H}}{\partial \mathcal{R}} \mathcal{R}\Big]\varepsilon \;, \tag{3.26a}$$

$$l_a \mathcal{H}^{ab} \boldsymbol{n} \cdot \delta \boldsymbol{e}_b \;=\; -\Big[\frac{\partial \mathcal{H}}{\partial K} \underline{K}_\perp + \frac{\partial \mathcal{H}}{\partial \mathcal{R}} \underline{R}\Big]\varepsilon \;. \tag{3.26b}$$

The total contact line variation is therefore given by

$$\delta H_{\mathrm{cl}} \;=\; -\int_{\mathcal{C}} \mathrm{d}s \; \bigg\{ \underline{\mathcal{H}} - w \\ - \mathcal{H} + \frac{\partial \mathcal{H}}{\partial K} K_\perp + \frac{\partial \mathcal{H}}{\partial \mathcal{R}} \mathcal{R} \\ - \frac{\partial \mathcal{H}}{\partial K} \underline{K}_\perp - \frac{\partial \mathcal{H}}{\partial \mathcal{R}} \underline{\mathcal{R}} \bigg\} \; \varepsilon(s) \;. \tag{3.27}$$

The requirement $\delta H_{\mathrm{cl}} = 0$ now gives rise to the remarkably succinct boundary condition

$$(\underline{\mathcal{H}} - \mathcal{H}) - \frac{\partial \mathcal{H}}{\partial K}(\underline{K}_\perp - K_\perp) - \frac{\partial \mathcal{H}}{\partial \mathcal{R}}(\underline{\mathcal{R}} - \mathcal{R}) \;=\; w \;. \tag{3.28}$$

This equation generalizes the contact curvature condition (3.23) to arbitrary Hamiltonians of curvature order. Notice that despite its rather "systematic" appearance, this general condition is not symmetric between surface and substrate, *i. e.*, it does not remain invariant when replacing underlined and not-underlined quantities – unlike the special case of the contact curvature condition (3.23) for Helfrich membranes. Also, the parallel curvature $K_\parallel$ will generally enter the boundary condition, exposing the cancellation in the case of the Helfrich Hamiltonian as "accidental".

We can readily see how Eqn. (3.28) reduces to the special cases we have treated above: for $\mathcal{H} = \frac{1}{2}\kappa K^2$ we have $\partial \mathcal{H}/\partial K = \kappa K$ and $\partial \mathcal{H}/\partial \mathcal{R} = 0$, such that the left hand side of Eqn. (3.28) becomes $\frac{1}{2}\kappa(\underline{K}^2 - K^2) - \kappa K(\underline{K}_\perp - K_\perp) = \frac{1}{2}\kappa(\underline{K}_\perp - K_\perp)^2$, which leads to the contact curvature condition (3.23). For a contribution $\frac{1}{2}\bar{\kappa}\mathcal{R}$ in a Hamiltonian which enforces differentiability by the presence of other terms we have $\partial(\frac{1}{2}\bar{\kappa}\mathcal{R})/\partial K = 0$ and $\partial(\frac{1}{2}\bar{\kappa}\mathcal{R})/\partial \mathcal{R} = \frac{1}{2}\bar{\kappa}$, such that it cancels in the left hand side of Eqn. (3.28). We thereby see once more that the Gaussian curvature term in the Helfrich Hamiltonian (and thus the saddle splay modulus $\bar{\kappa}$) does not contribute to the boundary condition for the case of surface adhesion.

Let us conclude this section by casting a quick glance onto one more interesting special case, namely the Hamiltonian

$$\mathcal{H} \;=\; \frac{1}{2}\bar{\kappa}_2 \mathcal{R}^2 \;. \tag{3.29}$$

This quartic expression, which also enters the theory developed in Ref. [GH96], is the lowest order *intrinsic* curvature Hamiltonian one can write down for two-dimensional surfaces. Since $\partial \mathcal{H}/\partial K = 0$ and $\partial \mathcal{H}/\partial \mathcal{R} = \bar{\kappa}_2 \mathcal{R}$, we arrive at the

(purely intrinsic) boundary condition

$$\mathcal{R} - \underline{\mathcal{R}} \;=\; \sqrt{\frac{2w}{\bar{\kappa}_2}} \; , \tag{3.30}$$

whose similarity with the usual contact curvature condition (3.23) is quite striking.

The general quartic Hamiltonian

The Helfrich Hamiltonian terminates the expansion of the surface energy at the dimensional order LENGTH^{-2}. For up-down symmetric membranes the next order is the quartic one, LENGTH^{-4}, and it adds four more terms to the energy density [CGS03]

$$\mathcal{H}_4 = \frac{1}{4}\kappa_4 K^4 + \kappa_\times K^2\mathcal{R} + \frac{1}{2}\bar{\kappa}_2\mathcal{R}^2 + \frac{1}{2}\kappa_\nabla(\nabla K)^2 \; . \tag{3.31}$$

While all four moduli have the same units – ENERGY $\times$ LENGTH^4 – they are *not* of the same order in surface derivatives. The first three terms are scalar functions of the surface curvatures, *i. e.*, special cases of the Hamiltonian density (3.24), but the fourth term involves the *derivative* of the curvature and is therefore of *third* order in surface derivatives. This has significant implications for the boundary conditions holding at quartic order: while one might initially surmise that all quartic moduli (and possibly also the quadratic ones) enter in a presumably lengthy equation, the continuity considerations from Sec. 3.3.1 imply that all curvatures are continuous across the contact line due to the occurrence of the gradient-K-term in (3.31). In consequence, *none* of the undifferentiated curvature terms influences the boundary condition, which is exclusively determined by the gradient term.

We have thus seen that it suffices in quartic order to study the implications of curvature gradients alone, *i. e.* the Hamiltonian (3.7). From Tables 2.1 and B.1 we can derive that in this case

$$l_a \boldsymbol{f}^a \cdot \boldsymbol{l} \;=\; \kappa_\nabla\Big[(\nabla_\perp K)^2 - \frac{1}{2}(\nabla K)^2 - K_\perp \Delta K\Big] \; , \tag{3.32a}$$

$$\mathcal{H}^{ab} \;=\; -\kappa_\nabla(\Delta K)g^{ab} \; . \tag{3.32b}$$

However, simplemindedly inserting these expressions into the formulas we have used so far in this chapter does *not* give the correct result. This is because variation (3.12) is only valid for Hamiltonians up to curvature order. In Chap. 2 we have seen that gradients of curvature in the Hamiltonian imply that the variations with respect to δK_{ab} and δg_{ab} *do not* vanish at the boundary, *i. e.*, $\mathcal{G}^{abc}$ and $\mathcal{K}^{abc}$ are finite (see Eqn. (2.9) together with (2.2)). These terms result from an integration by parts which removes the covariant derivatives acting on δK_{ab} and δg_{ab} in the variation of the Hamiltonian (see App. B.2.2). They have to be added to Eqn. (3.12).

From Table B.1 we obtain

$$
\begin{aligned}
\mathcal{G}^{abc}\delta g_{bc} + \mathcal{K}^{abc}\delta K_{bc} &= \kappa_\nabla(\nabla^a K)(-K^{bc}\delta g_{bc} + g^{bc}\delta K_{bc}) \\
&= \kappa_\nabla(\nabla^a K)(K_{bc}\delta g^{bc} + g^{bc}\delta K_{bc}) ,
\end{aligned}
\tag{3.33}
$$

where we used Eqn. (B.I) in the second step to rewrite δg_{ab} in terms of the variation of the inverse metric. The two tensor variations can then be combined nicely into a single scalar one, since they occur in the combination $K_{ab}\delta g^{ab} + g^{ab}\delta K_{ab} = \delta K$. We end up with the additional boundary contribution

$$
\delta H_{\text{free},\nabla} = \kappa_\nabla \int_\mathcal{C} \mathrm{d}s\, l_a(\nabla^a K)\delta K .
\tag{3.34}
$$

This is of course exactly the boundary term one would expect for the variation of a Hamiltonian density whose functional form is the square of the gradient of a scalar, so everything is consistent.

To evaluate the right hand side of Eqn. (3.34), note that the variation is once more given by the Lie-derivative along the substrate. Since K is a scalar, we obtain the simple expression

$$
\delta K = \mathcal{L}_{\varepsilon\boldsymbol{l}}K \overset{\text{(A.21)}}{=} \varepsilon l^a \nabla_a \underline{K} = \varepsilon\nabla_\perp \underline{K} .
\tag{3.35}
$$

Together with Eqns. (3.32) we then obtain the total contact line variation as

$$
\begin{aligned}
\delta H_{\text{cl}} &= -\int_\mathcal{C} \mathrm{d}s\, \bigg\{ \frac{1}{2}\kappa_\nabla(\nabla\underline{K})^2 - w \\
&\qquad +\kappa_\nabla\Big[(\nabla_\perp K)^2 - \frac{1}{2}(\nabla K)^2 - K_\perp\Delta K\Big] \\
&\qquad +\kappa_\nabla(\Delta K)\underline{K}_\perp \\
&\qquad -\kappa_\nabla(\nabla_\perp K)(\nabla_\perp\underline{K}) \bigg\}\, \varepsilon(s)
\end{aligned}
\tag{3.36a}
$$

$$
= -\int_\mathcal{C} \mathrm{d}s\, \bigg\{ \frac{1}{2}\kappa_\nabla(\nabla_\perp K_\perp - \nabla_\perp\underline{K}_\perp)^2 - w \bigg\}\, \varepsilon(s) ,
\tag{3.36b}
$$

where in the last step we used the continuity of curvatures and their $\nabla_\parallel$-derivatives as discussed in Sec. 3.3.1, as well as the decomposition $(\nabla K)^2 = (\nabla_\perp K)^2 + (\nabla_\parallel K)^2$. The boundary condition following from this specifies a jump in the perpendicular *derivative* of the perpendicular curvature

$$
\nabla_\perp\big(K_\perp - \underline{K}_\perp\big) = \sqrt{\frac{2w}{\kappa_\nabla}} .
\tag{3.37}
$$

As remarked above, this constitutes the appropriate boundary condition for a curvature elastic theory including *all terms up to quartic order*. Its similarity with Eqns. (3.23) and (3.30) is again very striking, and one might surmise a pattern
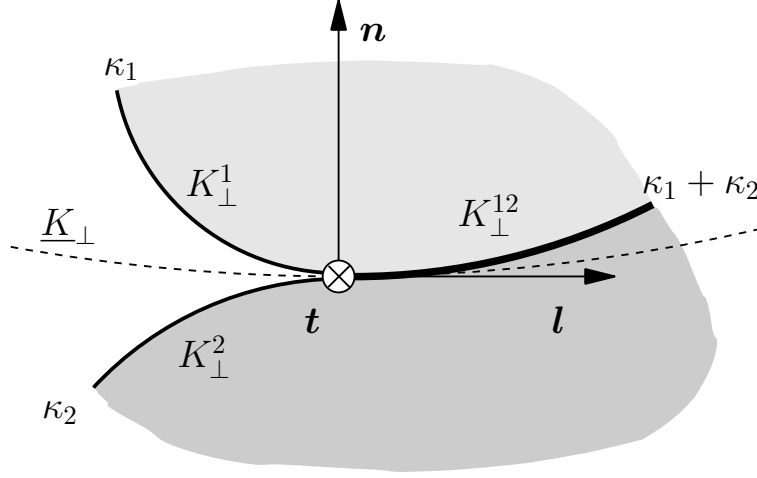
Figure 3.4: Illustration of the geometry at the contact line between two adhering vesicles.

that would be followed by even higher derivative theories. Notice, however, that the terms entering the derivation of Eqns. (3.37) are quite different and that the additional term stemming from Eqn. (3.34), which is absent in the simple curvature square case, is essential.

3.4.2 Adhesion to deformable surfaces

Compared to the previous section, there are two key differences if the substrate is not rigid. First, the absence of a known substrate shape along which a certain amount of deformation energy is to be paid removes the term involving $\underline{\mathcal{H}}$ in the bound variation (3.11). Second, for the same reason the contact line variation is no longer restricted to proceed along a substrate and will thus be of the more general form

$$\delta \boldsymbol{X} = \varepsilon_\perp \boldsymbol{l} + \varepsilon_n \boldsymbol{n} \ . \tag{3.38}$$

The corresponding tangent vector variation, which occurs if $\mathcal{H}^{ab} \neq 0$, then leaves a term

$$\boldsymbol{n} \cdot \delta \boldsymbol{e}_b = \boldsymbol{n} \cdot \nabla_b (\varepsilon_\perp \boldsymbol{l} + \varepsilon_n \boldsymbol{n}) = -\underline{K}_{bc} l^c \varepsilon_\perp + \nabla_b \varepsilon_n \ . \tag{3.39}$$

Note that $\underline{K}_{bc}$ plays a different role here than previously. It no longer describes the curvature of the evidently nonexistent substrate. Rather, the tangential variation may proceed locally along a *fictitious* surface which is tangential to the other three surfaces that meet at the contact line. Encoding higher order derivative information necessary here, $\underline{K}_{bc}$ describes the curvature of that fictitious surface, and $\underline{K}_\perp$ is the component perpendicular to $\mathcal{C}$ (see Fig. 3.4). This surface is of

course not unique, and thus $\underline{K}_\perp$ is arbitrary – just as the two variations $\varepsilon_\perp$ and ε_n themselves are.

Three phase capillary equilibrium

The simplest example of a three phase line between deformable surfaces occurs when three capillary interfaces meet, for instance, at the three-phase-line between three mutually immiscible fluids 1, 2, and 3, having mutual surface tensions σ^{12}, σ^{23} and σ^{31}. In this case no adhesion energy is involved (or, alternatively, it may be considered as part of the surface tension). The contact line variation thus consists of three identical boundary variations

$$
\begin{aligned}
\delta H_{\mathrm{cl}} &= -\int \mathrm{d}s \left\{ l_a^{12} \boldsymbol{f}^{12a} + l_a^{23} \boldsymbol{f}^{23a} + l_a^{31} \boldsymbol{f}^{31a} \right\} \cdot \delta \boldsymbol{X} \\
&= \int \mathrm{d}s \left\{ \sigma^{12} \boldsymbol{l}^{12} + \sigma^{23} \boldsymbol{l}^{23} + \sigma^{31} \boldsymbol{l}^{31} \right\} \cdot \delta \boldsymbol{X} \;,
\end{aligned} \tag{3.40}
$$

from which we immediately find the boundary condition

$$
\boldsymbol{\sigma}^{12} + \boldsymbol{\sigma}^{23} + \boldsymbol{\sigma}^{31} = 0 \;. \tag{3.41}
$$

This expresses nothing but the force balance between the three directional line tensions $\boldsymbol{\sigma}^{12} = \sigma^{12} \boldsymbol{l}^{12}$ etc. and is known as the *Neumann triangle* [RW02]. The vector equation (3.41) corresponds to *two* scalar equations (since there is no component along $\boldsymbol{t}$). These are sufficient to determine the three contact angles between the three phases (because their sum equals $360°$). Notice that this conversely implies that by measuring these angles one can only determine the *ratios* between the three tensions, not absolute values. How all this information is conveniently extracted is discussed in detail in Ref. [RW02, Chap. 8].

Adhesion of two vesicles

For the case of two adhering vesicles we assume that vesicle 1 has bending modulus κ_1 and tension σ_1, while vesicle 2 has corresponding values κ_2 and σ_2. *If* the two bilayers can slide past each other in the region where they adhere, their joint bending modulus is given by $\kappa_{12} = \kappa_1 + \kappa_2$, because the energies required to bend either one just add; the same applies to the tension: $\sigma_{12} = \sigma_1 + \sigma_2$. We will for simplicity look at the case where the spontaneous curvature is zero. Note that a term proportional to the Gaussian curvature can be neglected if $\bar{\kappa}_{12} = \bar{\kappa}_1 + \bar{\kappa}_2$. The easiest way to see this is to consider the two vesicles separately: integration of K_{G} over the closed surface of each vesicle yields a constant due to the Gauss-Bonnet theorem (see App. A.3). Thus, the energy does not change no matter how much the vesicles touch each other. Furthermore, one has two additional terms in the

energy that fix the volume of each of the vesicles (see Secs. 1.2.3 and 2.3.1). These will contribute terms to the variation which are proportional to the Jemal tensor (compare footnote 12 on page 43). In total, however, all terms will cancel as well because $l_a \boldsymbol{J}^a$ is continuous across the contact line.

The contact line variation contains one adhesion term and three free boundary variations. Using the decomposition of $\delta \boldsymbol{X}$ and $\delta \boldsymbol{e}_b$ as given in Eqns. (3.38) and (3.39), respectively, we find the total energy change to be[10,11]

$$
\begin{aligned}
\delta H_{\mathrm{cl}} \;=\; & -\int \mathrm{d}s \Bigg\{ \Big[-w - \frac{1}{2}(\kappa_1 + \kappa_2)(K_\perp^{12})^2 \\
& + \frac{1}{2}\kappa_1 (K_\perp^1)^2 + \frac{1}{2}\kappa_2 (K_\perp^2)^2 \Big]\varepsilon_\perp \\
& - \Big[\kappa_1 \nabla_\perp K^1 + \kappa_2 \nabla_\perp K^2 - (\kappa_1 + \kappa_2)\nabla_\perp K^{12} \Big]\varepsilon_n \\
& - \Big[\kappa_1 K_\perp^1 + \kappa_2 K_\perp^2 - (\kappa_1 + \kappa_2)K_\perp^{12} \Big]\underline{K}_\perp \varepsilon_\perp \\
& + \Big[\kappa_1 K_\perp^1 + \kappa_2 K_\perp^2 - (\kappa_1 + \kappa_2)K_\perp^{12} \Big]\nabla_\perp \varepsilon_n \Bigg\}.
\end{aligned} \qquad (3.42)
$$

All corresponding $K_\parallel$ contributions cancel, since $K_\parallel$ is again continuous across $\mathcal{C}$; the same happens to the tensions. The derivative $\nabla_\perp K_\parallel$, however, involves a term proportional to $K_\perp$ and does not cancel a priori (see Eqn. (3.8)).

The four terms belonging to the independent variations $\varepsilon_\perp$, ε_n, $\underline{K}_\perp \varepsilon_\perp$, and $\nabla_\perp \varepsilon_n$ must vanish individually. Notice that the last two have identical prefactors; in fact, using Eqn. (3.39) as well as the obvious identities $\varepsilon_\perp = \boldsymbol{l} \cdot \delta \boldsymbol{X}$ and $\varepsilon_n = \boldsymbol{n} \cdot \delta \boldsymbol{X}$, we can rewrite the total variation (3.42) in the more transparent form[12]

$$
\begin{aligned}
\delta H_{\mathrm{cl}} \;=\; & -\int \mathrm{d}s \Bigg\{ \Big[-w - \frac{1}{2}(\kappa_1 + \kappa_2)(K_\perp^{12})^2 \\
& + \frac{1}{2}\kappa_1 (K_\perp^1)^2 + \frac{1}{2}\kappa_2 (K_\perp^2)^2 \Big]\boldsymbol{l} \cdot \delta \boldsymbol{X} \\
& - \Big[\kappa_1 \nabla_\perp K^1 + \kappa_2 \nabla_\perp K^2 - (\kappa_1 + \kappa_2)\nabla_\perp K^{12} \Big]\boldsymbol{n} \cdot \delta \boldsymbol{X} \\
& - \Big[\kappa_1 K_\perp^1 + \kappa_2 K_\perp^2 - (\kappa_1 + \kappa_2)K_\perp^{12} \Big]\boldsymbol{l} \cdot \delta \boldsymbol{n} \Bigg\}.
\end{aligned} \qquad (3.43)
$$

This identifies clearly the three independent variations which matter: one tangential and one perpendicular *translation*, described by $\boldsymbol{l} \cdot \delta \boldsymbol{X}$ and $\boldsymbol{n} \cdot \delta \boldsymbol{X}$, respectively,

---

[10] To avoid confusion, note that we directly insert Eqn. (3.19b) for $l_a \boldsymbol{f}^a \cdot \boldsymbol{l}$ here in contrast to Eqn. (3.22a) where Eqn. (3.19a) was used.

[11] The curvatures of the bound part and the two free parts are all defined with respect to the same vectors $\boldsymbol{n}$, $\boldsymbol{l}$, and $\boldsymbol{t}$. The relative minus sign in the variation follows from this definition.

[12] Notice once more that since $\boldsymbol{n} \cdot \boldsymbol{e}_b = \boldsymbol{n} \cdot \boldsymbol{l} = 0$, we have $l^b \boldsymbol{n} \cdot \delta \boldsymbol{e}_b = \boldsymbol{n} \cdot \delta(l^b \boldsymbol{e}_b) = \boldsymbol{n} \cdot \delta \boldsymbol{l} = -\boldsymbol{l} \cdot \delta \boldsymbol{n}$.

and one *rotation* around the local contact line, specified by the variation $\boldsymbol{l} \cdot \delta \boldsymbol{n}$. The corresponding three boundary conditions are then given by

$$\kappa_1 (K_\perp^1)^2 + \kappa_2 (K_\perp^2)^2 - (\kappa_1 + \kappa_2)(K_\perp^{12})^2 = 2w , \tag{3.44a}$$

$$\nabla_\perp \Big(\kappa_1 K_\perp^1 + \kappa_2 K_\perp^2 - (\kappa_1 + \kappa_2) K_\perp^{12} \Big) = 0 , \tag{3.44b}$$

$$\kappa_1 K_\perp^1 + \kappa_2 K_\perp^2 - (\kappa_1 + \kappa_2) K_\perp^{12} = 0 , \tag{3.44c}$$

where Eqn. (3.44b) has already been simplified by rewriting $\nabla_\perp K_\parallel$ with the help of Eqn. (3.8) and subsequently inserting the third condition (3.44c).

Our identification of the independent variations permits an easy interpretation of these three conditions: the first two equations are an expression of a local stress balance (namely, of tangential and perpendicular forces). The third condition expresses the balance of *torques* around the contact line, a hypothesis confirmed by the general form of the membrane torque tensor (2.21).

Contrary to the case of vesicle adhesion to a rigid substrate, Eqn. (3.23), these conditions also contain one involving the *derivative* of curvatures, namely (3.44b). Its origin is the perpendicular variation $\boldsymbol{n} \cdot \delta \boldsymbol{X}$, forbidden if the substrate cannot move. Since this term multiplies the normal component of the stress tensor, which (as Eqn. (2.8) informs us) always contains one more derivative than the tangential one, this brings about the higher derivative condition.

Not surprisingly, the boundary conditions (3.44) look distinctly different from the contact curvature condition which holds for the adhesion of a single Helfrich membrane to a rigid substrate, Eqn. (3.23). However, it is possible to rewrite them in such a way that the relation becomes more visible. The *tangential stress* balance (3.44a) and the *torque* balance (3.44c) can be combined to yield the symmetric equations

$$\left(1 + \frac{\kappa_1}{\kappa_2}\right)\left(K_\perp^1 - K_\perp^{12}\right)^2 = \frac{2w}{\kappa_1} , \tag{3.45a}$$

$$\left(1 + \frac{\kappa_2}{\kappa_1}\right)\left(K_\perp^2 - K_\perp^{12}\right)^2 = \frac{2w}{\kappa_2} . \tag{3.45b}$$

From Eqn. (3.44c) it follows that one of the $K_\perp^i$ is bigger and the other one smaller than $K_\perp^{12}$. Hence, when taking the square root in Eqns. (3.45), exactly one of the two will necessitate a minus sign.

Let us look at two special cases of these boundary conditions which turn out to be quite instructive. First, if $\kappa_2 \to \infty$, the second vesicle approaches the limit of a rigid substrate. In this case Eqn. (3.45b) shows that $K_\perp^{12} = K_\perp^2$ and Eqn. (3.45a) reduces to the old contact-curvature-condition we have just derived for rigid substrates, Eqn. (3.23). The curvature of this effective substrate is determined from $\nabla_\perp (K_\perp^2 - K_\perp^{12}) = 0$. This latter condition shows that the "substrate"-curvature is even differentiable across $\mathcal{C}$ – or, in other words, the "substrate" shape is a three times continuously differentiable function.

And second, if the two membranes have identical bending moduli $\kappa_1 = \kappa_2 = \kappa$, a "symmetrized" contact curvature condition ensues which reads

$$\left(K_\perp^1 - K_\perp^{12}\right)^2 = \left(K_\perp^2 - K_\perp^{12}\right)^2 = \frac{w}{\kappa} \ . \tag{3.46}$$

It tells us that the (squared) curvature jump $2w/\kappa$ demanded by the rigid substrate version (3.23) is shared in equal parts between the two membranes, while the final condition of perpendicular force balance becomes $\nabla_\perp(K_\perp^1 + K_\perp^2 - 2K_\perp^{12}) = 0$. The specialization of Eqn. (3.46) to the adhesion between two vesicles of equal bending modulus in an axisymmetric configuration has previously been derived by Derganc *et al.* [DBSŽ03].

The balance of stresses and torques has emerged with remarkable directness as the necessary equilibrium condition for the case of adhering vesicles. Why is this so different from the contact curvature condition at a rigid substrate, where a simple stress balance fails? Looking at Eqn. (3.22a), we see indeed stress and torque contributions entering. Or even more generally, the term involving $\mathcal{H}^{ab}\boldsymbol{n} \cdot \delta\boldsymbol{e}_b$ in Eqn. (3.12) is the origin for the intrinsic torque since it is sensitive to local rotations of the surface normal (see Eqn. (2.21)). Yet, for the case of rigid substrates rotations are entirely "enslaved" to translations since the rotation of the tangent vectors must follow the local substrate curvature – see Eqn. (3.15). Consequently, stresses and torques enter a *single* balance condition and cannot be disentangled. How their contributions conspire to create a single combined equilibrium is probably most easily traced back on the detour via the two-vesicle-case: as we have seen above, tangential stress and torque balance *together* are responsible for the symmetrized equations (3.45), whose rigid substrate limit $\kappa_2 \to \infty$ then yields the entangled balance condition (3.23).

To summarize, let us close this section with a few

Remarks:

- Integrability of the surface energy density $\mathcal{H}$ enforces continuity of certain geometric variables across the contact line.

- The highest derivative in $\mathcal{H}$ dictates which geometric variables may change discontinuously across $\mathcal{C}$ in response to adhesion. Hence, for the Helfrich Hamiltonian the tension σ does not enter the boundary condition even if it enters $\mathcal{H}$; likewise, neither the tension σ nor the bending modulus κ enter the boundary condition if also a gradient-curvature-squared term is present in $\mathcal{H}$.[13]

- Higher order derivatives in $\mathcal{H}$ create boundary terms in the variation which pick up surface variations that are one order lower. If the curvature enters

---

[13] In the next section we will discuss a case where this is not true because the material parameters change across the contact line.

$\mathcal{H}$, then a change in slope is noticed, if a gradient in curvature enters $\mathcal{H}$, then changes in curvature are noticed. For this reason the capillary Hamiltonian is the *only one* which only picks up translations, such that the energy minimization can be reinterpreted as a force balance. In all other cases higher derivative deformations (such as torques or even more complicated constructs) contribute to the boundary variation.

- More formally, the presence of a rigid substrate enslaves all higher order variations (such as rotations or curvature changes) to the contact line translation, and thus mixes their corresponding generalized stress contributions (such as torques) into a *single* balance equation. Under these conditions a simple stress balance must fail.

- The boundary conditions studied in this section are local in nature and depend only on the highest derivative term in the Hamiltonian. Yet, lower order terms may affect the surface shape in the proximity of the contact line, more precisely, on length scales where these terms dominate the energy density, as previously pointed out by Seifert and Lipowsky [SL90]. For instance, Helfrich membranes under tension exhibit the characteristic length scale $\lambda = \sqrt{\kappa/\sigma}$ as introduced in Sec. 2.2.2. It signifies the crossover between small-scale bending-domination and the large-scale tension-regime. Hence, adhesion of a vesicle large compared to λ may be characterized on scales larger than λ by an *effective* contact angle determined from the Young-Dupré equation (3.1), even though upon closer inspection the membrane really adheres smoothly, obeying the contact curvature condition (3.23). Likewise, a quartic term such as the one from the Hamiltonian (3.7) is only expected to influence the neighborhood of the contact line within a proximity region $\ell_\nabla = \sqrt{|\kappa_\nabla|/\kappa}$.

- Notice that the previous remark demands a subtle consistency check: for the presented framework to be applicable, the proximity length associated with the highest order term dictating the nature of the boundary condition must still be larger than the length scale characterizing the finite range of the adhesion potential between the surfaces, which we have from the outset assumed to be zero. In other words, the notion of a contact interaction would be inconsistent if it implies shape features on scales smaller than the actual potential range.

- Generalizations to surfaces hosting additional scalar or vector fields (such as composition or tilt order discussed in Sec. 1.2.2) are straightforward since these are readily incorporated into the present framework (see App. B.2.3 for the relevant expressions for the tensors $\mathcal{H}^{ab}$ etc.). Instead of considering these cases though we will leave adhesion for now and study surfaces with different domains.
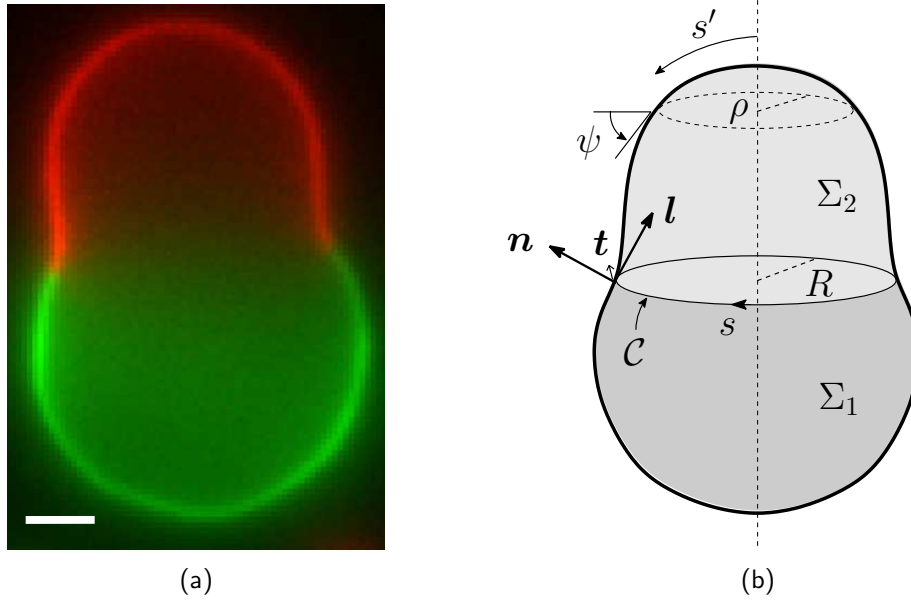
Figure 3.5: (a) Fluorescence image of a phase separated giant unilamelar vesicle (GUV) produced by electroformation from a mixture of 30% DOPC, 50% (brain) sphingomyelin and 20% cholesterol (green: L_d domain; red: L_o domain which is enriched in sphingomyelin and cholesterol (see Sec. 1.1.1)). The scale bar represents $2\,\mu$m *(with courtesy of C. Storm and S. Semrau)* [SIH+06]. (b) Geometry of an axisymmetric vesicle with two domains.

3.5 Specific examples II – Domains on a vesicle

The boundary conditions at the contact line between two domains on a membrane vesicle entail a subtle balance between curvatures and tensions. Remarkably, the Gaussian curvature contribution to the Hamiltonian cannot be neglected as before as the conditions now include the change of the saddle-splay moduli across the line of contact.

As a final example, let us consider a closed membrane vesicle consisting of two different domains such as, for instance, a liquid ordered (L_o) and a liquid disordered (L_d) domain [BHW03, SIH+06] (see Sec. 1.1.1 and Fig 3.5). We assume that the elastic energy density of domain $i \in (1, 2)$ is given by the Helfrich Hamiltonian (1.2)

$$\mathcal{H}^i_\mathrm{capillary} + \mathcal{H}^i_\mathrm{bend} = \sigma_i + \frac{\kappa_i}{2}(K - K_0^i)^2 + \frac{\bar{\kappa}_i}{2}\mathcal{R} \,, \qquad (3.47)$$

where the elastic moduli σ_i, κ_i, $\bar{\kappa}_i$, and the spontaneous curvatures K_0^i are different for the two domains.

Additional energy contributions stem from the line energy (3.4) and a term $-PV$ due to the fixed volume of the closed vesicle (see Secs. 1.2.3 and 2.3.1). In total,

we arrive at the Hamiltonian [JL96][14]

$$H = \sum_i \int_{\Sigma_i} \mathrm{d}A \; (\mathcal{H}^i_{\text{capillary}} + \mathcal{H}^i_{\text{bend}}) + H_{\text{line}} - PV \; , \tag{3.48}$$

where Σ_i denotes the surface of domain i.

Exactly as in the case of adhesion to a deformable surface the contact line variation is not restricted to proceed along a substrate and will thus be of the form (3.38). Consequently, the variation of the tangent vectors is given by Eqn. (3.39).

The tensor $\mathcal{H}^{ab}$ for the Helfrich membrane can be read off from Eqn. (3.20). We decompose its contribution to the variation in the following way

$$\begin{aligned}
l_a \mathcal{H}^{ab} \boldsymbol{n} \cdot \delta \boldsymbol{e}_b &= -l_a \mathcal{H}^{ab} \boldsymbol{e}_b \cdot \delta \boldsymbol{n} = -\big[\kappa (K - K_0) + \bar\kappa K_\parallel \big] \boldsymbol{l} \cdot \delta \boldsymbol{n} \\
&\quad + \bar\kappa K_{\perp\parallel} \big[\underline{K}_{\perp\parallel} \, \boldsymbol{l} \cdot \delta \boldsymbol{X} - \nabla_\parallel (\boldsymbol{n} \cdot \delta \boldsymbol{X}) \big] \; ,
\end{aligned} \tag{3.49}$$

where we rewrote $\boldsymbol{t} \cdot \delta \boldsymbol{n} = -t^a \boldsymbol{n} \cdot \delta \boldsymbol{e}_b \overset{(3.39)}{=} \underline{K}_{\perp\parallel} \varepsilon_\perp - \nabla_\parallel \varepsilon_n$. Inserting this expression together with the variation (3.13) of the line energy and decomposing $l_a \boldsymbol{f}^a$ in the $(\boldsymbol{l}, \boldsymbol{n})$ frame finally yields[15]

$$\begin{aligned}
\delta H_{\text{cl}} = -\oint \mathrm{d}s \; \bigg\{ &\Big[\frac{\kappa_1}{2} \big[(K_\perp^1)^2 - (K_\parallel - K_0^1)^2 \big] - \frac{\kappa_2}{2} \big[(K_\perp^2)^2 - (K_\parallel - K_0^2)^2 \big] \\
&+ (\bar\kappa_1 - \bar\kappa_2)(K_{\perp\parallel})^2 - \sigma_1 + \sigma_2 - \gamma K_{\text{g}} \Big] \boldsymbol{l} \cdot \delta \boldsymbol{X} \\
&- \Big[\kappa_1 (\nabla_\perp K^1) - \kappa_2 (\nabla_\perp K^2) - (\bar\kappa_1 - \bar\kappa_2)(\nabla_\parallel K_{\perp\parallel}) + \gamma K_\parallel \Big] \boldsymbol{n} \cdot \delta \boldsymbol{X} \\
&- \Big[\kappa_1 (K^1 - K_0^1) + \bar\kappa_1 K_\parallel - \kappa_2 (K^2 - K_0^2) - \bar\kappa_2 K_\parallel \Big] \boldsymbol{l} \cdot \delta \boldsymbol{n} \bigg\} \tag{3.50}
\end{aligned}$$

for the variation of the contact line. In Eqn. (3.50), we performed an integration by parts on the term involving $\nabla_\parallel (\boldsymbol{n} \cdot \delta \boldsymbol{X})$ and inserted $K_{\perp\parallel}^1 = K_{\perp\parallel}^2 = \underline{K}_{\perp\parallel} = K_{\perp\parallel}$ and $K_\parallel^1 = K_\parallel^2 = K_\parallel$.

Remarks:

- Again, the three independent variations are one tangential and one perpendicular *translation*, described by $\boldsymbol{l} \cdot \delta \boldsymbol{X}$ and $\boldsymbol{n} \cdot \delta \boldsymbol{X}$, respectively, and one *rotation* around the local contact line, $\boldsymbol{l} \cdot \delta \boldsymbol{n}$. The other possible rotation, $\boldsymbol{t} \cdot \delta \boldsymbol{n}$, which tilts the contact line about the outward pointing normal vector $\boldsymbol{l}$ is *not* independent as it can be rewritten in terms of the two translations.

---

[14] The same situation has been studied in Ref. [Bou99] with a Hamiltonian which also accounts for internal parameters such as chemical composition.

[15] Note that, analogous to the previous example, the constant volume term $-PV$ does not contribute to the variation of the contact line.

- The resulting boundary conditions are parametrization-free and do not depend on symmetries. They entail a subtle balance between curvatures and tensions of the contact line and the surrounding two domains.

- We have finally found a case where the Gaussian term in the Helfrich Hamiltonian *is* relevant and contributes to the boundary conditions. Recent experiments exploit that fact in order to find out more about the saddle-splay modulus of lipid bilayer phases [SIH$^+$06]. Note, however, that only the difference $\bar{\kappa}_1 - \bar{\kappa}_2$ can be determined because the $\bar{\kappa}_i$ enter the boundary conditions only in this combination. This is different to the bending rigidities which also appear separately.

- The conditions are a generalization of the results from Ref. [CGS02] where *one* domain with a free edge was considered (see also [TOY03]). Setting the contributions of one domain in Eqn. (3.50) to zero (for instance, of domain 2, *i. e.*, $\sigma_2 = \kappa_2 = \bar{\kappa}_2 = 0$) one recovers Eqns. (58)–(60) from Ref. [CGS02]. For axisymmetric two-domain vesicles the conditions have been derived previously in [JL96]. To understand their implications, let us consider the three conditions one by one, starting with the last one.

If we rewrite the trace of the extrinsic curvature as $K^i = K^i_\perp + K_\parallel$ we obtain

$$\kappa_1 K^1_\perp - \kappa_2 K^2_\perp = -(\Delta\kappa + \Delta\bar{\kappa})K_\parallel + \Delta K^\kappa_0 \ . \tag{3.51}$$

where we defined $\Delta\kappa := \kappa_1 - \kappa_2$, $\Delta\bar{\kappa} := \bar{\kappa}_1 - \bar{\kappa}_2$, and $\Delta K^\kappa_0 := \kappa_1 K^1_0 - \kappa_2 K^2_0$. This condition generalizes Eqn. (52) from Ref. [Fou07] with $\Delta K^\kappa_0 = 0$. It states how perpendicular, parallel, and spontaneous curvatures of the two domains are related to each other at the contact line. Assume, for instance, that the bending rigidities and the saddle-splay moduli of both domains are the same. From Eqn. (3.51) then follows that the difference $K^1_\perp - K^2_\perp$ of the perpendicular curvatures is equal to the difference $K^1_0 - K^2_0$ of the spontaneous curvatures. On the other hand, if all curvatures and bending rigidities are known, the difference $\Delta\bar{\kappa}$ of the saddle-splay moduli can be determined directly from the condition.

To obtain the axisymmetric version of Eqn. (3.51), we change to angle-arc length parametrization (see Fig. 3.5(b) and App. A.4.2): the angle $\psi(s')$ between the horizontal axis and the tangent to the profile completely describes the vesicle shape as a function of arc length s'. The curvatures are then given by $K_\parallel = \sin\psi(s')/\rho(s')$ and $K_\perp = \dot{\psi}(s')$, where the dot denotes a derivative with respect to s' (see also Eqns. (A.77)).[16]

---

[16] The signs of the curvature expressions given here are different compared to Chap. 4 and App. A.4.2 because there, the normal vector $\boldsymbol{n}$ and the tangent vector $\boldsymbol{l}$, respectively are pointing in the opposite direction (compare Figs. 3.5(b) and A.9).

Let $s' = S$ be the arc length at the contact line and $\rho(S) = R$ its radius. For an axisymmetric vesicle boundary condition (3.51) is then given by

$$\kappa_1 \dot{\psi}(S + \epsilon) - \kappa_2 \dot{\psi}(S - \epsilon) = -(\Delta\kappa + \Delta\bar{\kappa})\frac{\sin\psi(S)}{R} + \Delta K_0^\kappa \,, \qquad (\epsilon > 0) \quad (3.52)$$

which is exactly Eqn. (A22) from Ref. [JL96] (see also [SIH$^+$06, Eqn. (6)][17]).
The tangential variation along the vector $\boldsymbol{l}$ yields another boundary condition. From Eqn. (3.50) we obtain

$$\frac{\kappa_1}{2}(K_\perp^1)^2 - \frac{\kappa_2}{2}(K_\perp^2)^2 = \frac{\kappa_1}{2}(K_\parallel - K_0^1)^2 - \frac{\kappa_2}{2}(K_\parallel - K_0^2)^2 - \Delta\bar{\kappa}(K_{\perp\parallel})^2 + \Delta\sigma + \gamma K_{\mathrm{g}} \,, \tag{3.53}$$

where we defined $\Delta\sigma := \sigma_1 - \sigma_2$. Surface tension enters the boundary condition even though the membrane has no kinks since the Helfrich Hamiltonian dictates the behavior of each domain. The corresponding term in Eqn. (3.53) is due to the fact that the surface tension now changes across the contact line in contrast to the previous section.
For an axisymmetric vesicle, the curvature $K_{\perp\parallel}$ vanishes. The geodesic curvature of the contact line is given by $K_{\mathrm{g}} = -\cos\psi(S)/R$ (see Eqn. (A.78); for the sign, see footnote 16). Thus,

$$\frac{\kappa_1}{2}\big[\dot{\psi}(S + \epsilon)\big]^2 - \frac{\kappa_2}{2}\big[\dot{\psi}(S - \epsilon)\big]^2 = \frac{\kappa_1}{2}\left(\frac{\sin\psi(S)}{R} - K_0^1\right)^2 - \frac{\kappa_2}{2}\left(\frac{\sin\psi(S)}{R} - K_0^2\right)^2$$
$$+ \Delta\sigma - \gamma\frac{\cos\psi(S)}{R} \,. \tag{3.54}$$

A quick glance into Ref. [JL96, Eqn. (A17)] helps to interpret this boundary condition: in fact, it states that the Hamiltonian function $\mathscr{H}$, which is conserved in each domain, does not change across the contact line.[18] We will come back to that point on page 88 in the next chapter where the Hamiltonian function for a similar problem will be discussed.
Finally, the variation along $\boldsymbol{n}$ yields a condition involving the perpendicular derivatives of the two mean curvatures

$$\kappa_1(\nabla_\perp K^1) - \kappa_2(\nabla_\perp K^2) = \Delta\bar{\kappa}\left(\nabla_\parallel K_{\perp\parallel}\right) - \gamma K_\parallel \,. \tag{3.55}$$

For an axisymmetric surface, $K_{\perp\parallel}$ vanishes and the derivative $\nabla_\perp K_\parallel^i$ can be expressed in terms of curvatures with the help of Eqns. (3.8) and (A.55):

$$\nabla_\perp K_\parallel^i = (K_\perp^i - K_\parallel)K_{\mathrm{g}} \,. \tag{3.56}$$

---

[17] Note that the numbering of the domains in [SIH$^+$06] is exactly opposite to the definition of this work.
[18] The Hamiltonian function $\mathscr{H}$ must not be mistaken for the Hamiltonian H or the Hamiltonian density $\mathcal{H}$.

The boundary condition turns into

$$
\begin{aligned}
\kappa_1(\nabla_\perp K_\perp^1) - \kappa_2(\nabla_\perp K_\perp^2) &= -\kappa_1(K_\perp^1 - K_\parallel)K_{\mathrm{g}} + \kappa_2(K_\perp^2 - K_\parallel)K_{\mathrm{g}} - \gamma K_\parallel \\
&= \big[(2\Delta\kappa + \Delta\bar\kappa)K_{\mathrm{g}} - \gamma\big]K_\parallel - K_{\mathrm{g}}\Delta K_0^\kappa \,, \qquad (3.57)
\end{aligned}
$$

where we inserted Eqn. (3.51) in the second step. The geodesic curvature enters the second term on the right-hand side of the equation if the spontaneous curvatures of the domains do not vanish and $\Delta K_0^\kappa \neq 0$. It additionally occurs in combination with the line tension γ. However, its prefactor contributes a nontrivial sign which decides whether K_{g} opposes or increases the effect of γ.

In angle-arc length parametrization we finally obtain the equation[19]

$$
\kappa_1\big[\ddot\psi(S+\epsilon)\big] - \kappa_2\big[\ddot\psi(S-\epsilon)\big] = \Big[(2\Delta\kappa + \Delta\bar\kappa)\frac{\cos\psi(S)}{R} + \gamma\Big]\frac{\sin\psi(S)}{R} - \frac{\cos\psi(S)}{R}\Delta K_0^\kappa \,,
$$
$$
(3.58)
$$

which is given explicitly in [SIH$^+$06, Eqn. (6)] (see also [JL96] again).

Imagine we had only considered the boundary conditions in angle-arc length parametrization. It would not have been straightforward at all to identify contributions such as the geodesic curvature K_{g}. The disadvantage of a parametrization-dependent compared to a covariant approach is immediately apparent.

In this chapter we have seen how boundary conditions can be extracted from a systematic boundary variation in a completely parametrization independent way. However, knowing the boundary conditions does not mean that one also knows the position of the contact line. Rather, the latter has to be determined simultaneously with the surface shape. In general this task is difficult, as we will see for one specific example in the next chapter.

---

[19] Note that $\nabla_\perp = -\mathrm{d}/\mathrm{d}s'$, which generates an additional minus sign in the condition.

4 How to determine elastic properties of a membrane on the nano-scale

In the previous chapters we have developed a mathematical toolbox for describing the mechanical properties of fluid surfaces in general and lipid bilayer membranes in particular. To predict the behavior of a membrane in "real" life, however, *quantitative* knowledge of its material parameters – most notably the bending modulus κ – is necessary.

4.1 Experiments

> *Measurements with an atomic force microscope (AFM) offer a direct way to probe elastic properties of lipid bilayer membranes locally; provided the underlying stress-strain relation is known, material parameters such as the bending rigidity may be deduced.*

Several methods for the experimental determination of κ have been proposed, such as monitoring the spectrum of thermal undulations via light microscopy [BL75, FMM⁺89], analyzing the relative area change of vesicles under micropipette aspiration [ER90, ROM⁺00], or measuring the force required to pull thin membrane tubes, so-called "tethers" [DS95, HSDS96, DS99, MSdM02, CDBN05]. With the possible exception of the tether experiments, these techniques are *global* in nature, *i. e.*, they supply information averaged over millions of lipids, if not over entire vesicles or cells. Yet, in a biological context this may be insufficient [HW04]. In Sec. 1.1.1 we have, for instance, seen that membrane properties such as lipid composition or bilayer phase (and thus mechanical rigidity) may potentially vary on submicroscopic length scales. This raft hypothesis still remains disputed precisely because the existence of such small domains is extremely hard to show.

In the following we will discuss an atomic force microscope experiment which may offer the possibility to check this hypothesis in the near future as it can probe the elastic properties of a membrane with the necessary spatial resolution.
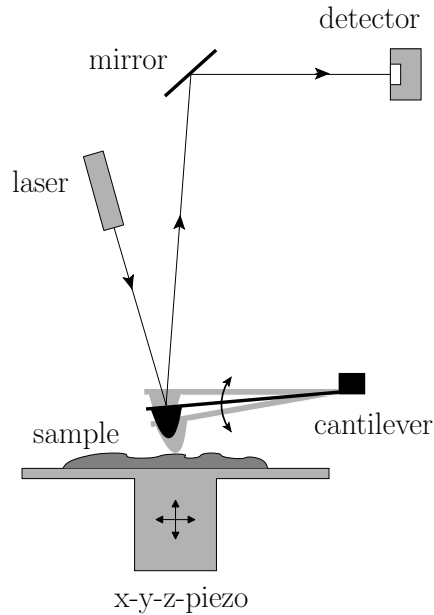
Figure 4.1: Simplified scheme of an atomic force microscope (AFM) [Ste06a].

4.1.1 Atomic force microscopy

The atomic force microscope (AFM) is a versatile tool to obtain topographic and mechanical information of small samples [JNOF00, BCK05, AF05]. In an AFM measurement the sample is scanned by a tiny tip which is mounted at the end of a cantilever spring (see Fig. 4.1). The relative motion between tip and sample is controlled by a piezoelectric actuator. During the scan the force between tip and sample changes and causes the spring to bend. To detect its deflection a laser beam is focused on the back of the cantilever: a small movement of the tip changes the position of the reflected light in a split photo detector, hence giving information about the position of the tip.

One important mode of operation is the *contact mode*. This mode is comparable to the functional principle of a gramophone: the tip is in gentle touch with the sample exerting a constant vertical force during the horizontal scan. Its position changes due to the interactions with the surface yielding a topographic image of the sample.

The AFM can also be used for force spectroscopy: in the measurement the tip is moved towards the sample in normal direction. The position of the tip and the deflection of the cantilever are recorded and can be converted to force-versus-distance curves, or briefly, force-distance curves. These curves contain information about the mechanical properties of the sample; one may thus try to extract local material parameters from them.
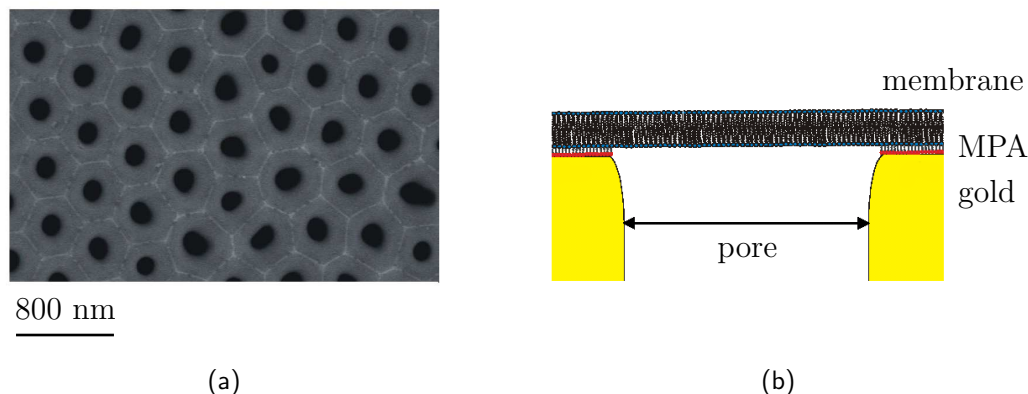
Figure 4.2: (a) Scanning electron micrograph of highly ordered gold-coated porous alumina *(reprinted from [SMD⁺06] with permission of authors and the Biophysical Journal).*
(b) In the experiment a lipid bilayer was suspended over the pores and subsequently probed with the AFM [SMD⁺06].

Indeed, the AFM has been used to probe cell elastic properties (such as, for instance, their Young modulus) [Rad02, Kos04]. Yet, obtaining truly *local* information still poses a formidable challenge. Apart from several complications associated with the inhomogeneous cell surface and intra-cellular structures beneath the lipid bilayer, one particularly notable difficulty emerges: the boundary conditions of the cell membrane away from the spot where the AFM tip indents are not known. This precludes a quantitative interpretation of the measured force, *i. e.* a clean way to translate this force into local material properties.

Appropriate model systems with defined geometry and membrane composition are thus required. One possible realization which complies with these requirements is the "nanodrum" setup.

4.1.2 Measurements on the nanodrum

The nanodrum setup consists of a lipid bilayer membrane which is spread over an adhesive substrate featuring circular pores of well-defined radius [SMD⁺06, Ste06a]. The boundary conditions at the rim of the drum are known. Centrally indenting it with the AFM tip yields force-distance curves for a system with precisely defined geometry.

The first measurements using the nanodrum setup were done on fluid DOTAP and gel-like DODAB membranes (see Figs. 1.2(b) and 1.2(c) in Sec. 1.1.1). As a substrate planar gold-coated alumina was used onto which a 3-mercaptopropionic acid (MPA) monolayer was chemisorbed. The negatively charged MPA monolayer ensured that the positively charged membrane could spread evenly on the substrate
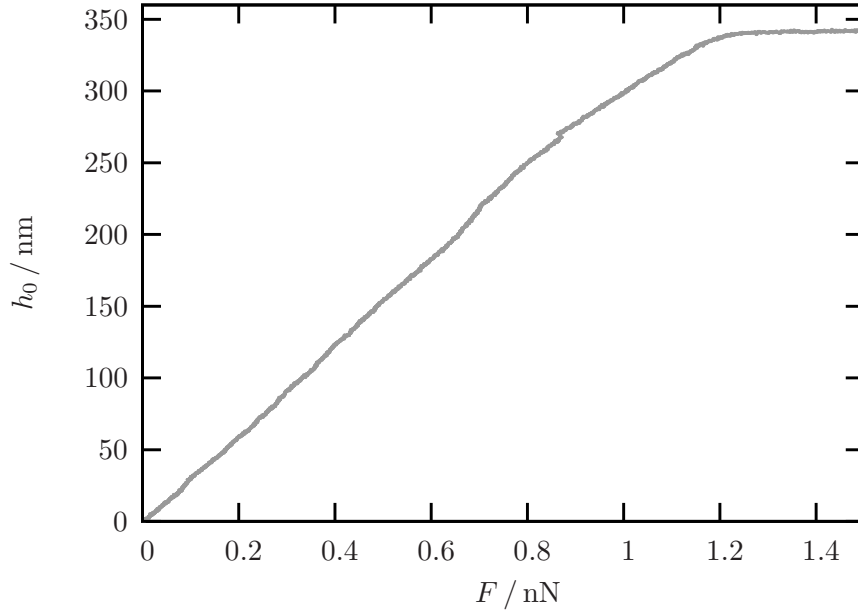
Figure 4.3: Force-distance curve of a pore-spanning fluid DOTAP bilayer on a pore with $R_{\mathrm{pore}} = 90\,\mathrm{nm}$ *(with courtesy of Andreas Janshoff and Siegfried Steltenkamp).*

(see Fig. 4.2). The radius of the drum was either 33.5 nm or 90 nm.[1]

Fig. 4.3 shows a typical force-distance curve for which a DOTAP membrane was suspended over a pore of radius $R_{\mathrm{pore}} = 90\,\mathrm{nm}$ and subsequently probed with an AFM tip (see Fig. 4.4(a) for a picture of the tip). Remarkably, the curve is linear even for significant indentations,[2] a finding in agreement with the initial regime of membrane tether pulling [PHG02, DJP02]. In the following we will develop a theoretical model that reproduces this behavior qualitatively and quantitatively. Yet, we will see that the linearity of the curve makes a unique extraction of the two main mechanical properties, tension and bending modulus, difficult.

To overcome this impasse, the theoretical basis for a slight extension of the nanodrum experiment will also be developed here. It will be shown that an additional *adhesion* between the AFM tip and the pore-spanning membrane will change the situation very significantly. Force-distance curves cease to be linear, hysteresis, nonzero detachment forces and membrane overhangs can show up, and various new stable and unstable equilibrium branches emerge.

---

[1] More experimental details can be found in [SMD⁺06] and [Ste06a].
[2] The plateau for high forces is due to the fact that the tip broadens away from its apex. It simply gets stuck if the indentation becomes too large.
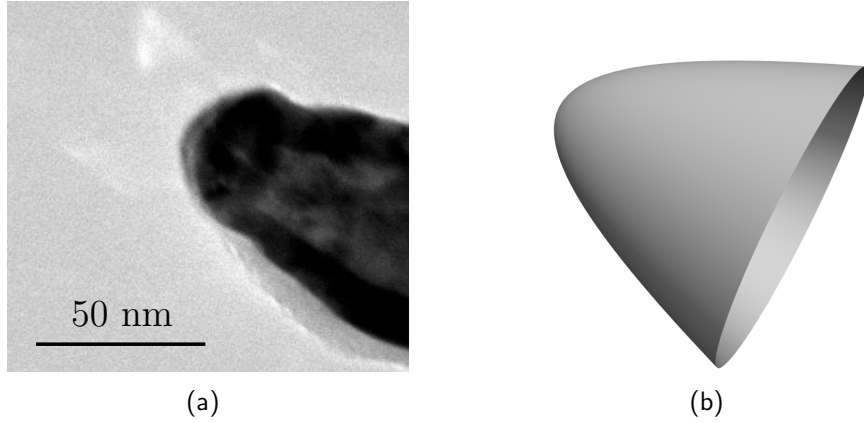
(a)   (b)

Figure 4.4: (a) Transmission electron microscopy image of an AFM tip after usage *(reprinted from [SMD⁺06] with permission of authors and the Biophysical Journal).* (b) Theoretical model of the tip.

4.2 Theoretical model of the nanodrum

To model the nanodrum experiment, a static axisymmetric system is considered in which the parabolic AFM tip indents the pore-spanning membrane in the middle of the circular pore. The membrane is modeled as a Helfrich membrane with no spontaneous curvature. The adhesion between tip and membrane is also taken into account.

As (*i*) the pore radius as well as (*ii*) length scales of interest such as local radii of curvature are typically much larger than the thickness of the bilayer (which is approx. 5 nm, see Sec. 1.1.1), we can model the membrane as a two-dimensional surface (see Sec. 1.2). This allows us to grab some tools from our box and apply them to the nanodrum.

4.2.1 Geometry

In our modeling we consider a flat solid substrate with one circular pore of radius R_{pore}. The lipid bilayer membrane is adsorbed evenly onto the substrate and spans the pore. We assume that the AFM tip has a parabolic shape with curvature radius R_{tip} at its apex. Furthermore, we restrict ourselves to the static axisymmetric situation in which the tip pokes the free-standing membrane exactly in the middle of the pore (see Fig. 4.5). It is then sufficient to consider a cross section of the setup. The point at which the membrane detaches from the tip will be denoted as the "contact point".

For a certain downward force $F > 0$ the membrane is indented to a corresponding depth $h_0 > 0$ which is measured from the plane of the substrate to the depth of the
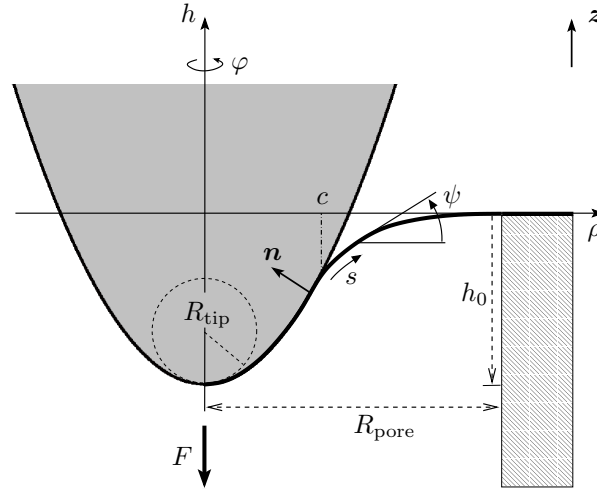
Figure 4.5: Illustration of the geometry. A parabolic tip with curvature radius R_{tip} indents a pore-spanning membrane with a force F to a certain depth h_0. The radius of the pore is R_{pore}. The membrane detaches from the tip at a radial distance $\rho = c$. The two possible parametrizations $h(\rho)$ and $\psi(s)$ are explained in the beginning of Chap. 4.3 and in App. A.4. Note also the direction of the normal vector $\boldsymbol{n}$ which points inside the tip.

apex of the tip. Note that it is also possible to pull the membrane up with a force $F < 0$ in the opposite direction if attractive interactions attach the membrane to the tip.

4.2.2 Energy considerations

The total energy of the pore-tip system comprises different contributions: first, the membrane is under a *lateral tension σ*. To pull excess area into the pore, work has to be done against the adhesion between membrane and flat substrate.[3] It is given by σ times the excess area [DL91]. Second, a *curvature energy* is associated with the membrane. Summing up both contributions and assuming that the bilayer has no spontaneous curvature (which is true for the membranes used in the experiment) we arrive at the Helfrich Hamiltonian for an up-down symmetric membrane (see Eqn. (1.2) with $K_0 = 0$)

$$H_{\text{elast}} = \int_{\Sigma} \mathrm{d}A \left(\sigma + \frac{\kappa}{2} K^2 + \bar{\kappa} K_{\text{G}} \right) , \tag{4.1}$$

---

[3] The part of the system outside the pore just acts like a reservoir fixing the lateral tension. Its energetics do not have to be considered explicitly.

where Σ denotes the surface of the membrane part which spans the pore. The Gaussian curvature term in H_{elast} can be safely discarded in the following as it yields zero in our specific problem (compare Technical Point 2.3).[4]

Apart from tension and bending, an *adhesion between tip and membrane* may contribute to the total energy. Just as in Chap. 3 we will assume that it is proportional to the contact area A_{contact} between tip and membrane with a proportionality constant w, the adhesion energy per area.

If the indentation h_0 is given and one wants to determine the force F, the total energy can thus be written as

$$E_{\text{total}}^{h_0} = \int_{\Sigma} \mathrm{d}A \left(\sigma + \frac{\kappa}{2} K^2 \right) - w A_{\text{contact}} \ . \tag{4.2}$$

Under certain circumstances, however, it is more convenient to consider the problem for a given force F. Both ensembles ("constant indentation" *vs.* "constant force") are connected via a Legendre transformation [SSS03, SSS04], $E_{\text{total}}^{F} = E_{\text{total}}^{h_0} - F h_0$. While the ground states one obtains for the two ensembles will be the same, questions of stability depend on the ensemble: a profile found to be stable under constant height conditions is not necessarily stable under constant force conditions.[5]

The route we want to follow here in order to find force-distance curves is to determine the equilibrium shapes of the non-bound section of the membrane by solving the shape equation (2.33) for $K_0 = 0$.[6] It is given by:

$$-\Delta K + \frac{1}{2} K (K^2 - 2 K_{ab} K^{ab}) + \lambda^{-2} K = 0 \ , \tag{4.3}$$

where $\lambda := \sqrt{\kappa/\sigma}$ is the characteristic length introduced in Eqn. (2.34). Notice that the contact point c is not known a priori but has to be determined via an adhesion balance, a "moving boundary problem" exactly as in Chap. 3.

In the next section we will show how one can set up the appropriate mathematical formulation of the problem to get membrane profiles and force-distance curves.

---

[4] The Gauss-Bonnet theorem states that:

$$\int_{\Sigma} \mathrm{d}A \ K_{\text{G}} = 2\pi - \int_{\partial\Sigma} \mathrm{d}s \ K_{\text{g}} \ ,$$

for a simply connected surface (see Eqn. (A.59) in App. A.3). In our case the boundary $\partial\Sigma$ of the surface Σ is a circle of radius R_{pore}. Its geodesic curvature K_{g} is equal to R_{pore}^{-1}, such that the second integral yields 2π. Thus, the integral over the Gaussian curvature K_{G} is zero as long as no topological changes occur.

[5] In Sec. 1.2.3 we have already encountered a similar case: a closed surface which is stable under constant volume is not necessarily stable under constant pressure conditions and vice versa (see also Technical Point 2.5 in which the closed spherical soap bubble is discussed).

[6] The profile of the bound part is equivalent to the (known) shape of the tip.

We can thereby resort to established techniques which have previously been used successfully to study vesicle shapes [SŽ89, MFR$^+$91, SBL91, JS94, JL96, Sei97], vesicle adhesion [SL90, Sei95], colloidal wrapping [DB03, Des04a, Des04b] or tether pulling [PHG02, DJP02, SSS03, SSS04, KCD$^+$05].

4.3 Solving the shape equation

The shape equation can be solved either in small gradient approximation using Monge gauge or in a Hamiltonian formulation using the angle-arc length parametrization. In the former case one considers the problem in the constant indentation ensemble, in the latter case one prescribes the force.

To describe the shape of the membrane, we use two different kinds of parametrization (see Fig. 4.5 and App. A.4): for the linear approximation it is sufficient to use the Monge parametrization (Monge gauge) where the position of the membrane is given by a height $h(\rho)$ above (or below) the underlying reference plane. The disadvantage of this parametrization is that it does not allow for overhangs. Since these may be present in the full nonlinear problem, we will use the angle-arc length parametrization in the exact calculations: the angle $\psi(s)$ with respect to the horizontal substrate as a function of arc length s fully describes the shape.

4.3.1 Linear approximation

The profile of the bound membrane is equivalent to the shape of the tip and thus given by

$$h(\rho) = -h_0 + \frac{\rho^2}{2R_{\text{tip}}} , \qquad \text{for } \rho \leq c . \tag{4.4}$$

To get the profile of the free membrane, one has to solve the shape equation (4.3). As was argued in Sec. 2.2.2 it is impossible to do this analytically in most cases. One may, however, consider configurations where the membrane is indented only a little and gradients are small. In that case the energy functional and the shape equation can be linearized as we will see now.

In the constant indentation ensemble the energy of the free part is given by

$$E = \int_{\Sigma_{\text{free}}} \mathrm{d}A_\parallel \ \sqrt{1 + (\boldsymbol{\nabla}^2 h)^2} \left\{ \frac{\kappa}{2} \left[\boldsymbol{\nabla} \cdot \frac{\boldsymbol{\nabla} h}{\sqrt{1 + (\boldsymbol{\nabla}^2 h)^2}} \right]^2 + \sigma \right\} , \tag{4.5}$$

where we used Eqns. (A.64) and (A.68) from App. A.4.1. The symbol $\mathrm{d}A_\parallel$ is the area element on the flat reference plane, Σ_{free} is the projected surface of the free pore-spanning membrane, and $\boldsymbol{\nabla}$ the two-dimensional nabla operator in the reference plane.

─── **Technical Point 4.1:** *Modified Bessel functions* ───

The second order linear differential equation

$$\rho^2\, h''(\rho) + \rho\, h'(\rho) - (\rho^2 + n^2)\, h(\rho) = 0$$

has two linearly independent solutions: the modified Bessel functions of first and second kind, $I_n(\rho)$ and $K_n(\rho)$, respectively. A comprehensive compilation of the main properties of these functions can be found in Ref. [AS70].
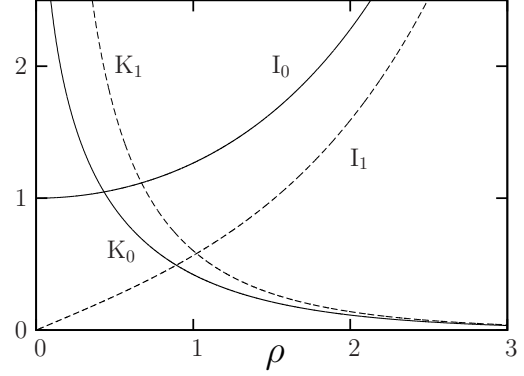
In this work we explicitly need the first derivatives with respect to ρ:

$$
\begin{aligned}
I_0'(\rho) &= I_1(\rho)\,, & K_0'(\rho) &= -K_1(\rho)\,, & \text{(4.I)}\\
I_1'(\rho) &= I_0(\rho) - \frac{1}{\rho}\,I_1(\rho)\,, & K_1'(\rho) &= -K_0(\rho) - \frac{1}{\rho}\,K_1(\rho)\,, & \text{(4.II)}
\end{aligned}
$$

and the behavior for $\rho \to \infty$

$$I_n(\rho) = \frac{e^\rho}{\sqrt{2\pi\rho}}\Big(1 - \frac{4n^2+3}{8\rho} + \dots\Big)\,, \quad K_n(\rho) = \sqrt{\frac{\pi}{2\rho}}\,e^{-\rho}\Big(1 + \frac{4n^2-1}{8\rho} + \dots\Big)\,.$$

$$\text{(4.III)}$$

───────────

Expanding the terms in the integrand up to lowest order in $\boldsymbol{\nabla}h$ gives the small gradient expansion of the energy

$$E = \int_{\Sigma_{\text{free}}} dA_\parallel \left[\frac{\kappa}{2}(\boldsymbol{\nabla}^2 h)^2 + \frac{\sigma}{2}(\boldsymbol{\nabla}h)^2\right]\,, \tag{4.6}$$

where we have discarded a constant surface integral over Σ_{free}.

The appropriate shape equation can be derived by setting the first variation of energy (4.6) to zero, yielding[7]

$$\boldsymbol{\nabla}^2\big(\boldsymbol{\nabla}^2 - \lambda^{-2}\big)h = 0\,. \tag{4.7}$$

The solution to Eqn. (4.7) is a linear combination of the eigenfunctions of the Laplacian corresponding to the eigenvalues 0 and λ^{-2}. For axial symmetry it

───────────

[7] Note that one may alternatively obtain this equation from the shape equation (4.3) directly by neglecting terms of higher than linear curvature order in Eqn. (4.3) and subsequently inserting the small gradient expression (A.72) for K.

is given by $h(\rho) = h_1 + h_2 \ln(\rho/\lambda) + h_3 \, \mathrm{I}_0(\rho/\lambda) + h_4 \, \mathrm{K}_0(\rho/\lambda)$, where I_0 and K_0 are modified Bessel functions of the first and the second kind, respectively (see Technical Point 4.1).

The constants $h_1, \ldots, h_4$ are determined from the appropriate boundary conditions (see App. C.2):

$$h(R_{\mathrm{pore}}) \;=\; 0 \,, \quad h(c) = -h_0 + \frac{c^2}{2R_{\mathrm{tip}}} \,, \tag{4.8a}$$

$$h'(R_{\mathrm{pore}}) \;=\; 0 \,, \quad h'(c) = \frac{c}{R_{\mathrm{tip}}} \,, \tag{4.8b}$$

$$\text{and} \quad h''(c) \;=\; \frac{1}{R_{\mathrm{tip}}} - \sqrt{\frac{2w}{\kappa}} \,, \tag{4.8c}$$

where a dash denotes a derivative with respect to ρ. Eqns. (4.8a) follow simply from the requirement of continuity at the pore rim and the point where the membrane leaves the tip. Asking for a membrane that has no kinks and thus no diverging bending energy gives Eqns. (4.8b). Even though the differential equation is of fourth order, *five* conditions are required due to its moving boundary nature, *i. e.*, c is to be determined from an adhesion balance. In Sec. 3.4.1 we have derived the appropriate covariant expression (3.23).[8] In the small gradient expansion the contact curvatures are given by $\underline{K}_{\perp} \approx -1/R_{\mathrm{tip}}$ and $K_{\perp} \approx -h''(c)$ (see Eqn. (A.81a)). Inserting these curvatures into Eqn. (3.23) yields condition (4.8c). The solution of the boundary value problem (4.7, 4.8) can be used in two ways to calculate the force for a prescribed indentation: first, one can insert the profile of the free membrane together with the shape (4.4) of the bound part back into (the linearized version of) the functional (4.2) to obtain the energy of the equilibrium solution. This energy will then parametrically depend on the indentation h_0. Its derivative with respect to h_0 yields the force F. Second, one can also consider stresses: in Sec. 2.1.2 we have seen that the external force on a surface patch is given by the integral of the flux of surface stress through a closed contour around the patch.

The second approach is used here; it has the advantage that the final expression for the force can be written in the closed form (see Technical Point 4.2):

$$F = 2\pi R_{\mathrm{pore}} \times \kappa \left. \frac{\partial K}{\partial \rho} \right|_{\rho = R_{\mathrm{pore}}} . \tag{4.9}$$

This equation is *exact* for *all* indentations as its derivation does not rely on any approximations (such as a small gradient expansion). Inserting the solution $h(\rho)$ of the boundary value problem (4.7, 4.8) into (4.9) yields the value of the force,

---

[8] Observe that this derivation assumes differentiability of the energy as a function of contact point position. We will come back to that point in Sec. 4.4.2.

───── **Technical Point 4.2:** *Calculation of the force via the stress tensor* ─────

If the shape of the free membrane is known, the stress tensor $\boldsymbol{f}^a$ can be evaluated at every point of the surface Σ_{free}. The integral of its flux through an arbitrary contour $\mathcal{C}$ which encloses the tip gives the force. From Eqn. (2.32) one obtains with $K_0 = K_{\perp\|} = 0$:

$$F = -\boldsymbol{z} \cdot \oint_{\mathcal{C}} \mathrm{d}s \left\{ \left[\frac{\kappa}{2}(K_\perp^2 - K_\|^2) - \sigma \right] \boldsymbol{l} - \kappa(\nabla_\perp K)\,\boldsymbol{n} \right\}, \qquad (4.\mathrm{IV})$$

where $\boldsymbol{z}$ is the upward pointing unit normal vector (see Fig. 4.5 on page 82). The unit vectors $\boldsymbol{l}$ and $\boldsymbol{n}$, the curvatures $K_\perp$ and $K_\|$, and the directional derivative $\nabla_\perp$ are defined as before (see App. A.2 and previous chapters).

Expression (4.IV) can be translated into Monge gauge. If we exploit axial symmetry and integrate around a circle of radius $\rho = R_{\mathrm{int}}$, we obtain, with the help of Eqns. (A.79)–(A.81),

$$F = -2\pi R_{\mathrm{int}} \left\{ \left[\frac{\kappa}{2} \left(\frac{h''(\rho)^2}{g_\perp^3} - \frac{h'(\rho)^2}{\rho^2 g_\perp} \right) - \sigma \right] \frac{h'(\rho)}{\sqrt{g_\perp}} + \kappa \left(\frac{h''(\rho)}{\sqrt{g_\perp}^3} + \frac{h'(\rho)}{\rho\sqrt{g_\perp}} \right)' \frac{1}{g_\perp} \right\} \Bigg|_{\rho = R_{\mathrm{int}}},$$
$$(4.\mathrm{V})$$

where $g_\perp = 1 + h'(\rho)^2$. If in particular we choose to evaluate the force at $R_{\mathrm{int}} = R_{\mathrm{pore}}$, $h'(R_{\mathrm{int}}) = 0$, and the expression (4.V) simplifies considerably to Eqn. (4.9).

━━

however, only in the linear regime because $h(\rho)$ is the small gradient solution of the shape equation.

A warning is due here: expression (4.9) is evaluated at the rim of the pore where the profile is flat even for high indentations. One might thus wonder whether inserting the small gradient solution would actually lead to an exact result. This, however, is not the case because the membrane shape at the rim predicted by the linear calculation is not identical to the prediction from the full nonlinear theory—except for its flatness, which is enforced by the boundary conditions. There is no magical way to avoid solving the nonlinear shape equation if one wants the exact answer.

4.3.2 Complete nonlinear formulation

Let us now shift to the angle-arc length parametrization and consider the full nonlinear problem. In principle, the constant height ensemble could be used here as well. It is, however, technically much easier to fix F instead in order to reduce the number of boundary conditions one has to fulfill at the rim of the pore (see below and Technical Point 4.3).

In this paragraph all variables with a tilde are scaled with $\pi\kappa$, *i. e.*: $\tilde{E} := E/(\pi\kappa)$, $\tilde{F} := F/(\pi\kappa)$, etc. The energy functional of the free membrane can then be written as [SBL91, JS94, JL96, Sei97, SSS03, DB03, Des04a] (see also App. A.4.2):

$$
\begin{aligned}
\tilde{E} &= \int_{\underline{s}}^{\bar{s}} \mathrm{d}s \, \tilde{\mathscr{L}} = \int_{\underline{s}}^{\bar{s}} \mathrm{d}s \left\{ \rho \left(\dot{\psi} + \frac{\sin\psi}{\rho} \right)^2 + \frac{2\rho}{\lambda^2} \right. \\
&\quad \left. + \lambda_\rho(\dot{\rho} - \cos\psi) + \lambda_z(\dot{z} - \sin\psi) - \tilde{F}\dot{z} \right\},
\end{aligned}
\tag{4.10}
$$

where $\underline{s}$ is the arc length at the contact point c and $\bar{s}$ the arc length at R_{pore}. The dot denotes the derivative with respect to s. The Lagrange multiplier functions λ_ρ and λ_z ensure that the geometric conditions $\dot{\rho} = \cos\psi$ and $\dot{z} = \sin\psi$ are fulfilled everywhere (compare Eqns. (A.76)).

In order to make the numerical integration easier let us rewrite the problem in a Hamiltonian formulation [SBL91, JS94, JL96, SSS03, DB03, Des04a]: the conjugate momenta are

$$
p_\psi = \frac{\partial\tilde{\mathscr{L}}}{\partial\dot{\psi}} = 2\rho \left[\dot{\psi} + \frac{\sin(\psi)}{\rho} \right],
\tag{4.11a}
$$

$$
p_\rho = \frac{\partial\tilde{\mathscr{L}}}{\partial\dot{\rho}} = \lambda_\rho,
\tag{4.11b}
$$

$$
p_z = \frac{\partial\tilde{\mathscr{L}}}{\partial\dot{z}} = \lambda_z - \tilde{F}.
\tag{4.11c}
$$

The (scaled) Hamiltonian function is then given by

$$
\begin{aligned}
\tilde{\mathscr{H}} &= \dot{\psi}p_\psi + \dot{\rho}p_\rho + \dot{z}p_z - \tilde{\mathscr{L}} \\
&= \frac{p_\psi^2}{4\rho} - \frac{p_\psi \sin\psi}{\rho} - \frac{2\rho}{\lambda^2} + p_\rho \cos\psi + (p_z + \tilde{F})\sin\psi.
\end{aligned}
\tag{4.12}
$$

Remarks:

- The Hamiltonian function $\tilde{\mathscr{H}}$ is not explicitly dependent on s and is thus a conserved quantity.

- In fact it is zero. The reason for this is that the total arc length is not a conserved quantity, which it would be if we used a fixed interval of integration. Relaxing this unphysical constraint requires the Hamiltonian function $\tilde{\mathscr{H}}$ to vanish [JS94, CVG07]. This is one of the boundary conditions we will use in the following.

- According to Eqn. (3.54) the Hamiltonian function does not change its value across the separating boundary between two membrane domains on a vesicle.

The previous remark thus implies that $\tilde{\mathscr{H}}$ has to be zero at every point of the surface of the vesicle in Sec. 3.5. In analogy to the calculations presented in this chapter this fact yields one of the boundary conditions needed to calculate the shape of a two-domain vesicle in a Hamiltonian formulation (see, for instance, Ref. [JL96]).

- Instead of one fourth order one now has six first order ordinary differential equations, the Hamilton equations.[9]

These are given by

$$\dot{\psi} = \frac{\partial \tilde{\mathscr{H}}}{\partial p_\psi} = \frac{p_\psi}{2\rho} - \frac{\sin \psi}{\rho} \tag{4.13a}$$

$$\dot{\rho} = \frac{\partial \tilde{\mathscr{H}}}{\partial p_\rho} = \cos \psi \tag{4.13b}$$

$$\dot{z} = \frac{\partial \tilde{\mathscr{H}}}{\partial p_z} = \sin \psi \tag{4.13c}$$

$$\dot{p}_\psi = -\frac{\partial \tilde{\mathscr{H}}}{\partial \psi} = \left[\frac{p_\psi}{\rho} - (p_z + \tilde{F}) \right] \cos \psi + p_\rho \sin \psi \tag{4.13d}$$

$$\dot{p}_\rho = -\frac{\partial \tilde{\mathscr{H}}}{\partial \rho} = \frac{p_\psi}{\rho} \left(\frac{p_\psi}{4\rho} - \frac{\sin \psi}{\rho} \right) + \frac{2}{\lambda^2} \tag{4.13e}$$

$$\dot{p}_z = -\frac{\partial \tilde{\mathscr{H}}}{\partial z} = 0 \,. \tag{4.13f}$$

According to the last equation, p_z has to be constant along the profile. Its value can be found by considering the integral over the flux of surface stress again which has to equal the applied force.

In angle-arc length parametrization, the curvatures are given by: $K_\perp = -\dot{\psi}$, $K_\parallel = -\sin(\psi)/\rho$, and $K = -p_\psi/(2\rho)$ (see App. A.4.2). Eqn. (4.IV) can then be written as

$$F = -2\pi R_{\text{int}} \frac{\kappa}{2} \left\{ \left[\left(\dot{\psi}^2 - \frac{\sin^2 \psi}{\rho^2} \right) - \frac{2}{\lambda^2} \right] \sin \psi + \frac{1}{\rho} \left(\dot{p}_\psi - \frac{p_\psi}{\rho} \dot{\rho} \right) \cos \psi \right\} \Big|_{\rho=R_{\text{int}}} \,, \tag{4.14}$$

where we exploited axial symmetry again by integrating around a circle of radius $\rho = R_{\text{int}}$ and inserting Eqns. (A.79). The integrand can be evaluated further by inserting the Hamilton equations (4.13) and making use of the fact that the Hamiltonian function (4.12) is zero. One obtains $\tilde{F} = p_z + \tilde{F}$; hence, the momentum p_z conjugate to z has to vanish identically. This implies that the Lagrange multiplier

---

[9] One might naively expect to obtain four first order ordinary differential equations from one fourth order one. However, two additional geometrical equations are necessary to connect the angle $\psi(s)$ to ρ and z.

━━━ **Technical Point 4.3:** *Numerical profile calculations* ━━━

The Hamilton equations (4.13) were solved by using a shooting method [PTVF92]: for a trial contact point c Eqns. (4.13) were integrated with a fourth-order Runge-Kutta method. The value of c determined the contact angle α and with it ψ, ρ, p_ψ, and p_ρ at $s = \underline{s}$ via the boundary conditions (4.15). The integration was stopped as soon as ρ was equal or greater than R_{pore}. To reach R_{pore}, exactly one extra integration with the correct stepsize backwards was performed. Finally, the value(s) of c for which $\psi = 0$ at R_{pore} were identified for fixed parameters F, σ, w, etc.

If the calculation had been done in the constant height ensemble, one would additionally have to check whether the correct indentation h_0 was reached at $\rho = R_{\text{pore}}$ after shooting. In the constant force ensemble this complication of meeting a second condition is avoided which is why it was used for the nonlinear calculations.

---

function λ_z is equal to $\tilde{F}$ (see Eqn. (4.11c)). This seemingly surprising result is no coincidence at all. In fact, in Ref. [CVG07] it was shown that the Lagrange multiplier functions which fix these geometrical constraints are closely related to the external forces via the conservation of stresses.

Equations (4.13) can be solved numerically (see Technical Point 4.3) subject to the boundary conditions:

$$\psi(\bar{s}) = 0 \, , \quad \psi(\underline{s}) = \alpha \, , \tag{4.15a}$$

$$\dot{\psi}(\underline{s}) = \frac{(\cos \alpha)^3}{R_{\text{tip}}} - \sqrt{\frac{2w}{\kappa}} \, , \tag{4.15b}$$

$$\text{and} \quad \tilde{\mathscr{H}} = 0 \, , \tag{4.15c}$$

where contact point c and contact angle α are connected via $c = R_{\text{tip}} \tan \alpha$. Eqns. (4.15a) follow from the requirement that the membrane must not have kinks; Eqn. (4.15b) is again due to the adhesion balance.[10] The reason for the vanishing Hamiltonian was given in the second Remark on page 88.

The solution to (4.13, 4.15) gives the indentation h_0 for some prescribed force $\tilde{F}$.

---

[10] In the force ensemble an extra term $\tilde{F}\delta h$ has to be added to the variation of the bound membrane. A term that is equal and opposite, however, enters the variation of the free membrane via the Hamiltonian (4.12). In total, both terms cancel and one again obtains the same condition (3.23) (Eqn. (4.15b) in angle-arc length parametrization).

4.4 Results

The linear behavior of the measurements is reproduced if one neglects the influence of adhesion between tip and membrane. Including it via an adhesion balance changes the situation significantly: force-distance curves cease to be linear, hysteresis and nonzero detachment forces can show up.

This section will summarize the characteristic features of the solution to the boundary value problems (4.7, 4.8) and (4.13, 4.15). In addition, the theory will be compared to the experimental results from Sec. 4.1.2.

We will introduce some additional variable rescaling in order to make generalizations of the results easier: lengths will be scaled with R_{tip}. We also define

$$\tilde{\sigma} := \frac{\sigma R_{\text{tip}}^2}{\kappa} \quad , \quad \tilde{w} := \frac{2w R_{\text{tip}}^2}{\kappa} \quad \text{and} \quad \tilde{f} := \frac{F R_{\text{tip}}}{\pi \kappa} . \tag{4.16}$$

In a typical experiment the radius of curvature of the tip is of the order of ten nanometer (5–40 nm) and pore radii may in principal lie between 30 and 200 nm [Ste06b]. As already mentioned in Sec. 1.2.1, the bending rigidity of a fluid membrane is of the order of a few tens of $k_{\text{B}}T$ [SL95]. If we use Helfrich theory to describe membranes in the gel phase (which is only a crude approximation as in-plane shear stresses play a role in this case), their bending rigidity turns out to be about ten times higher than the one of the fluid phase [LLW01]. One expects a maximum surface tension of the order of a few mN/m, which is approximately the rupture tension for a fluid phospholipid bilayer [EHLR03]. A maximum value of the adhesion can be found by assuming that a few $k_{\text{B}}T$ per lipid is stored if membrane and tip are in contact. One arrives at $w_{\text{max}} \approx 10 \, \text{mJ/m}^2$. For the continuum theory to be valid Eqns. (4.8c, 4.15b) imply that $\sqrt{2w_{\text{max}}/\kappa} \lesssim 1/d$, where $d \approx 5 \, \text{nm}$ is the bilayer thickness. This estimate yields approx. the same maximum value for w_{max} as before since κ is at most $100 \, k_{\text{B}}T$.

Thus, $\tilde{\sigma}$ and $\tilde{w}$ can in principal vary between 0 and 10^3. Realistically, if we set $R_{\text{tip}} = 10$ nm and consider a typical fluid phospholipid bilayer with $\kappa \simeq 20 \, k_{\text{B}}T$, $\tilde{\sigma}$ and $\tilde{w}$ are of the order of 1. Furthermore, we will focus on a pore radius of $\tilde{R}_{\text{pore}} = 3$ in the following.

Let us first discuss the case where there is no adhesion between tip and membrane ($\tilde{w} = 0$) and see how the theoretical force-distance curves compare to the measurements from Sec. 4.1.2.

4.4.1 No adhesion between tip and membrane

In Fig. 4.6 the shapes of the membrane for different values of indentation are presented in scaled units. The linear calculations are dotted whereas the exact result is plotted with solid lines. For small indentations the two solutions overlap;
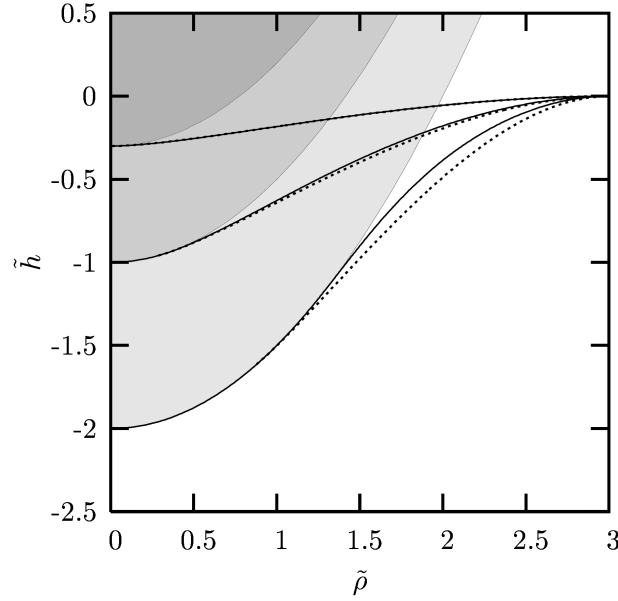
Figure 4.6: Membrane profiles for different indentations $\tilde{h}_0$, all for $\tilde{\sigma} = 1$ and $\tilde{w} = 0$ (solid lines: nonlinear calculations, dashed lines: linear approximation, grey shades: AFM tips). The corresponding forces $\tilde{f}(\tilde{h}_0)$ for the three different indentations are (nonlinear calculations): $\tilde{f}(0.3) = 0.81$, $\tilde{f}(1) = 2.45$, $\tilde{f}(2) = 4.27$.

for increasing $\tilde{h}_0$, however, the deviations become larger just as one expects for a small gradient approximation (see also Ref. [Des04a] for another example). While the differences are noticeable, they appear fairly benign, such that one would maybe not expect big changes in the force-distance behavior. We will soon find out that these hopes will not be fulfilled.

A deeper indentation also means that the tip has to exert a higher force. In Figs. 4.7 and 4.8 log-log plots of force-distance curves for different values of $\tilde{\sigma}$ are shown. The dashed line marks the maximum indentation $\tilde{h}_{0,\mathrm{max}} = \tilde{R}^2_{\mathrm{pore}}/2$ which is allowed by the geometry of tip and pore. In the limit of high forces all curves converge and approach $\tilde{h}_{0,\mathrm{max}}$; for small forces the curves are linear in $\tilde{f}$. The theoretical curves thus exhibit a functional form which qualitatively matches the behavior of the measured force-distance curves (see Sec. 4.1.2 and Refs. [SMD$^+$06, Ste06a]).

To quantify the indentation response, let us define the (scaled) apparent spring constant $\tilde{\mathcal{K}}$ of the nanodrum-AFM system via

$$\tilde{\mathcal{K}} = \left.\frac{\partial \tilde{f}}{\partial \tilde{h}_0}\right|_{\tilde{w},\tilde{\sigma}} . \tag{4.17}$$
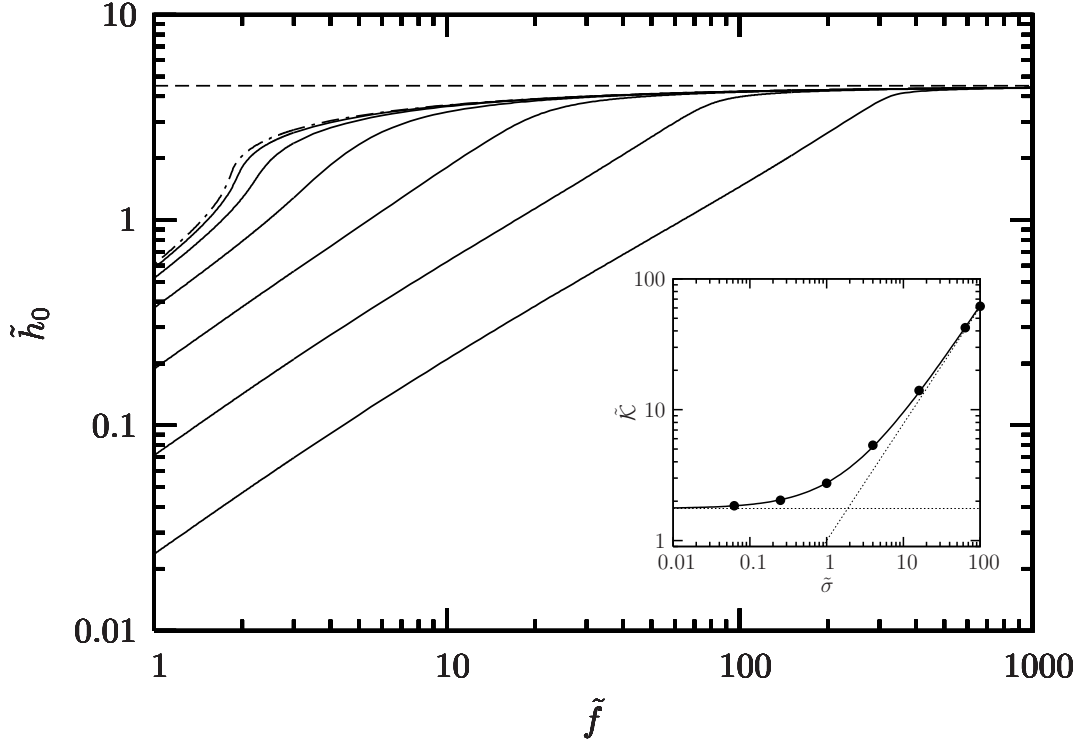
Figure 4.7: Force-distance curves for $\tilde{w} = 0$ and $\tilde{\sigma} = \frac{1}{16}, \frac{1}{4}, 1, 4, 16$ and 64 (σ increasing from left to right). The curve for $\tilde{\sigma} = 0$ is dashed-dotted. The inset shows the corresponding scaled apparent spring constant $\tilde{\mathcal{K}}$ (see Eqn. (4.17)) in the small force limit, illustrating its two different regimes of small and large tension with a crossover around $\tilde{\sigma} \simeq 1$.

A linear force-distance curve has a constant $\tilde{\mathcal{K}}$ and thus follows an apparent Hookean behavior $\tilde{f} = \tilde{\mathcal{K}}\tilde{h}_0$. In unscaled units, the spring constant is given by $\mathcal{K} = \partial F/\partial h_0 = \tilde{\mathcal{K}}\pi\kappa/R_{\text{tip}}^2$. For typical values $R_{\text{tip}} = 10\,\text{nm}$ and $\kappa = 20\,k_{\text{B}}T$ this implies $\mathcal{K} = \tilde{\mathcal{K}} \times 2.6\,\text{mN/m}$.

The smaller $\tilde{\sigma}$, the less force has to be applied to reach the same indentation (see Fig. 4.7). For decreasing $\tilde{\sigma}$ the force-distance curves converge to the limiting curve of the pure bending case, for which $\tilde{\sigma} = 0$; this is plotted dashed-dotted in Fig. 4.7. In the opposite pure tension limit ($\kappa \to 0$ or $\tilde{\sigma} \to \infty$) the curves become essentially linear in $\tilde{\sigma}$, as can be seen clearly after scaling out the tension (see Fig. 4.8). It is possible to calculate this second limiting curve in the linear approximation (see Technical Point 4.4). The final result for the indentation depth is:

$$\tilde{h}_0^{\tilde{\sigma} \to \infty} = \frac{\tilde{f}/\tilde{\sigma}}{4}\left[1 - \ln\left(\frac{\tilde{f}/\tilde{\sigma}}{2\tilde{R}_{\text{pore}}^2}\right)\right], \tag{4.18}$$
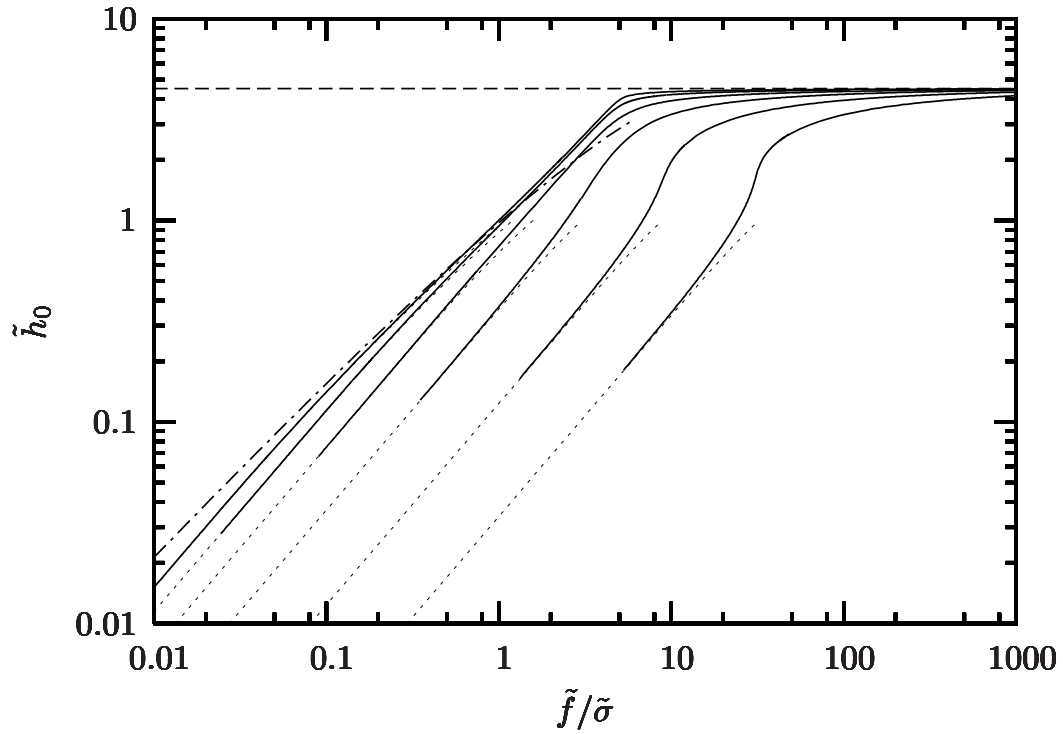
Figure 4.8: Scaled force-distance curves for $\tilde{w} = 0$ and $\tilde{\sigma} = \frac{1}{16}, \frac{1}{4}, 1, 4, 16$ and 64 (σ increasing from right to left). The solution for $\tilde{\sigma} \to \infty$ in the linear approximation is dashed-dotted. Nonlinear results are plotted with solid lines, the linear approximation is dotted.

which is plotted dashed-dotted in Fig. 4.8. At any given penetration the force is now strictly proportional to the tension. Notice also the remarkably weak (logarithmic) dependency of penetration on pore size.

All force-distance curves presented in this section exhibit a linear behavior for small forces. In this limit the scaled spring constant for the systems just discussed is well described by the empirical relation $\tilde{\mathcal{K}} \simeq 1.76 + \tilde{\sigma}^{0.89}$ (see inset in Fig. 4.7).[11] Combining this with our observation that for typical system parameters $\mathcal{K} = \tilde{\mathcal{K}} \times 2.6 \, \text{mN/m}$, it turns out that our theory predicts a nanodrum's stiffness which can be very well matched by available (soft) AFM cantilevers.

To see how the theoretical results compare to the experiment quantitatively, let us come back to the example given in Fig. 4.3. Fig. 4.9 shows the measured force-distance curve again (solid grey line). As mentioned in Sec. 4.1.2, a fluid DOTAP membrane was suspended over a pore of radius $R_{\text{pore}} = 90 \, \text{nm}$ and subsequently probed with a tip of radius $R_{\text{tip}} = 20 \, \text{nm}$ [SMD⁺06, Ste06a]. The apparent spring

---

[11] Note that this relation is only correct for the set of parameters chosen in this section.

━━ **Technical Point 4.4:** *Force-distance curve in the pure tension limit* ━━

In the pure tension limit the linearized Euler-Lagrange equation (4.7) reduces to the Laplace equation, $\Delta h = 0$, which is solved by $h(\rho) = d_1 + d_2 \ln(\rho/R_{\rm pore})$ in the present axial symmetry. The constants d_1 and d_2 can be determined with the help of the two boundary conditions $h(R_{\rm pore}) = 0$ and $h(c) = -h_0 + c^2/2R_{\rm tip}$. One obtains $h(\rho; c) = (-h_0 + \frac{c^2}{2R_{\rm tip}})\frac{\ln(\rho/R_{\rm pore})}{\ln(c/R_{\rm pore})}$. The contact point c can now be determined by an energy minimization. With $E(c) = \frac{\sigma}{2}\int_\Sigma {\rm d}A\, [\partial_\rho h(\rho; c)]^2$, we get

$$
\begin{aligned}
E(c) &= \frac{\sigma}{2}\left\{ \int_0^c {\rm d}\rho\, 2\pi\rho \left(\frac{\rho}{R_{\rm tip}}\right)^2 + \int_c^{R_{\rm pore}} {\rm d}\rho\, 2\pi\rho \left[\left(-h_0 + \frac{c^2}{2R_{\rm tip}}\right)\frac{1}{\rho \ln\left(\frac{c}{R_{\rm pore}}\right)}\right]^2 \right\} \\
&= \frac{\sigma\pi}{4R_{\rm tip}^2}c^4 \left[1 - \left(1 - \frac{2R_{\rm tip}h_0}{c^2}\right)^2 \frac{1}{\ln\left(\frac{c}{R_{\rm pore}}\right)}\right] .
\end{aligned}
$$

Energy minimization, $\partial_c E(c) = 0$, leads to

$$
\frac{c^3}{\ln^2\left(\frac{c}{R_{\rm pore}}\right)}\left[1 - \frac{2R_{\rm tip}h_0}{c^2} - 2\ln\left(\frac{c}{R_{\rm pore}}\right)\right]^2 = 0 .
$$

For $c \neq 0$ this equation can be written as $\mathscr{W}_{-1}(\mathfrak{h}) = \ln(c^2/[{\rm e}R_{\rm pore}^2])$, where $\mathscr{W}_{-1}$ is branch -1 of the Lambert-W-function [CGH+96] and $\mathfrak{h} = -2R_{\rm tip}h_0/({\rm e}R_{\rm pore}^2)$. Thus,

$$
c = R_{\rm pore} \exp\left\{[1 + \mathscr{W}_{-1}(\mathfrak{h})]/2\right\}
$$

and the force is given by

$$
F = \oint_\mathcal{C} {\rm d}s\, \sigma\,(\boldsymbol{l}\cdot\boldsymbol{z}) \stackrel{\rm (A.79a)}{\approx} \sigma 2\pi R_{\rm pore} h'(R_{\rm pore}) = -\frac{4\pi\sigma h_0}{\mathscr{W}_{-1}(\mathfrak{h})} .
$$

This expression can finally be inverted yielding Eqn. (4.18) after scaling.

━━

constant is found to be $3.9\,{\rm mN/m}$. To fit the data, the values of σ and κ have been optimized.

The linear approximation (asymptotically) matches the curve down to an indentation depth of about 40 nm as one can see in Fig. 4.9 (dashed line). For larger indentations the small gradient assumption breaks down. The nonlinear calculation (solid black line) describes the data correctly down to a much deeper penetration depth of 150 nm but deviates for larger values. This deviation is most likely *not* a failure of the elastic model but a consequence of our simplified assumptions for the tip geometry. As shown in Fig. 4.4 on page 81 the tip is parabolic at its apex, but
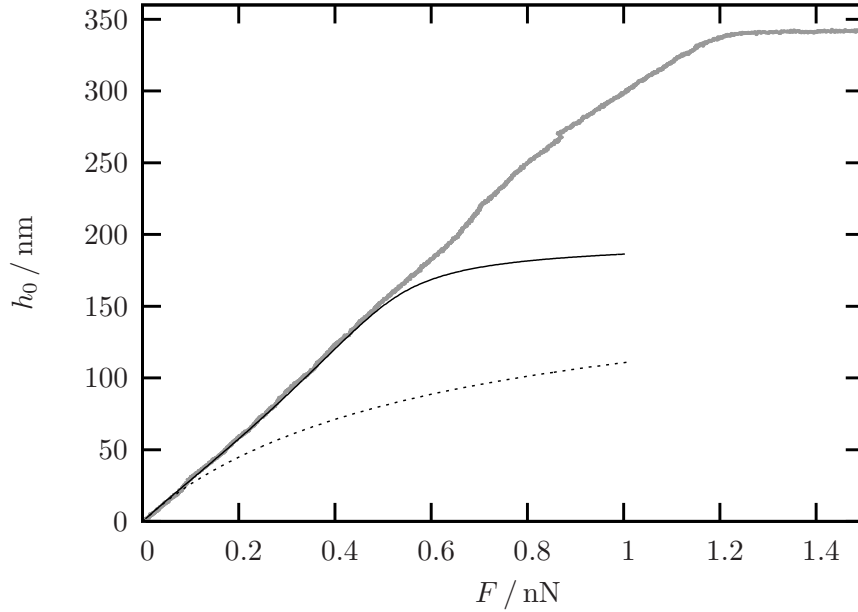
Figure 4.9: Comparison between experiment (solid grey line; from Fig. 4.3) and theory (dashed line: linear approximation; solid black line: nonlinear calculations). The theoretical curves are obtained with the following parameters: $R_{\text{pore}} = 90\,\text{nm}$, $R_{\text{tip}} = 20\,\text{nm}$, $\kappa = 10^{-19}\,\text{J} \approx 24\,k_{\text{B}}T$, $\sigma = 1.1\,\text{mN/m}$.

further up it narrows quicker and assumes a more cylindrical shape. It therefore can penetrate the pore much deeper than one would expect if the parabolic shape were correct for the entire tip.

Apart from this difficulty, theory and experiment are in good agreement. There is, however, a catch. Since we cannot trust the force-distance behavior close to the depth-saturation (due to its displeasingly strong dependence on the actual tip shape), the remaining interpretable part of the force-distance curve is linear, and its slope is the only parameter that can be extracted from the data.[12] For the theoretical calculation one needs two parameters, σ and κ. Fitting both to a line is not possible. One possibility to overcome this obstacle is to estimate κ from other measurements to be about $10^{-19}\,\text{J}$. The surface tension σ can then be adjusted to $1.1\,\text{mN/m}$ to match the data—which, reassuringly, is a very realistic value.

Alternatively, one may proceed in a manner which was already adumbrated in Sec. 4.1.2. In the experiment a small snap-off peak could be observed upon retraction of the AFM tip which was due to the attraction between tip and membrane.

---

[12] The axis intercept is needed to gauge the distance between AFM tip and substrate in the experiment and can therefore not be extracted as a second parameter.

Although this can be neglected in the interpretation of all existing measurements one may think of deliberately increasing the adhesion between membrane and tip in a follow-up experiment by chemically functionalizing the tip. Whether with this additional tuning parameter one may get further information on the values of the material parameters in question will be the subject of the rest of this chapter.

4.4.2 Including adhesion between tip and membrane

In the following, we will also allow for adhesion between tip and membrane, *i. e.* $\tilde{w}$ is not necessarily equal to zero. This will change the qualitative behavior of the force-distance curves dramatically: for fixed $\tilde{\sigma}$ and $\tilde{w}$ different solution branches can be found. A hysteresis may occur as well. Additionally, stable membrane profiles exist even if the tip is pulled upwards. It is therefore possible to calculate the maximum pulling force that can be applied before the tip detaches from the membrane and relate it to the value of the adhesion between tip and membrane.

Weak adhesion energy

In this section, we will first investigate the case of weak adhesion, $\tilde{w} \leq 5$. The scaled surface tension $\tilde{\sigma}$ will be fixed to 1. It turns out that once the tip is adhesive, overhang profiles may occur, *i. e.*, shapes where at some point $|\psi(s)| > 90°$ (compare Fig. A.8). We will first ignore these solution branches and come back to them later.

Fig. 4.10 illustrates force-distance curves for $\tilde{w} = 0, 1, \ldots, 5$. Compared to the non-adhesive case, for which an essentially linear behavior levels off towards maximum penetration, adhesive tips behave quite differently. Already for $\tilde{w} = 1$ an initial Hookean response at small forces is soon followed by a regime in which the system displays a much greater sensitivity towards an externally applied stress, *i. e.*, where the scaled spring constant $\tilde{\mathcal{K}}$ drops at intermediate penetrations. Physically this of course originates from the fact that adhesion *helps* to achieve higher penetrations, because the tip is pulled towards the membrane, but notice that this does not lead to a uniform reduction of $\tilde{\mathcal{K}}$: softening only sets in beyond a certain indentation. Shortly beyond $\tilde{w} = 1$ a point is reached where the force-distance curve displays a vertical slope at which the apparent spring constant $\tilde{\mathcal{K}}$ vanishes. For even larger values of adhesion a hysteresis loop opens, featuring a locally unstable region with $\tilde{\mathcal{K}} < 0$. This is the case for $\tilde{w} = 2$, and the region around the instability is magnified in the inset of Fig. 4.10. Notice that the dotted branch corresponding to $\tilde{\mathcal{K}} < 0$ still belongs to solutions for which the functional (4.2) is stationary, yet the energy plotted against penetration $\tilde{h}_0$ (or, alternatively, contact angle α) has a local *maximum*, confirming that these solutions are unstable against contact point variations. The two dashed branches in the inset of Fig. 4.10 have a positive $\tilde{\mathcal{K}}$ and correspond to local minima in the energy, however, they are *globally* unstable
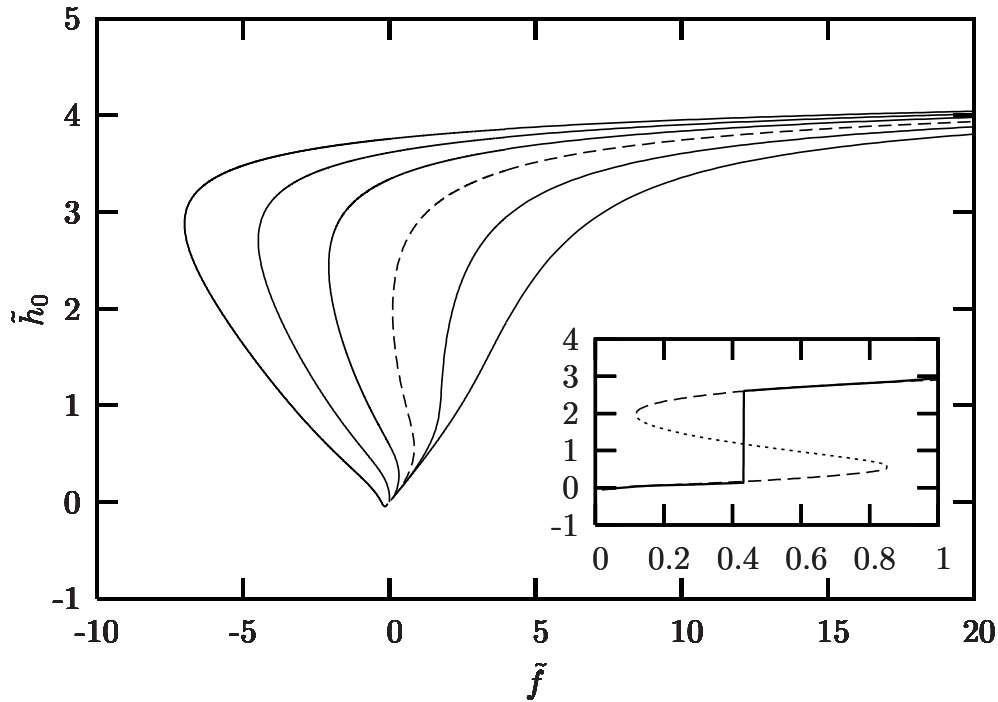
Figure 4.10: Force-distance curves for $\tilde{\sigma} = 1$ and $\tilde{w} = 0, 1, 2, 3, 4, 5$ (from right to left). The region of hysteresis in the curve for $\tilde{w} = 2$ is magnified in the inset. In this case the energy barrier at $\tilde{f} = 0.414$ is approx. $1\,\kappa$. Overhang branches are omitted.

against the alternative minimum of larger or smaller $\tilde{h}_0$. The true global minimum is indicated by the bold solid curve, which exhibits a discontinuity at $\tilde{f} = 0.414$. Depending on the current scanning direction this hysteretic force-distance curve manifests itself in a snap-on or snap-off event. Notice, however, that the membrane does *not* stay flat up to a critical buckling force at which it suddenly yields; rather, the system starts off with a linear stress-strain relation and only later undergoes an adhesion-driven discontinuity. Appreciating this point is quite important for the interpretation of measured force-distance curves: upon approach of tip and membrane the snap-on will occur *neither* at zero force *nor* at zero penetration. Furthermore, one should not forget that hysteresis is ultimately a consequence of the energy barrier which goes along with such discontinuities. For macroscopic systems this barrier is typically so big that the transition actually happens at either of the two end-points of the S-shaped hysteresis curve, where the barrier vanishes (the spinodal points). However, for nano-systems barriers are much smaller, comparable to thermal energy $k_\mathrm{B}T$, such that thermal fluctuations can assist the barrier-crossing event. In the present case the barrier at the equilibrium transition point is about $1\,\kappa$, *i. e.*, about $20\,k_\mathrm{B}T$ for typical bilayers. However, already at

$\tilde{f} = 0.5$ its magnitude has decreased by about 20%. This shows that we have to expect a narrowing-down of the hysteresis amplitude compared to a macroscopic system.

Upon increasing the adhesion $\tilde{w}$ even further, one will reach a critical value $\tilde{w}_0$ at which the "back-bending branch" of the force-distance curve touches the vertical line $\tilde{f} = 0$. At this point the tip is being pulled into the pore even if there is no force at all. Conversely, neglecting barrier complications, this also implies that at the critical adhesion energy $\tilde{w} = \tilde{w}_0$ an *infinitesimal* pulling force will suffice to unbind tip and membrane, *even though* the adhesion between tip and membrane is greater than zero. It is very important to keep this fact in mind if one wants to use AFM measurements for the determination of adhesion energies.

For $\tilde{w} > \tilde{w}_0$ one obtains stable solutions even when pulling the tip upwards (where $\tilde{f} < 0$).[13] The maximum possible force before detachment, $\tilde{f}_{\mathrm{det}}$, again corresponds to the leftmost point of the back-bend, and it increases with increasing $\tilde{w}$; we will come back to this later. Notice that detachment always happens for values of $\tilde{h}_0$ which are *positive*, *i. e.*, when the AFM tip is still *below* the substrate level. Contrary to what one might have expected, pulling will in this case *not* draw the membrane upwards into a tubular lipid bilayer structure (a tether), which at some specific elongation will fall off from the tip and snap back. Rather, the strong adhesion pulls the tip far into the pore, and while pulling on it indeed lifts it up, unbinding still happens below pore rim level.

Strong adhesion energy

At even larger adhesion energy entirely new stationary solution branches emerge, as Fig. 4.11 illustrates for $\tilde{w} \in \{5, 10, 15\}$ and $\tilde{\sigma} = 1$. We first recognize the well-known hysteretic branch, already seen in Fig. 4.10, which for increasing $\tilde{w}$ extends to much larger negative forces, even though the snap-off height $\tilde{h}_0$ only changes marginally. The shapes of two typical profiles are illustrated in the insets c and d. Notice that this branch is always connected to the origin, but for larger values of $\tilde{w}$ it starts off into the third quadrant (negative values for $\tilde{f}$ and $\tilde{h}_0$). At first sight it seems that we finally get solutions which correspond to a pulled-up membrane; however, this region close to the origin corresponds to a maximum and is thus unstable.

Overhang branches Contrary to the hysteretic branches, the new branches depicted in Fig. 4.11 do *not* connect to the origin. This classifies them as a genuinely nonlinear phenomenon, since they cannot be obtained as a small perturbation around the state $\tilde{f} = \tilde{h}_0 = 0$. In the first quadrant ($\tilde{f}, \tilde{h}_0 > 0$) they all

---

[13] Strictly speaking *all* of these solutions are metastable with respect to detachment of the tip from the membrane.
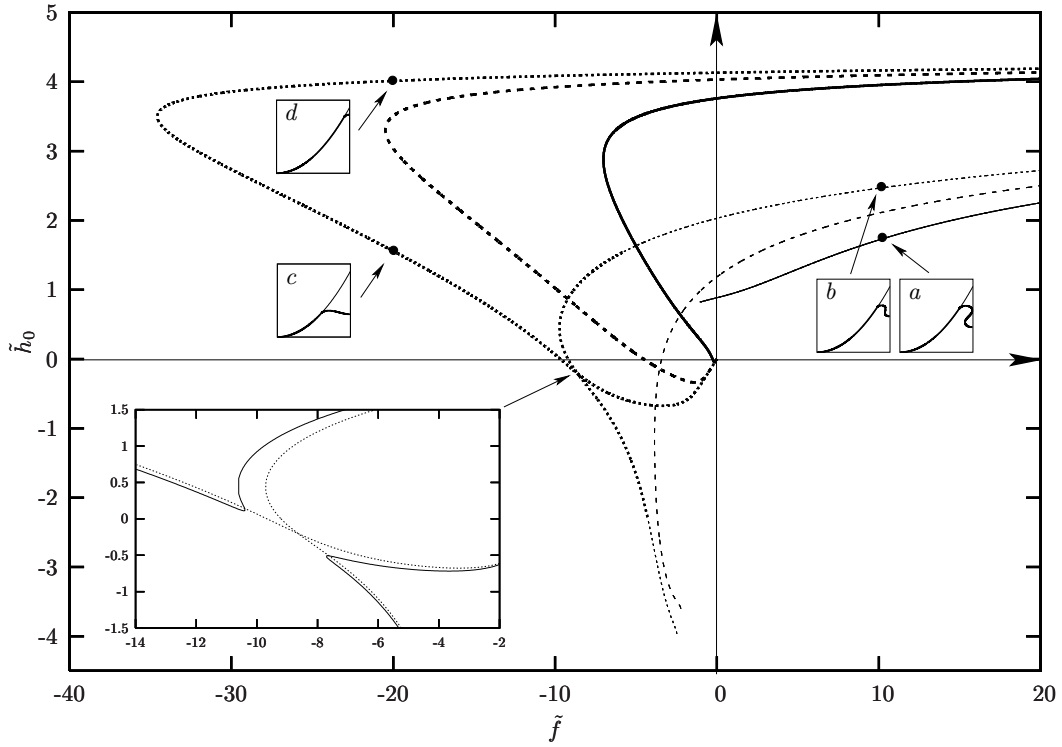
Figure 4.11: Force-distance curves for $\tilde{\sigma} = 1$ and $\tilde{w} = 5$ (solid), 10 (dashed) and 15 (dotted). A thinner line style is used for those parts of the curves where the corresponding profiles exhibit overhangs. In the insets a–d profiles for different values of $(\tilde{f}, \tilde{h}_0)$ are depicted (scaling is $\tilde{h} : \tilde{\rho} = 5 : 3$). In the inset on the lower left corner the "branch splitting" is shown as discussed in the text ($\tilde{w} = 15.0$ (dotted line) and 15.5 (solid line)).

correspond to profiles which show overhangs (see inset a and b). These branches had been omitted in Fig. 4.10, since for weak adhesion they always correspond to maxima and are thus irrelevant. This changes for stronger adhesion, though, where they become stable in certain regions (for instance, inset b is locally stable). The details by which this happens are complicated and will be discussed in more detail below.

Following the new branches to negative forces we see that the one for $\tilde{w} = 15$ loses its overhang around $\tilde{f} \approx -6$. That this can happen continuously is not surprising, since within angle-arc-length parametrization there is nothing special about the point where $|\psi| = 90°$ (only the shooting method might use occurrences of $|\psi| > 90°$ as a potential termination criterion for integration (see Technical Point 4.3)).

Branch splitting   We also see that (for sufficiently large $\tilde{w}$) there is a point where the hysteresis branch *intersects* the new nonlinear branch. There the values of $\tilde{f}$ and $\tilde{h}_0$ coincide for both branches, but the detachment angle α and the total energy of the profile are generally different. However, the difference in energy at the intersection decreases with increasing $\tilde{w}$, and around $\tilde{w} = 15.3$ it finally vanishes. At this degenerate point a *branch splitting* occurs, where the connectivity of the two branches re-bridges, as illustrated in the lower left inset in Fig. 4.11. Rather than connecting to the origin, the wide loop of the original hysteresis branch now joins into the overhang branch of the first quadrant, while the part that was connected to the origin now joins into the overhang branch in the third quadrant.

Cusps   Figure 4.12 shows the force-distance curve branches for the even larger adhesion energy $\tilde{w} = 20$. This depicts a situation well after the branch-splitting, so we recognize the old hysteretic branch connecting with overhangs, and the branch connecting to the origin extending exclusively in the third quadrant. In contrast to Fig. 4.11, the line styles in Fig. 4.12 are chosen to illustrate local minima (solid) or maxima (dotted). What immediately strikes one as surprising is that the profiles at $\tilde{f} = -4$ belonging to the insets f and h *both* correspond to maxima, even though they sit on both sides of a back-bending branch, close to its end (compare this to the "usual" scenario at ($\tilde{f} \approx -49$, $\tilde{h}_0 \approx 3.6$). Moreover, the solution belonging to inset f turns into a local minimum for slightly more negative forces, *without* any noticeable features of the branch. How can this happen?

The explanation is illustrated in the lower left inset in Fig. 4.12, which shows the total energy as a function of detachment angle α. Recall that extrema in this plot correspond to stationary solutions. As can be seen, the energy is *multivalued*, meaning that there exists more than one solution at a given detachment angle (these would then also differ in their value of their penetration $\tilde{h}_0$). But more excitingly, this graph exhibits a *boundary extremum* at a lowest possible nonzero value of α in the form of a *cusp*. This is how one can have two successive maxima on a curve without an intervening minimum—the minimum is simply not differentiable. Hence, there is a *third* solution branch, corresponding to the cusp, at which the contact curvature condition from Eqn. (4.15b) is *not* satisfied, because this condition is blind to the possibility of having non-differentiable extrema. Plotting this cusp branch also into Fig. 4.12, we finally understand how the switching of a maximum into a minimum happens: it occurs at the point of intersection with the cusp branch. As the lower left inset in Fig. 4.12 illustrates, the maximum belonging to the solution f joins the cusp-minimum (belonging to solution g) in a *boundary flat point*, roughly at force $\tilde{f} = -4.8$. For more negative forces this flat point turns up, leaving a boundary cusp *maximum* and a new differentiable minimum. Notice that a similar exchange happens once more at ($\tilde{f} \approx -26.4$, $\tilde{h}_0 \approx 1.6$). Incidentally, since at the cusp the contact curvature condition is not
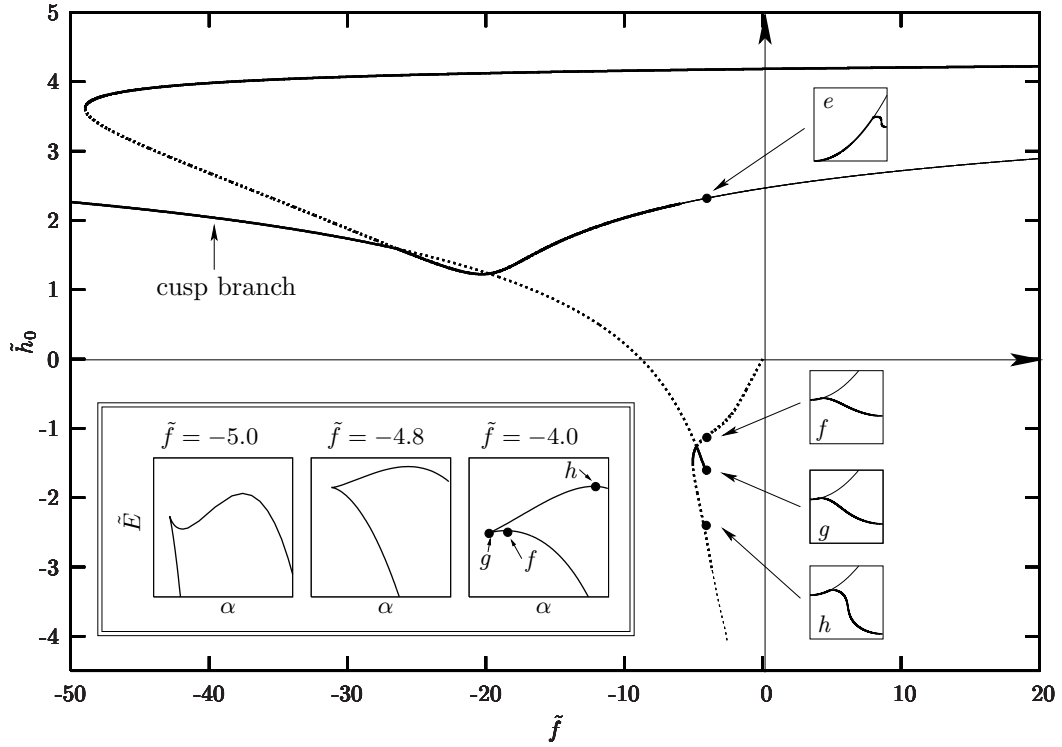
Figure 4.12: Force-distance curves for $\tilde{\sigma} = 1$ and $\tilde{w} = 20$ (including cusp branch). Solid lines correspond to local minima, dotted lines to local maxima. A thinner line style is used for those parts of the curves where the corresponding profiles exhibit overhangs. In the insets e–h profiles for different values of $(\tilde{f}, \tilde{h}_0)$ are depicted (scaling is $\tilde{h} : \tilde{\rho} = 5 : 3$). In the inset on the left lower corner the total energy $\tilde{E}$ is plotted as a function of detachment angle α for different forces $\tilde{f}$ (see text for further explanation).

satisfied, and since this is the only point where the adhesion energy $\tilde{w}$ enters, the location and form of the cusp branch is *independent* of the value of $\tilde{w}$.

The existence of the cusp branch poses the question whether the solutions corresponding to it are physically relevant (at least the ones which are minima). It is not so much the lack of differentiability at a cusp minimum which causes concern, but rather the fact that it is located at a *boundary*. Take for instance the $\tilde{E}(\alpha)$ curve in the lower left inset of Fig. 4.12 corresponding to $\tilde{f} = -4$. Now consider a (nonequilibrium) solution which sits on the upper branch, somewhere between the solutions g and h. To lower the energy, this solution will reduce the detachment angle α, thereby approaching the minimum at g. But once g has been reached, no further reduction in α seems possible, since for smaller values no equilibrium solution exists. The crucial point is that our present theory is insufficient to answer what *else* would be going on for smaller α. It could, for instance, be that there
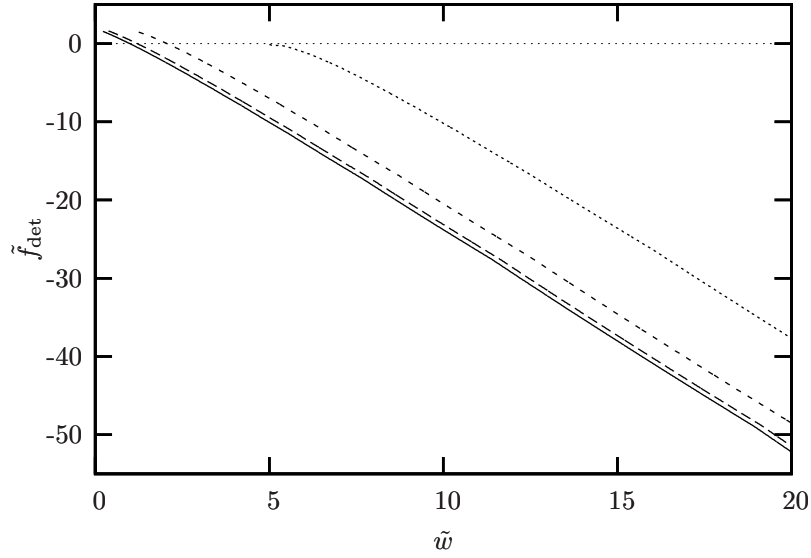
Figure 4.13: Scaled detachment force $\tilde{f}_{\mathrm{det}}$ as a function of scaled adhesion energy $\tilde{w}$ for four values of the scaled tension, $\tilde{\sigma} = \frac{1}{16}$, $\frac{1}{4}$, 1 and 4 ($\tilde{\sigma}$ increasing from left to right).

are indeed solutions, *but they are not time-independent.* This might be analogous to the well-known situation of a soap film spanned in the form of a catenoidal minimal surface between two coaxial circular rings of equal radius d (see Technical Point 2.2 on page 35). For a ring separation exceeding $1.325\,d$ no more stationary solution exists, even though the limiting profile is in no way singular. However, when slowly pulling the two rings beyond this critical separation, the soap film does not suddenly rupture. Rather, it becomes *dynamically* unstable and begins to collapse. In the case we are studying here, the system drives itself to the singular boundary point, and without a truly dynamical treatment it is not possible to conclude whether it would remain there or start to dynamically approach a different solution. For this reason we do not want to overrate the significance of the cusp branch; yet, its existence is still important in order to explain the behavior of the other "regular" branches, for instance their metamorphosis from maximum-branches into minimum-branches or vice versa.

Detachment forces A measurable quantity in the experiment is the detachment force between tip and membrane, which is the maximum pulling force $\tilde{f}_{\mathrm{det}}$ that can be applied before the tip detaches from the membrane. In Fig. 4.13 this force is plotted as a function of adhesion energy $\tilde{w}$ for different values of the scaled tension $\tilde{\sigma}$. Starting from a certain threshold adhesion $\tilde{w}_{\mathrm{thr}}(\tilde{\sigma})$, below

103

which no hysteresis occurs, $\tilde{f}_{\text{det}}$ decreases with increasing $\tilde{w}$ and exhibits a linear behavior for higher adhesions. Increasing $\tilde{\sigma}$ also increases the threshold adhesion (*e. g.* $\tilde{w}_{\text{thr}}(1/16) = 0.22$ compared to $\tilde{w}_{\text{thr}}(1) = 1.25$). In the large-$\tilde{w}$-limit $\tilde{f}_{\text{det}}/\tilde{w} = F_{\text{det}}/2\pi Rw$ finally approaches a limit which is independent of κ and σ and only depends on the geometry. The elasticity of the membrane no longer influences the measurement of the adhesion energy – not because the membrane is not deformed, but rather because its deformation energy is subdominant to adhesion. But for more realistic smaller values of $\tilde{w}$ this decoupling does not happen, and adhesion energies can only be inferred from the detachment force when a full profile calculation is performed.

At higher values of $\tilde{\sigma}$ also other qualitative features (such as additional instabilities) occur. However, these ramifications will not be discussed in the present work.

Tethers Characteristically, the detachment happens at deep indentations ($\tilde{h}_0$ close to the maximum indentation possible). Long pulled-out membrane tubes (tethers), as they have been studied in the literature [PHG02, DJP02, KCD$^+$05], are not observed. Even though in our calculations we find profiles with $\tilde{h}_0 < 0$, these solutions either correspond to energetic maxima, or they are only *local* minima – with the global minimum at $\tilde{h}_0 > 0$ corresponding to a significantly lower energy. This is a consequence of the adhesion balance present in our situation: upon pulling upwards, it is more favorable for the tip either to be "sucked in" completely or to detach from the membrane, rather than forming a long tether. As Fig. 4.12 shows, there is a very small "window of opportunity" at $\tilde{f} \approx -5$ where (locally) stable solutions pulled above the surface exist. Yet, their profiles look essentially like the ones of inset f or g and show no resemblance to real long tethers. Upon increasing the force they become unstable, such that the tip either falls off the membrane, or is drawn below the membrane plane (notice that there exist two minima at $\tilde{f}$ slightly smaller than -5, but both at positive indentation). This analysis shows that it appears impossible to pull tethers using a probe with a certain binding energy, despite existing experiments in which tethers of micrometer size were generated [DS95, DS99, MSdM02, KCD$^+$05]. Consequently, the assumption of an adhesion balance does not seem to be correct in these cases. Indeed, in these studies the experimental setup was different (membrane-covered micron-sized beads [DS95, DS99, KCD$^+$05] and AFM tips covered by lipid multilayers [MSdM02]). In the present situation tethers are also observed [SMD$^+$06], but these events are not very reproducible, and based on the above calculations we would tentatively attribute them to a pinning of the membrane at some irregularity of the tip.

4.5 What can be learnt in future experiments?

The values of σ and κ can be obtained by repeating the nanodrum experiment with the same membrane for different pore radii R_{pore}. For the same purpose, the adhesion between tip and membrane can be increased to exploit the rich scenario discussed in the previous section.

In the previous sections we have discussed the indentation of a pore-spanning bilayer by an AFM tip. We have seen that the force-distance curves show a linear behavior for small forces in a broad parameter range if the adhesion between tip and membrane vanishes. This result is in agreement with recent experiments (see Sec. 4.1.2 and Fig. 4.9). However, such a linear behavior is unfortunately too featureless to reveal the values of both elastic parameters, σ and κ.

One way out of this apparent cul-de-sac would be to repeat the experiment for different pore radii R_{pore} while keeping all other parameters fixed. Since σ and κ are the same for all pore sizes in that case, it should be possible to extract their value from the spring constants $\mathcal{K}$ of the measured force-distance curves.

The elastic parameters can also be obtained by considering systems where the adhesion w between tip and membrane has been increased experimentally. As we have seen, the curves change their behavior dramatically for $w \neq 0$. It should thus be possible to fit two parameters to the resulting curves which would yield a local κ and σ in one fell swoop whereas w can simultaneously be determined from the snap-on of the tip upon approach to the bilayer. The experimentalist, however, has to make sure in that case that the line of contact between tip and membrane is really due to a force balance as described in this chapter and not due to other effects such as pinning of the membrane to single spots on the tip. In practice, this is rather difficult and will be a challenge for future experiments.

One also has to keep in mind that the assumption of a perfect parabolic tip is quite simplistic compared to the experimental situation. It is probably valid in the vicinity of the apex but generally fails further up. Since the force-distance behavior close to the depth-saturation depends strongly on the actual tip shape, one can only use that part of the force-distance curve for data interpretation where the indentation is still small. To predict the whole behavior, the exact indenter shape has to be known: as long as the situation stays axisymmetric one may, in principle, redo the calculations of this chapter with the new shape. This is, however, rather tedious and therefore inexpedient in practice.

Our theoretical approach does not account for hydrodynamic effects although the whole experimental setup is in water and the AFM tip is moved with a certain velocity. First measurements have shown, however, that it is possible to increase the velocity of the tip up to $60\,\mu\mathrm{ms}^{-1}$ without altering the force-distance curves dramatically [SMD+06]. One can understand this result with the help of the following simple estimate: assume that the tip is a sphere of radius R_{tip} moving

with the velocity v in water. When indenting the membrane to a distance d it will also have to overcome a dissipative hydrodynamic force F_{diss} in addition to the elastic resistance of the membrane. The energy dissipated in this process, $E_{\mathrm{diss}} = F_{\mathrm{diss}}d = 6\pi\eta R_{\mathrm{tip}}vd$, is of the order of the thermal energy if typical values are inserted ($\eta = 10^{-3}\mathrm{Pa}\,\mathrm{s}$, $R_{\mathrm{tip}} = 10\,\mathrm{nm}$, $v = 60\,\mu\mathrm{ms}^{-1}$, $d = 100\,\mathrm{nm}$). This is substantially smaller than the corresponding elastic energy E_{elast}. Complications arising from a correct hydrodynamical treatment were thus omitted here.

Including adhesion, the velocity of the measurement should nevertheless be as slow as possible to ensure that the line of contact equilibrates due to the force balance. If this is guaranteed, one can also check whether the predicted linear behavior between detachment force and adhesion is actually valid.

This chapter has presented a new setup with which elastic parameters of a membrane can be obtained on the nano-scale. Once these parameters are known, problems of membrane mechanics can be addressed quantitatively. One particularly interesting problem in this context involves *interface-mediated interactions*, which will be discussed in the final part of this thesis.

5 Membrane-mediated interactions between particles

Particles bound to an interface may interact via the changes they impose on the surface geometry or on internal degrees of freedom such as a lipid tilt. The induced forces and torques are called *interface-mediated interactions*.

These indirect interactions play an important role in technological processes such as ore flotation or foam stabilization [RSS89, NS03]. Other research suggests that such forces can induce the self-assembly of small-scale structures which could offer, for instance, new ways of manufacturing components of micro-electromechanical systems [VM04].

In nature, interface-mediated interactions are a possible candidate to explain membrane remodeling in the biological cell (see Chap. 1): curvature-mediated attractive interactions could aid cooperation of proteins in the membrane and complement the effects of direct van der Waals' or electrostatic attractions [BV06, Ant06, Koz07]. Whereas it is difficult to isolate the different contributions experimentally, theory provides a possibility to do so.

Unfortunately, theoretical considerations of such interactions are mathematically involved because the membrane shape equation is a nonlinear differential equation as seen in Chap. 2. Most present calculations therefore yield approximate results for the forces. Even the sign of the interaction is not obvious.

Nevertheless, substantial progress can still be made if the problem is tackled with all possible means: following the techniques developed in Chap. 2, forces and torques on the particles can be directly related to the local membrane geometry via stress and torque tensors. A host of valuable exact nonlinear results for symmetric two-particle configurations can be established. Additionally, the nonlinear shape equation can be solved in terms of elliptic functions for the easiest case of two cylinders on a membrane.

If more than two particles adhere to the membrane, multi-body forces become important: the interaction energy is generally not expressible as a sum over pair potentials. The superposition principle does not hold due to the nonlinearity of the theory. To include multi-body forces as well, coarse-grained computer simulations are presented and compared to the results of a cell model, similar in spirit to that used in Poisson-Boltzmann theory.
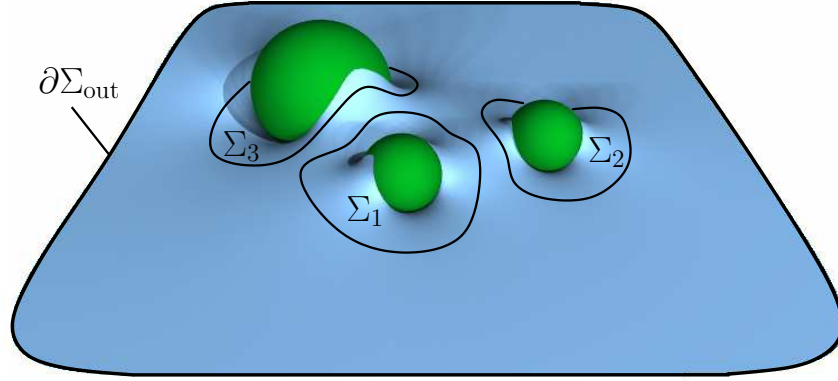
Figure 5.1: Interface-mediated interactions. Forces as well as torques act on each particle due to the distortions of the interface shape caused by the other particles.

5.1 Forces and torques on particles adhering to an up-down symmetric membrane

Analytical expressions for the membrane-mediated force between two particles can be obtained with the help of the stress tensor. Additionally, torque and force balance yield several analytical conditions on the membrane geometry.

Let us again consider the membrane from a mesoscopic point of view. In the following we will assume that solid particles are bound to it. These can either represent proteins or other objects like viruses.

5.1.1 Balance of forces and torques

Consider a multiparticle configuration such as the one depicted in Fig. 5.1: forces as well as torques act on each of the particles due to the distortions of the shape caused by the other particles. Such a situation can thus only be stationary if the particle positions and orientations are constrained by external forces and torques, respectively. As we have seen in Chap. 2, these forces and torques are determined completely by the surface geometry.[1] The external force acting on the particle that adheres to the surface patch Σ_1, for instance, is equal to the external force $\boldsymbol{F}_{\text{ext}}$ acting on the whole patch as given by Eqn. (2.16); this is because the stress tensor is divergence-free on any part of the surface not acted upon externally. The force $\boldsymbol{F}^{(i)}$ we will consider in the following is the force on the particle i mediated by the interface *counteracting* the corresponding external force; the former is evidently

---

[1] Note that we neglect bulk stresses at first.

equal to minus the latter (for $i = 1$ one thus has $\boldsymbol{F}^{(1)} = -\boldsymbol{F}_{\mathrm{ext}}$). Similar arguments apply to the torque $\boldsymbol{M}^{(i)}$ on the ith particle.

The total force and the total torque on the system must vanish if the multiparticle configuration is in mechanical equilibrium:

$$\sum_{i=1}^{N} \boldsymbol{F}^{(i)} = \boldsymbol{F}_{\mathrm{out}} \qquad \text{and} \qquad \sum_{i=1}^{N} \boldsymbol{M}^{(i)} = \boldsymbol{M}_{\mathrm{out}} \ , \tag{5.1}$$

where $\boldsymbol{F}_{\mathrm{out}}$ is the force and $\boldsymbol{M}_{\mathrm{out}}$ the torque on the outer boundary $\partial\Sigma_{\mathrm{out}}$ (see again Fig. 5.1). The number N of particles will be finite except for Sec. 5.3 where the phase behavior of an infinite amount of particles will be studied.

As in the previous chapter, we will mainly consider an up-down symmetric fluid membrane with nonvanishing surface tension σ characterized by the Hamiltonian density

$$\mathcal{H} = \sigma + \frac{1}{2}\kappa K^2 \ , \tag{5.2}$$

where the Gaussian curvature term is discarded directly as it plays no role in the following (see Technical Point 2.3 on page 38 for a discussion). The ground state of the membrane in the absence of particles is an infinite flat plane with zero curvature. In this case the energy is proportional to the area and thus infinite. This constant energy will play no role in the following. The energy is recalibrated to set it to zero.

Particles that are bound to the membrane typically deform its shape and increase its energy. These energy changes, however, must be *finite* whenever the forces and torques applied to fix the particle configuration are finite.[2] This implies that the interface becomes asymptotically flat remote from the particles, even if σ is infinitesimally small (see Technical Point 5.1).

It is useful to decompose forces and torques into a horizontal part parallel to the asymptotic plane and a vertical part orthogonal to it. When the surface tension vanishes, Kim *et al.* have shown that the vertical force and the horizontal torque on the outer boundary at infinity must vanish in equilibrium [KNO98]. Their discussion can be extended to treat situations in which $\sigma \neq 0$. The change is, however, nontrivial as we will see in the next section.

5.1.2 Forces and torques on the outer boundary

Since the membrane becomes asymptotically flat if $\sigma \neq 0$, we can use linearized Monge gauge to describe its behavior remote from the particles (see Technical Point 5.1 and App. A.4.1). For the following assume that the outer boundary

---

[2] This holds for a finite number of particles. If infinitely many particles adhere to the membrane and deform its shape, the energy change can be infinite. However, one then requires the change *per particle* to be finite.

━━━━ **Technical Point 5.1:** *Asymptotic behavior of the membrane* ━━━━

Consider an up-down symmetric fluid membrane with a finite number of finite-sized particles bound to it. What is the asymptotic behavior of surface properties such as the curvature K and its derivatives far away from the particles?

To answer this question, let us adapt a line of argument originally introduced in [KNO98] for the case of vanishing surface tension. The excess membrane energy E induced by the particles is finite. From this requirement it immediately follows that K has to be square integrable and thus vanishes far away from the particles; the membrane becomes asymptotically flat.

This fact allows us to use linearized Monge gauge to describe its behavior remote from the particles (see App. A.4.1): in contrast to the previous chapter where we considered an axisymmetric situation, the height $h(\rho, \varphi)$ above the asymptotic plane does generally not only depend on the radial distance ρ but also on the azimuthal angle φ. We choose to place the origin somewhere in the middle of the surface region to which the particles adhere. For large ρ, the curvature K is then equal to the negative (base plane) Laplacian of h, $K \stackrel{(A.72)}{=} -\boldsymbol{\nabla}^2 h$.

The energy can be written as $E = E_\sigma + E_\kappa$, where $E_\sigma = (\sigma/2) \int \mathrm{d}\varphi\,\mathrm{d}\rho\,\rho\,(\boldsymbol{\nabla} h)^2$ and $E_\kappa = (\kappa/2) \int \mathrm{d}\varphi\,\mathrm{d}\rho\,\rho\,(\boldsymbol{\nabla}^2 h)^2$ are both positive and thus finite (compare Eqn. (4.6)). The corresponding membrane shape equation, expressed in terms of K, is given by $\boldsymbol{\nabla}^2 K \stackrel{(4.7, A.72)}{=} \lambda^{-2} K$ which has the general solution [WKH98]

$$
\begin{aligned}
K(\rho, \varphi) &= a_0\,\mathrm{K}_0(\rho/\lambda) + \sum_{n=1}^{\infty} (a_n \cos n\varphi + b_n \sin n\varphi)\,\mathrm{K}_n(\rho/\lambda) \\
&\quad + \sum_{n=1}^{\infty} (c_n \cos n\varphi + d_n \sin n\varphi)\,\mathrm{I}_n(\rho/\lambda) ,
\end{aligned} \tag{5.I}
$$

where K_n and I_n are modified Bessel functions of the first and second kind, respectively (see Technical Point 4.1 on page 85 and Ref. [AS70]). The functions I_n tend to infinity as $\rho \to \infty$ (see (4.III) in Technical Point 4.1). Thus, c_n and d_n must vanish. The asymptotic expansion of K_n for large ρ is also given in (4.III) and shows that the functions $\mathrm{K}_n(\rho)$ decay essentially exponentially for increasing ρ.

━━

lies at a certain radial distance $\rho = R$ away from the surface region to which the particles adhere.

The force $\boldsymbol{F}_\mathrm{out}$ on the outer boundary is a line integral over the appropriate projection of the stress tensor, $-\int_{\partial\Sigma_\mathrm{out}} \mathrm{d}s\,l_a \boldsymbol{f}^a$. Its integrand $l_a \boldsymbol{f}^a$ depends on derivatives and powers of K plus a surface tension term (see Eqn. (2.31) with $K_0 = 0$). For $R \to \infty$ the contribution to the force due to curvature vanishes.[3] The only sur-

---

[3] All curvature terms in the integrand decay essentially exponentially for increasing R as $\sigma \neq 0$

viving contribution at infinity is a horizontal pulling force proportional to σ.

What about $\boldsymbol{M}_{\text{out}}$? A *vertical* torque cannot be compensated by the outer boundary at infinity. The physical explanation for this is that the surface does not resist shear forces. One now might naively expect that for $R \to \infty$ a *horizontal* torque vanishes as well: the membrane becomes asymptotically flat at infinity and the corresponding force has no vertical component. It appears to be self-evident that the line integral $-\int_{\partial\Sigma_{\text{out}}} \mathrm{d}s\, l_a \boldsymbol{m}^a$ vanishes.

A closer inspection of the integral shows, however, that it does not necessarily always vanish: while the vertical force component converges to zero, the length R of the corresponding lever arm goes to infinity simultaneously. Additionally, one integrates along a contour whose length depends linearly on R. These two effects permit a finite value to remain.

Up to terms of $\mathcal{O}(1/R)$ or higher order the torque at $\rho = R$ is given by

$$
\begin{aligned}
\boldsymbol{M}_{\text{out}} &= \sigma \oint_{\partial\Sigma_{\text{out}}} \mathrm{d}s\, (\boldsymbol{X} \times \boldsymbol{l}) = \sigma \int_0^{2\pi} \mathrm{d}\varphi\, R\, [R\boldsymbol{\rho} + h(R,\varphi)\boldsymbol{z}] \times \boldsymbol{l} \\
&= \sigma \int_0^{2\pi} \mathrm{d}\varphi\, R \left\{ -h(R,\varphi)l_\varphi \boldsymbol{\rho} + [h(R,\varphi)l_\rho - Rl_z]\boldsymbol{\varphi} + Rl_\varphi \boldsymbol{z} \right\}, \quad (5.3)
\end{aligned}
$$

where $\boldsymbol{l} = l_\rho \boldsymbol{\rho} + l_\varphi \boldsymbol{\varphi} + l_z \boldsymbol{z}$ in cylindrical coordinates with basis vectors $\{\boldsymbol{\rho}, \boldsymbol{\varphi}, \boldsymbol{z}\}$. The unit vectors $\boldsymbol{\rho}$ and $\boldsymbol{\varphi}$ lie on the reference plane whereas $\boldsymbol{z}$ is normal to it. The moving trihedron of the boundary curve consists of the vectors $\boldsymbol{l}$, $\boldsymbol{t}$, and $\boldsymbol{n}$ which are perpendicular to each other (see also App. A.2). In particular, $\boldsymbol{l}$ may be expanded in terms of the height function h and its derivatives:

$$
\boldsymbol{l} = \frac{\boldsymbol{\rho} - \frac{1}{qR}\left[(\partial_\varphi h)(\partial_\rho h)\right]\big|_{\rho=R} \boldsymbol{\varphi} + \frac{1}{q}(\partial_\rho h)\big|_{\rho=R} \boldsymbol{z}}{\sqrt{1 + \left\{ \frac{1}{qR}\left[(\partial_\varphi h)(\partial_\rho h)\right]\big|_{\rho=R} \right\}^2 + \left\{ \frac{1}{q}(\partial_\rho h)|_{\rho=R} \right\}^2}}, \qquad (5.4)
$$

where $q := 1 + \left[\frac{(\partial_\varphi h)|_{\rho=R}}{R} \right]^2$.

The height function $h(\rho,\varphi)$ satisfies the linearized shape equation $\boldsymbol{\nabla}^2(\boldsymbol{\nabla}^2 h) = \lambda^{-2}\boldsymbol{\nabla}^2 h$ (see Eqn. (4.7)). The solution of this equation consistent with a finite

---

(see Eqn. (5.I) in Technical Point 5.1 where c_n and d_n are zero). Integrating these terms along a contour whose length depends linearly on R yields zero for $R \to \infty$.

value for E_σ is [WKH98][4]

$$
\begin{aligned}
h(\rho, \varphi) \;=\; & C_0 + A_0\,\mathrm{K}_0(\rho/\lambda) \\
& + \sum_{n=1}^{\infty} (A_n \cos n\varphi + B_n \sin n\varphi)\,\mathrm{K}_n(\rho/\lambda) \\
& + \sum_{n=1}^{\infty} (C_n \cos n\varphi + D_n \sin n\varphi)\,\rho^{-n}\,.
\end{aligned}
\tag{5.5}
$$

Inserting Eqn. (5.4) and (5.5) into the equation of the torque (5.3) one obtains

$$
\boldsymbol{M}_{\mathrm{out}} = \sigma \int_0^{2\pi}\!\!\mathrm{d}\varphi\, R\Big[\frac{2(C_1 \cos\varphi + D_1 \sin\varphi)}{R}\boldsymbol{\varphi} + \mathcal{O}\Big(\frac{1}{R^2}\Big)\Big]\,.
\tag{5.6}
$$

The unit vector $\boldsymbol{\varphi}$ still depends on the coordinate φ. To evaluate the integral over φ in (5.6), we rewrite $\boldsymbol{\varphi}$ as $\boldsymbol{\varphi} = -\sin\varphi\,\boldsymbol{x} + \cos\varphi\,\boldsymbol{y}$, where $\boldsymbol{x}$ and $\boldsymbol{y}$ are the Cartesian coordinates parallel to the asymptotic plane and φ is measured from the x axis. We finally obtain for $R \to \infty$:

$$
\boldsymbol{M}_{\mathrm{out}} = 2\pi\sigma(-D_1\boldsymbol{x} + C_1\boldsymbol{y})\,.
\tag{5.7}
$$

Hence, the horizontal torque at infinity is in general not equal to zero even though the vertical force is. Its contributions stem from those terms of the height function (5.5) which are proportional to ρ^{-1} and decay slowest for increasing distance from the particles. Conversely, the existence of an external torque forces the surface to display a very slow $1/\rho$ decay.

In antisymmetric configurations, such as the ones that we will consider in the following, it is this horizontal contribution on the outer boundary that makes it possible to balance an external torque.

Knowing what happens at the outer boundary, we can now derive analytical expressions for the force between two particles in a symmetrical configuration, thereby extending the results of Ref. [Mül04]. Furthermore, the complete set of equations describing force and total torque balance (see Eqns. (5.1)) will be derived.

5.1.3 Two-particle configurations with symmetry

Consider a symmetrical configuration of two identical particles bound to an asymptotically flat surface as sketched schematically in Fig. 5.2. We label by $\{\boldsymbol{x}, \boldsymbol{y}, \boldsymbol{z}\}$ the Cartesian orthonormal basis vectors of three-dimensional space $\mathbb{R}^3$ aligned with the asymptotic plane. The vectors $\boldsymbol{x}$ and $\boldsymbol{y}$ lie parallel to this plane whereas $\boldsymbol{z}$ is its upward pointing unit normal.

---

[4] Note that we now consider a membrane which is not axisymmetric in general. The height function is therefore a series expansion and does not consist of only four terms as in Chap. 4.
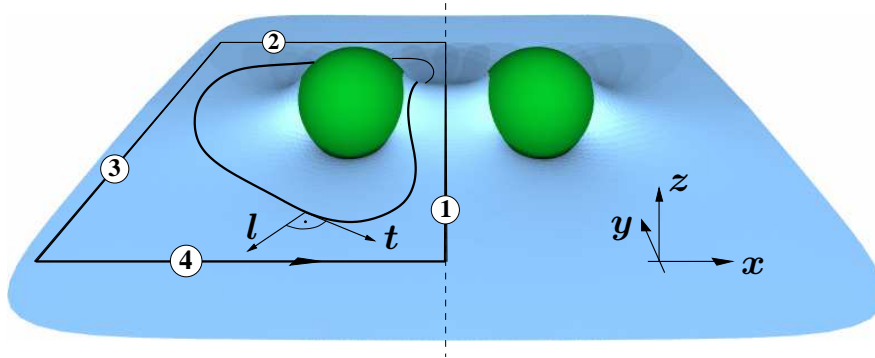
Figure 5.2: Two identical particles bound to an interface. As described in the text, it is possible to deform the contour of integration in order to exploit the available symmetries (see also Ref. [Mül04]).

We will discuss two possible symmetries: mirror symmetry in the (y, z) plane (the symmetric case) or a twofold rotational symmetry with respect to the y axis (the antisymmetric case). The line joining corresponding points on the particles lies parallel to the (x, z) plane. We place the origin of the coordinate system in the middle between the two particles on the intersection line of the asymptotic and symmetry plane (symmetric case) or the line of symmetry (antisymmetric case), respectively.

In the previous section we have seen that external horizontal torques can be balanced by the outer boundary. This is necessary for a stable configuration: we consider configurations where the separation between the particles is fixed by *horizontal* constraining forces. In the antisymmetric case, the two particles do not generally lie on the same line of action. Thus the forces will apply a horizontal torque M_y to the surface which has to be balanced by the outer boundary. In the following, we will consider situations in which this torque is the only external torque *on the entire surface*.

This restriction does not exclude external vertical torques $\boldsymbol{M}^{(i)}$ *on the individual particles*; the symmetry will not be broken as long as all these torques cancel. Think, for instance, of a symmetric configuration consisting of two spheres on a soap film with a saddle-shaped (quadrupolar) line of contact [SDJ00, FG02]. A vertical torque M_z on one of the particles is consistent with the symmetry so long as a torque $-M_z$ is applied to its partner. Such possibilities may, in principle, be accommodated within the formalism. Here, however, we will only consider situations in which the particle orientations have equilibrated and these torques vanish.

Before considering torques more closely, let us first derive analytical expressions for the pair force.
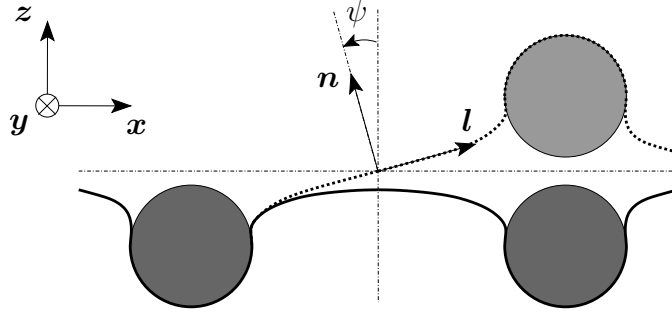
Figure 5.3: Illustration of the geometry of a symmetric (solid line) and an antisymmetric (dotted) two-particle attachment.

5.1.4 Analytical force expressions

As explained in Chap. 2 and Sec. 5.1.1, the force on the left particle can be obtained by integrating the proper projection of the stress tensor along a contour surrounding the particle (see Fig. 5.2). Since the stress tensor is divergence-free on any part of the surface not acted upon externally, the contour of integration can be deformed to exploit the available symmetry: as it is sketched in Fig. 5.2, it can be pulled open to infinity such that the surface is finally flat at branches 2, 3, and 4 and the stress tensor thus very simple. The contribution from branch 2 will cancel that from 4; the only difficult term stems from branch 1. The force on the particle is thus given by

$$\boldsymbol{F} = -\left(\int_1 + \int_3\right) \mathrm{d}s \, l_a \boldsymbol{f}^a \; . \tag{5.8}$$

Helfrich membrane

For the up-down symmetric Helfrich membrane, the force can be obtained by inserting the corresponding stress tensor (2.30) into Eqn. (5.8) and setting K_0 to zero. The resulting expression

$$\boldsymbol{F} = -\int_1 \mathrm{d}s \, \left\{ \frac{\kappa}{2}(K_\perp^2 - K_\parallel^2 - \sigma)\boldsymbol{l} + \kappa K_{\perp\parallel} K \, \boldsymbol{t} - \kappa(\nabla_\perp K)\boldsymbol{n} \right\} + \sigma \int_3 \mathrm{d}s \, \boldsymbol{l} \; . \tag{5.9}$$

can be simplified further due to the symmetry: both mirror and twofold axial symmetry of branch 1 imply that the term proportional to $\boldsymbol{t}$ vanishes. In the first case this follows from the fact that branch 1 becomes a line of curvature, *i.e.*, a curve that follows a principal direction at every point (see page 172 in App. A.1); hence, the curvature tensor is diagonal in $(\boldsymbol{l}, \boldsymbol{t})$ coordinates and thus $K_{\perp\parallel}$ vanishes. In the second case twofold axial symmetry forces both $K_\parallel$ as well as $K_\perp$ to be

zero, since branch 1 becomes a straight line and the profile is antisymmetric. In consequence, $K = K_\perp + K_\parallel = 0$. Thus, the force on that branch can be written as:

$$\boldsymbol{F}_1 = -\int_1 \mathrm{d}s \left\{ \frac{\kappa}{2}(K_\perp^2 - K_\parallel^2 - \sigma)\boldsymbol{l} - \kappa(\nabla_\perp K)\boldsymbol{n} \right\} . \tag{5.10}$$

This equation was one of the central results of Ref. [Mül04]. As was shown there, it can be simplified further if one looks separately at the two different possible symmetries (see Fig. 5.3).

Symmetric case   The tangent and normal vectors on branch 1 lie in the (y, z) plane, hence $\boldsymbol{l} = \boldsymbol{x}$. The derivative of K in the direction of $\boldsymbol{l}$ along branch 1, $\nabla_\perp K$, is zero due to mirror symmetry. On branch 3, the surface is flat and thus the stress tensor is equal to $-\sigma \boldsymbol{e}_a$. With this information we can calculate the total force $\boldsymbol{F}_1 + \boldsymbol{F}_3 = F_{\mathrm{sym}}\boldsymbol{x}$ on the particle:

$$F_{\mathrm{sym}} = \sigma \Delta L - \frac{1}{2}\kappa \int_1 \mathrm{d}s \left(K_\perp^2 - K_\parallel^2 \right) , \tag{5.11}$$

where ΔL is the excess length of branch 1 compared to branch 3.

Thus, the force can be attractive or repulsive, depending on the values of the perpendicular and parallel curvatures at the mid-line. If we restrict ourselves to the case of two parallel cylinders adhering to the same side of the membrane, however, the overall sign becomes obvious as long as the particles are long enough such that end effects can be neglected: the contribution $K_\parallel^2$ then vanishes because branch 1 becomes a line. For the same reason $\Delta L = 0$. This leads to the formula

$$F_{\mathrm{sym,cyl}}/L = -\frac{1}{2}\kappa K_\perp^2 , \tag{5.12}$$

where L is the length of one cylinder. Thus, the two cylinders repel each other.

The derived force expressions can very naturally be generalized to Hamiltonians of higher order in curvature. For example, sticking with an up-down symmetric fluid membrane, the next curvature order would be quartic (see page 63). If added to Hamiltonian (5.2), additional contributions to the force arise which are given in Technical Point 5.2 for the case of the two cylinders.

Antisymmetric case   Here branch 1 is a twofold symmetry axis and, as we have seen above, $K_\parallel = K_\perp = 0$. We fix the horizontal separation of the particles and allow other degrees of freedom, such as height or tilt, to equilibrate (see Sec. 5.1.3).

▬▬▬ **Technical Point 5.2:** $F_{sym,cyl}/L$ *including the quartic Hamiltonian (1)* ▬

The quartic Hamiltonian density (3.31) (see page 63) gives rise to three more scalars which are quartic in the curvature: K^4, $K^2\mathcal{R}$, and $\mathcal{R}^2$. For cylinders, $\mathcal{R} = 0$, which just leaves $\mathcal{H}'_4 = (1/4)\kappa_4 K^4$ as the only nonvanishing term. Using the general expression of the stress tensor for the scalar K^n as calculated in the Appendix (see Eqn. (B.12)) and going through the calculation from Sec. 5.1.4 we find $F_{\text{sym,cyl}}/L = -\frac{3}{4}\kappa_4 K_\perp^4$ for the two parallel cylinders in symmetric configuration. This term increases the repulsion between the cylinders found on the linear elastic level (see Eqn. (5.12)), *provided* $\kappa_4 > 0$, *i. e.*, provided the additional term further stiffens the membrane.

Assuming that $\mathcal{H}'_4$ perturbs the usual bending Hamiltonian $\frac{1}{2}\kappa K^2$, we can use the two moduli to define a characteristic length scale $\ell_4 := \sqrt{|\kappa_4|/\kappa}$. The overall force up to quartic order in the curvature can then be written as

$$F_{\text{sym,cyl}}/L = -\frac{1}{2}\kappa K_\perp^2 \left[1 \pm \frac{3}{2}(\ell_4 K_\perp)^2\right], \qquad (5.\text{II})$$

where the positive sign corresponds to stiffening. Notice that the correction term becomes only noticeable once the curvature radius of the membrane is no longer large compared to the length scale ℓ_4. It appears natural that ℓ_4 is related to the membrane *thickness*, which for phospholipid bilayers is about $5\,\text{nm}$ (see Sec. 1.1.1). Assuming a (quadratic order) bending stiffness of $\kappa \simeq 20\,k_{\text{B}}T$, we thus expect values for the modulus κ_4 on the order of $10^3\,k_{\text{B}}T\,\text{nm}^2$.

The complete Hamiltonian density (3.31) is of order LENGTH^{-4} and contains also the term $\mathcal{H}_\nabla = \frac{1}{2}\kappa_\nabla(\nabla_a K)(\nabla^a K)$, which depends on *derivatives* of the surface curvature. Using the expression for the stress tensor derived in the Appendix (see Eqn. (B.25)) and again going through the calculation in Sec. 5.1.4, we find

$$F_{\text{sym,cyl}}^\nabla/L = \frac{1}{4}\kappa_\nabla \nabla_\perp^2 K_\perp^2 = \frac{1}{4}\kappa_\nabla \frac{\text{d}^2}{\text{d}s^2} K_\perp^2 \qquad (5.\text{III})$$

as the additional contribution to the force due to $\mathcal{H}_\nabla$. It depends on very subtle details of the membrane shape: the curvature is (roughly) a second derivative of the membrane position, and this we need to square and differentiate two more times. Unfortunately, the sign of the force contribution is not obvious here, as the second derivative of $K_\perp^2$ with respect to s may be either positive or negative. If the quartic Hamiltonian density is treated as a perturbation, however, one can say a bit more about the sign as we will see in Technical Point 5.7 on page 143.

Finally, we can again consider the characteristic length scale here, $\ell_\nabla = \sqrt{|\kappa_\nabla|/\kappa}$ (compare page 70). The importance of a perturbation $\mathcal{H}_\nabla$ of the usual bending Hamiltonian depends on whether or not the curvature *changes* significantly on length scales comparable to ℓ_∇.

The force on the particle is thus parallel to $\boldsymbol{x}$, $\boldsymbol{F}_{\text{antisym}} = F_{\text{antisym}}\boldsymbol{x}$, and given by

$$
\begin{aligned}
F_{\text{antisym}} &= \kappa \int_1 \mathrm{d}s \left[\lambda^{-2}(\boldsymbol{x} \cdot \boldsymbol{l} - 1) + (\nabla_\perp K)(\boldsymbol{x} \cdot \boldsymbol{n}) \right] \\
&= \kappa \int_1 \mathrm{d}s \left[\lambda^{-2}(\cos \psi(s) - 1) - \sin \psi(s)(\nabla_\perp K) \right] ,
\end{aligned}
\tag{5.13}
$$

where ψ is the angle between $\boldsymbol{x}$ and $\boldsymbol{l}$ (or $\boldsymbol{z}$ and $\boldsymbol{n}$, respectively, see also Fig. 5.3 and Eqns. (A.74)). Again, the sign of the force is not obvious. For the case of two parallel cylinders adhering to opposite sides of the interface, however, $\nabla_\perp K_\parallel$ vanishes at the midpoint. The angle $\psi = \psi_{\text{mid}}$ is constant along branch 1 and Eqn. (5.13) reduces to (see [Mül04])

$$
F_{\text{antisym,cyl}}/L = \pm\sqrt{\sigma^2 + (\kappa\nabla_\perp K_\perp)^2} - \sigma ,
\tag{5.14}
$$

where the positive sign is valid for $0° < \psi_{\text{mid}} < 90°$ and the negative sign for $90° < \psi_{\text{mid}} < 180°$. In Sec. 5.2 we will see that the latter case is not relevant if the separation between the centers of the two cylinders is larger than their diameter. We will therefore focus on the case $0° < \psi_{\text{mid}} < 90°$ in the following, for which the cylinders attract.

In Sec. 5.2, the two cylinder problem will be solved in the nonlinear regime for both symmetries. Before, we will take a short look at how internal degrees of freedom, such as a lipid tilt, and bulk stresses can be incorporated into the formalism.

Tilt degree of freedom

In Sec. 1.2.2 we introduced a tangential vector field m^a on the membrane, thereby modeling the degrees of freedom associated with the tilt of the lipids. The minimal intrinsic Hamiltonian density Eqn. (1.6) already gives rise to a quite formidable additional metric stress, Eqn. (2.39). Yet, for sufficiently symmetric situations the expression for the force simplifies quite dramatically as we will now see.

Let us consider two conical membrane inclusions which are inserted with the same orientation into a membrane at some fixed distance apart. Each inclusion will, due to its up-down-asymmetry, act as a *local source of tilt*. Provided the membrane is not in a spontaneously tilted phase, this tilt will decay with some characteristic decay length as described in Sec. 2.2.3 (in particular in Technical Point 2.4 on page 40). A typical situation may then look like the one depicted in Fig. 5.4. What can we say about the forces between the two inclusions mediated by the tilt field?

Following the same reasoning as for the geometrical forces discussed above, and assuming that the tilt vanishes on branch 3 so that this contribution vanishes, we find using Eqn. (2.40a)

$$
\boldsymbol{F}_{\text{m}} = - \int_1 \mathrm{d}s \, l_a T_{\text{m}}^{ab} \boldsymbol{e}_b ,
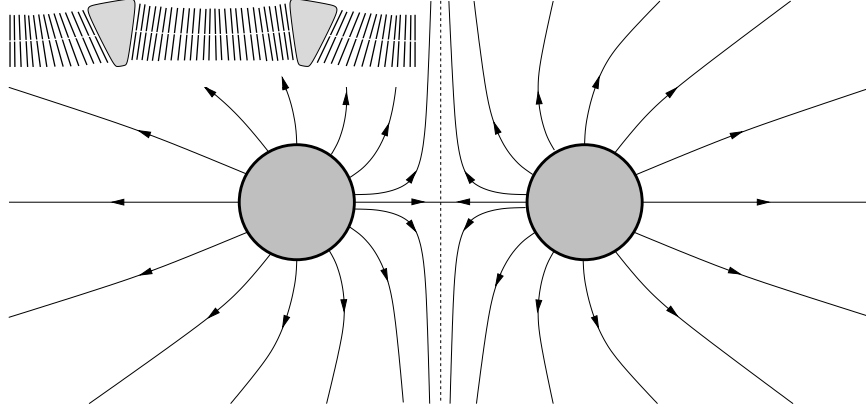\tag{5.15}
$$

Figure 5.4: Two conical inclusions act as sources of a local membrane tilt (inset). The tilt-field-lines are illustrated qualitatively in this symmetric situation.

where T_{m}^{ab} is given by Eqn. (2.39). To simplify this expression, we examine the symmetry. For this it is very helpful to again expand vectors and tensors on branch 1 in local $(\boldsymbol{l}, \boldsymbol{t})$-coordinates, just as we did in the geometrical case above. Mirror symmetry then means that $m_{\parallel} = t_a m^a$ is an *even* function along the direction perpendicular to branch 1, whereas $m_{\perp} = l_a m^a$ is an odd function and thus zero everywhere on that branch. It follows that both $\nabla_{\perp} m_{\parallel}$ and $\nabla_{\parallel} m_{\perp}$ vanish everywhere on branch 1. Thus we have

$$M \overset{1}{=} (\nabla_{\perp} m_{\perp}) + (\nabla_{\parallel} m_{\parallel}) \,, \tag{5.16a}$$

$$M_{ab} M^{ab} \overset{1}{=} (\nabla_{\perp} m_{\perp})^2 + (\nabla_{\parallel} m_{\parallel})^2 \,, \tag{5.16b}$$

$$\varepsilon^{ab} \nabla_a m_b \overset{1}{=} \nabla_{\perp} m_{\parallel} - \nabla_{\parallel} m_{\perp} = 0 \,, \tag{5.16c}$$

where the "1" above the equation signs reminds us that this only holds on branch 1. We next need to look at the contractions of the individual terms in the metric material stress with $l_a \boldsymbol{e}_b$. We find:

$$l_a (\nabla_c m^a)(\nabla^c m^b) \boldsymbol{e}_b \overset{1}{=} (\nabla_{\perp} m_{\perp})^2 \boldsymbol{l} \,, \tag{5.17a}$$

$$l_a (\nabla^a m_c)(\nabla^b m^c) \boldsymbol{e}_b \overset{1}{=} (\nabla_{\perp} m_{\perp})^2 \boldsymbol{l} \,, \tag{5.17b}$$

$$l_a M M^{ab} \boldsymbol{e}_b \overset{1}{=} M(\nabla_{\perp} m_{\perp}) \boldsymbol{l} \,. \tag{5.17c}$$

The two terms involving the derivatives $m^c \nabla_c$ can be rewritten by extracting a complete derivative:

$$l_a m^c (\nabla_c M) g^{ab} \boldsymbol{e}_b \overset{1}{=} \boldsymbol{l} \, m_{\parallel} \nabla_{\parallel} M \overset{1}{=} \boldsymbol{l} \big[\nabla_{\parallel}(m_{\parallel} M) - (\nabla_{\parallel} m_{\parallel}) M \big] \,. \tag{5.18a}$$

118

The total derivative will yield a boundary term once integrated along branch 1, and since we assume that we are not in a spontaneously tilted phase, $|m^a|$ will go to zero at infinity and thus the boundary term vanishes. With the same argument we find

$$l_a m^c (\nabla_c M^{ab}) \boldsymbol{e}_b \overset{1}{=} \boldsymbol{l} \left[\nabla_\| (m_\| (\nabla_\perp m_\perp)) - (\nabla_\| m_\|)(\nabla_\perp m_\perp) \right] . \tag{5.18b}$$

Again, the total derivative integrates to zero. Finally, the potential terms simplify to

$$l_a V(m^2) g^{ab} \boldsymbol{e}_b \overset{1}{=} V(m^2) \boldsymbol{l} , \tag{5.19a}$$

$$l_a V'(m^2) m^a m^b \boldsymbol{e}_b \overset{1}{=} 0 . \tag{5.19b}$$

Collecting all results, we arrive at the remarkably simple exact force expression $\boldsymbol{F}_\mathrm{m} = F_\mathrm{m} \boldsymbol{x}$, with

$$F_\mathrm{m} = -\left(\tfrac{1}{2}\lambda_\mathrm{m} + \mu_\mathrm{m}\right) \int_1 \mathrm{d}s \left[(\nabla_\perp m_\perp)^2 - (\nabla_\| m_\|)^2 \right] + \int_1 \mathrm{d}s \, V(m^2) . \tag{5.20}$$

There are two contributions to the force, one stemming from *gradients* of the tilt, the other from the *tilt potential V*. Remarkably, the tilt gradient contribution from each of the first two quadratic invariants has the same structural form, thus the Lamé coefficients λ_m and μ_m occur only as a combination in front of the integral. The modulus ν_m has dropped out since the corresponding stress vanishes on the mid-curve (see Eqn. (5.16c)).

The structural similarity of Eqn. (5.20) to curvature-mediated forces – Eqn. (5.11) – is very striking. Since $\tfrac{1}{2}\lambda_\mathrm{m} + \mu_\mathrm{m} > 0$ (see footnote 13 on page 20), the first integral states that perpendicular gradients of the perpendicular tilt lead to repulsion, while parallel gradients of the parallel tilt imply attractions – the same "$\perp^2 - \|^2$" motif as found in Eqn. (5.11). Since in the untilted phase $V(m^2) \geq 0$, the last term of Eqn. (5.20) shows that the integrated excess potential drives attraction, just as the excess length (something like an integrated "surface tilt") drives attraction in Eqn. (5.11). Unfortunately, the overall sign of the force is not obvious. Looking at the field lines in Fig. 5.4, the visual analogy with electrostatic interactions between like charged particles would suggest a repulsion, but the above analysis advises caution (in Technical Point 5.3 it is shown that this naive guess is at least borne out on the linearized level). Moreover, we should not forget that tilt *does* couple to geometry (namely, via the covariant derivative) and that the membrane need not be flat; hence, the contribution due to tension and bending given by Eqn. (5.11) must be added, the sign of which is equally unclear.

So far we have neglected stresses from the bulk. If the space surrounding the membrane provides additional *continuous* sources of stress, $\boldsymbol{f}^a$ is no longer divergence-free (see Sec. 2.3). It may appear at first glance that the presented approach fails. This is, however, not true in all cases as we will see in the next example where a constant pressure difference will be discussed.

━━━ **Technical Point 5.3:** *Tilt-mediated force between two inclusions* ━━━

Obtaining the exact tilt field for two inclusions is very difficult, since satisfying the boundary conditions is troublesome. However, if we use the Nicolson approximation [Nic49] and assume that the total tilt distribution is given by the superposition of two solutions of the kind (2.III), things become manageable. The tilt-mediated force between two symmetric inclusions is then obtained by inserting the appropriate values and derivatives of the tilt field $\boldsymbol{m}(x, y)$ on the mid-line into Eqn. (5.20). After some straightforward calculations we get the force[§]

$$
\begin{aligned}
F_{\mathrm{m}} &= 4t\ell_{\mathrm{m}}m_0^{*2} \int_{d^*}^{\infty} \mathrm{d}\xi \, \frac{1}{\xi\sqrt{\xi^2 - d^{*2}}} \Big[(\xi^2 - 2d^{*2}) \, \mathrm{K}_0(\xi) \, \mathrm{K}_2(\xi) + (\xi^2 - d^{*2}) \, \mathrm{K}_1^2(\xi) \Big] \\
&= -2\pi t\ell_{\mathrm{m}}m_0^{*2} \, \mathrm{K}_1(d/\ell_{\mathrm{m}}) \, .
\end{aligned} \tag{5.IV}
$$

where $m_0^* = m_0/\, \mathrm{K}_1(r_0/\ell_{\mathrm{m}})$, $d^* = d/2\ell_{\mathrm{m}}$, and d is the separation between the inclusions. As we see, the force is *repulsive* and decays essentially exponentially with distance over the decay length $\ell_{\mathrm{m}} = \sqrt{(\lambda_{\mathrm{m}} + 2\mu_{\mathrm{m}})/t}$ (see Eqn. (2.45)). Integrating it, we get the repulsive interaction potential

$$
U_{\mathrm{m}}(d) = 2\pi t\ell_{\mathrm{m}}^2 m_0^{*2} \, \mathrm{K}_0(d/\ell_{\mathrm{m}}) \, .
$$

Let us try to make a very rough estimate of how big such a force might be. For this we need to obtain some plausible values for the numbers entering into Eqn. (5.IV). For t we use the equipartition theorem and argue that $\frac{1}{2}t\langle m^2\rangle a = \frac{1}{2}k_{\mathrm{B}}T$, where a is the area per lipid and $k_{\mathrm{B}}T$ the thermal energy. Assuming that the root-mean-square fluctuations of m are $10°$ and using the typical value $a \simeq 0.75\,\mathrm{nm}^2$, we get $t \simeq 40\,k_{\mathrm{B}}T/\mathrm{nm}^2$. Assuming further a rather conservative tilt decay length of the order of the bilayer thickness, *i.e.* $\ell_{\mathrm{m}} \simeq 5\,\mathrm{nm}$, that the inclusion has a radius of $r_0 \simeq 3\,\mathrm{nm}$ and imposes there a local tilt of $m \simeq 0.2$, we find that two inclusions at a distance of $10\,\mathrm{nm}$ feel a significant force of about $17\,\mathrm{pN}$. At a distance of $d \approx 22\,\mathrm{nm}$ their mutual potential energy is $1\,k_{\mathrm{B}}T$ compared to the separated state. Notice that this is much larger than the Debye length in physiological solution, which is typically only $1\,\mathrm{nm}$. Hence, tilt-mediated forces can compete with more conventional forces, such as (screened) electrostatic interactions. It should be kept in mind, however, that if we permit the membrane to bend, some of the tilt strain can be relaxed, thereby lowering the energy.

[§] Obtaining the integral is straightforward, solving it is not. The large-d-asymptotics of the integral and the right hand side of Eqn. (5.IV) are the same. However, Eqn. (5.IV) indeed holds for *all* distances d, a fact that unfortunately could only be verified numerically.
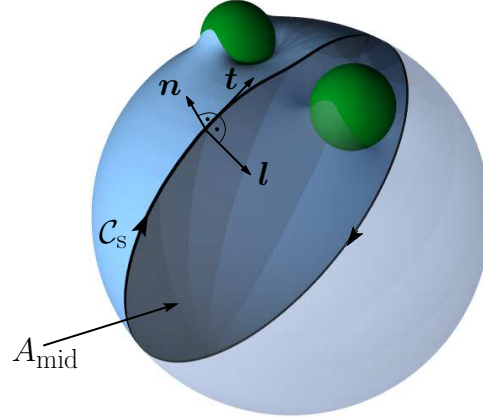
Figure 5.5: Deformation of a closed surface due to two particles bound to it.

Global pressure difference

If the pressure is different between its two sides, the membrane will not be asymptotically flat but will close and form a vesicle (see Sec. 1.2.3). Consider as an example a closed surface Σ with two particles bound to it in a symmetric configuration (see Fig. 5.5). As before the interface-mediated force on one of the particles is given by the negative value of the external force $\boldsymbol{F}_{\text{ext}}$ acting on the patch of surface the particle adheres to. In Sec. 2.3.1 we have seen that $\boldsymbol{F}_{\text{ext}}$ can be written in terms of an effective surface stress tensor $\check{\boldsymbol{f}}^{a}$. This tensor combines geometric and bulk stresses and *is* divergence-free. It allows us to adapt our original idea and choose the planar mid-line $\mathcal{C}_{\text{s}}$ as contour of integration (see again Fig. 5.5). Following Eqn. (2.54), the force $\boldsymbol{F}_P$ on the rear particle is thus given by

$$
\begin{aligned}
\boldsymbol{F}_P &= -\oint_{\mathcal{C}_{\text{s}}} \mathrm{d}s \, l_a \check{\boldsymbol{f}}^{a} \overset{(2.53)}{=} -\oint_{\mathcal{C}_{\text{s}}} \mathrm{d}s \left\{ l_a \boldsymbol{f}^{a} - \frac{1}{2} P \left[\underbrace{(\boldsymbol{X} \cdot \boldsymbol{l})}_{=\text{const}} \boldsymbol{n} - (\boldsymbol{X} \cdot \boldsymbol{n}) \boldsymbol{l} \right] \right\} \\
&= -\oint_{\mathcal{C}_{\text{s}}} \mathrm{d}s \, l_a \boldsymbol{f}^{a} \;-\; P A_{\text{mid}} \, \boldsymbol{x} \,,
\end{aligned}
\tag{5.21}
$$

where $\boldsymbol{l} \equiv \boldsymbol{x}$ is constant along the contour. In Eqn. (5.21) we made use of the fact that the integral over the normal vector $\boldsymbol{n}$ yields zero because $\mathcal{C}_{\text{s}}$ is closed. Furthermore, we defined

$$
A_{\text{mid}} = \frac{1}{2} \oint_{\mathcal{C}_{\text{s}}} \mathrm{d}s \, \boldsymbol{X} \cdot \boldsymbol{n}
\tag{5.22}
$$

as the planar area enclosed by the contour $\mathcal{C}_{\text{s}}$.

Eqn. (5.21) is a covariant and exact expression for the interface-mediated force between two particles in a symmetric configuration. Compared to the case of a flat surface (where $P = 0$) an additional term proportional to the mid-plane area

enters the scene. The whole equation can be understood as a force balance on the cross section of the closed surface Σ [dGBWQ03] where in equilibrium the surface forces and the integrated pressure have to cancel the external force acting on the surface patch.[5]

We would get the same result for the force if we had not used the effective stress tensor but integrated $(\nabla_a \boldsymbol{f}^a - \mathcal{E}\,\boldsymbol{n})$ directly (where $\mathcal{E} = P$ in this case, see Eqns. (2.12) and (2.51)). Whereas this seems to be a bit more complicated here, it is sometimes the only way to obtain the force one is searching for as we have seen in Sec. 2.3.2 for the case of gravity.

Let us specialize Eqn. (5.21) to an up-down symmetric fluid bilayer membrane, characterized by the Hamiltonian density (5.2). One obtains $\boldsymbol{F}_P = F_P\,\boldsymbol{x}$ with

$$F_P = - \oint_{\mathcal{C}_{\mathrm{s}}} \mathrm{d}s\, \left[\frac{1}{2}\kappa(K_\perp^2 - K_\parallel^2) - \sigma \right] - PA_{\mathrm{mid}} \;, \qquad (5.23)$$

Setting κ to zero corresponds to the case of a soap film. The result then simplifies further to

$$F_P = (\sigma L_{\mathrm{c}} - PA_{\mathrm{mid}}) = \sigma\,(L_{\mathrm{c}} - KA_{\mathrm{mid}}) \;, \qquad (5.24)$$

where $L_{\mathrm{c}} = \oint_{\mathcal{C}_{\mathrm{s}}}\mathrm{d}s$ is the length of the contour $\mathcal{C}_{\mathrm{s}}$. In the second step the Young-Laplace law (2.52) was inserted.

The solution to the isoperimetric problem helps to find an inequality between L_{c} and A_{mid}: if one searches for the closed plane curve which has the smallest length when enclosing a given area, one arrives at the circle. Thus, $A_{\mathrm{mid}} \leq \frac{L_{\mathrm{c}}^2}{4\pi}$ and we get a lower bound for the force:

$$F_P \geq \sigma\,L_{\mathrm{c}}\Big(1 - \frac{KL_{\mathrm{c}}}{4\pi}\Big) \;. \qquad (5.25)$$

If the particles deform the closed surface only slightly, one may think of expanding the contour $\mathcal{C}_{\mathrm{s}}$ around a circle to get an approximate expression for the force. It is, however, not clear how the constraint on the volume can be incorporated since this requires knowledge of the whole three-dimensional shape of the surface. To implement this constraint and obtain more information about the force, numerical calculations in the spirit of Ref. [DFG98] may be helpful but will not be done here. Instead let us check how much more can be said about interface-mediated interactions using the analytical tools developed in Chap. 2.

Up to this point we have only analyzed forces. However, interface-mediated interactions may also induce torques on the particles. In the following we will include

---

[5] One can perform a simple consistency check of Eqn. (5.21) by imagining that the surface was a spherical soap bubble of radius a with no particles adhering to it (compare Technical Point 2.5 on page 44). In this case $\boldsymbol{f}^a \overset{(2.24)}{=} -\sigma\boldsymbol{e}^a$. The external force is equal to zero. Thus, $0 = (2\pi a\,\sigma - P\pi a^2)\,\boldsymbol{x}$ which indeed yields expression (2.IV) for the Laplace pressure of a spherical bubble.

these in our considerations and focus again on two-particle configurations on an asymptotically flat Helfrich membrane with symmetry and no bulk stresses.

5.1.5 Equilibrium conditions from torque balance

Analogous to the force, the torque on the left particle in Fig. 5.2 on page 113 can be obtained by integrating the appropriate projection of the torque tensor along a contour surrounding the particle

$$\boldsymbol{M} = - \oint_{1-4} \mathrm{d}s \, l_a \boldsymbol{m}^a \; . \tag{5.26}$$

We choose the same contour of integration as before (see again Fig. 5.2)
Using the balance of torques, Eqn. (5.1), together with the assumptions made about the external torques in Sec. 5.1.3 we conclude that

$$\boldsymbol{M} = \boldsymbol{X}_{\mathrm{p}} \times \boldsymbol{F} = M\boldsymbol{y} \; , \tag{5.27}$$

where $\boldsymbol{F} = F\boldsymbol{x}$ is, as before, the force on the left particle and $\boldsymbol{X}_{\mathrm{p}}$ is the position vector pointing from the fulcrum (*i. e.* the point about which the torque is acting) to the point where the force $\boldsymbol{F}$ is applied. We evaluate the torque about the origin in the Euclidean coordinate system $\{\boldsymbol{x}, \boldsymbol{y}, \boldsymbol{z}\}$. The torque on the outer boundary enclosing the particles is then given by $\boldsymbol{M}_{\mathrm{out}} = 2\boldsymbol{M}$ in the antisymmetric case; it vanishes in the symmetric case.

The condition (5.27), together with the explicit expression for torque $\boldsymbol{M}$ and force $\boldsymbol{F}$ derived previously, permit one to establish nonlinear relationships between geometrical quantities such as particle penetration or height differences for a given model.

General expressions for two finite-sized particles

For a fluid membrane, the torque $\boldsymbol{M}$ on a particle can be obtained by inserting the corresponding torque tensor (2.36) into Eqn. (5.26) and setting K_0 to zero. As it evidently has to cancel the external torque on the particle, it can also be read off directly from the right hand side of Eqn. (2.37) with the replacement of $\partial\Sigma_1$ by the contour $1 - 4$ and an additional minus sign at the front.

The resulting expression can be simplified further if one takes into account that the surface is asymptotically flat and possesses a certain symmetry. For finite-sized particles it is shown in Sec. 5.1.2 that the curvature terms of the torque tensor do not contribute to the torque on the membrane at infinity; the only term in the expression for the torque due to bending stems from branch 1. Furthermore, the term proportional to $(\boldsymbol{X} \times \boldsymbol{t})$ vanishes for the two symmetries because $K_{\perp\parallel} K = 0$

on branch 1 (see Sec. 5.1.4). The torque $\boldsymbol{M}$ on the left particle is thus given by

$$
\begin{aligned}
\boldsymbol{M} &= \sigma \oint_{1-4} \mathrm{d}s \, (\boldsymbol{X} \times \boldsymbol{l}) - \kappa \int_1 \mathrm{d}s \left[\frac{1}{2}(K_\perp^2 - K_\parallel^2)(\boldsymbol{X} \times \boldsymbol{l}) - (\nabla_\perp K)(\boldsymbol{X} \times \boldsymbol{n}) - K\boldsymbol{t} \right] \\
&= \sigma \oint_{2-4} \mathrm{d}s \, (\boldsymbol{X} \times \boldsymbol{l}) - \kappa \int_1 \mathrm{d}s \left[\boldsymbol{X} \times \boldsymbol{f} - K\boldsymbol{t} \right] ,
\end{aligned}
\tag{5.28}
$$

where $\boldsymbol{f} = [\frac{1}{2}(K_\perp^2 - K_\parallel^2) - \lambda^{-2}]\,\boldsymbol{l} - (\nabla_\perp K)\,\boldsymbol{n}$.

The term due to surface tension along branches 2–4 does not vanish necessarily. As we have seen in Sec. 5.1.2 a non-vanishing horizontal torque can remain at infinity if the surface displays a very slow $1/|\boldsymbol{X}|$ decay, *i.e.*, if either of the corresponding constants C_1 and D_1 in the height function (5.5) does not vanish. A closer inspection of the line integral along branches 2–4 reveals that the term with coefficient C_1 contributes to a torque about the y axis whereas the one including D_1 does so about $\boldsymbol{x}$ (*cf.* calculation in Sec. 5.1.2 for $\boldsymbol{M}_\mathrm{out}$). The latter coefficient has to be equal to zero as we require the x component of the torque $\boldsymbol{M}_\mathrm{out}$ at the complete outer boundary to vanish (see Sec. 5.1.3).

Bearing these considerations in mind, one obtains the following important relations by combining Eqns. (5.27) and (5.28).

$$
\boldsymbol{x} \cdot \boldsymbol{M} = -\kappa \int_1 \mathrm{d}s \left[\boldsymbol{X} \cdot (\boldsymbol{f} \times \boldsymbol{x}) \right] = 0 ,
\tag{5.29}
$$

$$
\boldsymbol{y} \cdot \boldsymbol{M} = \sigma \oint_{2-4} \mathrm{d}s \, \boldsymbol{X} \cdot (\boldsymbol{l} \times \boldsymbol{y})
\tag{5.30}
$$

$$
\qquad\qquad - \kappa \int_1 \mathrm{d}s \left[\boldsymbol{X} \cdot (\boldsymbol{f} \times \boldsymbol{y}) - K(\boldsymbol{y} \cdot \boldsymbol{t}) \right] = F(\boldsymbol{z} \cdot \boldsymbol{X}_\mathrm{p}) ,
$$

$$
\boldsymbol{z} \cdot \boldsymbol{M} = -\kappa \int_1 \mathrm{d}s \left[\boldsymbol{X} \cdot (\boldsymbol{f} \times \boldsymbol{z}) - K(\boldsymbol{z} \cdot \boldsymbol{t}) \right] = 0 ,
\tag{5.31}
$$

where $F = -\kappa \int_1 \mathrm{d}s \, (\boldsymbol{f} \cdot \boldsymbol{x}) - \sigma \int_3 \mathrm{d}s$ (see Eqn. (5.9)). These expressions place strong constraints on the geometry of the membrane. They can be simplified further for the two different symmetries.

Symmetric case In the symmetric case, the derivative of K in the direction of $\boldsymbol{l}$ along branch 1, $\nabla_\perp K$, is zero. The curvature tensor is diagonal in $(\boldsymbol{l}, \boldsymbol{t})$ coordinates and thus $K_{\perp\parallel}$ vanishes. This implies that $K_\parallel \boldsymbol{t}$ is equal to $\nabla_\parallel \boldsymbol{n}$ [*cf.* Eqn. (A.57b)], and $\int_1 \mathrm{d}s \, K_\parallel \boldsymbol{t} = \boldsymbol{n}|_{y=\infty} - \boldsymbol{n}|_{y=-\infty} = 0$.

Furthermore, branches 2–4 do not provide a torque: the term in the height function (5.5) that could give rise to a torque about the y axis is forbidden by the symmetry, *i.e.* its constant coefficient $C_1 = 0$. Thus,

$$
\sigma \oint_{2-4} \mathrm{d}s \, (\boldsymbol{X} \times \boldsymbol{l}) = 0 ,
\tag{5.32}
$$

and Eqn (5.28) simplifies to the expression

$$\boldsymbol{M}_{\text{sym}} = -\kappa \int_1 \mathrm{d}s \left[\left(\frac{1}{2}(K_\perp^2 - K_\parallel^2) - \lambda^{-2} \right) (\boldsymbol{X} \times \boldsymbol{x}) - K_\perp \boldsymbol{t} \right] , \tag{5.33}$$

which depends only on geometrical properties of the membrane at the symmetry plane. The force acting at each point along the mid-line is horizontal and Eqn. (5.29) is fulfilled identically. The two relations (5.30) and (5.31) turn into

$$-\kappa \int_1 \mathrm{d}s \left[f_{\text{sym}}(\boldsymbol{z} \cdot \boldsymbol{X}) - K_\perp (\boldsymbol{y} \cdot \boldsymbol{t}) \right] = F_{\text{sym}}(\boldsymbol{z} \cdot \boldsymbol{X}_{\text{p}}) , \tag{5.34}$$

$$\kappa \int_1 \mathrm{d}s \left[f_{\text{sym}}(\boldsymbol{y} \cdot \boldsymbol{X}) + K_\perp (\boldsymbol{z} \cdot \boldsymbol{t}) \right] = 0 , \tag{5.35}$$

where F_{sym} is given by Eqn. (5.11) and $f_{\text{sym}} = [\frac{1}{2}(K_\perp^2 - K_\parallel^2) - \lambda^{-2}]$.

Antisymmetric case In the antisymmetric case branch 1 is a straight line and $K_\perp = K_\parallel = 0$. The torque is now given by

$$\boldsymbol{M}_{\text{antisym}} = \sigma \oint_{1-4} \mathrm{d}s \, (\boldsymbol{X} \times \boldsymbol{l}) + \kappa \int_1 \mathrm{d}s \left[(\nabla_\perp K)(\boldsymbol{X} \times \boldsymbol{n}) \right] . \tag{5.36}$$

In contrast to the symmetric case, the torque does not possess an internal part because the curvature K vanishes everywhere along the contour. The force acting at each point along the mid-line is perpendicular to the y axis. As the origin lies on this line the only components of the torque transmitted through branch 1 which are potentially non-vanishing are the x and the z component. We have chosen, however, to set these components to zero (see Sec. 5.1.3 and Eqns. (5.29,5.31)). Thus, the contribution from branch 1 vanishes

$$\sigma \int_1 \mathrm{d}s \, (\boldsymbol{X} \times \boldsymbol{l}) + \kappa \int_1 \mathrm{d}s \left[(\nabla_\perp K)(\boldsymbol{X} \times \boldsymbol{n}) \right] = 0 , \tag{5.37}$$

and the torque can be written as an integral along the boundaries 2-4

$$\boldsymbol{M}_{\text{antisym}} = \sigma \int_{2-4} \mathrm{d}s \, (\boldsymbol{X} \times \boldsymbol{l}) = F_{\text{antisym}}(\boldsymbol{z} \cdot \boldsymbol{X}_{\text{p}}) \boldsymbol{y} , \tag{5.38}$$

where F_{antisym} is given by Eqn. (5.13).
This equation implies a strong constraint on the asymptotics of the membrane. Far from the particles the term of leading order in the height function (5.5) *has* to be proportional to $|\boldsymbol{X}|^{-1}$. Otherwise, the external torque would not be balanced. The coefficient C_1 has to be finite, its value fixed by the external force responsible for the torque.
If the height function of the membrane is known, $\boldsymbol{M}_{\text{antisym}}$ can be easily calculated and vice versa: in Sec. 5.1.2 we have derived expression (5.7) for $\boldsymbol{M}_{\text{out}}$ in terms of the coefficients of the height function (5.5). From this expression we obtain $\boldsymbol{M}_{\text{antisym}} = (1/2)\boldsymbol{M}_{\text{out}} = \pi \sigma C_1 \boldsymbol{y}$.
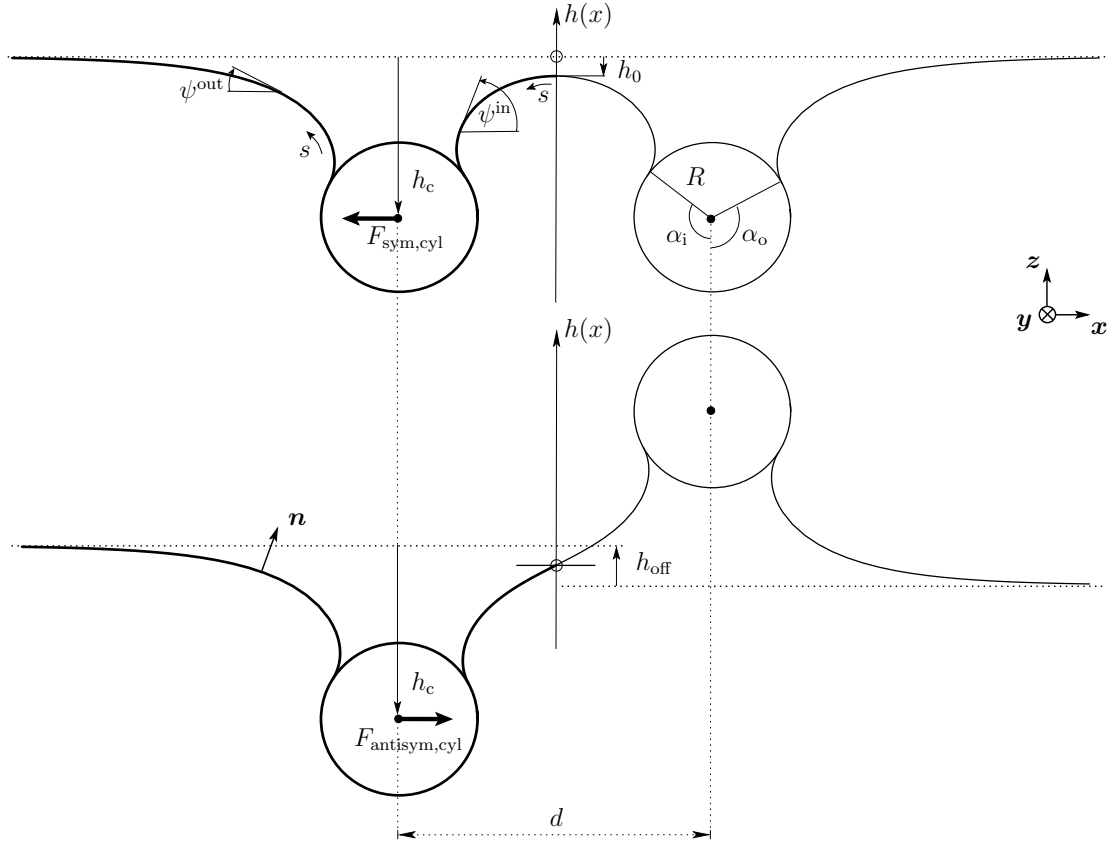
Figure 5.6: Two parallel cylinders on a fluid membrane (symmetric and antisymmetric cases). The profiles are determined as explained in Sec. 5.2 using the following parameters: $\alpha_c = \alpha_i + \alpha_o = 240°$, $d = 4$, $R = 1$, and $\lambda = 1$. The point about which the torques are evaluated is marked with $\circ$.

Two infinitely long cylinders

The situation changes if we again consider two infinitely long cylinders of radius R parallel to the y axis that are separated by a distance d (see Fig. 5.6). The size of the particles is no longer finite. Thus, it is necessary to exercise a little care when carrying over expressions derived for finite-sized particles.

Symmetric case The symmetric case corresponds to two cylinders adhering to one side of the membrane. The curvature parallel to branch 1, $K_\parallel$, vanishes as branch 1 degenerates into a line. The contributions from branch 2 and 4 cancel. No torque is exerted from branch 3: in contrast to the configurations with two finite-sized particles, the shape equation does not admit a term proportional to

$|\boldsymbol{X}|^{-1}$ in the height function (see Sec. 5.2).

The torque per length L of the cylinder with respect to the origin of the Euclidean coordinate system $\{\boldsymbol{x}, \boldsymbol{y}, \boldsymbol{z}\}$ is thus given by

$$M_{\text{sym,cyl}}/L = \left(\frac{\kappa}{2} K_\perp^2 - \sigma\right) \cdot h_0 + \kappa K_\perp \, , \qquad (5.39)$$

where the length h_0 is the distance between the origin and the mid-point of the profile (see Fig. 5.6). It is positive if this point lies *below* the origin.

Let $h_{\text{c}} := -(\boldsymbol{z} \cdot \boldsymbol{X}_{\text{p}})$ be the distance between the center of the cylinder and the asymptotic plane (see again Fig. 5.6). It is positive if the two cylinders are located *below* the asymptotic plane.

Torque balance establishes a relationship between h_0 and h_{c}, involving only the geometry on the midline, $M_{\text{sym,cyl}}$ given by Eqn (5.39): $M_{\text{sym,cyl}} \overset{(5.34)}{=} -h_{\text{c}} \, F_{\text{sym,cyl}}$ where $F_{\text{sym,cyl}}/L \overset{(5.12)}{=} -\frac{\kappa}{2} K_\perp^2$ implies

$$h_0 = \frac{\kappa K_\perp - \frac{\kappa}{2} K_\perp^2 h_{\text{c}}}{\sigma - \frac{\kappa}{2} K_\perp^2} = \frac{\lambda^2 K_\perp - \frac{\lambda^2}{2} K_\perp^2 h_{\text{c}}}{1 - \frac{\lambda^2}{2} K_\perp^2} \, . \qquad (5.40)$$

Eqn. (5.40) remains valid if the interface is a soap film. The bending rigidity κ then equals zero and we immediately obtain the result that $h_0 = 0$. This is confirmed by the observation that the interface is flat everywhere and the forces on the left and right cylinder vanish [Mül04].

If we parametrize the profile as a height $h(x)$ above the asymptotic reference plane, the curvature $K_\perp$ at branch 1 is exactly equal to $-h''(0)$ in the symmetric geometry, where dashes denote derivatives with respect to x. In Ref. [Wei03] the height function $h(x)$ was determined at the linearized level in the small gradient regime. Inserting it into Eqn. (5.40) validates this relation within the accuracy of the linear approximation (see Technical Point 5.4).

Antisymmetric case In the antisymmetric case the two cylinders adhere to opposite sides of the membrane. The torque on the left cylinder is determined as follows: at branch 1, the line integral is zero (compare Eqn. (5.37)). The contributions from branches 2 and 4 cancel as before. Thus, the torque at branch 3 should not vanish if the horizontal torque due the force F is to be balanced. However, the vertical force decreases faster than $1/x$ as $x \to \pm\infty$ and thus cannot provide such a torque (*cf.* previous paragraph and Sec. 5.2). How can torques balance under these circumstances?

The solution to this apparent contradiction is the following: the asymptotic plane for positive values of x does not necessarily coincide with the one for negative values. This is because the corresponding sections of the profile are *disconnected*. It becomes possible for the membrane to shift vertically with an offset h_{off} at the

━━━━ **Technical Point 5.4:** *Calculation of h_0 on the linearized level* ━━━━

To show that Eqn. (5.40) is consistent with the results of Ref. [Wei03], we calculate $h(0) = -h_0$ and compare it with the right hand side of Eqn. (5.40).

Due to the symmetry it is sufficient to consider only the left cylinder. Its axis is located at $x = -d/2$ (see Fig. 5.6). For $-d/2-\delta_o \leq x \leq -d/2+\delta_i$, cylinder and membrane are in contact. In small gradient approximation the shape of the outer membrane segment ($x \leq d/2 - \delta_o$) is given by [Wei03]: $h_{\mathrm{out}}(x) = B \exp(-|x + d/2|/\lambda)$, where $B = -\delta_o \lambda/R$ to first order in δ_o (strictly speaking, the expansion is in δ_o/λ here and below). The membrane segment adhering to the left cylinder has the circular profile: $h_{\mathrm{cyl}}(x) = -\left[h_c + \sqrt{R^2 - (x + d/2)^2} \right]$, where h_c is defined in Fig. 5.6. The profile has to be continuous at $x = -d/2 - \delta_o$. This condition yields

$$h_c = -\sqrt{R^2 - \delta_o^2} + \frac{\delta_o \lambda}{R} \exp\left(-\frac{\delta_o}{\lambda}\right) = -R + \frac{\lambda}{R}\,\delta_o + \mathcal{O}(\delta_o^2) = -R + \frac{\lambda \coth \frac{d}{2\lambda}}{R}\,\delta_i + \mathcal{O}(\delta_i^2)\,. \tag{5.V}$$

In the last step we exploited the fact that $\delta_o = \coth\left(\frac{d}{2\lambda}\right)\delta_i$ to first order [Wei03]. The profile of the membrane between the cylinders in the symmetric case is given by [Wei03]: $h_{\mathrm{in}}(x) = C + D\cosh(x/\lambda)$, where C and D are constants that can be determined from the conditions of continuous profile and slope at $x = -d/2 + \delta_i$. The latter condition yields

$$D = \frac{\lambda\,\delta_i}{\sqrt{R^2 - \delta_i^2}} \cdot \frac{1}{\sinh\left(\frac{-\frac{d}{2}+\delta_i}{\lambda}\right)} = -\frac{\lambda \delta_i}{R \sinh\left(\frac{d}{2\lambda}\right)} + \mathcal{O}(\delta_i^2)\,, \qquad \text{the former} \quad (5.\mathrm{VI})$$

$$C = -\left(h_c + \sqrt{R^2 - \delta_i^2}\right) - D\cosh\left(\frac{-\frac{d}{2} + \delta_i}{\lambda}\right) \overset{(5.\mathrm{V},5.\mathrm{VI})}{=} \mathcal{O}(\delta_i^2)\,.$$

To first order the depth h_0 at the mid-line of the profile[†] is thus given by

$$h_0 = -h_{\mathrm{in}}(0) = -(C + D) = \frac{\lambda \delta_i}{R \sinh\left(\frac{d}{2\lambda}\right)} + \mathcal{O}(\delta_i^2)\,.$$

It can also be obtained from Eqn. (5.40). Using $K_\perp = -h_{\mathrm{in}}''(0) = -D/\lambda^2$ yields

$$h_0 = -\frac{D + \frac{D^2}{2\lambda^2} h_c}{1 - \frac{D^2}{2\lambda^2}} = \frac{\lambda \delta_i}{R \sinh\left(\frac{d}{2\lambda}\right)} + \mathcal{O}(\delta_i^2)\,. \tag{5.VII}$$

The two results coincide at first order which confirms the validity of Eqn. (5.40) within this approximation.

[†] Note that h_0 is defined differently in Ref. [Wei03]; there it is given by $-(h_c + R)$.

origin with respect to the asymptotic plane(s) (see Fig. 5.6). The torque is then simply given by

$$M_{\mathrm{antisym,cyl}}/L = -\frac{h_{\mathrm{off}}}{2}\sigma \; . \tag{5.41}$$

This offset may be related to h_{c} as follows. One has $M_{\mathrm{antisym,cyl}} \overset{(5.38)}{=} -(h_{\mathrm{c}} - \frac{h_{\mathrm{off}}}{2})F_{\mathrm{antisym,cyl}}$ where $F_{\mathrm{antisym,cyl}}/L \overset{(5.14)}{=} \sqrt{\sigma^2 + (\kappa\nabla_\perp K_\perp)^2} - \sigma$ for $0° < \psi_{\mathrm{mid}} < 90°$. One obtains

$$\frac{h_{\mathrm{off}}}{2h_{\mathrm{c}}} = 1 - \frac{1}{\sqrt{1 + \lambda^4(\nabla_\perp K_\perp)^2}} \; , \tag{5.42}$$

where h_{c} is now measured from the *left* asymptotic plane to the center of the cylinder (see again Fig. 5.6).

Expanding the inverse square root in Eqn. (5.42) up to zeroth and second order, respectively, yields a lower and an upper bound on the ratio of h_{off} to h_{c}:

$$0 \leq \frac{h_{\mathrm{off}}}{h_{\mathrm{c}}} \leq \lambda^4(\nabla_\perp K_\perp)^2 \; . \tag{5.43}$$

Obviously, the offset h_{off} and h_{c} have the same sign. If $h_{\mathrm{c}} > 0$, the left asymptotic plane lies above the right one as depicted in Fig. 5.6; for $h_{\mathrm{c}} < 0$ the situation is reversed.

By setting $\kappa = 0$, we can again provide a check for consistency. The offset is zero as in the symmetric case. This is in agreement with the result from Ref. [Mül04] that the interface is flat and no force acts on the cylinders.

In Ref. [Wei03] the offset is set to zero in the ansatz for the height function. On first inspection, this may appear to be an error. However, it turns out to be consistent if Equation (5.42) is written in the small gradient regime: the first non-vanishing term is of second order in the smallness parameter. As the height function of [Wei03] is itself correct only to first order, the two results agree at the level of the approximation.

5.2 Two cylinders on a fluid membrane – exact solution

The nonlinear membrane shape equation can be solved exactly for the case of two cylindrical particles ("1D problem"). Two cylinders in a symmetric configuration repel—in contrast to two cylinders floating on water, despite an identical shape equation.

In the previous section several analytical conditions were derived which link different geometric properties of the interfacial profile to each other. For the antisymmetric case we saw that the external torque is compensated either by a *vertical*

force component (if the particles are finite) or by an *offset* (if the particles are infinitely long cylinders). In this section the value of the developed framework will be demonstrated by showing how it can be applied to determine the exact shape of the membrane with two adhering cylinders.

5.2.1 Determining the profile

Shape equation

If two parallel cylinders adhere to the membrane, the profile can be decomposed into the following parts: two bound sections in which the cylinder and membrane are in contact, an inner section between the cylinders, and two outer sections that become flat for $x \rightarrow \pm\infty$ (see Fig. 5.6). The shape of the bound parts is determined by the geometry of the attached particle, *i. e.* a circular arc; the profiles of the free membrane sections are determined by solving the nonlinear shape equation (4.3) in one dimension. The equation itself is easily solved in terms of elliptic functions (see below and App. C.1); the subtlety, as we will see, is in the implementation of the boundary conditions.

We will use the "angle-arc length" parametrization to describe the profile (see App. A.4.2 and Fig. 5.6). The angle $\psi(s)$ between the x axis and the tangent to the profile is connected to the curvature K via the relationship $K = -\dot{\psi}$, where the dot denotes a derivative with respect to s. In contrast to Chap. 4, where an axisymmetric situation was considered, the profile now obeys translational symmetry along the y axis.

The nonlinear shape equation that determines the profile of the free membrane can be obtained by rewriting Eqn. (4.3) in 1D (see also [Sei97, ACCG02]):

$$2\ddot{K} + K^3 - 2\lambda^{-2}K = 0 \ . \tag{5.44}$$

It possesses the first integral

$$\dot{K}^2 + \frac{1}{4}K^4 - \lambda^{-2}K^2 = E \ , \tag{5.45}$$

where E is a constant of integration.

It is straightforward to integrate Eqn. (5.45) after a separation of variables to determine s as a function of K which can be inverted to express K as a function of s. An additional integration yields the shape of the membrane, $\psi(s)$. One can do better, however, by taking advantage of the fact that the force $\boldsymbol{F}_{\mathrm{mem}}$ per length L of the cylinder at every point of the membrane is not only constant but also horizontal on each membrane section. Thus,

$$\boldsymbol{F}_{\mathrm{mem}}/L = -l_a \boldsymbol{f}^a = -\left(\frac{1}{2}\kappa K^2 - \sigma\right)\boldsymbol{l} + \kappa\dot{K}\,\boldsymbol{n} = f_{\mathrm{mem}}\boldsymbol{x} \ . \tag{5.46}$$

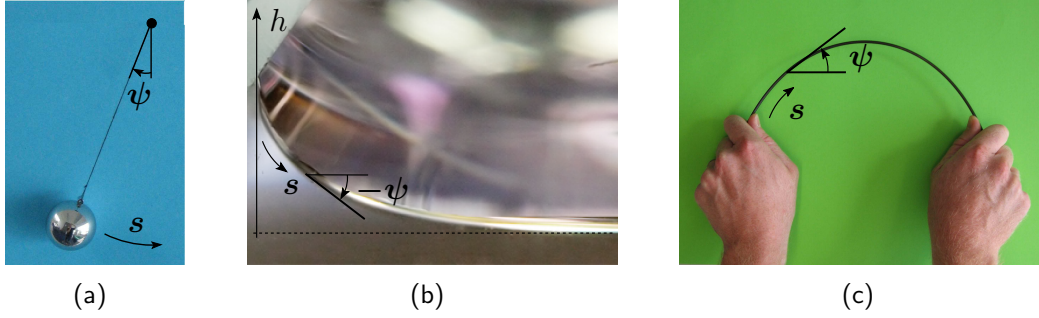**Figure 5.7:** Analogy between (a) planar pendulum, (b) fluid meniscus, and (c) an elastic rod (Euler elasticum).

━━━━ **Technical Point 5.5:** *Shape of a fluid meniscus under gravity* ━━━━

The shape of the interface between two incompressible fluids under gravity (with density difference $\rho > 0$ and gravitational acceleration g) is determined by the Young-Laplace law (2.52) which states that the hydrostatic pressure $P = -\rho g h$ equals the interfacial tension σ times the curvature K (see Eqn. (2.64)):

$$\dot{\psi} = h/\ell^2 \,, \tag{5.VIII}$$

where $\ell = \sqrt{\sigma/(\rho g)}$ is the capillary length (see Eqn. (2.65)). By differentiating Eqn. (5.VIII) and equating it with $\dot{h} = \sin\psi$ we obtain Eqn. (5.48) where $\lambda = \ell$ and $\eta = 1$.

━━━

For the following let us define the scaled force

$$\eta = \frac{f_{\mathrm{mem}}}{\sigma} = \mathrm{const.} \tag{5.47}$$

Projecting Eqn. (5.46) onto $\boldsymbol{n}$ then yields

$$\lambda^2 \ddot{\psi} - \eta \sin\psi = 0 \,. \tag{5.48}$$

where we have used $K = -\dot{\psi}$ and $\boldsymbol{x} \cdot \boldsymbol{n} = -\sin\psi$ (see also Eqns. (A.74)). Eqn. (5.48) appears in a number of other physical applications which include the motion of a simple pendulum [LL76], the shape of a fluid meniscus under gravity (see Technical Point 5.5) or the behavior of elastic rods (Euler elastica) [NG99] (see Fig. 5.7).[6]

---

[6] A similar analogy can be found in 3D: if we allow the elastic rod to bend out of the plane, its shape is described by the same Euler-Lagrange equations as the motions of a spinning top [NG99], as was first pointed out by Kirchhoff more than a century ago [Kir59].

Despite appearances, it is completely equivalent to Eqn. (5.45): both are of the same order in derivatives of ψ; furthermore, as we will show, the constant of integration E can be written in terms of the scaled force η and vice versa. Eqn. (5.48), however, has the advantage that it possesses an obvious first integral with an integration constant that can be deduced from Eqn. (5.46): the projection of the latter onto $\boldsymbol{l}$ yields, with $\boldsymbol{x} \cdot \boldsymbol{l} = \cos \psi$,

$$\frac{\lambda^2}{2} \dot{\psi}^2 + \eta \cos \psi = 1 \; . \tag{5.49}$$

Eqn. (5.49) can be interpreted as an energy balance of a fictitious particle moving in the potential $V(\psi) = \eta \cos \psi$, with displacement variable ψ, mass λ^2 and energy 1. The details of the "motion" depend on the value of η (see below and Fig. 5.8). From Eqn. (5.49) follows

$$K = \pm \lambda^{-1} \sqrt{2(1 - \eta \cos \psi)} \; . \tag{5.50}$$

It is simple to check that K satisfies the shape equation (5.44). The constants η and E are not independent; the relation between them, $\eta = \pm\sqrt{E\lambda^4 + 1}$, is found by substituting K into Eqn. (5.45).

Another interesting observation can be made if the problem is rewritten in a Hamiltonian formulation in analogy to Sec. 4.3.2. The (scaled) Lagrange function $\tilde{\mathscr{L}} = \mathscr{L}/\sigma$ is now given by

$$\tilde{\mathscr{L}} = \left(\frac{\lambda^2}{2} \dot{\psi}^2 + 1 \right) + \lambda_x (\dot{x} - \cos \psi) + \lambda_z (\dot{z} - \cos \psi) \; , \tag{5.51}$$

where the Lagrange multiplier functions λ_x and λ_z ensure that the angle ψ is anchored to the geometry (compare Eqns. (A.76)). The scaled Hamiltonian can be obtained as usual:

$$\tilde{\mathscr{H}} = \dot{\psi} \frac{\partial \tilde{\mathscr{L}}}{\partial \dot{\psi}} + \dot{x} \frac{\partial \tilde{\mathscr{L}}}{\partial \dot{x}} + \dot{z} \frac{\partial \tilde{\mathscr{L}}}{\partial \dot{z}} - \tilde{\mathscr{L}} = \left(\frac{\lambda^2}{2} \dot{\psi}^2 - 1 \right) + \lambda_x \cos \psi + \lambda_z \sin \psi \; . \tag{5.52}$$

The Hamilton equations for $p_x = \partial \tilde{\mathscr{L}}/\partial \dot{x} = \lambda_x$ and $p_z = \partial \tilde{\mathscr{L}}/\partial \dot{z} = \lambda_z$ directly tell us that both Lagrange multiplier functions have to be constant. Furthermore, we know that $\tilde{\mathscr{H}}$ vanishes in every point because the arc length is not fixed (compare Sec. 4.3.2). From this follows:

$$\frac{\lambda^2}{2} \dot{\psi}^2 + \lambda_x \cos \psi + \lambda_z \sin \psi = 1 \; . \tag{5.53}$$

If we compare this equation with Eqn. (5.49), we notice two things: (i) the values of the Lagrange multiplier functions are given by $\lambda_x = \eta$ and $\lambda_z = 0$. They are closely related to the external force (see also Chap. 4). (ii) The derivation reveals
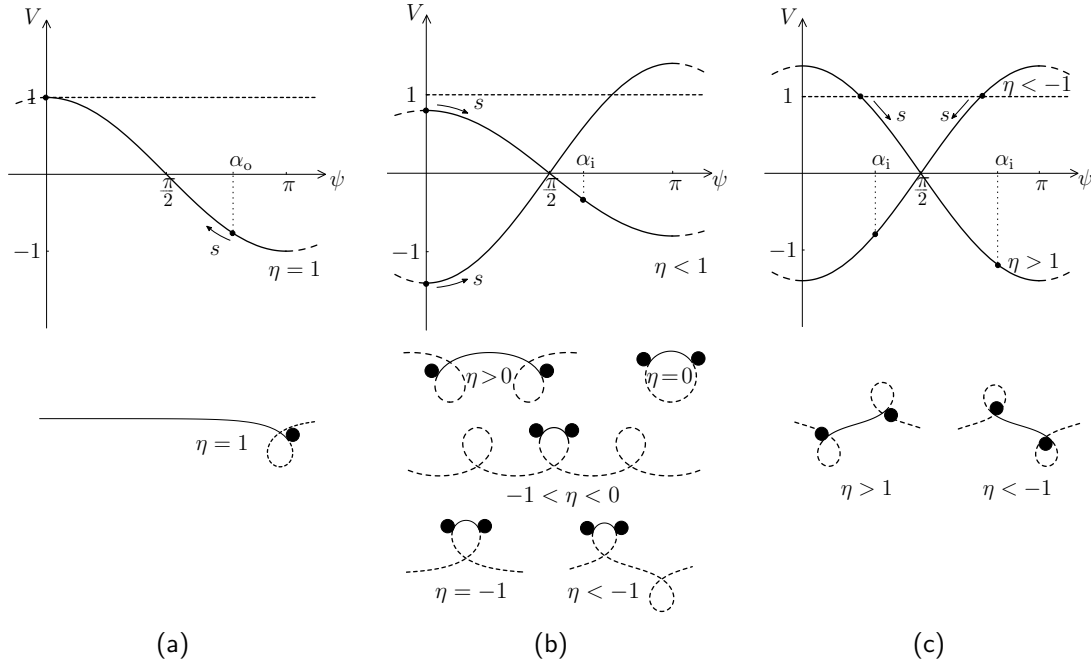
Figure 5.8: *Above:* Fictitious particle moving in the potential $V(\psi) = \eta \cos \psi$ (a) outer section (b) inner section - symmetric case (c) inner section - antisymmetric case; *below:* corresponding solutions (5.54,5.57,5.60) of Eqn. (5.49). For the explicit calculations, see App. C.1.

where the constant of integration in the first integral of the shape equation comes from: it is ultimately due to the fact that the arc length of the membrane is not a conserved quantity.

In the following, the solutions of Eqn. (5.49) for the free sections of the profile will be presented. The explicit calculations can be found in App. C.1. The cylinders are separated by a distance d. Due to the symmetry it is sufficient to consider only the left half of the membrane (where $x < 0$, see Fig. 5.6). The outer sections are qualitatively identical for the two symmetries whereas the inner sections differ. Eqn. (5.49) is a first order differential equation involving one unknown constant η. Thus two boundary conditions are required for each section.

Outer section

The boundary conditions for the outer section are the following: the free profile leaves the cylinder at a fixed contact angle $\psi(0) = \alpha_{\rm o}$. We assume without loss of generality that $\alpha_{\rm o} > 0$ and $\dot{\psi} \leq 0$.[7] At infinity, both ψ and $\dot{\psi}$ vanish. If we insert

---

[7] The other solution with $\alpha_{\rm o} < 0$ and $\dot{\psi} \geq 0$ can be simply obtained by a reflection on the (x, y) plane.

these two conditions into Eqn. (5.49), we obtain $\eta = 1$ on this section, *i. e.*, the force is just a surface tension pulling at infinity. This implies that $E = 0$ everywhere along the profile. The corresponding potential $V(\psi)$ is plotted in Fig. 5.8(a): the solution with $\psi(0) = \alpha_\mathrm{o}$ decreases monotonically to $\psi = 0$ (where $V = 1$) as $s \to \infty$.

The corresponding shape equation can be solved in terms of elementary functions (see App. C.1.1). One obtains

$$\psi^\mathrm{out}(\tilde{s}) = 4 \arctan \left[\tan \left(\frac{\alpha_\mathrm{o}}{4} \right) \mathrm{e}^{-\tilde{s}} \right] , \tag{5.54}$$

where $\tilde{s} := s/\lambda$. Incidentally, the function (5.54) also describes the shape of a straight fluid meniscus that approaches a solid surface at the angle α_o (see Technical Point 5.5 and Fig. 5.7(b)).

The function (5.54) decays exponentially with increasing arc length. Thus, in contrast to the case of finite-sized particles, the horizontal torque due to a vertical force component, $|M| \approx \sigma |x| \sin \psi^\mathrm{out} \approx \sigma |x| \psi^\mathrm{out}$ vanishes at infinity (see Technical Point 5.1 and Sec. 5.1.5).

Inner section

We first establish the connection between the total arc length of the inner profile, $2s_\mathrm{mid}$, and the contact angle between the cylinder and the inner membrane, α_i. If arc length is measured from the mid-line, we have

$$\frac{\tilde{d}}{2} - \tilde{R} \sin \alpha_\mathrm{i} = \int_0^{\tilde{s}_\mathrm{mid}} \mathrm{d}\tilde{s} \, \cos \psi(\tilde{s}) , \tag{5.55}$$

where all lengths, as before, are scaled with λ. This condition determines the value of $\tilde{s}_\mathrm{mid}$ implicitly in terms of α_i. Although its right-hand side can be written in terms of standard functions (see App. C), it can only be solved numerically.

We again consider only positive values of ψ. The solution for negative angles is obtained by reversing the sign of the functions (5.57) and (5.60) which corresponds to a reflection of the profile in the (x, y) plane. Note also that $K = +\dot{\psi}$ for all shapes of the inner section due to the chosen orientation of the arc length.

Symmetric case In the symmetric case, $\psi(0)$ is equal to zero. From Eqn. (5.49) we thus obtain

$$\eta = 1 - \frac{\lambda^2}{2} K_\perp^2 \leq 1 . \tag{5.56}$$

For $\eta = 1$, the cylinders are infinitely far apart and do not interact. If we omit this trivial case, the following solutions for different values of η are obtained [NG99,

Kul04] (see App. C.1.2 and Fig. 5.8(b)):[8]

$$\psi_{\text{sym}}^{\text{in}}(\tilde{s}) = \begin{cases} \pi + 2\,\text{am}\left[\!\!\left[\tilde{s}\sqrt{\frac{\eta}{m}} - \mathcal{K}[\![m]\!], m\right]\!\!\right] & , \; 0 < \eta < 1 \\ \sqrt{2}\tilde{s} & , \; \eta = 0 \\ 2\,\text{am}\left[\!\!\left[\tilde{s}\sqrt{\frac{|\eta|}{m}}, m\right]\!\!\right] & , \; -1 < \eta < 0 \\ 4\arctan\left[\tanh\left(\frac{\tilde{s}}{2}\right)\right] & , \; \eta = -1 \\ \arccos\left(1 - \frac{2}{m}\,\text{sn}^2\left[\!\!\left[\tilde{s}\sqrt{|\eta|}, m^{-1}\right]\!\!\right]\right) & , \; \eta < -1 \end{cases} , \quad (5.57)$$

where $\text{am}[\![s, m]\!]$ is the Jacobi amplitude with parameter m and $\text{sn}[\![s, m]\!]$ its sine, $\sin\left(\text{am}[\![s, m]\!]\right)$. The symbol $\mathcal{K}[\![m]\!]$ denotes the complete elliptic integral of the first kind [AS70] (see also Table C.1 on page 200). The parameter m is given by $m := \frac{2|\eta|}{1+|\eta|} \in [0, 2[$.

Antisymmetric case If the two cylinders adhere antisymmetrically, $\dot{\psi}$ must vanish at the mid-line. Thus,

$$\cos\psi_{\text{mid}} \overset{(5.49)}{=} \frac{1}{\eta} , \quad (5.58)$$

where $\psi_{\text{mid}} = \psi(0)$ is the angle at the mid-line. The case where ψ_{mid} equals zero or $180°$ corresponds again to the trivial solution with the two cylinders infinitely far apart. No solution exists for $\psi_{\text{mid}} = 90°$ as the scaled force η has to remain finite in an equilibrium situation. If $0° < \psi_{\text{mid}} < 90°$,

$$\eta \overset{(5.46)}{=} +\sqrt{1 + \lambda^4 \dot{K}_\perp^2} > 1 , \quad (5.59)$$

and, for $-\frac{1}{\sqrt{\eta}}\mathcal{K}[\![m^{-1}]\!] \leq \tilde{s} \leq \frac{1}{\sqrt{\eta}}\mathcal{K}[\![m^{-1}]\!]$ [NG99, Kul04] (see App. C.1.2 and Fig. 5.8(c))

$$\psi_{\text{antisym}}^{\text{in}}(\tilde{s}) = \arccos\left(\frac{2}{m}\,\text{sn}^2\left[\!\!\left[\tilde{s}\sqrt{\eta} - \mathcal{K}[\![m^{-1}]\!], m^{-1}\right]\!\!\right] - 1\right) . \quad (5.60\text{a})$$

If ψ_{mid} is greater than $90°$ and lower than $180°$ [NG99] (see again App. C.1.2 and Fig. 5.8(c)),

$$\psi_{\text{antisym}}^{\text{in}}(\tilde{s}) = \arccos\left(1 - \frac{2}{m}\,\text{sn}^2\left[\!\!\left[\tilde{s}\sqrt{|\eta|} - \mathcal{K}[\![m^{-1}]\!], m^{-1}\right]\!\!\right]\right) , \quad (5.60\text{b})$$

for $-\frac{1}{\sqrt{|\eta|}}\mathcal{K}[\![m^{-1}]\!] \leq \tilde{s} \leq \frac{1}{\sqrt{|\eta|}}\mathcal{K}[\![m^{-1}]\!]$, where

$$\eta \overset{(5.46)}{=} -\sqrt{1 + \lambda^4 \dot{K}_\perp^2} < 1 . \quad (5.61)$$

The parameter m is defined as above and varies now between 1 and 2.

---

[8] The expression for $\eta < 1$ in Eqn. (5.57) is valid for $0 \leq \tilde{s} \leq \frac{2}{\sqrt{|\eta|}}\mathcal{K}[\![m^{-1}]\!]$.

Boundary conditions at the cylinders

To obtain the profile of the membrane for given separation $\tilde{d}$ and cylinder radius $\tilde{R}$, one has to determine the values of the scaled force η and the contact angles α_o and α_i. The value of η for any given α_i is determined implicitly by the requirement that

$$\psi(\tilde{s}_\mathrm{mid}) = \alpha_\mathrm{i} \ , \tag{5.62}$$

where $\tilde{s}_\mathrm{mid}$ is itself implicitly given by Condition (5.55); the values of α_i and α_o depend on the boundary conditions at the cylinder. We will discuss two possibilities here: we either fix the area of contact between the cylinders and the membrane, or consider attachment due to a finite adhesion energy w per area between the membrane and the cylinders similar to the problems discussed in the two previous chapters.

Fixed area of contact Suppose that the area of contact is fixed to

$$\alpha_\mathrm{c} = \alpha_\mathrm{o} + \alpha_\mathrm{i} = \text{const.} \tag{5.63}$$

Torque balance will fix the individual values of α_o and α_i.

The torque about the cylinder axis has to vanish in equilibrium. This is the case if the total energy $E_\mathrm{tot}(\alpha_\mathrm{i})$ of the system exhibits a local extremum (see Technical Point 5.6).

The corresponding torque balance can be written as

$$0 = \tilde{K}_\mathrm{i} - \tilde{K}_\mathrm{o} - \tilde{R}(\eta \cos \alpha_\mathrm{i} - \cos \alpha_\mathrm{o}) \overset{(5.50)}{=} \tilde{K}_\mathrm{i} - \tilde{K}_\mathrm{o} + \frac{\tilde{R}}{2}(\tilde{K}_\mathrm{i}^{\,2} - \tilde{K}_\mathrm{o}^{\,2}) \ , \tag{5.64}$$

where $\tilde{K}_\mathrm{i} := \lambda K_\mathrm{i}$ and $\tilde{K}_\mathrm{o} := \lambda K_\mathrm{o}$. Eqn. (5.64) has two solutions: $\tilde{K}_\mathrm{i} = \tilde{K}_\mathrm{o}$ and $\tilde{K}_\mathrm{i} = -\tilde{K}_\mathrm{o} - 2/\tilde{R}$. The latter implies that either $\tilde{K}_\mathrm{i}$ or $\tilde{K}_\mathrm{o}$ is smaller than $-1/\tilde{R}$. Since the cylinder has a curvature of $-1/\tilde{R}$ in scaled units and membrane and cylinder must not intersect, the second solution can be ruled out. Hence, the two contact curvatures must coincide:

$$\tilde{K}_\mathrm{i} = \tilde{K}_\mathrm{o} \overset{(C.9)}{=} 2 \sin(\alpha_\mathrm{o}/2) \ , \tag{5.65}$$

and

$$\eta \cos \alpha_\mathrm{i} \overset{(5.64)}{=} \cos \alpha_\mathrm{o} \ . \tag{5.66}$$

The values of η, α_i, α_o, and $\tilde{s}_\mathrm{mid}$ for given separation and cylinder radius can be determined numerically by solving the conditions (5.55), (5.62), (5.63), and (5.65) simultaneously. As an example, the two profiles for $\tilde{d} = 4$, $\tilde{R} = 1$, and $\alpha_\mathrm{c} = 240°$ are plotted in Fig. 5.6.

━━━ **Technical Point 5.6:** *Energy minimum implies torque balance* ━━━

The total energy E_{tot} of the system is given by:

$$
E_{\mathrm{tot}}/(2\kappa) = \int_0^{s_{\mathrm{mid}}} \mathrm{d}s \left\{ \frac{1}{2} K^{\mathrm{in}}(s)^2 + \lambda^{-2}[1 - \cos\psi^{\mathrm{in}}(s)] \right\} + \int_0^\infty \mathrm{d}s \left\{ \frac{1}{2} K^{\mathrm{out}}(s)^2 \right.
$$
$$
\left. + \lambda^{-2}[1 - \cos\psi^{\mathrm{out}}(s)] \right\} - \lambda^{-2} R \left(\sin\alpha_i + \sin\alpha_o \right) ,
$$

where the terms due to surface tension give the *excess* energy in comparison to the planar state without cylinders (in other words we have subtracted an infinite constant contribution from the energy). Using Eqn. (5.50) for the curvature K we can rewrite:

$$
\lambda^{-2}[1 - \cos\psi^{\mathrm{in}}(s)] = \lambda^{-2}[1 - \eta\cos\psi^{\mathrm{in}}(s) + (\eta - 1)\cos\psi^{\mathrm{in}}(s)]
$$
$$
= \frac{1}{2} K^{\mathrm{in}}(s)^2 + \lambda^{-2}(\eta - 1)\cos\psi^{\mathrm{in}}(s) ,
$$

and, since $\eta = 1$ on the outer section, $\lambda^{-2}[1 - \cos\psi^{\mathrm{out}}(s)] = \frac{1}{2} K^{\mathrm{out}}(s)^2$. Inserting this into the energy yields

$$
E_{\mathrm{tot}}/(2\kappa) = \int_0^{s_{\mathrm{mid}}} \mathrm{d}s \left\{ K^{\mathrm{in}}(s)^2 + \lambda^{-2}(\eta - 1)\cos\psi^{\mathrm{in}}(s) \right\} + \int_0^\infty \mathrm{d}s\, K^{\mathrm{out}}(s)^2
$$
$$
- \lambda^{-2} R \left(\sin\alpha_i + \sin\alpha_o \right)
$$
$$
\overset{(5.55)}{=} \int_0^{\alpha_i} K^{\mathrm{in}}(\psi)\mathrm{d}\psi + \int_0^{\alpha_c - \alpha_i} K^{\mathrm{out}}(\psi)\mathrm{d}\psi + \lambda^{-2}(\eta - 1)\left(\frac{d}{2} - R\sin\alpha_i \right)
$$
$$
- \lambda^{-2} R \left[\sin\alpha_i + \sin(\alpha_c - \alpha_i) \right] .
$$

If we now set the derivative with respect to α_i at constant d and α_c to zero, we obtain the torque balance (5.64):

$$
0 \overset{!}{=} \frac{1}{2\kappa} \frac{\partial E_{\mathrm{tot}}}{\partial \alpha_i} \bigg|_{d,\alpha_c} = K_i - K_o - \lambda^{-2} R \left(\eta\cos\alpha_i - \cos\alpha_o \right) .
$$

Thus, the torque on the cylinder is balanced if the total energy exhibits a local extremum and vice versa.

━━━━━━━━━━━━━━━━━━━━━━━

Adhesion balance If the cylinders attach to the membrane due to a finite adhesion energy w, the contact curvature condition (3.23) holds:

$$
\tilde{K}_i = \tilde{K}_o = -1/\tilde{R} + \sqrt{\tilde{w}} , \tag{5.67}
$$

where $\tilde{w} := \frac{2w\lambda^2}{\kappa}$. The curvatures are equal as before and torque balance (5.64) is fulfilled automatically. The contact angle α_o can be determined from Eqn. (5.65).

Finally, η, α_i, and $\tilde{s}_\mathrm{mid}$ can be calculated using Eqns. (5.55), (5.62), and (5.67). The adhesion energy $\tilde{w}$ and the wrapping angle α_c are conjugate variables. Setting one of them to a constant value implies that the other will adjust in equilibrium. Questions of stability depend on which of the two variables is fixed: a profile found to be stable under constant α_c is not necessarily stable under the constant $\tilde{w}$.[9] To avoid problems of this kind, we will focus on the constant wrapping angle scenario in the following.

Note that the boundary condition (5.65) does not always fix a unique profile. The total energy $E_\mathrm{tot}(\alpha_\mathrm{i})$ of the system may possess more than one minimum; thus profiles which are stable locally may exist.[10] In the next paragraph we will see that this is indeed the case for certain ranges of values of $\tilde{d}$, $\tilde{R}$, and α_c.

5.2.2 Conditions from torque balance

Now that we possess the complete profile we can go back to Eqns. (5.40) and (5.42) and study the behavior of $\tilde{h}_0 := h_0/\lambda$ and $\tilde{h}_\mathrm{off} := h_\mathrm{off}/\lambda$ as a function of distance $\tilde{d}$ for different values of $\tilde{R}$ and α_c.

Symmetric case   In the symmetric case, $\tilde{K}_\perp = \sqrt{2(1-\eta)}$ and Eqn. (5.40) can be written as

$$\tilde{h}_0 = \eta^{-1}[\sqrt{2(1-\eta)} - (1-\eta)\tilde{h}_\mathrm{c}] \ , \tag{5.68}$$

where

$$\tilde{h}_\mathrm{c} \overset{\text{(C.12)}}{=} 2\sin(\alpha_\mathrm{o}/2) - \tilde{R}\cos\alpha_\mathrm{o} \ . \tag{5.69}$$

The height $\tilde{h}_0$ can be determined as a function of separation $\tilde{d}$ for fixed cylinder radius $\tilde{R}$ and different wrapping angles α_c. If the value of α_c is small, the solution coincides with the result of the small gradient approximation (5.VII), as expected. The value of $\tilde{h}_0$ falls off exponentially with the decay length $\ell := 2\lambda$ for increasing separation $\tilde{d}$.

For higher angles α_c, however, the behavior changes at small values of $\tilde{d}$ due to the breakdown of the small gradient approximation (see Fig. 5.9 for $\tilde{R} = 1$): the energy $E_\mathrm{tot}(\alpha_\mathrm{i})$ exhibits two minima instead of one.[11] These minima correspond to distinct stable profiles with different α_i and $\tilde{h}_0$. If $\alpha_\mathrm{c} = 180°$, they possess the same energy. If $\alpha_\mathrm{c} < 180°$, the global minimum is located at the smaller value of α_i and the corresponding $\tilde{h}_0$ is always positive, *i. e.* the mid-point lies below the reference plane (see again Fig. 5.9). For larger contact angles α_c this behavior is

---

[9] We have met the same motif already twice: in Sec. 1.2.3 where volume and pressure were conjugate variables and in Chap. 4 where force and indentation ensemble were considered.

[10] Solutions with one or even more loops between the cylinders, however, have a much higher energy than the cases shown in Fig. 5.8 and will therefore be discarded.

[11] The intermediate maximum is not considered in the following as it does not correspond to a stable profile.
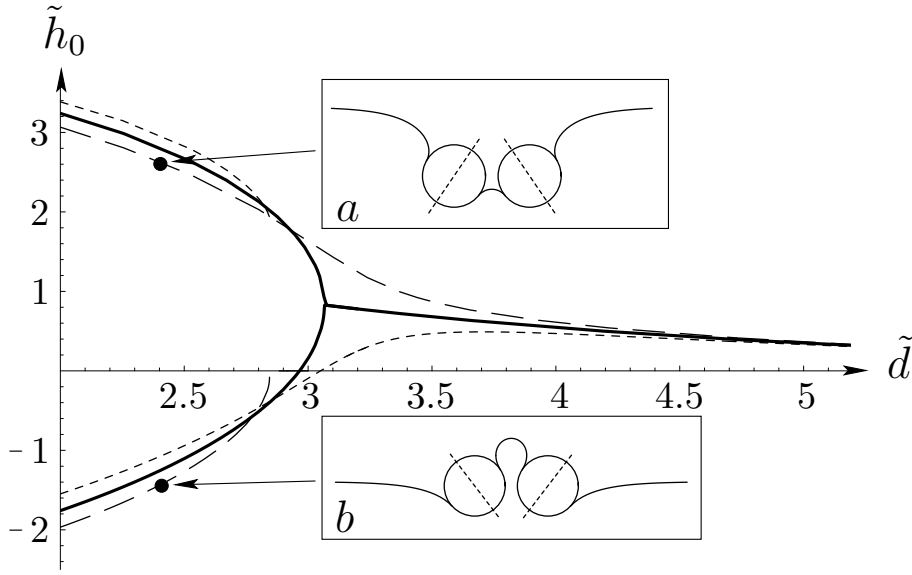
Figure 5.9: The height $\tilde{h}_0$ at the mid-line as a function of separation $\tilde{d}$ for $\tilde{R} = 1$ and $\alpha_c = 170°$ (long dashes), $180°$ (bold solid line), and $190°$ (short dashes). At $\tilde{d} = 2$ the two cylinders are in contact with each other and cannot approach closer. For $\tilde{d} \lesssim 3$ two locally stable solutions can be found which correspond to different angles α_i. In the insets a and b the two solutions for $\tilde{d} = 2.4$ and $\alpha_c = 170°$ are plotted where $\alpha_i = 50.9°$ (a) and $122.2°$ (b), respectively. Profile a corresponds to the global energy minimum here.

reversed: the higher value of α_i and the lower value of $\tilde{h}_0$ correspond to the global energy minimum. The mid-point may now even lie above the reference plane.

In Fig. 5.10 the tilt angle $\alpha_t := \frac{\alpha_c}{2} - \alpha_i$ is plotted as a function of distance $\tilde{d}$ for $\tilde{R} = 1$. It decays exponentially with length λ at large separations. If $\alpha_c < 180°$ the tilt angle of the global energy minimum is always positive which corresponds to profiles such as the one plotted in Fig. 5.9, a. If $\alpha_c > 180°$, the tilt angle of the global energy minimum is negative. For $\alpha_c = 180°$ and for all $\tilde{d} \gtrsim 3$, α_t is equal to zero; at $\tilde{d} \approx 3$ the function bifurcates into two branches of equal energy. A closer inspection of Eqn. (5.66) explains these findings: either α_i is exactly $90°$ and thus $\alpha_t = 0$, or $\eta = -1$. At the bifurcation point both conditions hold. For $\tilde{d} \lesssim 3$ the profiles with $\eta = -1$ are local minima of same energy[12] whereas $\alpha_t = 0$

---

[12] That both minima have the same energy can, for instance, be explained like this: imagine you bring together both cylinders from infinity to a distance $\tilde{d} \lesssim 3$ in infinitesimal steps. At every step a certain force has to be applied which is always the same for both solutions (see also Sec. 5.2.3). Thus, the energy (= force integrated over the distance) stays the same as well no matter how close the cylinders are brought together.
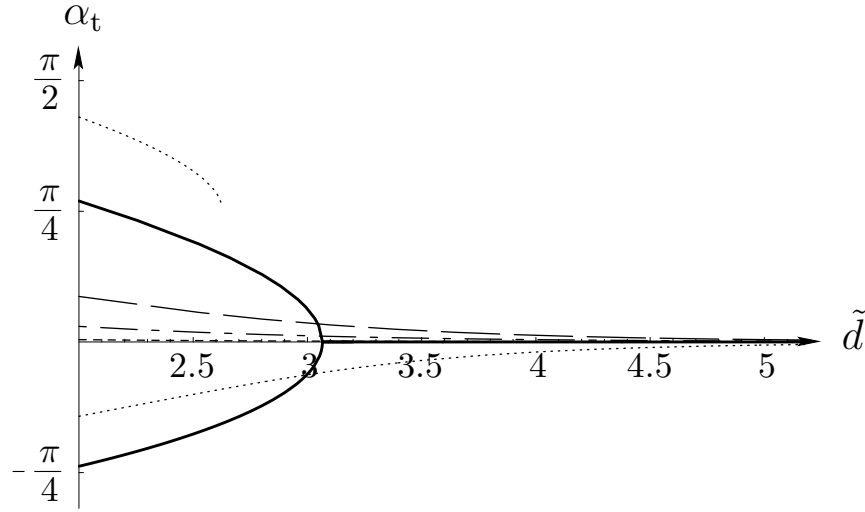
Figure 5.10: The tilt angle α_t (symmetric case) as a function of separation $\tilde{d}$ for $\tilde{R} = 1$ and $\alpha_c = 10°$ (short dashes), $45°$ (dashed-dotted line), $90°$ (long dashes), $180°$ (bold solid line), and $240°$ (dotted line).

corresponds to the intermediate maximum we do not discuss further here.

Antisymmetric case If the two cylinders are closer than $2\tilde{R}$, one must check whether the particles overlap or not. To avoid complications of this kind, we will only consider separations of $\tilde{d} \geq 2\tilde{R}$. In contrast to the symmetric case, one then finds a single solution for given $\tilde{d}$, $\tilde{R}$, and α_c where η is always greater than 1. From Eqns. (5.42) and (5.59) one obtains

$$\frac{\tilde{h}_{\text{off}}}{2\tilde{h}_{\text{c}}} = 1 - \frac{1}{\eta} \, , \tag{5.70}$$

where $\tilde{h}_{\text{c}}$ is given by Eqn. (5.69).

In Fig. 5.11 $\tilde{h}_{\text{off}}$ is plotted as a function of distance $\tilde{d}$. For small contact angles, $\tilde{h}_{\text{off}}$ is negative which implies that the asymptotic plane on the left lies below the one on the right and below the center of the left cylinder. For intermediate values of α_c (such as $90°$ if $\tilde{R} = 1$) $\tilde{h}_{\text{off}}$ can be either positive or negative depending on the separation of the cylinders (see again Fig. 5.11). If α_c is further increased, $\tilde{h}_{\text{off}}$ is positive for all separations and the profiles resemble the one which is plotted in the lower part of Fig. 5.6.

The tilt angle α_t is always equal to zero for $\alpha_c = 180°$. The solution $\eta = -1$ which also solves Eqn. (5.66) is now forbidden due to the symmetry. For $\alpha_c > 180°$
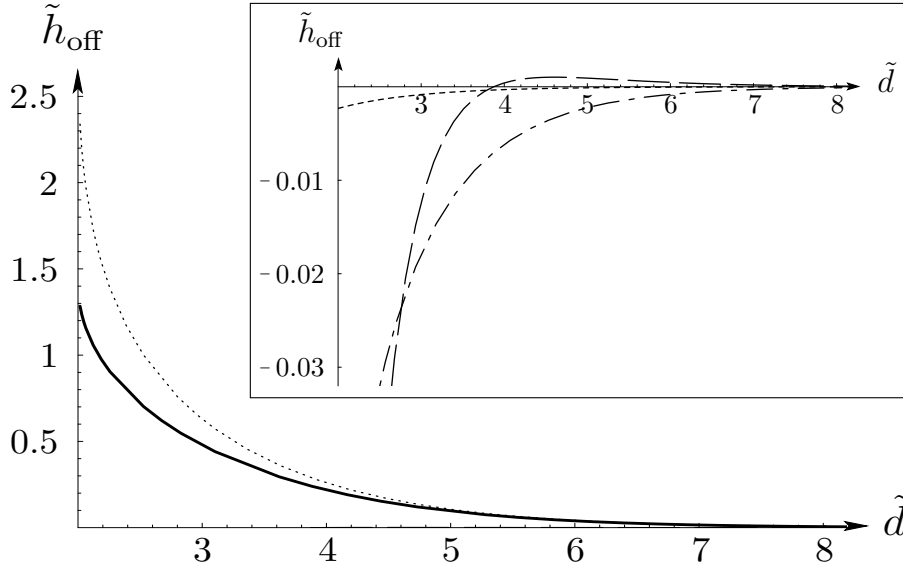
Figure 5.11: The offset $\tilde{h}_{\text{off}}$ as a function of separation $\tilde{d}$ for $\tilde{R} = 1$ and different contact angles. The line styles are chosen as in Fig. 5.10.

the tilt angle is positive; for $\alpha_{\text{c}} < 180°$ it is negative. In both cases it decays exponentially with length λ.

5.2.3 Forces between the cylinders

Using the stress tensor, the force on the left cylinder is given by

$$F_{\text{cyl}}/L \overset{(5.46)}{=} f_{\text{mem}} - \sigma = \sigma(\eta - 1) . \tag{5.71}$$

One only has to determine the value of η; the total force follows directly.

In Figs. 5.12 and 5.13 the absolute value of the scaled force, $|\eta - 1|$, is plotted for the symmetric and antisymmetric cases. At large separations it decays exponentially as predicted by the linearized theory [Wei03]. The underlying small gradient approximation, however, breaks down if the curvatures along the profile become too high, *i. e.* for large contact area and small separation. In Fig. 5.14 the exact solutions are compared with the small gradient approximation for the symmetric geometry by plotting $|\eta - 1|$ as a function of α_{c} for $\tilde{d} = 3$ and $\tilde{R} = 1$. The approximate solution increasingly underestimates the force as the contact angle is increased.

As soon as the small gradient approximation breaks down, different features appear: in the antisymmetric case, $|\eta - 1|$ increases faster for decreasing separation than a small gradient approximation would anticipate. In the symmetric case,
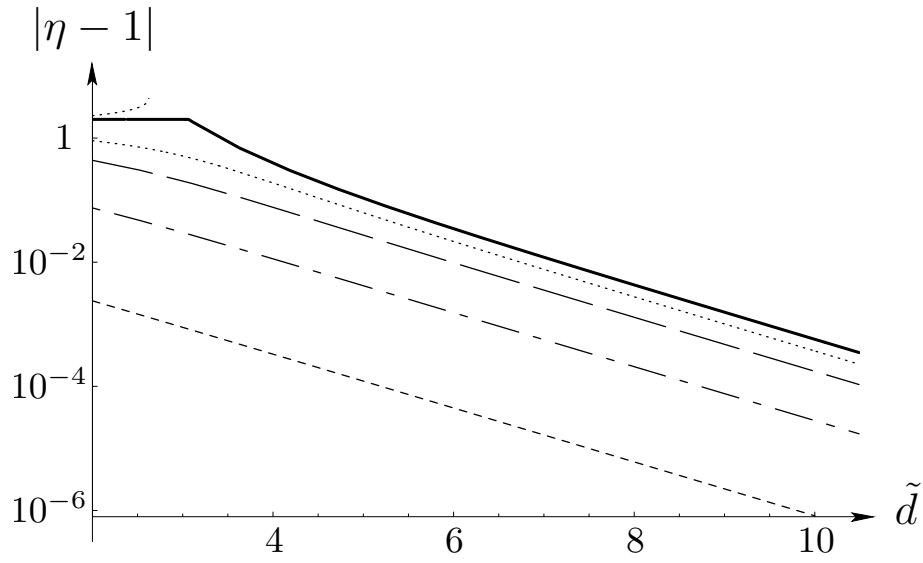
Figure 5.12: Absolute value of the scaled force $|\eta - 1|$ as a function of separation $\tilde{d}$ for $\tilde{R} = 1$ and different contact angles (symmetric case). The line styles are again chosen as in Fig. 5.10.
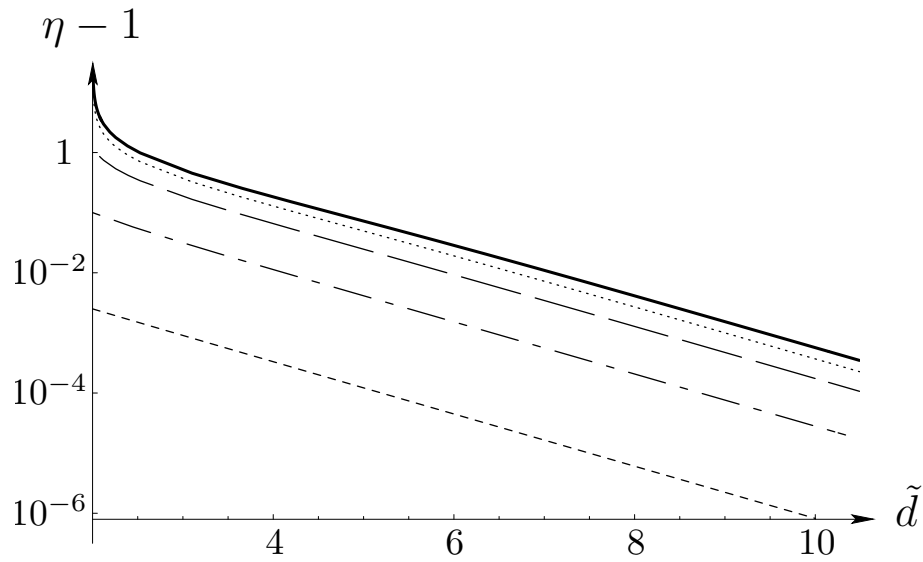
Figure 5.13: Scaled force $\eta - 1$ as a function of separation $\tilde{d}$ for $\tilde{R} = 1$ and different contact angles (antisymmetric case). The line styles are chosen as in Fig. 5.10.

━━━ **Technical Point 5.7:** *$F_{sym,cyl}/L$ including the quartic Hamiltonian (2)* ━

If a term $\mathcal{H}_\nabla$ is added to the Helfrich Hamiltonian, a contribution to the force (5.71) results which is given in Eqn. (5.III) for the symmetric case. Assume that $\mathcal{H}_\nabla$ is just a small perturbation so that we can insert the solution of the shape equation of the unperturbed Helfrich Hamiltonian into Eqn. (5.III). From Eqn. (5.50) we obtain[‡]

$$\frac{\mathrm{d}^2}{\mathrm{d}s^2}K^2\Big|_{s=0} = \frac{2}{\lambda^2}\eta\big(\ddot{\psi}\sin\psi + \dot{\psi}^2\cos\psi\big)\Big|_{s=0} = \frac{2}{\lambda^2}\eta K_\perp^2 \ . \qquad (5.\text{IX})$$

Thus, the force (5.III) can be written as:

$$F_{\text{sym,cyl}}^\nabla/L \approx \frac{1}{4}\kappa_\nabla\frac{2}{\lambda^2}\eta K_\perp^2 = \frac{1}{2}\kappa_\nabla\Big(\lambda^{-2} - \frac{1}{2}K_\perp^2\Big)K_\perp^2 \ .$$

The sign of the force $F_{\text{sym,cyl}}^\nabla/L$ depends on the signs of κ_∇ and η. For instance, at large distances d where $\eta > 0$ the term decreases the repulsion between the two cylinders for positive κ_∇ and increases it if κ_∇ is negative. The overall force including all terms of quartic order is given by the sum of the right hand sides of Eqns. (5.II) and (5.III):

$$F_{\text{sym,cyl}}/(\sigma L) \approx -\frac{1}{2}(\lambda K_\perp)^2\left\{1 \pm \frac{3}{2}(\ell_4 K_\perp)^2 \pm \left(\frac{\ell_\nabla}{\lambda}\right)^2\Big[\frac{1}{2}(\lambda K_\perp)^2 - 1\Big]\right\} ,$$

where the signs depend on whether the proportionality constants κ_4 and κ_∇ are positive or negative (see Technical Point 5.2). The correction term due to $\mathcal{H}_\nabla$ only becomes noticeable once the characteristic length scale λ is no longer large compared to the length scale $\ell_\nabla = \sqrt{|\kappa_\nabla|/\kappa}$. In that case, however, the assumption that we can use the profile of the unperturbed Helfrich Hamiltonian is questionable. To be on the safe side, the quartic order shape equation would have to be solved numerically.

[‡] Eqn. (5.IX) is intuitively understandable if one has a look at the corresponding shapes in Fig. 5.8(b): if $\eta > 0$, $K_\perp$ at the mid-line is the *minimum curvature* of all curvatures of the inner section; for $\eta < 0$, $K_\perp$ is the *maximum*.

━━━━━━━━━━━━━━━━━━

two solutions can be found (*cf.* previous paragraph). The global energy minimum typically corresponds to the solution with the smaller absolute value of the force. Remarkably, the force is constant $[F_{\text{cyl}}/(L\sigma) = -2]$ for $\alpha_{\text{c}} = 180°$ and $\tilde{d} \lesssim 3$.

How big are these membrane-mediated forces for real particles? As an example, let us look at a cylindrical nanoparticle of radius $R \simeq 50\,\text{nm}$ adsorbed onto a fluid membrane with a bending stiffness of $\kappa \simeq 20\,k_{\text{B}}T$. Using a typical value for membranes of $\lambda \approx 50\,\text{nm}$, we obtain $\tilde{R} = 1$. Furthermore, if we assume that two particles are separated by a distance d of $200\,\text{nm}$, η is of the order of $10^{-2}\ldots 1$
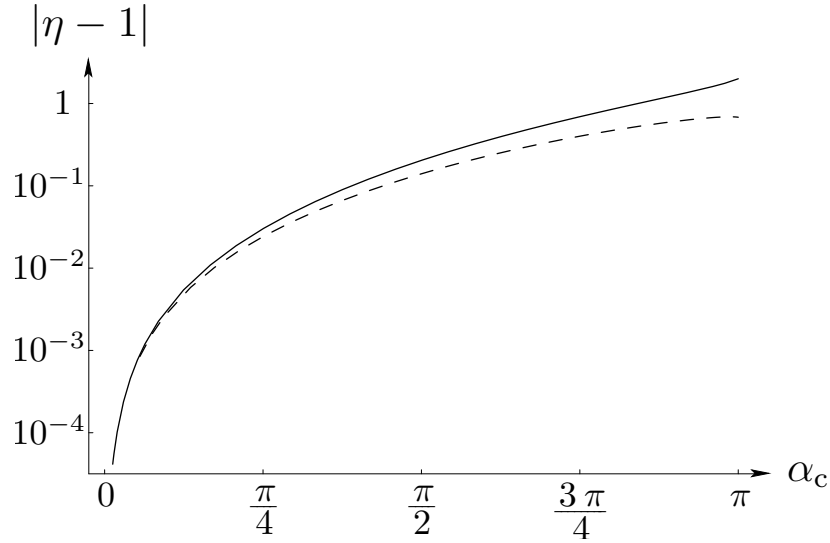
Figure 5.14: $|\eta - 1|$ as a function of α_c for $\tilde{d} = 3$ and $\tilde{R} = 1$ in the symmetric case. The small gradient approximation is plotted with a dashed line, the numerically exact solution with a solid line.

for wrapping angles α_c greater than 45° (see Figs. 5.12 and 5.13). Thus, the force F_{cyl} can reach up to 3 pN for a particle of length $L = 100$ nm, which shows rather vividly that membrane-mediated forces can be very significant in the nanoworld. Estimates for smaller particles such as proteins or actin filaments (where $R \simeq 5$ nm) lead to similar results.

5.2.4 Two sewing needles on water – a brief interlude

For one-dimensional problems the shape of the interface between two incompressible fluids under gravity is also described by the membrane shape equation (5.48) (see Technical Point 5.5 on page 131). It therefore proves worthwhile to investigate the interface-mediated force between two cylinders floating on such a fluid-liquid interface and compare it to the results we have derived for the membrane.

To this end, let us specialize to surfaces where surface tension is the only *surface* energy contribution and consider at first two particles of arbitrary shape and orientation adhering to the interface, *e. g.* two needles floating on an air-water interface (see Fig. 5.15) [GS71] or two cheerios on the milk surface of your breakfast bowl [VM05].

The force is now not only given by a boundary integral alone but contains an additional area integral over the stresses from gravity as we have seen in Sec. 2.3.2. This prevents us from following the approach exploited in Sec. 5.1 where the con-

(a)   (b)

(c)   (d)
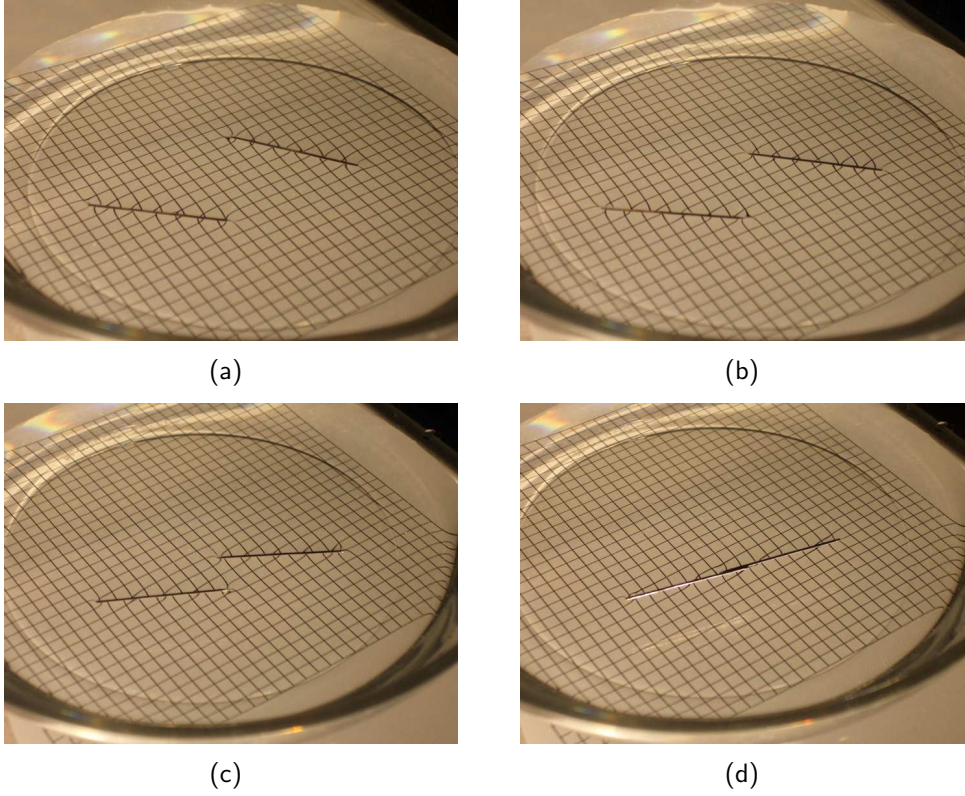
Figure 5.15: Attraction of two sewing needles floating on water (see also [GS71]). The whole process proceeds on a timescale of a few seconds, becoming increasingly faster from (a) to (d) *(from [Mül04])*.

tour of integration could be deformed without changing the value of the force. One may, however, analyze both terms of the force separately: according to Eqn. (2.66) the force on one of the particles is given by

$$\boldsymbol{F} = -\boldsymbol{F}_{\text{ext}} = \sigma \oint_{\partial \Sigma_{\text{c}}} \mathrm{d}s \, \boldsymbol{l} \; - \; \rho \, g \int_{\Sigma_{\text{c}}} \mathrm{d}A \, h \, \boldsymbol{n} \; , \tag{5.72}$$

where Σ_{c} is the contact surface between particle and water or milk, respectively. This expression quite vividly illustrates the two different contributions to the force:

1. The first term is only proportional to the surface tension. It adds up all the contributions which originate from the surface locally pulling in $\boldsymbol{l}$ direction outward with a strength σ per unit length.

2. The second term is proportional to the gravitational acceleration g and integrates over the patch covered by the particle. Since $\rho g h$ is the excess pressure across the surface, it describes the buoyancy force due to the Young-Laplace pressure across the patch.
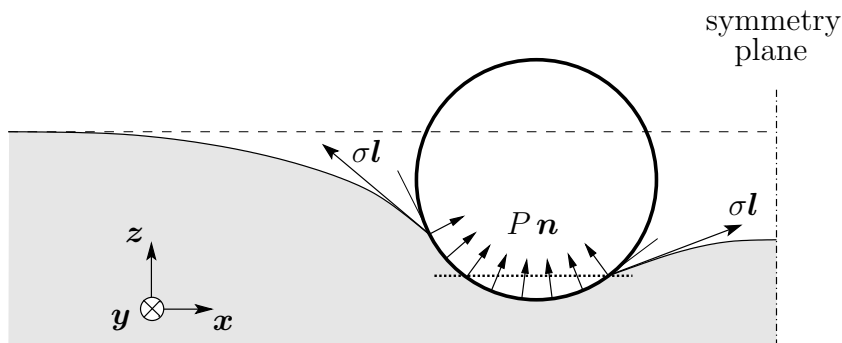
Figure 5.16: Illustration that for two floating cylinders (symmetric case) the two different forces acting on one of them have an unbalanced horizontal component, leading to an attraction between the two particles.

In Fig. 5.16 these two components of the force on the left particle are depicted for the case of two cylinders in a symmetric configuration. Since the cylinder is adhering asymmetrically to the water (due to the presence of the second cylinder), the horizontal contribution of both forces does not vanish. In fact, one can see that a net force in the direction of $\boldsymbol{x}$ remains (see again Fig. 5.16): the horizontal force contributions originating from the Laplace pressure below the dotted line cancel each other but are not balanced above this line. Additionally, surface tension pulls to the right as well because the outward pointing vector $\boldsymbol{l}$ at the right line of contact between substrate, water, and air has a larger component in the $\boldsymbol{x}$ direction than the one at the left has in the direction of $-\boldsymbol{x}$. Thus, the cylinders attract in this situation (see again Fig. 5.15). In contrast to that, two membrane-bound cylinders repel. This is quite surprising at first sight since the surface shapes for both cases are solutions of the same shape equation. However, the surface energies not only determine the *shape* but also the *stress tensor* which is different even though the shapes are the same. Consequently, the forces are different and even differ in their sign.

In this section we have seen that the simple two-cylinder problem already displays remarkably subtle behavior. For two spheres on the membrane (2D problem) the situation becomes even more complicated: the shape equation cannot be solved in terms of known functions any more. Even the sign is difficult to determine analytically. Although linear calculations predict a repulsion for the symmetric configuration [GBP93, WKH98, KNO98, BF03], the nonlinear expression (5.11) for the force F_{sym} does not rule out that the interaction between the particles is attractive for higher deformations. Furthermore, two particles are very often not isolated on the membrane *in vivo* but surrounded by many others. Multi-body effects will thus play a role as well: since the field equations are nonlinear, the
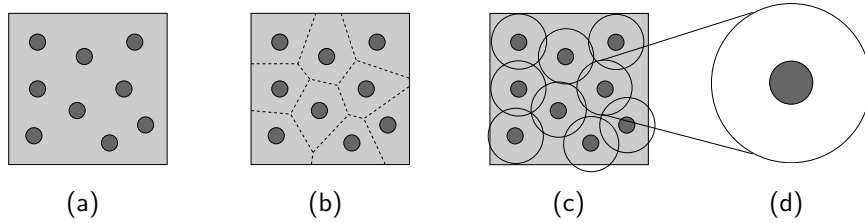
Figure 5.17: Approximation steps that lead to the cell model. The full solution (a) is partitioned into Wigner-Seitz cells (b), which are conveniently symmetrized (c). Subsequently just one cell is considered (d) [DH01].

interactions between more than two particles are not simply expressible as a sum of pair interactions.

In the following section tailored computer simulations will be presented that offer an alternative approach if one wants to consider more complicated situations than the humble 1D two-particle problem. Before studying the results of these simulations, however, we will discuss how the ground-state multi-body problem can be treated in an approximate way.

5.3 The multi-body problem

The phase behavior of an infinite number of membrane-curving spheres is analyzed using a cell model. If the spheres adhere to alternating sides, a phase separation can be found at high particle densities. Spheres at lower densities adhering to the same side of the membrane can aggregate if they also vesiculate subsequently. This agrees with results from computer simulations.

Multi-body effects become particularly important if one considers 2D bulk phases like a system consisting of many particles that adhere to the same side of the membrane and repel each other. To determine state variables like the lateral particle pressure, one may think about using a cell model like it is used, for instance, in nonlinear Poisson-Boltzmann theory [DH01].

5.3.1 Cell model

Approximations

In fact, the situations are quite similar: consider an overall neutral 3D system of like charged colloids together with the appropriate number of oppositely charged counterions. In Poisson-Boltzmann theory these counterions are replaced by a charge density, which is treated in a mean field way. The colloids will typically

organize such as to keep themselves mutually apart. One can then partition the volume into Wigner-Seitz cells, each containing one colloid. Every cell has essentially the same volume and is charge neutral by construction, which means that different cells do not significantly interact with each other. The cell model then considers just one cell, symmetrizes it, and calculates its free energy in dependence of the cell volume by solving the Poisson-Boltzmann equation (see Fig. 5.17). The remaining effect of all other colloids is to determine the volume of the cell. If one wants to know the pressure in the system, one has to differentiate the free energy of one cell with respect to the cell's volume. This pressure is proportional to the ion density at the cell boundary, a result which is exact and, incidentally, does not rely on the approximations of Poisson-Boltzmann theory [DH01].

In analogy to the 3D case, one can also partition the interface of a 2D bulk system of particles bound to a membrane into two-dimensional cells. Instead of solving the Poisson-Boltzmann equation, one now has to find a solution for the membrane shape equation.[13] Due to its nonlinearity, one cannot get analytical results in general as we have seen in this work. For an axisymmetric cell, however, a numerical solution can be found relatively easily. Moreover, it is possible to discuss stresses again and relate geometrical properties at the boundary to the lateral pressure of the system.

Lateral pressure

Consider one spherical particle of radius a in an axisymmetric cell of radius R_{cell} (see Fig. 5.18). The membrane wraps the particle up to a contact angle α_{c} which will be fixed in the following. Two configurations of the whole bulk system are of interest here: all colloids are either on the same side of the membrane ("symmetric" case) or on alternating sides ("antisymmetric" case). In each case different choices of boundary conditions at the cell boundary are possible (see again Fig. 5.18): (i) in the symmetric case the profile must be flat at the cell boundary if one asks for a homogeneous system which is infinite (*i. e.*, flat on a large scale). However, since the symmetry between the two sides of the membrane is explicitly broken, one might alternatively also consider states where colloids populate a membrane displaying large-scale curvature—a finite colloid-studded membrane bud. The angle at R_{cell}, ψ_{cell}, can then be obtained by searching for the profile that minimizes the (free) energy E of the system. (ii) In the antisymmetric case the system will always be flat on a large scale. The two-particle analog suggests that the curvatures $K_\perp$ and $K_\parallel$, and therefore K, all must be equal to zero at the straight boundaries between the Wigner-Seitz cells (see page 115). However, in an axisymmetric cell $K_\parallel = -\sin\psi_{\text{cell}}/R_{\text{cell}}$ does not vanish in general. One thus has to choose whether

---

[13] Note that this method has been used before to describe inclusion-containing and two-component membranes, respectively (see, for instance, Refs. [AEBD+96, NGA98, GG01, FIM06]).
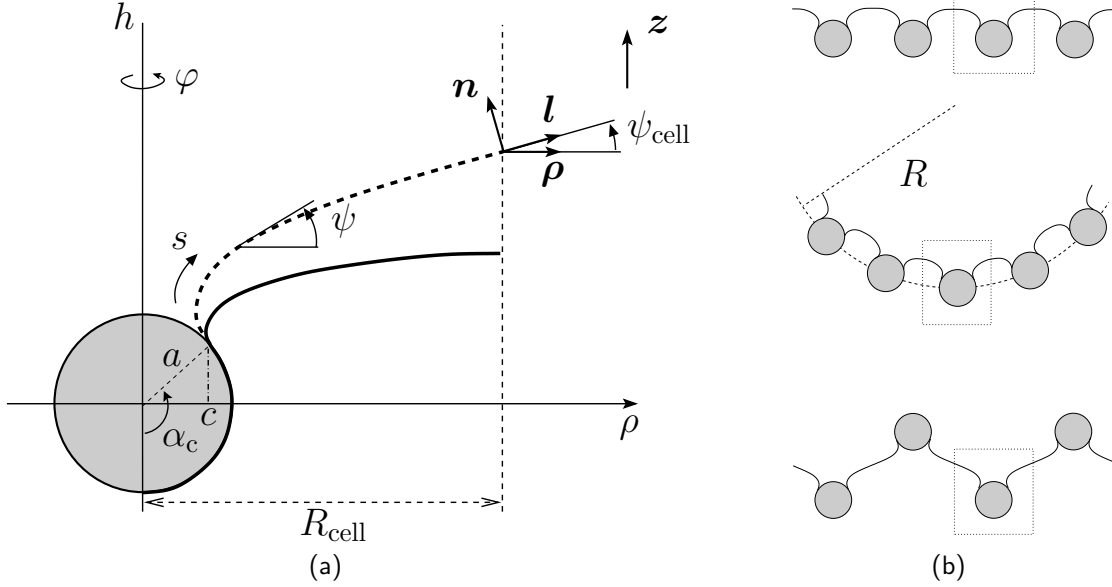
Figure 5.18: (a) Geometry of the axisymmetric cell. (b) Configurations of the bulk system (simplified 1D illustration): asymptotically flat symmetric case (above), membrane bud with curvature radius R (middle), asymptotically flat antisymmetric case (below). The cell size is indicated with a dotted rectangle for each case.

$K_\perp$ or $K = K_\perp + K_\parallel$ is set to zero at the cell boundary. This choice is part of the approximations of the cell model (a price we pay for axisymmetry) and yields different results as we will see below.

The membrane profile and the energy E of one cell will in general depend on the (projected) area of the cell, $A_\text{cell} = \pi R_\text{cell}^2$. A derivative of E with respect to A_cell gives the lateral pressure of the system in analogy to the 3D case:

$$\Pi = -\frac{\partial E}{\partial A_\text{cell}} = -\frac{1}{2\pi R_\text{cell}} \frac{\partial E}{\partial R_\text{cell}} \ . \tag{5.73}$$

This pressure can be related to the geometry of the membrane. Recall that a change in energy due to the variation of a boundary is given by Eqn. (3.12):

$$\delta E = -\oint_\mathcal{C} \mathrm{d}s \, l_a \Big[\boldsymbol{f}^a \cdot \delta \boldsymbol{X} - \mathcal{H}^{ab} \boldsymbol{e}_b \cdot \delta \boldsymbol{n} \Big] \, , \tag{5.74}$$

where $l_a \mathcal{H}^{ab} \boldsymbol{e}_b = \kappa K \boldsymbol{l}$ for a membrane (compare Eqn. (2.35)) and we have written $\boldsymbol{n} \cdot \delta \boldsymbol{e}_b = -\boldsymbol{e}_b \cdot \delta \boldsymbol{n}$ again. To determine the pressure, one has to calculate how the energy changes due to the variation $\delta \boldsymbol{X} = \boldsymbol{\rho} \, \delta R_\text{cell}$ where $\delta \boldsymbol{n} = -\boldsymbol{l} \, \delta \psi_\text{cell}$ (see again Fig. 5.18). Exploiting axial symmetry and integrating along a circle of radius

$\rho = R_{\text{cell}}$, one obtains

$$\delta E = -2\pi R_{\text{cell}} \left[l_a \boldsymbol{f}^a \cdot \boldsymbol{\rho} + \kappa K \frac{\partial \psi_{\text{cell}}}{\partial R_{\text{cell}}} \right]_{\rho=R_{\text{cell}}} \delta R_{\text{cell}} \ . \tag{5.75}$$

If this relation is combined with Eqn. (5.73), an expression for the lateral pressure in terms of the geometry at the boundary results:

$$\Pi = \left[l_a \boldsymbol{f}^a \cdot \boldsymbol{\rho} + \kappa K \frac{\partial \psi_{\text{cell}}}{\partial R_{\text{cell}}} \right]_{\rho=R_{\text{cell}}} \ . \tag{5.76}$$

The pressure is given as the projection of the stress tensor plus a term due to the intrinsic torque. This is strongly reminiscent of the discussion from Sec. 3.4 where both terms entered the balance equation at the contact line between a fluid surface and a rigid substrate. In both cases the variation is fixed: by the substrate in the case of fluid surface adhesion, by the definition of the lateral pressure in the case of the cell.

Let us for simplicity consider the case $\sigma = 0$ in the following. The Hamiltonian is then given by curvature alone,

$$\mathcal{H} = \frac{1}{2} \kappa K^2 \ , \tag{5.77}$$

and we can study Eqn. (5.76) for the different configurations which were introduced in the beginning of this section. Let us start with the symmetric case again: if one allows the membrane to form a bud (see Fig. 5.18(b)) and searches for the profile that minimizes the energy E of the cell, one will always arrive at the catenoid which has zero mean curvature everywhere and thus zero energy (see Technical Point 2.2 on page 35). This implies that the pressure will vanish as well. We will come back to that point in the next paragraph. If one wants the profile to be flat on a large scale, it has to be flat at the cell boundary. The angle ψ_{cell} is always zero; thus, $\partial \psi_{\text{cell}} / \partial R_{\text{cell}}$ vanishes and the pressure is given by

$$\Pi_{\text{sym}} = \frac{\kappa}{2} K_\perp^2 \ . \tag{5.78}$$

It is always positive and proportional to the squared perpendicular curvature at the boundary of the cell. Eqn. (5.78) resembles expression (5.12) for the force of the symmetric two-cylinder case. Note, however, that an additional surface tension σ in the Hamiltonian density (5.77) would enter Π_{sym} whereas such a term does not change the functional form of the repulsive force between two cylinders on the same side of a membrane.[14]

---

[14] One might expect that an additional surface tension will decrease the pressure. However, $K_\perp$ will change as well if σ is increased. The overall effect is not obvious at all.

In the antisymmetric case we have seen that either K or $K_\perp$ may be chosen to be zero at the cell boundary. The former case corresponds to a catenoid, implying zero lateral pressure, whereas in the latter one finds the expression:

$$\Pi_{\text{antisym}} = \left[-\frac{\kappa}{2} K_\parallel^2 (\boldsymbol{l} \cdot \boldsymbol{\rho}) - \kappa (\nabla_\perp K)(\boldsymbol{n} \cdot \boldsymbol{\rho}) \right] + \kappa K \frac{\partial \psi_{\text{cell}}}{\partial R_{\text{cell}}} \qquad (5.79)$$

for the lateral pressure of the system. In contrast to the symmetric case, Π_{antisym} does not only depend on the profile at a given cell radius R_{cell} but also on a derivative with respect to R_{cell}. The sign of Π_{antisym} is not fixed but may change depending on the parameters.

To obtain numbers for Π_{sym} and Π_{antisym}, the shape equation has to be solved numerically.

Numerical solutions

Fortunately, in Chap. 4 we considered a similar situation, a parabolic tip adhering to a membrane in an axisymmetric configuration. One can indeed use the same method as in Sec. 4.3.2 to solve the cell model. Rewriting the problem in a Hamiltonian formulation, one obtains the Hamilton equations (4.13) with two small differences: the force F as well as the surface tension σ are now equal to zero.

We assume that the angle at the contact point, where the membrane detaches from the particle, is fixed to α_{c}. The contact point c is then given by $c = a \sin \alpha_{\text{c}}$. Furthermore, either the angle ψ_{cell} (symmetric case) or the curvature $K_\perp$ (antisymmetric case) are set to zero at the cell boundary. Finally, the Hamiltonian function $\mathscr{H}$ is conserved and vanishes exactly as in Sec. 4.3.2.

Solving the Hamilton equations subject to these boundary conditions with a shooting method analogous to the one explained in Technical Point 4.3 yields profiles for given cell radius R_{cell}. The energy follows by numerically integrating the energy density (5.77) over the surface of the membrane. Its negative derivative with respect to the cell area then yields the lateral pressure (see Eqn. (5.73)). Alternatively, one can use Eqns. (5.78) and (5.79) to calculate Π.[15]

We will not discuss the numerical calculations in full detail here but will instead focus on a wrapping angle α_{c} of $120°$ which is high enough for nonlinear effects to appear in the solution.

Symmetric case Fig. 5.19 shows the scaled energy $\tilde{E} := E/\kappa$ of the cell as a function of the scaled cell area $\tilde{A}_{\text{cell}} := A_{\text{cell}}/a^2$ in the symmetric case. The energy increases for decreasing cell size until the point is reached at which the system is

---

[15] Comparing the results of both methods is in fact a nice consistency check for the numerical calculations.

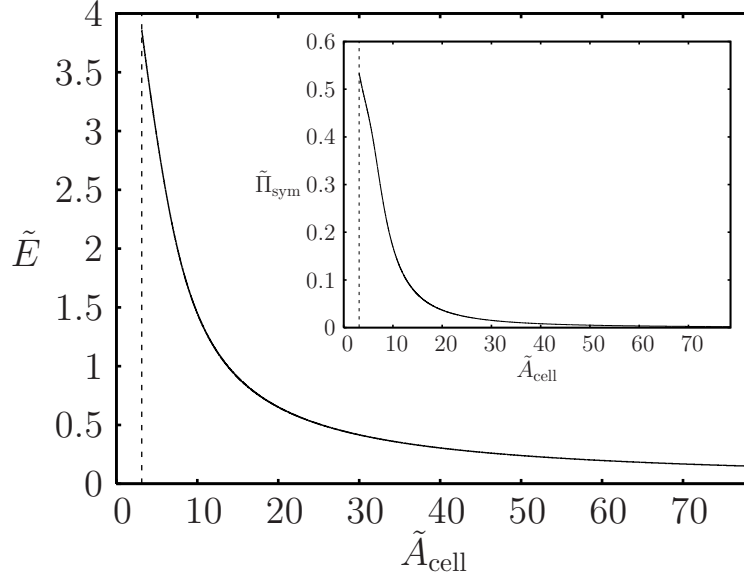**Figure 5.19:** Scaled energy and lateral pressure (inset) of the cell as a function of scaled cell area for $\alpha_c = 120°$ in the symmetric case. The dashed line denotes the cell area at which the system is densely packed ($\tilde{A}_{\mathrm{cell}} = \pi$) and the particles cannot approach closer.

densely packed and the particles cannot approach closer. In the symmetric case this happens at $\tilde{R}_{\mathrm{cell}} = 1$ where $\tilde{R}_{\mathrm{cell}} := R_{\mathrm{cell}}/a$.

The corresponding scaled pressure $\tilde{\Pi}_{\mathrm{sym}} := \Pi_{\mathrm{sym}} a^2/\kappa$ is plotted in the inset of Fig. 5.19. It is positive and is a monotonically falling function of $\tilde{A}_{\mathrm{cell}}$. Consequently, the cell model predicts that the colloids repel each other at all distances if the angle at the boundary is fixed to zero.

However, we did not yet take into account that *parts* of the system may bulge to evade the pressure and form buds, even if the system is flat at infinity. Such a bud will change the total energy: inside the bud the cell model predicts that the membrane in each cell will be a catenoid of zero energy (see above). With every particle in the bud one thus gains an energy of $\tilde{E}(\tilde{A}_{\mathrm{cell}})$ compared to the flat state. On the other hand, a neck of energy $\tilde{E}_{\mathrm{neck}}$ will form which connects the bud to the rest of the membrane. One arrives at

$$\tilde{E}_{\mathrm{bud}} = \tilde{E}_{\mathrm{neck}} - N_{\mathrm{bud}}\tilde{E}(\tilde{A}_{\mathrm{cell}}) \tag{5.80}$$

for the energy change due to the creation of one bud containing N_{bud} particles. If one assumes that the neck of the bud is a catenoid as well, the system will gain energy with every additional particle joining the bud. A small additional pair

attraction, *e. g.* due to fluctuation-induced Casimir forces, suffices for the number N_{bud} to increase over time. At some particle number the bud will pinch off and form a vesicle. When this happens cannot be predicted quantitatively within our simple model as it does not determine how much area in the bud will be occupied per cell.

Antisymmetric case If the colloids adhere to alternating sides of the membrane, the system has to stay flat. It can, however, pack denser than in the symmetric case because nearest neighbors do not lie in the same plane. For the axisymmetric cell the highest density is reached at $\tilde{A}_{\mathrm{cell}} = 2.12 < \pi$. For smaller cell areas no stable solution can be found.[16]

In the upper part of Fig. 5.20 the scaled energy is plotted. It exhibits a maximum at $\tilde{A}_{\mathrm{cell}} \approx 3.43$ which corresponds to a cell radius $\tilde{R}_{\mathrm{cell}}$ of 1.045. Around this maximum the energy is *concave.* Its second derivative with respect to the cell area is negative:

$$\frac{\partial^2 \tilde{E}}{\partial \tilde{A}_{\mathrm{cell}}^2} = -\frac{\partial \tilde{\Pi}}{\partial \tilde{A}_{\mathrm{cell}}} < 0 \; . \tag{5.81}$$

Such a behavior is unphysical since it implies that a *reduction* of the cell area will lead to a *reduction* of the pressure (see also lower part of Fig. 5.20). The system would be mechanically unstable and collapse. The reason for this peculiarity is that we implicitly assumed that the system consists of exactly one homogeneous phase. This is not correct for high particle densities. Between a cell area of $\tilde{A}_{\mathrm{cell}}^{\alpha}$ and $\tilde{A}_{\mathrm{cell}}^{\beta}$ the system will phase separate into a densely packed phase α and a less denser phase β which are in coexistence with each other (see again Fig. 5.20). This behavior resembles that of well-known systems such as a van der Waals gas below the critical temperature $T < T_c$ [Cal85].

Phase separation and Maxwell construction

In the coexistence region the system will always gain free energy by phase separating into the two phases. Their relative weight is given by the lever rule [Cal85]. The corresponding values of $\tilde{A}_{\mathrm{cell}}^{\alpha}$ and $\tilde{A}_{\mathrm{cell}}^{\beta}$ can be obtained by changing from the free energy E to the Gibbs free energy G with a Legendre transform:

$$\tilde{G}(\tilde{\Pi}) = \min_{\tilde{A}_{\mathrm{cell}}} \left\{ \tilde{E}(\tilde{A}_{\mathrm{cell}}) + \tilde{\Pi}\tilde{A}_{\mathrm{cell}} \right\} \; , \tag{5.82}$$

where $\tilde{G}$ is scaled with κ exactly as $\tilde{E}$. The Gibbs free energy depends on the pressure. If one plots $\tilde{E} + \tilde{\Pi}\tilde{A}_{\mathrm{cell}}$ for a fixed $\tilde{\Pi}$ as a function of $\tilde{A}_{\mathrm{cell}}$, the global

---

[16] Note, however, that one must be careful when interpreting results of the model for these high densities since an axisymmetric cell is a rather crude approximation of the real configuration if the colloids are very close to each other.
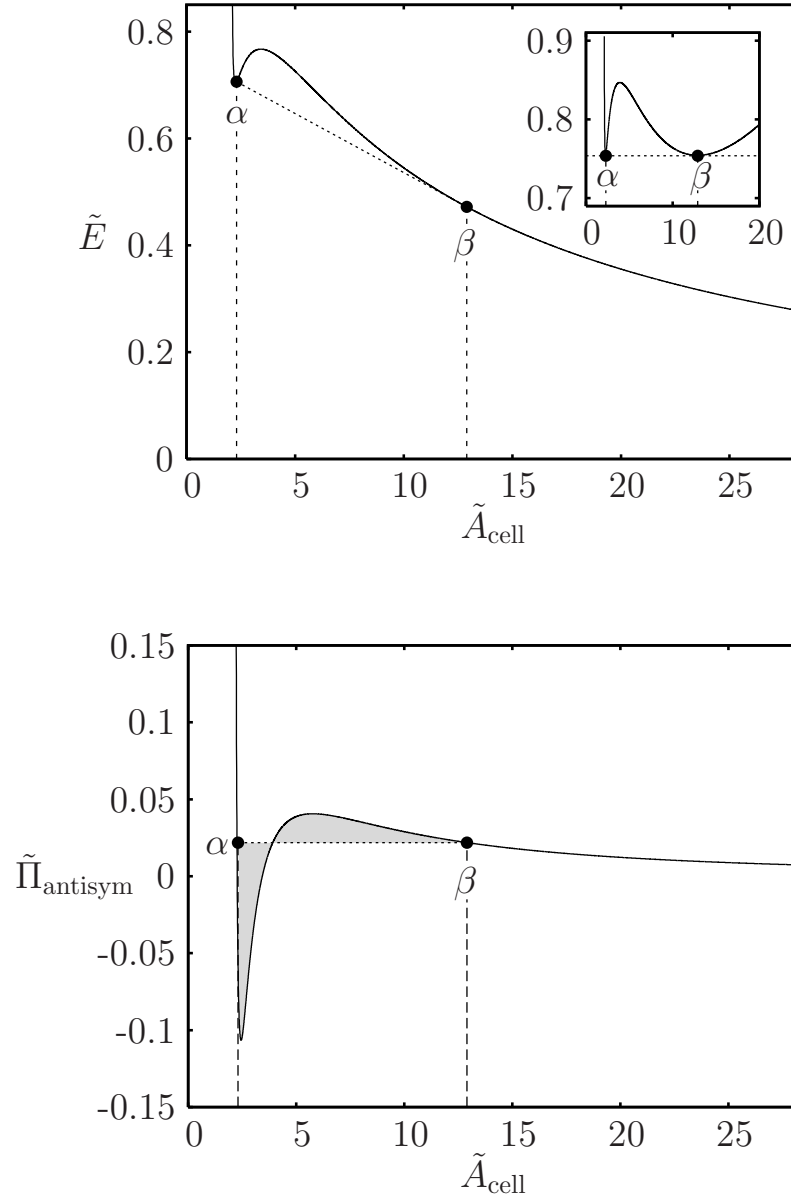
Figure 5.20: Scaled energy (above) and lateral pressure (below) of the cell as a function of scaled cell area for $\alpha_\mathrm{c} = 120°$ in the antisymmetric case (solid lines). In the inset above, $\tilde{E} + \tilde{\Pi}_{\alpha\beta}\tilde{A}_\mathrm{cell}$ is plotted as a function of $\tilde{A}_\mathrm{cell}$. The dashed lines denote the coexistence region, *i. e.*, the cell areas $\tilde{A}^\alpha_\mathrm{cell} = 2.3$ and $\tilde{A}^\beta_\mathrm{cell} = 12.9$ between which the system phase separates into a dense and a dilute phase, as explained in the text.

minimum is located at the cell area which corresponds to $\tilde{\Pi}$. At some particular pressure $\tilde{\Pi}_{\alpha\beta}$ two minima of equal height can be found (see inset in the upper part of Fig. 5.20). At this pressure the system phase separates into the two homogeneous phases α and β corresponding to the two minima. Thus,

$$\tilde{G}_{\alpha}(\tilde{\Pi}_{\alpha\beta}) = \tilde{G}_{\beta}(\tilde{\Pi}_{\alpha\beta}) \,, \tag{5.83}$$

where $\tilde{\Pi}_{\alpha\beta}$ does not depend on $\tilde{A}_{\text{cell}}$. In other words, the pressure is constant in the coexistence region and the free energy is a linear function of $\tilde{A}_{\text{cell}}$ (see dotted lines in the upper part of Fig. 5.20). The derivative $\partial\tilde{G}/\partial\tilde{\Pi}$ is equal to the cell area and displays a jump at $\tilde{\Pi}_{\alpha\beta}$. This implies that the phase transition is of first order.

For the given configuration Eqn. (5.83) holds if $\tilde{\Pi}_{\alpha\beta} = 0.022$. From Fig. 5.20 one can now read off the values of the cell areas of the two different phases: $\tilde{A}_{\text{cell}}^{\alpha} = 2.3$ and $\tilde{A}_{\text{cell}}^{\beta} = 12.9$. The former corresponds to a cell radius of $\tilde{R}_{\text{cell}}^{\alpha} = 0.86$, the latter to $\tilde{R}_{\text{cell}}^{\beta} = 2.03$.

The free energy difference between the phases α and β can be obtained from Eqn. (5.83) as well:

$$\Delta\tilde{E}_{\alpha\beta} := \tilde{E}_{\alpha} - \tilde{E}_{\beta} = \tilde{\Pi}_{\alpha\beta}(\tilde{A}_{\text{cell}}^{\beta} - \tilde{A}_{\text{cell}}^{\alpha}) \,. \tag{5.84}$$

If one uses the original (unphysical) pressure function, $\Delta\tilde{E}_{\alpha\beta}$ can also be written as

$$\Delta\tilde{E}_{\alpha\beta} = \int_{\tilde{A}_{\text{cell}}^{\alpha}}^{\tilde{A}_{\text{cell}}^{\beta}} \mathrm{d}\tilde{A}_{\text{cell}} \, \tilde{\Pi} \,. \tag{5.85}$$

The equivalence of Eqn. (5.84) and (5.85) implies that the shaded areas in the lower part of Fig. 5.20 are equal. This is also known as the *Maxwell construction* and provides an alternative way to obtain $\tilde{\Pi}_{\alpha\beta}$.

To conclude, we have used a cell model to study multi-body interactions between membrane-bound spherical particles. For high densities a phase separation could be found in the antisymmetric case if $K_{\perp}$ is set to zero at the cell boundary. In the symmetric case the formation of buds was predicted. Further studies with this model could include tension as well and investigate how a change of the contact angle influences the system. In the following we will see how the presented calculations compare to numerical computer simulations. In particular, we have to check whether the approximations of the cell model are still valid in these simulations.

5.3.2 Coarse-grained computer simulations

Modeling membrane-mediated interactions

In molecular dynamics (MD) computer simulations Newton's equations of motion are integrated numerically in discrete time steps to determine how a many-particle
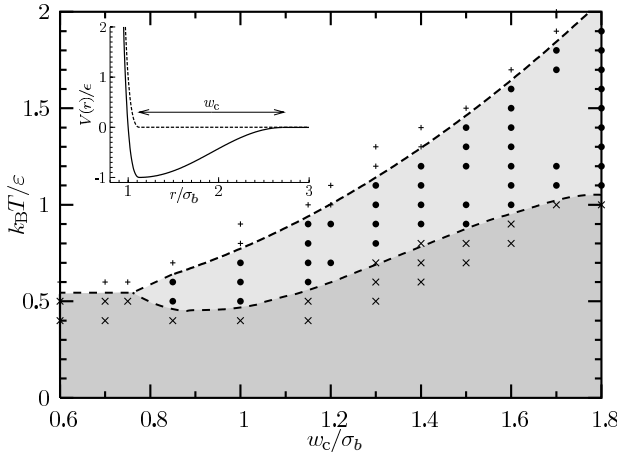
━━━━ **Technical Point 5.8:** *Coarse-grained membrane* model ━━━━

In the simulations, σ_b and ϵ are used as units of length and energy, respectively. Individual lipids are represented by one head bead and two tail beads. Their size is fixed via a Weeks-Chandler-Andersen (WCA) potential (see Eqn. (5.X) below). The three beads are linked by two finite extensible nonlinear elastic (FENE) bonds with $k_{\text{FENE}} = 30\epsilon/\sigma_b^2$ (see Eqn. (5.XI)).
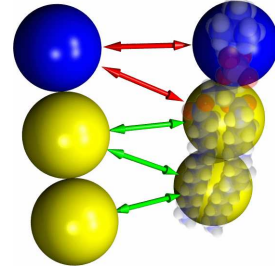
Between the head bead and the second tail-bead acts a harmonic spring with rest length $r_0 = 4\sigma_b$ and stiffness $k_{\text{bend}} = 10\epsilon/\sigma_b^2$. All *tail* beads attract according to $U_{\cos}(r)$ from Eqn. (5.XII) to mimic the hydrophobic effect and compensate the absence of explicit solvent molecules [CKD05, CD05]. The size b of the head bead can be tuned resulting in different self-assembled phases [CD06]. To ensure that a bilayer of appropriate thickness forms, b is set to $0.95\sigma_b$ where $\sigma_b \approx 1\,\text{nm}$.

The physical properties of the bilayer, *e. g.* its fluidity, can be widely tuned via the potential width w_c (see phase diagram on the left *(compare [CKD05])* for which the lateral tension is set to zero. The symbols denote the different phases •: fluid , ×: gel, and +: unstable). In the simulations of this section $w_c/\sigma_b = 1.6$ and $k_{\text{B}}T/\epsilon = 1.1$ which corresponds to $\kappa \approx 12\,k_{\text{B}}T$. All simulations were performed using the ESPResSo package [LAMH06, WWWa].

$$U_{\text{WCA}}(r) \;=\; 4\epsilon\left[\left(\frac{b}{r}\right)^{12} - \left(\frac{b}{r}\right)^{6} + \frac{1}{4}\right] \;,\; 0 < r < r_c = 2^{1/6}b \;, \qquad (5.\text{X})$$

$$U_{\text{FENE}}(r) \;=\; -\frac{1}{2}k_{\text{FENE}}\, r_\infty^2 \ln\left(1 - \frac{r^2}{r_\infty^2}\right) \;,\; 0 < r < r_\infty = 1.5\sigma_b \;, \qquad (5.\text{XI})$$

$$U_{\cos}(r) \;=\; \begin{cases} -\epsilon + U_{\text{WCA}}(r) & ,\; r < r_c = 2^{1/6}\sigma_b \\ -\epsilon \cos^2 \frac{\pi(r-r_c)}{2w_c} & ,\; r_c \leq r \leq r_c + w_c \end{cases} . \qquad (5.\text{XII})$$

system evolves in time [AT86, FS02]. A meaningful simulation of a membrane with tens of adhering proteins or viruses calls for model membranes extending in excess of 100 nm and simulation times of the order of milliseconds, which were until

(a)   (b)
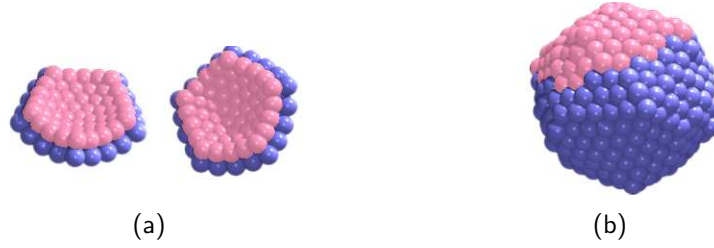
Figure 5.21: Curvature-inducing solid particles. (a) Caps   (b) Capsid. Only the light blue colored areas are attracted to the lipid head groups.

recently out of reach for conventional atomistic and many coarse-grained simulations. These problems are overcome with a recently developed coarse-grained model (see Technical Point 5.8 and Refs. [CKD05, CD05]) which achieves efficient simulation owing to the elimination of explicit solvent molecules.

The simulations discussed in this section use this model. They are performed at constant temperature and zero lateral pressure with periodic boundary conditions.[17] The simplified curvature-inducing particles are curved troughs, caps, or capsids (see Fig. 5.21 and inset of Fig. 5.22). They are created from beads of the same size $b = \sigma_b$ which are held together either by tight harmonic springs (troughs and caps) or FENE bonds and additional filler particles (spheres). The adhering beads interact with the lipid head beads attractively via a Lennard Jones potential ($\alpha = 2$ (troughs and caps), $\alpha = 1$ (capsids))

$$U_{\mathrm{LJ}} = 4\alpha\epsilon \left[\left(\frac{b}{r}\right)^{12} - \left(\frac{b}{r}\right)^{6} \right] \quad , \ 0 < r < r_c = 2.5\sigma_b \ , \qquad (5.86)$$

thus curving the membrane locally, whereas the nonadhering beads interact purely repulsively with a WCA potential (see Eqn. (5.X)). None of the beads of a solid particle attract other troughs, caps, or capsids.

Comparison to continuum theory

Like all coarse-grained approaches, the model eliminates atomistic detail and thus cannot be used to explore phenomena dependent on such detail. But on length scales of tens to hundreds of nanometers, relevant to the study of membrane-mediated interactions, it faithfully reproduces all key properties of self-assembling fluid bilayers, in particular the bending elasticity [CKD05]. In fact, Helfrich theory describes the behavior of the membrane surprisingly well. In a recent study no deviations from simple quadratic continuum theory could be found up to radii of curvature comparable to the bilayer thickness [HD06].

---

[17] For detailed information see the Supplementary Information of Ref. [RIH+07]
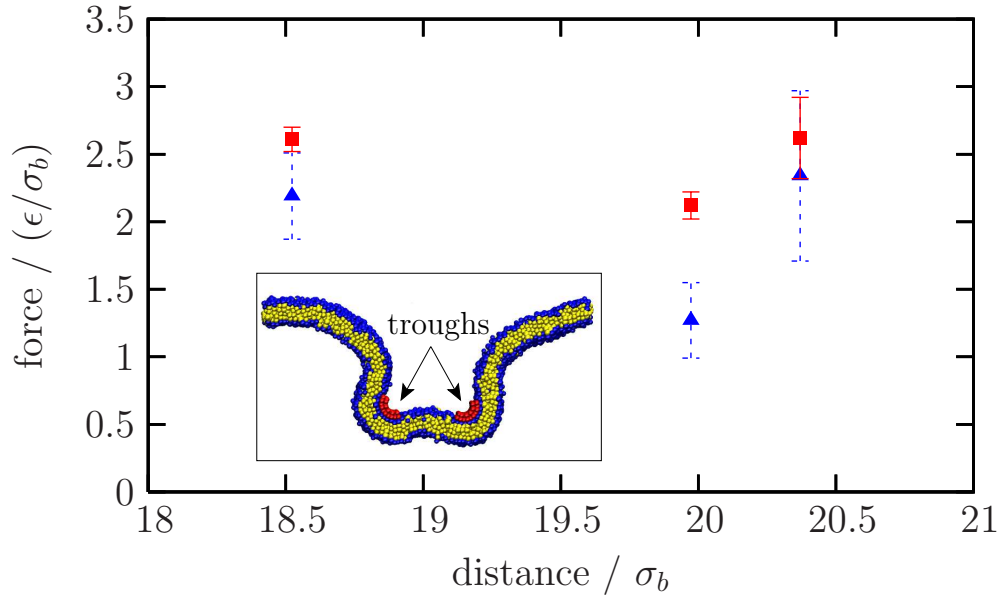
Figure 5.22: Calculation of the force between two cylinders on a membrane – comparison of the directly measured constraining force (■) vs. the force from a curvature analysis (▲). In the inset a snapshot of the simulation is shown (troughs: red; hydrophilic head beads: blue; hydrophobic tail beads: yellow) *(with courtesy of B. Reynwar)*.

To check whether the theory developed in this chapter can be applied to simulations of membrane-mediated interactions, two adhesive troughs of curvature radius $3\,\sigma_b$ are placed on a membrane in a symmetric configuration (see Fig. 5.22). These troughs model cylinders for which a (ground state) repulsive force is predicted analytically at all distances (see previous sections). Fixing the separation between the troughs, a curvature-mediated repulsion can indeed be measured. Two ways of obtaining the force are used: (i) a circle is fitted to the membrane region close to the mid-line between the two particles, giving $K_\perp$, which can then be inserted into the analytical force expression (5.12). (ii) The constraining force is measured that has to be applied during the simulation to keep the centers of mass of the two particles at the same horizontal distance. When comparing the results of both methods, one should be aware of the fact that finite size effects are neglected in method (i), *i. e.*, the curvature of the membrane at the boundaries of the simulation box which leads to an additional (small) contribution to the force is not taken into account. Despite this, the results agree qualitatively (see Fig. 5.22). The force measured in the simulation is thus most likely curvature-mediated. Therefore, we can use the model to study these interactions for a multi-body configuration.
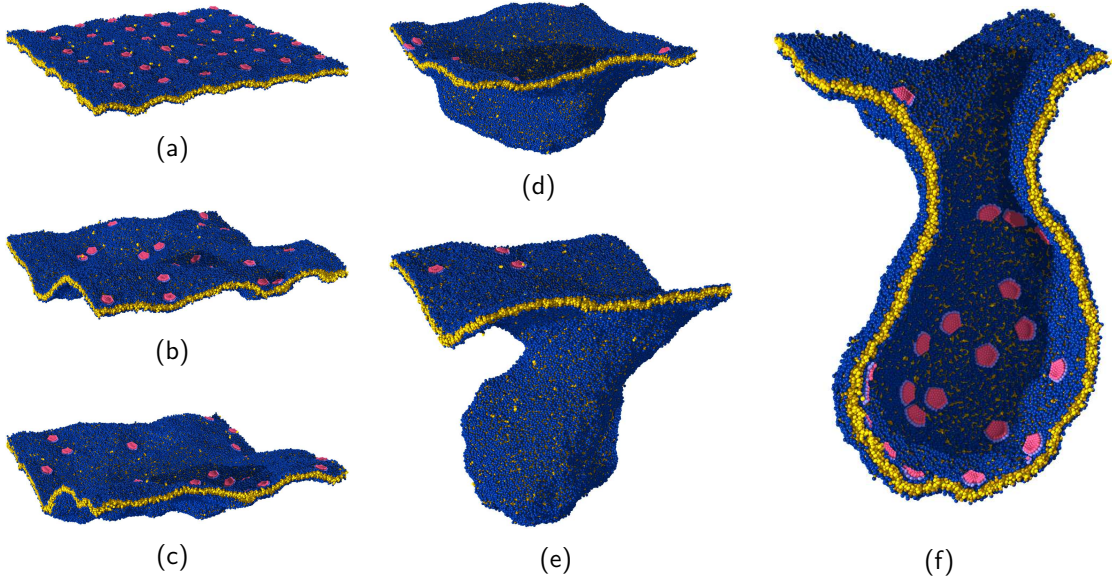
Figure 5.23: Vesiculation driven by 36 large caps on a membrane (series of simulation snapshots) [RIH$^+$07]. The times are: (a) $0\,\tau$ (b) $20,000\,\tau$ (c) $40,000\,\tau$ (d) $50,000\,\tau$ (e) $60,000\,\tau$ (f) $70,000\,\tau$.

Multibody interactions

Proteins To model curvature-inducing proteins, different cap sizes are used in the simulations, corresponding to 10% (small caps), 16 % (large caps), and 34 % (extra large caps) of a sphere of radius $5.5\,\sigma_b$. The size and degree of deflection of the two former are comparable to real proteins such as the BAR domain (see upper Fig. on page 5) [BV06].

Placing 36 small caps onto a tensionless square membrane with a side length of approximately 160 nm (46, 080 lipids), one observes only weak clustering for the entire $70,000\,\tau$ simulation time, where $\tau \approx 15$ ns based on lipid self-diffusion. Any mediated interaction is small compared to the thermal energy. In stark contrast, the large caps behave qualitatively differently (see Fig. 5.23 and Supplementary Video 1 at [WWWb]). After initial weak clustering, a sudden transition happens at approximately $40,000\,\tau$: most caps have by now aggregated into a single, almost flat cluster, which rapidly vesiculates within the subsequent $30,000\,\tau \approx 0.5$ ms. Notice that throughout this process individual caps neither touch nor order in a crystalline-like fashion. For extra large caps one observes that aggregation happens quicker, the aggregates are denser, and the vesicle sizes are smaller because fewer proteins suffice to create them (see Supplementary Video 2 at [WWWb]). Notice that in cellular organelles this mechanism additionally has to compete against a residual bilayer tension that suppresses vesicle formation beyond a critical size.

The vesiculation pathway observed in the simulations differs fundamentally from

scaffolding [MG05, ZK06] schemes, such as clathrin-dependent endocytosis, that require proteins to contact *directly* and *specifically*. Evidently, curvature-mediated interactions alone can induce aggregation and vesiculation (see also the Supplementary Information of Ref. [RIH$^+$07] for a detailed discussion of the energetics). This effect has not been seen in approximate linearized continuum theories for isotropic benders, possibly because the induced deformations are too strong to permit linearization—an approximation to which the sign of an interaction is known to be sensitive [GH99]. Conversely, while the observed attraction weakens and ultimately vanishes at diminishing curvature imprint, a crossover into the linearly predicted repulsive behavior could not be identified with statistical significance for the caps. Yet, in this limit other contributions to mediated interactions (such as fluctuation [GBP93], depletion, or tilt-mediated (see Sec. 5.1.4) forces) compete with the diminishing ground state curvature term, for which, furthermore, only the large-separation behaviour is known. It is thus not clear which force law one should expect for small deformations.

Viral capsids Let us finally look at spherical particles with a radius comparable to the cap-radius, attracting the membrane with 75% of their surface. Unlike model proteins, these objects may represent viral capsids or nanoparticles. Viral capsids are typically an order of magnitude larger than the particles used in the simulation but modeling them at a realistic scale becomes infeasible even for the type of coarse-grained model simulation presented here. However, due to the scale invariance of the Helfrich Hamiltonian the fundamental physics is not expected to change (except that the necessary adhesion energy would become smaller).

Within the first $2000\,\tau$ of placing 16 such capsids onto a tensionless square membrane of initial side-length $160\,\sigma_b$, the membrane contracts to $\approx 140\,\sigma_b$ as it coats the attractive part of the colloidal spheres (Fig. 5.24(a) to Fig. 5.24(b)). After the initial contraction, clustering sets in, always starting by the formation of *pairs* (Fig. 5.24(c)), and followed by subsequent tight vesiculation (Fig. 5.24(d)–5.24(f) and Supplementary Video 3 at [WWWb]). The resulting multi-capsid structures closely resemble morphologies encountered in the cooperative budding of late domain mutated Mason-Pfizer monkey viruses (MPMV) [GBM$^+$03], which also lack individual budding activity (Fig. 5.24(g)).

To quantify the pair attraction, two capsids are placed on a membrane analogous to the troughs in Fig. 5.22. For separations smaller than $16\,\sigma_b$ a significant attraction exists which is strongest around a separation of $12\,\sigma_b$ (for very short distances capsids repel due to direct contact). Because of system size requirements and slow thermal shape fluctuations the large distance asymptotics even for such strong deformers remains difficult to determine, but recent simulations show a crossover into the repulsive regime [Rey07].

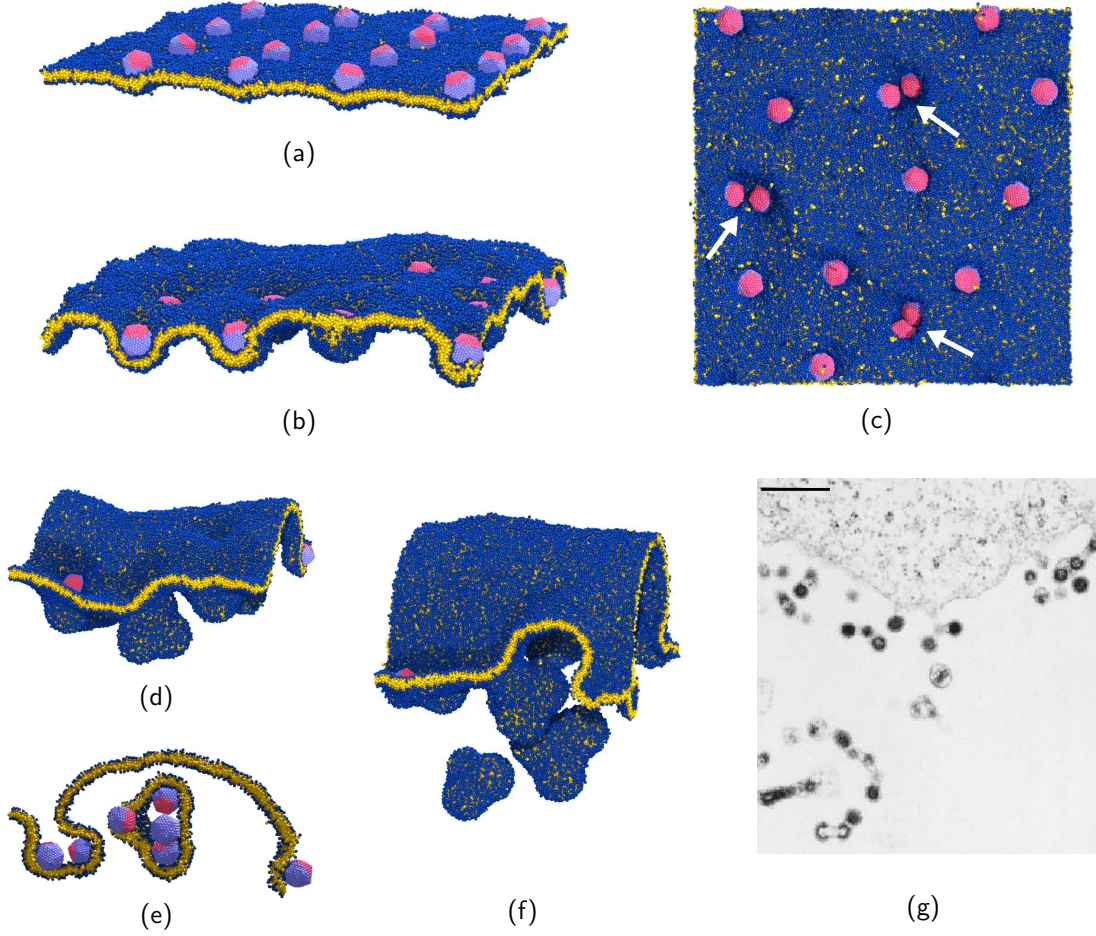For small separations the capsids tilt towards each other similar to the troughs.

Figure 5.24: Attraction and cooperative budding of 16 capsids on a membrane (series of simulation snapshots) [RIH$^+$07]. The times are: (a) $0\,\tau$ (b) $1,000\,\tau$ (c) $7,000\,\tau$ (d) $16,000\,\tau$ (e) $18,000\,\tau$ (f) $23,500\,\tau$. (g) Electron micrograph of late domain mutated MPMV virions. Scale bar in (g): 500nm *(reprinted from Ref. [GBM$^+$03] with permission of authors and publisher; copyright 2003, The American Society for Microbiology).*

From Eqn. (5.11) we know that for vanishing surface tension $\sigma = 0$ the net force between the two particles results from a competition between the force associated with the curvature $K_\perp$ along the direction joining the particles (which drives repulsion) and the force associated with the curvature $K_\parallel$ perpendicular to it (which drives attraction). Taken together this information points towards a possible mechanism for capsid attraction: as the spherical particles approach each other they flatten the former curvature by tilting, thus enabling the attractive forces associated with the second curvature direction to take over. This effect may be supplemented by a slight peeling of the membrane from the front and back of the capsids which could be observed in the simulations. Although it is difficult

to predict the outcome of this subtle balance analytically, the simulations clearly show that a sufficiently large curvature imprint will result in an overall attraction between membrane-adsorbed particles. The universal nature of this effect renders it extremely robust, and suggests that cells take advantage of it. In fact, cellular membrane control might even require measures to prevent such omnipresent aggregation.

Comparison between cell model and simulations

How do the cell model and the simulations compare? The parameters chosen for the sphere in the cell coincide with those of the capsid in the previous section: a contact angle α_c of 120° implies that the membrane covers 75% of the surface of the spherical particle. Asking for a cell radius $\tilde{R}_{\text{cell}}$ which corresponds to the configuration of the simulations one obtains a value between 3 and 4, which is in the range of cell radii discussed in Sec. 5.3.1. Furthermore, the model membrane in the simulations can be described by the pure bending Hamiltonian (5.77).[18] Comparing the results from the cell model and the simulations we see that they agree qualitatively. In the simulations the membrane bulges, forms buds and vesiculates as anticipated by the calculations of the cell model. However, a *quantitative* comparison is nontrivial as the approximations made in the cell model are too crude. Whether or not the cell model can be refined in such a way that it predicts results of the simulations such as the number of particles per bud remains to be seen and is an interesting question for future investigations.

---

[18] In fact, in the simulations the lateral pressure is fixed which implies that a very small surface tension can remain as the membrane is curved at the boundaries of the box.

Conclusions

The mechanics of fluid membranes and similar surfaces were studied using a combination of analytical theory, numerical calculations, and computer simulations. These techniques proved complementary to one another yielding results which would probably have been overlooked if just one approach was chosen. For example, in the context of interface-mediated interactions between two particles, several analytical conditions on the interface geometry could be derived within the geometrical framework introduced in Chap. 2. For the simple 1D problem this tool was complemented with profile calculations to extract numbers for the strength of interaction. To analyze more complicated configurations quantitatively, tailored computer simulations were presented and compared to the predictions of a cell model.

When asking whether these theoretical studies are relevant for the biological membrane, one always has to be aware that simplifications and approximations are involved which have to be checked carefully. Membrane-mediated interactions, for example, will certainly be influenced by other components of the cell, such as the cytoskeleton, especially if the length scales of interest are larger than the cytoskeletal mesh size; in the other limit, a continuum description of the membrane will certainly fail at length scales smaller than the bilayer thickness.

Yet, the hope is that investigations of simpler systems may further the understanding of the fundamental mechanisms underlying biological function, an idea which is quite familiar to the physicist. Using synthetic soft materials in a well-defined setup indeed paves the way for quantitative predictions as we have seen for the nanodrum in Chap. 4. To check predictions such as these and apply the resulting insights to nature, biologists and physicists must join forces and share their expertise. The author hopes that the results obtained and the techniques discussed in this thesis will be helpful; maybe they add a few tesserae to the final picture which will contain an explanation of how the biological cell functions.

A Classical differential geometry of two-dimensional surfaces

A.1 Basic definitions

This section gives an overview of the basic notions of differential geometry for two-dimensional surfaces. It follows mainly Ref. [Kre91] in its discussion and is an extension of App. B from Ref. [Mül04]. For more information on the differential geometry of two-dimensional surfaces see also Refs. [Car76], [Spi76], and [NPW04, Chap. 7].

Definition of a surface

Let us consider the vector function $\boldsymbol{X}(\xi^1, \xi^2) \in \mathbb{R}^3$ with

$$\boldsymbol{X} : \mathbb{R}^2 \supset \Xi \ni (\xi^1, \xi^2) \mapsto \boldsymbol{X}(\xi^1, \xi^2) \in U \subset \mathbb{R}^3 \ , \tag{A.1}$$

where Ξ is an open subset of $\mathbb{R}^2$. Let $\boldsymbol{X}(\xi^1, \xi^2)$ be of class $r \geq 1$ in Ξ, which means that one of its component functions X_i ($i \in \{x, y, z\}$) is of class r and the other ones are at least of this class.[1] Let furthermore the Jacobian matrix $\frac{\partial(X_x, X_y, X_z)}{\partial(\xi^1, \xi^2)}$ be of rank 2 in Ξ which implies that the vectors

$$\boldsymbol{e}_a := \frac{\partial \boldsymbol{X}}{\partial \xi^a} = \partial_a \boldsymbol{X} \ , \quad a \in \{1, 2\} \ , \tag{A.2}$$

are linearly independent. The mapping (A.1) then defines a smooth two-dimensional surface patch U embedded in three-dimensional Euclidean space $\mathbb{R}^3$ with coordinates ξ^1 and ξ^2 (see Fig. A.1). A union Σ of surface patches is called a surface if two arbitrary patches U and U' of Σ can be joined by finitely many patches $U = U_1, U_2, \ldots, U_{n-1}, U_n = U'$ in such a way that the intersection of two subsequent patches is again a surface patch. This implies that for $U_j \cap U_k \neq \emptyset$ ($j, k \in \{1, \ldots, n\}$) a mapping of class r between the two planar images of the intersection exists, *i. e.*, a transformation between the coordinates corresponding to U_j and U_k [Kre91, p. 76]. To simplify the following, let us restrict ourselves to a surface that can be covered by one patch U only.

---

[1] A function of one or several variables is called a *function of class r* if it possesses continuous partial derivatives up to order r.
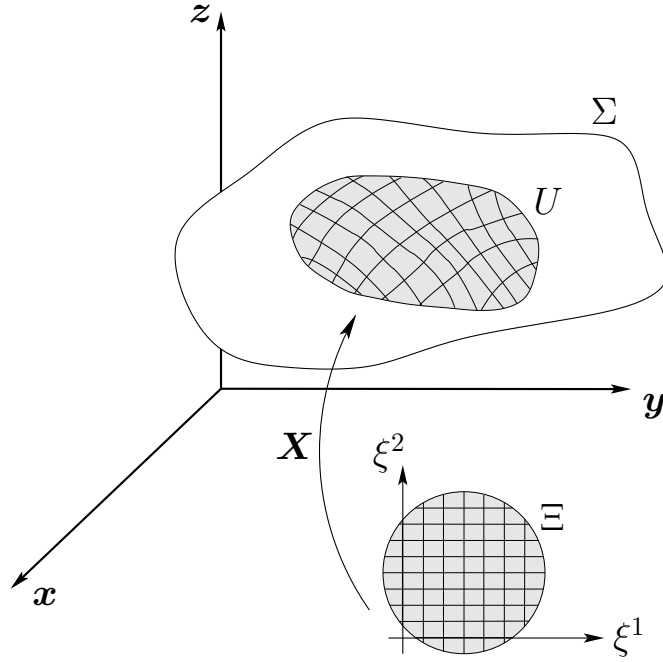
Figure A.1: Parametrization of a surface

The vectors $\boldsymbol{e}_a$, defined in Eqn. (A.2), are the tangent vectors of the surface. They are not normalized in general. Together with the unit normal

$$\boldsymbol{n} := \frac{\boldsymbol{e}_1 \times \boldsymbol{e}_2}{|\boldsymbol{e}_1 \times \boldsymbol{e}_2|} \ , \tag{A.3}$$

they form a local basis (*local frame*) in $\mathbb{R}^3$ (see Fig. A.2):

$$\boldsymbol{e}_a \cdot \boldsymbol{n} = 0 \ , \quad \text{and} \quad \boldsymbol{n} \cdot \boldsymbol{n} = 1. \tag{A.4}$$

The metric tensor (first fundamental form)

With the tangent vectors $\boldsymbol{e}_a$, one can define the *metric tensor* (also called the *first fundamental form*)

$$g_{ab} := \boldsymbol{e}_a \cdot \boldsymbol{e}_b \ . \tag{A.5}$$

This covariant second rank tensor is symmetric ($g_{ab} = g_{ba}$) and positive definite [Kre91, p. 86]. It helps to determine the infinitesimal Euclidean distance in terms of the coordinate differentials [Kre91, p. 82]

$$
\begin{aligned}
\mathrm{d}s^2 &= [\boldsymbol{X}(\xi^1 + \mathrm{d}\xi^1, \xi^2 + \mathrm{d}\xi^2) - \boldsymbol{X}(\xi^1, \xi^2)]^2 = (\boldsymbol{e}_1 \, \mathrm{d}\xi^1 + \boldsymbol{e}_2 \, \mathrm{d}\xi^2)^2 \\
&= (\boldsymbol{e}_a \, \mathrm{d}\xi^a)^2 = (\boldsymbol{e}_a \cdot \boldsymbol{e}_b) \, \mathrm{d}\xi^a \, \mathrm{d}\xi^b \\
&= g_{ab} \, \mathrm{d}\xi^a \, \mathrm{d}\xi^b \ ,
\end{aligned}
\tag{A.6}
$$
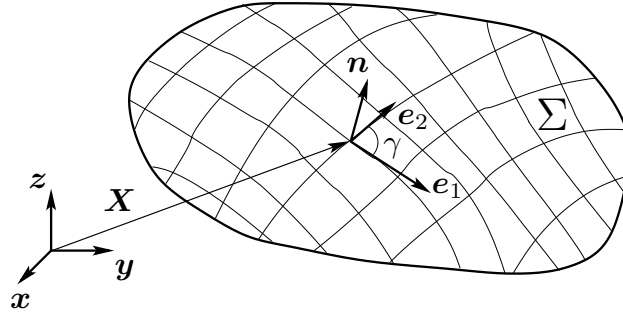
Figure A.2: Local frame on the surface

where the sum convention is used in the last two lines (see footnote 10 on page 18). The contravariant dual tensor of the metric may be defined via

$$g_{ac}\, g^{cb} := \delta_a^b := \begin{cases} 1, & \text{if } a = b \\ 0, & \text{if } a \neq b \end{cases}, \tag{A.7}$$

where δ_a^b is the Kronecker symbol. The metric and its inverse can be used to raise and lower indices in tensor equations. Consider, for instance, the second rank tensor t_{ab}:

$$\text{Raising:} \quad t_{ac}\, g^{cb} = t_a{}^b\,, \qquad \text{and lowering:} \quad t_a{}^c\, g_{cb} = t_{ab}\,. \tag{A.8}$$

The determinant of the metric[2]

$$g := \det \mathbf{g} = \det (g_{ab}) = g_{11}g_{22} - g_{12}g_{21} \tag{A.9}$$

can be exploited to calculate the infinitesimal area element dA: let γ be the angle between $\boldsymbol{e}_1$ and $\boldsymbol{e}_2$ (see Fig. A.2). Then

$$\begin{aligned} |\boldsymbol{e}_1 \times \boldsymbol{e}_2|^2 &= |\boldsymbol{e}_1|^2 |\boldsymbol{e}_2|^2 \sin^2 \gamma = g_{11}g_{22}(1 - \cos^2 \gamma) = g_{11}g_{22} - (\boldsymbol{e}_1 \cdot \boldsymbol{e}_2)^2 \\ &= g_{11}g_{22} - g_{12}g_{12} = g\,, \end{aligned} \tag{A.10}$$

and thus

$$dA = |\boldsymbol{e}_1 \times \boldsymbol{e}_2|\, d\xi^1\, d\xi^2 = \sqrt{g}\, d^2\xi\,. \tag{A.11}$$

The epsilon-tensor

The epsilon-tensor

$$\varepsilon_{ab} := \boldsymbol{n} \cdot (\boldsymbol{e}_a \times \boldsymbol{e}_b)\,. \tag{A.12}$$

---

[2] Note that $\mathbf{g}$ is the matrix consisting of the metric tensor components g_{ab}.

is antisymmetric in its two indices $\varepsilon_{ab} = -\varepsilon_{ba}$. It can also be written as $\varepsilon_{ab} = \sqrt{g}\,\epsilon_{ab}$ with $\epsilon_{12} = -\epsilon_{21} = 1$ and $\epsilon_{11} = \epsilon_{22} = 0$. This implies $\varepsilon^{ab} = \sqrt{g}^{-1}\epsilon_{ab}$. The metric and the epsilon tensor are connected via

$$\varepsilon_{ab}\varepsilon_{cd} = g_{ac}g_{bd} - g_{ad}g_{bc}\,, \tag{A.13}$$

which can be checked by straightforward calculation using all existing symmetries. Eqn. (A.13) can be contracted twice

$$\varepsilon_{ac}\varepsilon_b{}^c = g_{ab} \quad \text{and} \quad \varepsilon_{ab}\,\varepsilon^{ab} = g_{ab}\,g^{ab} = 2\,. \tag{A.14}$$

The covariant derivative

The partial derivative ∂_a of a tensor is generally not a tensor itself. One therefore defines the covariant derivative ∇_a on a tensor $t^{a_1 a_2 \ldots a_n}_{b_1 b_2 \ldots b_m}$ by incorporating all terms which spoil the transformation law directly into the new derivative:

$$\begin{aligned}
\nabla_c t^{a_1 a_2 \ldots a_n}_{b_1 b_2 \ldots b_m} &= \partial_c t^{a_1 a_2 \ldots a_n}_{b_1 b_2 \ldots b_m} \\
&+ t^{d\,a_2 \ldots a_n}_{b_1 b_2 \ldots b_m}\Gamma_{dc}{}^{a_1} + t^{a_1 d \ldots a_n}_{b_1 b_2 \ldots b_m}\Gamma_{dc}{}^{a_2} + \ldots + t^{a_1 a_2 \ldots d}_{b_1 b_2 \ldots b_m}\Gamma_{dc}{}^{a_n} \\
&- t^{a_1 a_2 \ldots a_n}_{d\,b_2 \ldots b_m}\Gamma_{b_1 c}{}^{d} - t^{a_1 a_2 \ldots a_n}_{b_1 d \ldots b_m}\Gamma_{b_2 c}{}^{d} - \ldots - t^{a_1 a_2 \ldots a_n}_{b_1 b_2 \ldots d}\Gamma_{b_m c}{}^{d}\,,
\end{aligned} \tag{A.15}$$

where the $\Gamma_{ab}{}^c$ are the *Christoffel symbols of the second kind* with

$$\Gamma_{ab}{}^c = (\partial_a \boldsymbol{e}_b) \cdot \boldsymbol{e}^c = \frac{1}{2}g^{cd}(\partial_a g_{bd} + \partial_b g_{da} - \partial_d g_{ab})\,, \tag{A.16}$$

and ∇_a acting on a tensor again yields a tensor. For the covariant differentiation of sums and products of tensors the usual rules of differential calculus hold. This includes, for instance, integration by parts. The metric-compatible Laplacian Δ can be defined as $\Delta := \nabla_a \nabla^a$.

Note in particular that

$$\begin{aligned}
\nabla_a \boldsymbol{n} &= \partial_a \boldsymbol{n}\,, && \text{and} & \tag{A.17a} \\
\nabla_a \boldsymbol{e}_b &= \partial_a \boldsymbol{e}_b - \Gamma_{ab}{}^c \boldsymbol{e}_c\,. & & & \tag{A.17b}
\end{aligned}$$

We also have the so-called *Lemma of Ricci*

$$\nabla_a g_{bc} = \nabla_a g^{bc} = \nabla_a g = 0\,. \tag{A.18}$$

It implies that raising and lowering of indices commutes with the process of covariant differentiation.

However, covariant derivatives do not commute with each other. For a contravariant vector t^c, one obtains, for instance,

$$[\nabla_a, \nabla_b]\,t^c = (\nabla_a \nabla_b - \nabla_b \nabla_a)t^c = R_{ab}{}^c{}_d t^d\,, \tag{A.19}$$

where $R_{ab}{}^c{}_d$ is the *Riemann curvature tensor* (compare Eqn. (A.45) on page 173). For contravariant tensors of rank 2 a second Riemann tensor arises:

$$[\nabla_a, \nabla_b]\,t^{cd} = R_{ab}{}^c{}_e t^{ed} + R_{ab}{}^d{}_e t^{ce}\,. \tag{A.20}$$

Lie derivative

The Lie derivative describes how a tensor changes along some given "direction" on the surface, specified by a vector field $\boldsymbol{Y} = Y^a \boldsymbol{e}_a$ [Fra03]. Contrary to the covariant derivative it does not change the order of the tensor it differentiates.

If the tensor is a scalar function ϕ on the surface, its Lie derivative is just the directional derivative along $\boldsymbol{Y}$:

$$\mathcal{L}_{\boldsymbol{Y}}\phi = Y^a \, \partial_a \phi = Y^a \, \nabla_a \phi \; . \tag{A.21}$$

For tensors of higher order such as a vector field $\boldsymbol{V} = V^a \boldsymbol{e}_a$ one can define the Lie derivative with the help of the local flow Φ_t generated by $\boldsymbol{Y}$.[3] Since $\Phi_t(P)$ shifts the point P for a "time" t along the flow, its differential can be used to compare vectors at different points with each other. Consider the two following vectors: $\boldsymbol{V}_P$, the representative of the vector field $\boldsymbol{V}$ at the point P, and $(\Phi_{-t})_* \boldsymbol{V}_{\Phi_t(P)}$, the representative of the vector field $\boldsymbol{V}$ at the point $\Phi_t(P)$ pushed backward to the point P by means of the differential $(\Phi_{-t})_*$.

The difference between the two can be used to define the Lie derivative of $\boldsymbol{V}$ with respect to $\boldsymbol{Y}$ at the point P:

$$(\mathcal{L}_{\boldsymbol{Y}}\boldsymbol{V})_P = \lim_{t \to 0} \frac{(\Phi_{-t})_* \boldsymbol{V}_{\Phi_t(P)} - \boldsymbol{V}_P}{t} \; . \tag{A.22}$$

In local coordinates this can be written as [Fra03]

$$(\mathcal{L}_{\boldsymbol{Y}}\boldsymbol{V})^a = Y^c \, \partial_c V^a - V^c \, \partial_c Y^a \; . \tag{A.23}$$

In general, the Lie derivative of a tensor $t^{a_1 a_2 \ldots a_n}_{b_1 b_2 \ldots b_m}$ with respect to $\boldsymbol{Y}$ is given by

$$
\begin{aligned}
(\mathcal{L}_{\boldsymbol{Y}}t)^{a_1 a_2 \ldots a_n}_{b_1 b_2 \ldots b_m} \;=\;\; & Y^c \partial_c t^{a_1 a_2 \ldots a_n}_{b_1 b_2 \ldots b_m} \\
& - t^{c\, a_2 \ldots a_n}_{b_1 b_2 \ldots b_m} \, \partial_c Y^{a_1} - t^{a_1 c \ldots a_n}_{b_1 b_2 \ldots b_m} \, \partial_c Y^{a_2} - \ldots - t^{a_1 a_2 \ldots c}_{b_1 b_2 \ldots b_m} \, \partial_c Y^{a_n} \\
& + t^{a_1 a_2 \ldots a_n}_{c\, b_2 \ldots b_m} \, \partial_{b_1} Y^c + t^{a_1 a_2 \ldots a_n}_{b_1 c \ldots b_m} \, \partial_{b_2} Y^c + \ldots + t^{a_1 a_2 \ldots a_n}_{b_1 b_2 \ldots c} \, \partial_{b_m} Y^c \; ,
\end{aligned} \tag{A.24}
$$

in local coordinates. The partial derivatives can be replaced by covariant ones as one can check by straightforward calculation. This observation confirms that the Lie derivative does indeed produce a tensor.

Curvature in one dimension

Consider a curve $\mathcal{C}$ in $\mathbb{R}^2$. Its curvature k at a given point has a magnitude equal to the reciprocal of the radius of an osculating circle, a circle that "kisses" or closely touches the curve at the given point having the same tangent (see Fig. A.3). To describe the curvature properties of a (non-planar) surface embedded in $\mathbb{R}^3$, a tensor is needed, the extrinsic curvature tensor K_{ab}.

---

[3] The flow Φ_t is the solution of the differential equation $(\mathrm{d}/\mathrm{d}t)\Phi_t(P) = \boldsymbol{Y}_P$ which states that the tangent vector to the flow at the point P on the surface always coincides with the vector $\boldsymbol{Y}_P$ at that point (see, for instance, Ref. [Fra03, Sec. 1.4a]).
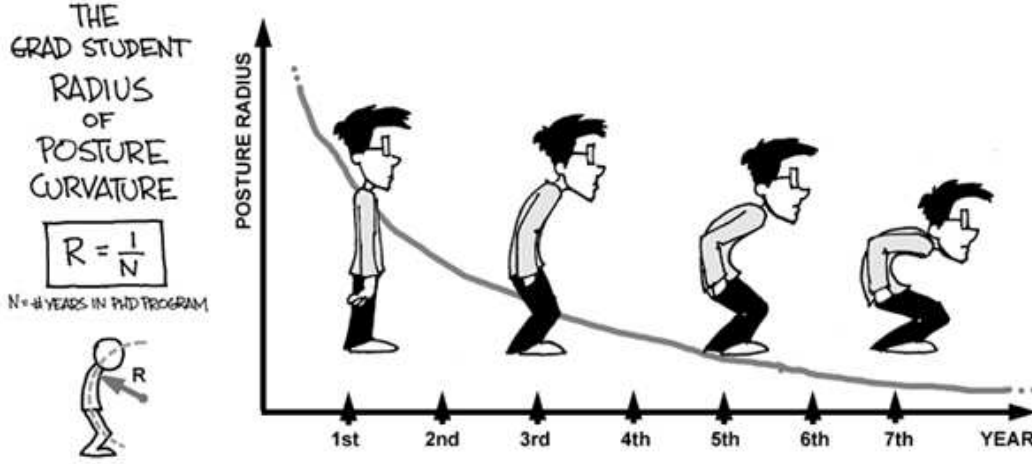
Figure A.3: Curvature in one dimension *("Piled Higher and Deeper" by Jorge Cam;* `http://www.phdcomics.com`*).* The author finished this thesis after three years. Fortunately, this was early enough to avoid serious backaches.

The extrinsic curvature tensor (second fundamental form)

Two surfaces may have the same metric tensor g_{ab} but different curvature properties in $\mathbb{R}^3$. In order to describe such properties let us consider a surface Σ of class[4] $r \geq 2$ and a curve $\mathcal{C}$ of the same class on Σ with the parametrization $\boldsymbol{X}(\xi^1(s), \xi^2(s))$ on Σ, where s is the arc length of the curve (see Fig. A.4).

At every point of the curve where its curvature $k > 0$, one may define a moving trihedron $\{\boldsymbol{t}, \boldsymbol{p}, \boldsymbol{b}\}$ where $\boldsymbol{t} = \dot{\boldsymbol{X}}$ is the unit tangent vector, $\boldsymbol{p} = \dot{\boldsymbol{t}}/|\dot{\boldsymbol{t}}| = \dot{\boldsymbol{t}}/k$ is the unit principal normal vector, and $\boldsymbol{b} = \boldsymbol{t} \times \boldsymbol{p}$ is the unit binormal vector of the curve.[5] Furthermore, let η be the angle between the unit normal vector $\boldsymbol{n}$ of the surface and the unit principal normal vector $\boldsymbol{p}$ of the curve with $\cos\eta = \boldsymbol{p} \cdot \boldsymbol{n}$ (see again Fig. A.4).

The curvature k of the curve can then be decomposed into a part which is due to the fact that the *surface* is curved in $\mathbb{R}^3$ and a part due to the fact that the *curve* itself is curved. The former will be called the normal curvature K_n, the latter the geodesic curvature K_g. One defines:

$$
\begin{aligned}
K_\mathrm{n} &:= -\dot{\boldsymbol{t}} \cdot \boldsymbol{n} = -k\,(\boldsymbol{p} \cdot \boldsymbol{n}) = -k\cos\eta\,, \qquad \text{and} & \text{(A.25)}\\
K_\mathrm{g} &:= \boldsymbol{t} \cdot (\dot{\boldsymbol{t}} \times \boldsymbol{n}) = k\,\boldsymbol{t} \cdot (\boldsymbol{p} \times \boldsymbol{n}) = k\sin\eta\,\operatorname{sign}(\boldsymbol{n} \cdot \boldsymbol{b})\,. & \text{(A.26)}
\end{aligned}
$$

Here, we are interested in the curvature properties of the surface. Therefore, the

---

[4] This means that its parametrization $\boldsymbol{X}(\xi^1, \xi^2)$ is of class $r \geq 2$.
[5] The dot denotes the derivative with respect to the arc length s.
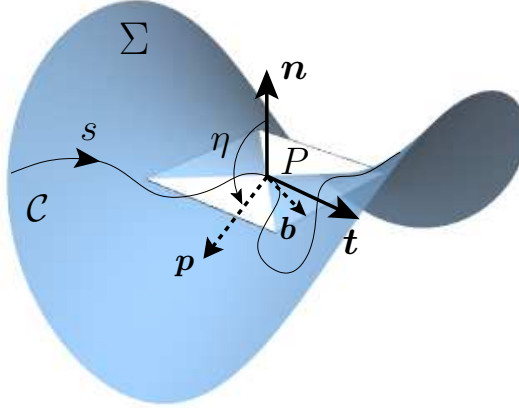
Figure A.4: Curve $\mathcal{C}$ on a surface. Notice that the unit principal normal vector $\boldsymbol{p}$ of the curve and the unit normal vector $\boldsymbol{n}$ of the surface do not coincide but form the angle η.

normal curvature K_{n} is the relevant quantity that has to be studied a bit further.[6] The vector $\dot{\boldsymbol{t}}$ may be written as

$$\dot{\boldsymbol{t}} = \ddot{\boldsymbol{X}} = \frac{\mathrm{d}}{\mathrm{d}s}(\boldsymbol{e}_a \dot{\xi}^a) = (\partial_b \boldsymbol{e}_a)\, \dot{\xi}^a \dot{\xi}^b + \boldsymbol{e}_a \ddot{\xi}^a \ . \tag{A.27}$$

Thus, Eqn. (A.25) turns into

$$K_{\mathrm{n}} = -k \cos \eta = (-\boldsymbol{n} \cdot \partial_a \boldsymbol{e}_b)\, \dot{\xi}^a \dot{\xi}^b \ , \tag{A.28}$$

where it has been exploited that $\partial_a \boldsymbol{e}_b = \partial_b \boldsymbol{e}_a$. The expression in brackets is the *extrinsic curvature tensor* or *second fundamental form*

$$K_{ab} := -\boldsymbol{n} \cdot \partial_a \boldsymbol{e}_b = \boldsymbol{e}_a \cdot \partial_b \boldsymbol{n} \ . \tag{A.29}$$

It is a symmetric covariant second rank tensor such as the metric. The second relation in Eqn. (A.29) follows if one differentiates the first equation of (A.4) with respect to ξ^a.

The extrinsic curvature can be written covariantly by inserting Eqn. (A.17b) into Eqn. (A.29):

$$K_{ab} := -\boldsymbol{n} \cdot \nabla_a \boldsymbol{e}_b \ . \tag{A.30}$$

This is possible because $\partial_a \boldsymbol{e}_b$ differs from $\nabla_a \boldsymbol{e}_b$ only by terms proportional to the tangent vectors $\boldsymbol{e}_c$, which vanish when multiplied by $\boldsymbol{n}$ (see Eqn. (A.17b)).

---

[6] The minus sign in the definition of K_{n}, Eqn. (A.25), is unfortunately a matter of convention and is here chosen in accordance to the literature where the surface stress tensor for fluid membranes has been introduced [CG02b, Guv04]. A sphere with outward pointing unit normal has a positive normal curvature then. Note that this differs from Ref. [Kre91].

One can easily see from Eqn. (A.29) that K_{ab} has got something to do with curvature: at every point of the surface it measures the change of the normal vector in $\mathbb{R}^3$ for an infinitesimal displacement in the direction of a coordinate curve.

To learn more about the normal curvature, let us consider a reparametrization of the curve $\mathcal{C}$ with the new parameter t. One gets

$$\dot{\xi}^a = \frac{\mathrm{d}\xi^a}{\mathrm{d}t}\frac{\mathrm{d}t}{\mathrm{d}s} = \frac{\xi^{a'}}{s'} \; , \tag{A.31}$$

where $'$ denotes the derivative with respect to t. Equation (A.28) thus takes the form

$$K_{\mathrm{n}} = K_{ab}\,\dot{\xi}^a\dot{\xi}^b = \frac{K_{ab}\,\xi^{a'}\xi^{b'}}{(s')^2} \stackrel{\text{(A.6)}}{=} \frac{K_{ab}\,\xi^{a'}\xi^{b'}}{g_{ab}\,\xi^{a'}\xi^{b'}} = \frac{K_{ab}\,\mathrm{d}\xi^a\,\mathrm{d}\xi^b}{g_{ab}\,\mathrm{d}\xi^a\,\mathrm{d}\xi^b} \; . \tag{A.32}$$

For a fixed point P, K_{ab} and g_{ab} are fixed as well. The value of K_{n} then only depends on the direction of the tangent vector $\boldsymbol{t}$ of the curve. One may search for extremal values of K_{n} at P by rewriting Eqn. (A.32):

$$(K_{ab} - K_{\mathrm{n}}g_{ab})\,\dot{\xi}^a\dot{\xi}^b = 0 \; . \tag{A.33}$$

A differentiation with respect to $\dot{\xi}^c$ yields the result

$$(K_{ac} - K_{\mathrm{n}}g_{ac})\,\dot{\xi}^a = 0 \; , \tag{A.34}$$

because $\mathrm{d}K_{\mathrm{n}} = 0$ is necessary for K_{n} to be extremal. Through the raising of one index, Eqn. (A.34) becomes an eigenvalue problem for K_a^b. Its eigenvectors are the tangent directions along which the normal curvature is extremal. They are called *principal directions* and are orthogonal to each other [Kre91, p. 129]. The eigenvalues will be called the *principal curvatures* k_1 and k_2 of the surface in point P. All other values of K_{n} in P in any direction can be calculated via Euler's theorem [Kre91, p. 132]. If the curve follows a principal direction at every point, it is also called a *line of curvature*.

It is useful to define the following two notions: the *trace of the extrinsic curvature tensor*

$$K := \mathrm{Tr}\,(K_a^b) = g^{ab}K_{ab} = k_1 + k_2 \; , \tag{A.35}$$

and the *Gaussian curvature*

$$K_{\mathrm{G}} := \det\,(K_a^b) = k_1 k_2 \; . \tag{A.36}$$

The quantities $|K|$ and K_{G} are invariant under surface reparametrizations because they only involve the eigenvalues of the extrinsic curvature tensor. Note that one can rewrite K_{G}

$$K_{\mathrm{G}} = \det\,(K_a^b) = \det\,(K_{ac}g^{cb}) = \det\,(K_{ac})\det\,(g^{cb}) = \frac{K_{11}K_{22} - K_{12}K_{21}}{g} \; . \tag{A.37}$$

The equations of Gauss and Weingarten

With the help of the extrinsic curvature it is also possible to find relations for the partial derivatives of the local frame vectors: the normal vector $\boldsymbol{n}$ is a unit vector (see Eqn. (A.4)) and therefore

$$\boldsymbol{n} \cdot \partial_a \boldsymbol{n} = 0 \ . \tag{A.38}$$

Thus, $\partial_a \boldsymbol{n}$ is a linear combination of the tangent vectors $\boldsymbol{e}_a$. We know that $(\partial_a \boldsymbol{n}) \cdot \boldsymbol{e}_b = K_{ab}$ (see Eqn. (A.29)). Together with Eqns. (A.17a) and (A.38) this yields the *Weingarten equations*

$$\partial_a \boldsymbol{n} = \nabla_a \boldsymbol{n} = K_a^b \boldsymbol{e}_b \ . \tag{A.39}$$

For the tangent vector $\boldsymbol{e}_a$ a decomposition yields

$$\partial_a \boldsymbol{e}_b = (\boldsymbol{n} \cdot \partial_a \boldsymbol{e}_b)\boldsymbol{n} + (\boldsymbol{e}^c \cdot \partial_a \boldsymbol{e}_b)\boldsymbol{e}_c \overset{(A.29,A.16)}{=} -K_{ab}\boldsymbol{n} + \Gamma_{ab}^{\ \ c}\boldsymbol{e}_c \ . \tag{A.40}$$

These are the *Gauss equations*, which can be rewritten covariantly:

$$\nabla_a \boldsymbol{e}_b \overset{(A.17b)}{=} -K_{ab}\boldsymbol{n} \ . \tag{A.41}$$

Intrinsic curvature and integrability conditions

Do the partial differential Eqns. (A.39) and (A.41) have solutions for any chosen g_{ab} and K_{ab}? The answer is no; certain integrability conditions have to be satisfied. We require the embedding functions $\boldsymbol{X}$ to be of class $r \geq 3$ and

$$\partial_a \partial_b \boldsymbol{e}_c = \partial_b \partial_a \boldsymbol{e}_c \ . \tag{A.42}$$

From this follows [Kre91, p. 142 et seq.]

$$R^a_{\ bcd} = K_{bd}K_c^a - K_{bc}K_d^a \ , \qquad \text{and} \tag{A.43}$$

$$\nabla_a K_{bc} = \nabla_b K_{ac} \ , \tag{A.44}$$

where

$$R^a_{\ bcd} := \partial_c \Gamma_{bd}^{\ \ a} - \partial_d \Gamma_{bc}^{\ \ a} + \Gamma_{bd}^{\ \ e}\Gamma_{ec}^{\ \ a} - \Gamma_{bc}^{\ \ e}\Gamma_{ed}^{\ \ a} \ , \tag{A.45}$$

is called the *mixed Riemann curvature tensor*. It is intrinsic because it does not depend on the normal vector $\boldsymbol{n}$. Expression (A.43) is also referred to as the *equation of Gauss-Codazzi*, whereas Eqn. (A.44) is called the *equation of Mainardi-Codazzi*. The latter can be contracted once

$$\nabla_a K = \nabla^b K_{ab} \ . \tag{A.46}$$

The *Ricci tensor* is defined as the contraction of the Riemann tensor with respect to its first and third index:

$$R_{ab} := R^c_{\ acb} \ . \tag{A.47}$$

A further contraction of the Ricci tensor yields the intrinsic *scalar curvature* of the surface (Ricci scalar)

$$\mathcal{R} := g^{ab} R_{ab} \ . \tag{A.48}$$

From Eqn. (A.43) one then obtains

$$R_{ab} = K K_{ab} - K_{ac} K_b^c \ , \qquad \text{and} \tag{A.49}$$
$$\mathcal{R} = K^2 - K^{ab} K_{ab} \ . \tag{A.50}$$

Combining Eqn. (A.37) with the completely covariant form of Eqn. (A.43), one gets after a few calculations:

$$R_{abcd} = K_{\mathrm{G}}(g_{ac} g_{bd} - g_{ad} g_{bc}) \overset{(A.13)}{=} K_{\mathrm{G}} \, \varepsilon_{ab} \varepsilon_{cd} \ , \tag{A.51a}$$
$$R_{ab} = K_{\mathrm{G}} \, g_{ab} \ , \qquad \text{and} \tag{A.51b}$$
$$\mathcal{R} = 2 \, K_{\mathrm{G}} \ . \tag{A.51c}$$

These equations confirm Gauss' Theorema Egregium, which states that the Gaussian curvature, even though originally defined in an extrinsic way, in fact only depends on the first fundamental form [Kre91, p. 145] and is thus an intrinsic surface property.

A.2 Geometry at a curve on the surface

Consider a curve $\mathcal{C}$ on the surface such as on page 170 of the previous section. At every point of the curve its unit tangent vector $\boldsymbol{t} = t^a \boldsymbol{e}_a$, the surface normal $\boldsymbol{n}$, and the vector $\boldsymbol{l} = \boldsymbol{t} \times \boldsymbol{n}$ define a moving trihedron in Euclidean space (see Fig. A.5). In contrast to the binormal vector $\boldsymbol{b}$ and the principal normal vector $\boldsymbol{p}$ (see Fig. A.4), the unit vector $\boldsymbol{l} = l^a \boldsymbol{e}_a$ is tangential to the surface. This allows us to express surface properties in terms of the orthonormal vector basis $\{\boldsymbol{l}, \boldsymbol{t}\}$ adapted to the curve $\mathcal{C}$. For instance, the projections of the extrinsic curvature tensor K_{ab} onto $\{\boldsymbol{l}, \boldsymbol{t}\}$ are given by

$$K_\perp = l^a l^b K_{ab} = -\boldsymbol{n} \cdot \nabla_\perp \boldsymbol{l} \ , \tag{A.52a}$$
$$K_{||} = t^a t^b K_{ab} = -\boldsymbol{n} \cdot \nabla_{||} \boldsymbol{t} \ , \qquad \text{and} \tag{A.52b}$$
$$K_{\perp||} = K_{||\perp} = l^a t^b K_{ab} = -\boldsymbol{n} \cdot \nabla_\perp \boldsymbol{t} = -\boldsymbol{n} \cdot \nabla_{||} \boldsymbol{l} \ , \tag{A.52c}$$

where the two directional surface derivatives perpendicular and parallel to $\mathcal{C}$ are introduced:

$$\nabla_\perp = l^a \nabla_a \qquad \text{and} \qquad \nabla_{||} = t^a \nabla_a \ . \tag{A.53}$$

The trace K of the extrinsic curvature tensor is then simply given by

$$K = K_\perp + K_{||} \ . \tag{A.54}$$
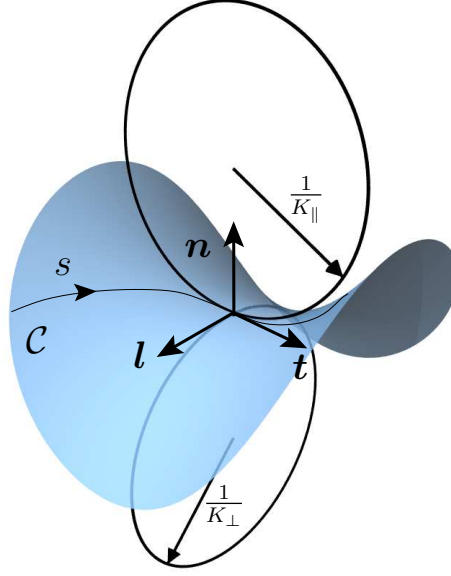
Figure A.5: Geometry at a curve $\mathcal{C}$ on a surface. Note that $K_{\perp\|}$ vanishes in the depicted situation.

The geodesic curvature of the curve $\mathcal{C}$ follows from Eqn. (A.26)

$$K_{\mathrm{g}} = (\boldsymbol{n} \times \boldsymbol{t}) \cdot \dot{\boldsymbol{t}} = -\boldsymbol{l} \cdot \nabla_{\|}\boldsymbol{t} = \boldsymbol{t} \cdot \nabla_{\|}\boldsymbol{l} \ . \tag{A.55}$$

Using the completeness of the tangent basis, $g_c^b = \delta_c^b = l_c l^b + t_c t^b$, the projections

$$
\begin{aligned}
l_a K^{ab} &= l_a (l_c l^b + t_c t^b) K^{ac} = K_\perp l^b + K_{\perp\|} t^b \ , \quad \text{and} \tag{A.56a} \\
t_a K^{ab} &= t_a (l_c l^b + t_c t^b) K^{ac} = K_{\perp\|} l^b + K_\| t^b \ , \tag{A.56b}
\end{aligned}
$$

are obtained.

Together with the Weingarten equations (A.39) one can then calculate the change of the surface normal $\boldsymbol{n}$ along $\boldsymbol{l}$ and $\boldsymbol{t}$

$$
\begin{aligned}
\nabla_\perp \boldsymbol{n} &= l_a K^{ab} \boldsymbol{e}_b = K_\perp \boldsymbol{l} + K_{\perp\|} \boldsymbol{t} \ , \quad \text{and} \tag{A.57a} \\
\nabla_\| \boldsymbol{n} &= t_a K^{ab} \boldsymbol{e}_b = K_{\perp\|} \boldsymbol{l} + K_\| \boldsymbol{t} \ . \tag{A.57b}
\end{aligned}
$$

Finally, the covariant derivatives of the vector components l_a and t_a are given by

$$
\begin{aligned}
\nabla_a l_b &= \nabla_a (\boldsymbol{l} \cdot \boldsymbol{e}_b) = \boldsymbol{l} \cdot (\nabla_a \boldsymbol{e}_b) + \boldsymbol{e}_b \cdot (\nabla_a \boldsymbol{l}) \stackrel{(A.41)}{=} \boldsymbol{e}_b \cdot (\nabla_a \boldsymbol{l}) \tag{A.58a} \\
&= \boldsymbol{e}_b \cdot (l_a \nabla_\perp \boldsymbol{l} + t_a \nabla_\| \boldsymbol{l}) \ , \quad \text{and} \tag{A.58b} \\
\nabla_a t_b &= \nabla_a (\boldsymbol{t} \cdot \boldsymbol{e}_b) = \boldsymbol{t} \cdot (\nabla_a \boldsymbol{e}_b) + \boldsymbol{e}_b \cdot (\nabla_a \boldsymbol{t}) \stackrel{(A.41)}{=} \boldsymbol{e}_b \cdot (\nabla_a \boldsymbol{t}) \tag{A.58c} \\
&= \boldsymbol{e}_b \cdot (l_a \nabla_\perp \boldsymbol{t} + t_a \nabla_\| \boldsymbol{t}) \ . \tag{A.58d}
\end{aligned}
$$

A.3 Gauss-Bonnet theorem

The Gauss-Bonnet theorem for simply connected surfaces

The Gauss-Bonnet theorem states the following [Kre91, p. 169]: Let Σ_0 be a simply connected surface patch of class $r_{\Sigma_0} \geq 3$ with simple closed boundary $\partial\Sigma_0$ of class $r_{\partial\Sigma_0} \geq 3$. Furthermore, let $\boldsymbol{X}(\xi^1(s), \xi^2(s))$ be the parametrization of the boundary curve, where s is the arc length. Then

$$\int_{\partial\Sigma_0} \mathrm{d}s\, K_\mathrm{g} + \int_{\Sigma_0} \mathrm{d}A\, K_\mathrm{G} = 2\pi \;, \tag{A.59}$$

where $\mathrm{d}A$ is the infinitesimal area element, K_g is the geodesic curvature of $\partial\Sigma_0$, and K_G is the Gaussian curvature of Σ_0. Note that the integration along the boundary curve has to be carried out in such a sense that the right-hand rule is satisfied: take your right thumb and point it in the direction of the normal vector $\boldsymbol{n}$. If you then curl your fingers, the tips indicate the direction of integration.

One can check the consistency of Eqn. (A.59) easily by considering a flat circle with radius a: Its Gaussian curvature is zero and therefore also the integral over it. The geodesic curvature, however, is equal to $1/a$ in every point of the boundary. Thus, the integral over K_g yields $2\pi a \times 1/a$, which is equal to the right-hand side of Eqn. (A.59).

Generalization to multiply connected surfaces

A generalization of this theorem to multiply connected surfaces is also possible [Kre91, p. 172]: One can cut multiply connected surfaces into simply connected ones. Take, for instance, a surface as in Fig. A.6. The path of integration along the boundary may be chosen as depicted by the arrows. The sections are passed twice in opposite directions; their contributions therefore cancel each other. The end points of every section, however, add a term of π each to the integral $\int \mathrm{d}s\, K_\mathrm{g}$. This is due to the rotation the tangent makes at each of these points. Every section therefore contributes 2π to the integral. For the case of Fig. A.6 we thus have an extra term of 4π which has to be added to the left-hand side of Eqn. (A.59).

Orientable surfaces

The orientation of the normal vector $\boldsymbol{n}$ in one point P of the surface depends on the choice of the coordinate system [Kre91, p. 108]: exchanging, for instance, ξ^1 and ξ^2 also flips $\boldsymbol{n}$ by 180 degrees. A surface is called *orientable* if no closed curve $\mathcal{C}$ through any point P of the surface exists which causes the sense of $\boldsymbol{n}$ to change when displacing $\boldsymbol{n}$ continuously from P along $\mathcal{C}$ back to P. An example of a surface that is not orientable is the *Möbius strip*.
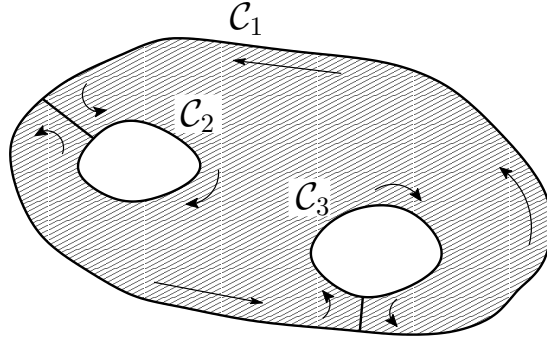
Figure A.6: Integration contour for multiply connected surface patches

Application to closed surfaces

It is also possible to apply the Gauss-Bonnet theorem to closed surfaces [Kre91, p. 172]. Topologically, any closed orientable surface is homeomorphic[7] to a sphere with p attached "handles". This number p is also called *genus* of the surface. Consequently, a sphere has genus 0, a torus genus 1, etc. One then obtains for any closed orientable surface Σ of genus p [Kre91, p. 172]:

$$\oint_{\Sigma} \mathrm{d}A \; K_{\mathrm{G}} = 4\pi(1-p) \; . \tag{A.60}$$

This implies that the integral over the Gaussian curvature is a topological invariant for any closed surface with fixed genus p.

A.4 Two important surface parametrizations

A.4.1 Monge parametrization

For surfaces with no overhangs (compare Fig. A.8) it is possible to describe their position in terms of a height $h(\boldsymbol{X}_{\parallel})$ above the underlying reference plane as a function of the orthonormal coordinates $\boldsymbol{X}_{\parallel}$ on this plane.

Cartesian coordinates

If we choose Cartesian coordinates on the reference plane, $\boldsymbol{X}_{\parallel} = x\,\boldsymbol{x} + y\,\boldsymbol{y}$, and the surface is given by

$$\boldsymbol{X}(x,y) = x\,\boldsymbol{x} + y\,\boldsymbol{y} + h(x,y)\boldsymbol{z} \; . \tag{A.61}$$

The direction of the basis vectors $\{\boldsymbol{x}, \boldsymbol{y}, \boldsymbol{z}\} \in \mathbb{R}^3$ is chosen as depicted in Fig. A.7. The tangent vectors on the surface can then be expressed as $\boldsymbol{e}_x = (1, 0, h_x)^{\mathrm{T}}$ and

---

[7] This means that the mapping and its inverse are continuous and bijective.
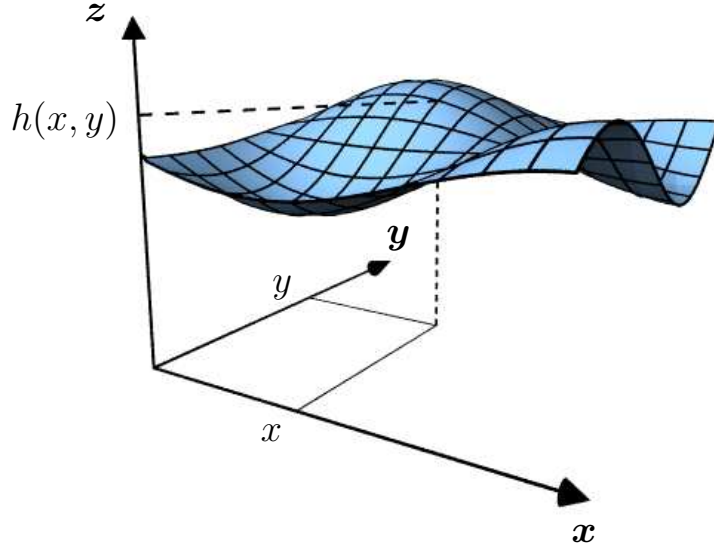
Figure A.7: Monge parametrization in Cartesian coordinates

$\boldsymbol{e}_y = (0, 1, h_y)^{\mathrm{T}}$, where $h_i = \partial_i h$ $(i, j \in \{x, y\})$. The metric is equal to

$$g_{ij} = \delta_{ij} + h_i h_j \, , \tag{A.62}$$

where δ_{ij} is the Kronecker symbol. Let the symbol $\boldsymbol{\nabla}$ denote the two-dimensional nabla operator in the flat reference plane. In Cartesian coordinates it is given by $\boldsymbol{\nabla} = \boldsymbol{x}\, \partial_x + \boldsymbol{y}\, \partial_y$. The metric determinant and the infinitesimal surface element can then be written as

$$
\begin{aligned}
g &= |g_{ij}| = 1 + (\boldsymbol{\nabla} h)^2 \quad \text{and} \tag{A.63} \\
\mathrm{d}A &= \sqrt{1 + (\boldsymbol{\nabla} h)^2}\, \mathrm{d}A_{\parallel} \, , \tag{A.64}
\end{aligned}
$$

where $\mathrm{d}A_{\parallel} = \mathrm{d}x\, \mathrm{d}y$ is the area element on the reference plane.
The inverse metric is given by

$$g^{ij} = \delta_{ij} - \frac{h_i h_j}{g} \, . \tag{A.65}$$

Note that Eqns. (A.62) and (A.65) are not tensor equations. The right-hand side gives merely numerical values for the components of the covariant tensors g_{ij} and g^{ij}. The unit normal vector is equal to

$$\boldsymbol{n} = \frac{\left(-\boldsymbol{\nabla} h + \boldsymbol{z} \right)}{\sqrt{1 + (\boldsymbol{\nabla} h)^2}} \, . \tag{A.66}$$

With the help of Eqn. (A.29) the extrinsic curvature tensor can be calculated:

$$K_{ij} = -\frac{h_{ij}}{\sqrt{g}} \, , \tag{A.67}$$

where $h_{ij} = \partial_i \partial_j h$. Note that Eqn. (A.67) again is not a tensor equation and gives only numerical values for the components of K_{ij}.

Finally, it is also possible to write the trace K of the extrinsic curvature tensor in Monge parametrization:

$$K = -\boldsymbol{\nabla} \cdot \left(\frac{\boldsymbol{\nabla} h}{\sqrt{1 + (\boldsymbol{\nabla} h)^2}} \right) \, . \tag{A.68}$$

Polar coordinates

Another possible choice of coordinates on the reference plane are the polar coordinates (ρ, φ), where $\boldsymbol{X}_\parallel = \rho \, \boldsymbol{\rho}$. The angle φ is measured from the x to the ρ axis. The surface is described by

$$\boldsymbol{X}(\rho, \varphi) = \rho \, \boldsymbol{\rho} + h(\rho, \varphi) \, \boldsymbol{z} \, . \tag{A.69}$$

Thus, the tangent vectors of the surface are given by $\boldsymbol{e}_\rho = \boldsymbol{\rho} + (\partial_\rho h) \boldsymbol{z}$ and $\boldsymbol{e}_\varphi = \rho \boldsymbol{\varphi} + (\partial_\varphi h) \boldsymbol{z}$. One obtains for the metric $(i, j \in \{\rho, \varphi\})$

$$g_{ij} = \begin{pmatrix} 1 + (\partial_\rho h)^2 & (\partial_\rho h)(\partial_\varphi h) \\ (\partial_\rho h)(\partial_\varphi h) & \rho^2 + (\partial_\varphi h)^2 \end{pmatrix} \tag{A.70}$$

and for the metric determinant

$$g = \rho^2 [1 + (\boldsymbol{\nabla} h)^2] \, , \tag{A.71}$$

where we exploited the fact that $\boldsymbol{\nabla} = \boldsymbol{\rho} \, \partial_\rho + \boldsymbol{\varphi} \, \frac{1}{\rho} \partial_\varphi$ in polar coordinates. The metric determinant factorizes into one part $(g_\parallel = \rho^2)$ which is due to the choice of coordinates on the base plane and one part $(g_\perp = 1 + (\boldsymbol{\nabla} h)^2)$ due to the height h.[8] The latter term involves the nabla operator and remains formally the same if the coordinate system of the reference plane is changed. This implies that the infinitesimal surface element $\mathrm{d}A$ can simply be obtained by inserting the nabla operator in polar coordinates into Eqn. (A.64), where $\mathrm{d}A_\parallel = \mathrm{d}\varphi \, \mathrm{d}\rho \, \rho$ now. Analogously, $\boldsymbol{n}$ and K follow from Eqns. (A.66) and (A.68), respectively.[9]

---

[8] We did not notice this fact before as $g_\parallel = 1$ in the previous case.
[9] One can also check that by straightforward calculation.
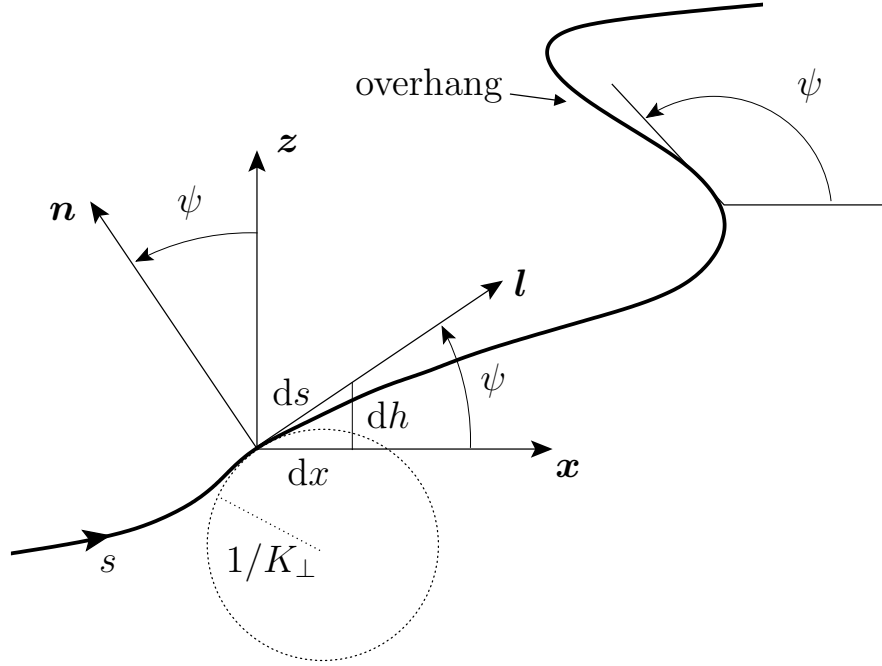
Figure A.8: Angle-arc length parametrization–translational symmetry. The advantage of this parametrization is that it allows for overhangs.

Small gradient approximation

In Chaps. 4 and 5 we are interested in surfaces that deviate only weakly from a flat plane. In this situation the gradients of h are small. Therefore, it is enough to consider only the lowest nontrivial order of a small gradient expansion. For both, Cartesian and polar coordinates, K and $\mathrm{d}A$ can then be written as

$$K \;=\; -\boldsymbol{\nabla}^2 h + \mathcal{O}[(\boldsymbol{\nabla}h)^2] \,, \tag{A.72}$$

$$\mathrm{d}A \;=\; \left\{ 1 + \frac{1}{2}(\boldsymbol{\nabla}h)^2 + \mathcal{O}[(\boldsymbol{\nabla}h)^4] \right\} \, \mathrm{d}A_{\parallel} \,. \tag{A.73}$$

A.4.2 Angle-arc length parametrization

If the surface possesses a rotational or translational symmetry, its shape can be described in terms of the angle $\psi(s)$ between the horizontal plane and the tangent to the profile as a function of arc length s. The advantage of this parametrization is that it allows overhangs (see Fig. A.8).

Translational symmetry

The situation for translational symmetry is depicted in Fig. A.8. The profile of the surface does not change along the y axis. The projections of the surface normal and tangent vectors, $\boldsymbol{n}$ and $\boldsymbol{l}$, onto the Cartesian basis vectors $\boldsymbol{x}$ and $\boldsymbol{z}$ are given by

$$\boldsymbol{x} \cdot \boldsymbol{l} \;=\; \boldsymbol{z} \cdot \boldsymbol{n} \;=\; \cos\psi \,, \tag{A.74a}$$

$$\boldsymbol{x} \cdot \boldsymbol{n} \;=\; -\boldsymbol{z} \cdot \boldsymbol{l} \;=\; -\sin\psi \,. \tag{A.74b}$$

The curvature $K_{\parallel}$ along the axis of symmetry is zero as well as the off-diagonal term $K_{\perp\parallel}$. Only the curvature $K_{\perp} = K$ perpendicular to the y axis does not vanish and is therefore equal to the trace K of the extrinsic curvature tensor. With the help of Eqns. (A.74) one obtains:

$$
\begin{aligned}
K \;=\; K_{\perp} \;\overset{(A.52a)}{=}\; -\boldsymbol{n} \cdot \frac{\mathrm{d}\boldsymbol{l}}{\mathrm{d}s} &= -\boldsymbol{n} \cdot \frac{\mathrm{d}}{\mathrm{d}s}\left(\cos\psi\,\boldsymbol{x} + \sin\psi\,\boldsymbol{z}\right) \\
&= -\boldsymbol{n} \cdot \left(-\sin\psi\,\boldsymbol{x} + \cos\psi\,\boldsymbol{z}\right)\dot{\psi} = -\dot{\psi} \,,
\end{aligned} \tag{A.75}
$$

where the dot denotes a derivative with respect to s.

Monge and angle-arc length parametrizations are connected via the geometrical relations (see again Fig. A.8)

$$\dot{x} \;=\; \cos\psi \,, \qquad \text{and} \tag{A.76a}$$

$$\dot{h} \;=\; \sin\psi \,. \tag{A.76b}$$

Note that the sign of these equations depends on the direction along which the arc length is increasing.[10]

Rotational symmetry

If the surface is axisymmetric, the coordinate lines in angle-arc length parametrization are given by circles of constant arc length s and curves of constant azimuthal angle φ; the latter are described by the angle $\psi(s, \varphi) = \psi(s)$ between the horizontal vector $\boldsymbol{\rho}$ and the tangent vector $\boldsymbol{l}$ (see Fig. A.9).

The coordinate lines are lines of curvature with principal curvatures

$$K_{\perp} \;=\; -\dot{\psi} \,, \qquad \text{and} \tag{A.77a}$$

$$K_{\parallel} \;\overset{(A.52b)}{=}\; -\boldsymbol{n} \cdot \frac{1}{\rho}\partial_{\varphi}\boldsymbol{t} = -\boldsymbol{n} \cdot \frac{1}{\rho}(-\boldsymbol{\rho}) = -\frac{\sin\psi}{\rho} \,. \tag{A.77b}$$

---

[10] In Chap. 5, for instance, the shape of a membrane between two cylinders is calculated. There, the direction of s is chosen exactly opposite to the one of this section which yields an additional minus sign (see also App. C.1).
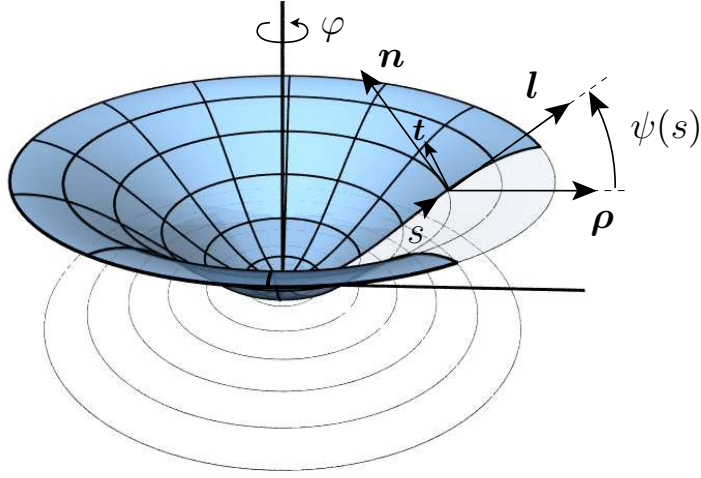
Figure A.9: Angle-arc length parametrization–rotational symmetry

where ρ is the radial distance from the axis of symmetry. The geodesic curvature of a circle of constant ρ and s can be obtained from Eqn. (A.55)

$$K_{\mathrm{g}} = -\boldsymbol{l} \cdot \frac{1}{\rho} \partial_\varphi \boldsymbol{t} = \frac{\cos\psi}{\rho} \; . \tag{A.78}$$

Note again that one has to be careful with signs. In Sec. 3.5 the directions of the normal vector $\boldsymbol{n}$ and the tangent vector $\boldsymbol{l}$ are opposite to the convention used here and in the rest of this thesis. Consequently, the curvatures (A.77) and (A.78) change sign.

The expressions from the previous section are valid for an axisymmetric surface if we replace x by ρ. This enables us to rewrite projections and curvatures in Monge parametrization: if we describe the surface in terms of the height function $h(\rho)$, Eqns. (A.76) yield $h'(\rho) = \tan\psi$, where the dash denotes a derivative with respect to ρ. The projections of $\boldsymbol{z}$ onto $\boldsymbol{l}$ and $\boldsymbol{n}$ can then be written as

$$\boldsymbol{z} \cdot \boldsymbol{l} \;\; = \;\; \sin\psi = \frac{\tan\psi}{\sqrt{1 + \tan^2\psi}} = \frac{h'(\rho)}{\sqrt{g_\perp}} \; , \qquad \text{and} \tag{A.79a}$$

$$\boldsymbol{z} \cdot \boldsymbol{n} \;\; = \;\; \cos\psi = \frac{1}{\sqrt{1 + \tan^2\psi}} = \frac{1}{\sqrt{g_\perp}} \; , \tag{A.79b}$$

where $g_\perp = g/\rho^2 = 1 + h'(\rho)^2$. Expressing the directional derivative along s in terms of h and ρ

$$\nabla_\perp = \partial_s \overset{(\mathrm{A.76a})}{=} \cos\psi \, \partial_\rho = \frac{1}{\sqrt{g_\perp}} \, \partial_\rho \; , \tag{A.80}$$

enables us to calculate the principal curvatures of an axisymmetric surface in Monge parametrization:

$$K_\perp \overset{(A.77a)}{=} -\frac{\partial_s(\sin\psi)}{\cos\psi} \overset{(A.79a,A.80)}{=} -\left(\frac{h'(\rho)}{\sqrt{g_\perp}}\right)' = -\frac{h''(\rho)}{\sqrt{g_\perp}^3} \;, \quad \text{and} \qquad \text{(A.81a)}$$

$$K_\parallel \overset{(A.77b,A.79a)}{=} -\frac{h'(\rho)}{\rho\sqrt{g_\perp}} \;. \qquad\qquad\qquad\qquad\qquad\qquad\qquad\quad \text{(A.81b)}$$

B Surface variations

In Sec. 2.1.1 we derived the general expression

$$\boldsymbol{f}^a = (T^{ab} - \mathcal{H}^{ac}K^b_c)\boldsymbol{e}_b - (\nabla_b\mathcal{H}^{ab})\boldsymbol{n} \tag{B.1}$$

for the surface stress tensor. In this appendix we will specialize (B.1) to a few important standard cases. Additionally, the tensors $\mathcal{H}^{ab}$, $\mathcal{G}^{abc}$, and $\mathcal{K}^{abc}$ which contribute to the boundary term (2.9) of variation (2.2) will be determined.

To simplify the corresponding calculations, we will first compute derivatives of surface scalars such as $\sqrt{g}$ or K with respect to g_{ab} and K_{ab}.

B.1 Derivatives of surface scalars

The derivative of the metric determinant g and its square root with respect to g_{ab} can be calculated in the following way [Mül04]: consider first quite generally a symmetric $n \times n$ matrix $\mathbf{M}$. It can be diagonalized with its eigenvalues $M_1, \ldots, M_n$ being the diagonal elements: $\mathbf{M} = \mathbf{T}\mathbf{M}_\mathrm{D}\mathbf{T}^{-1}$ where $\mathbf{M}_\mathrm{D}$ is the diagonal matrix. From this follows:

$$
\begin{aligned}
\log{(\det \mathbf{M})} &= \log{[\det{(\mathbf{T}\mathbf{M}_\mathrm{D}\mathbf{T}^{-1})}]} = \log{(M_1 \cdot M_2 \cdot \ldots \cdot M_n)} \\
&= \sum_{i=1}^n \log M_i = \mathrm{Tr}\,(\log \mathbf{M}_\mathrm{D}) = \mathrm{Tr}\,[\log{(\mathbf{T}^{-1}\mathbf{M}\mathbf{T})}] \\
&= \mathrm{Tr}\,[\mathbf{T}^{-1}\log{(\mathbf{M})}\mathbf{T}] = \mathrm{Tr}\,(\log \mathbf{M})\ .
\end{aligned}
\tag{B.2}
$$

Thus,

$$
\begin{aligned}
\frac{\partial g}{\partial g_{ab}} &= \frac{\partial \det \mathbf{g}}{\partial g_{ab}} = \frac{\partial}{\partial g_{ab}}\Big\{\exp{[\log{(\det \mathbf{g})}]}\Big\} \overset{\text{(B.2)}}{=} \frac{\partial}{\partial g_{ab}}\Big\{\exp{[\mathrm{Tr}\,(\log \mathbf{g})]}\Big\} \\
&= \Big\{\exp{[\mathrm{Tr}\,(\log \mathbf{g})]}\Big\}\frac{\partial}{\partial g_{ab}}\Big[\mathrm{Tr}\,(\log \mathbf{g})\Big] = g\,\mathrm{Tr}\,\Big[\frac{\partial}{\partial g_{ab}}(\log \mathbf{g})\Big] \\
&= g\,\mathrm{Tr}\,\Big[\mathbf{g}^{-1}\frac{\partial \mathbf{g}}{\partial g_{ab}}\Big] = gg^{cd}\frac{\partial g_{dc}}{\partial g_{ab}} = gg^{ab}\ ,
\end{aligned}
\tag{B.3}
$$

and

$$\frac{\partial \sqrt{g}}{\partial g_{ab}} = \frac{1}{2}\sqrt{g}\,g^{ab}\ . \tag{B.4}$$

━━━ **Technical Point B.1:** *Variation of the inverse metric* ━━━

Varying Eqn. (A.7) yields $g_{ac}\delta g^{cb} + \delta g_{ac}g^{cb} = 0$. From this follows that the variation of the inverse metric is given by

$$\delta g^{ab} = -g^{ac}g^{bd}\delta g_{cd} \,. \tag{B.I}$$

This implies that $\partial g^{ab}/\partial x = -g^{ac}g^{bd}\partial g_{cd}/\partial x$ for any x. If we especially insert $x = g_{ef}$, we obtain the derivative of the inverse metric with respect to the metric:

$$
\begin{aligned}
\frac{\partial g^{ab}}{\partial g_{ef}} &= -g^{ac}g^{bd}\frac{\partial g_{cd}}{\partial g_{ef}} = -g^{ac}g^{bd}\frac{1}{2}\left(\delta_c^e\,\delta_d^f + \delta_c^f\,\delta_d^e\right) \\
&= -\frac{1}{2}(g^{ae}g^{bf} + g^{af}g^{be}) \,. \tag{B.II}
\end{aligned}
$$

The derivatives of the trace $K = K_{ab}g^{ab}$ of the extrinsic curvature tensor are given by[1]

$$
\begin{aligned}
\frac{\partial K}{\partial g_{ab}} &= K_{cd}\frac{\partial g^{cd}}{\partial g_{ab}} = -K^{ab} \,, \quad \text{and} \tag{B.5a} \\
\frac{\partial K}{\partial K_{ab}} &= g^{ab} \,. \tag{B.5b}
\end{aligned}
$$

Using the doubly contracted Gauss-Codazzi equation $\mathcal{R} = K^2 - K_{ab}K^{ab}$ together with Eqns. (B.5), the derivatives of the Ricci scalar $\mathcal{R}$ can be determined[1]

$$
\begin{aligned}
\frac{\partial \mathcal{R}}{\partial g_{ab}} &= -2KK^{ab} + 2K^{ac}K_c^b \overset{(A.49)}{=} -2R^{ab} \overset{d=2}{=} -\mathcal{R}g^{ab} \,, \tag{B.6a} \\
\frac{\partial \mathcal{R}}{\partial K_{ab}} &= 2(Kg^{ab} - K^{ab}) \,. \tag{B.6b}
\end{aligned}
$$

Notice that the first equality in Eqn. (B.6a) holds generally, while the second is specific for surfaces, since it uses identity

$$R^{ab} = \frac{1}{2}\mathcal{R}g^{ab} \,, \tag{B.7}$$

valid only in two dimensions (see Eqns. (A.51b) and (A.51c)).

---

[1] One has to be careful when differentiating with respect to g_{ab}: the tensor K_{ab} is an independent variable, hence $\partial K_{ab}/\partial g_{cd} = 0$; but $K^{ab} = K_{cd}g^{ac}g^{bd}$ depends on the metric through its inverse and thus yields a nontrivial term when differentiated. Using Eqn. (B.II), one obtains $\partial K^{ab}/\partial g_{cd} = -\frac{1}{2}(K^{bd}g^{ac} + K^{bc}g^{ad} + K^{ad}g^{bc} + K^{ac}g^{bd})$.

B.2 The stress tensor for a few standard cases

B.2.1 General curvature Hamiltonians

The first example we consider is the general curvature Hamiltonian density $\mathcal{H} = \mathcal{H}(K, \mathcal{R})$.[2] The two tensors T^{ab} and $\mathcal{H}^{ab}$ can be determined by using the definitions (2.7), and the identities (B.4)-(B.6); a quick calculation leads to

$$
\begin{aligned}
T^{ab} &= -\frac{2}{\sqrt{g}}\frac{\delta(\sqrt{g}\mathcal{H})}{\delta g_{ab}} = -\left(\frac{2}{\sqrt{g}}\frac{\partial\sqrt{g}}{\partial g_{ab}}\right)\mathcal{H} - 2\frac{\partial\mathcal{H}}{\partial K}\frac{\partial K}{\partial g_{ab}} - 2\frac{\partial\mathcal{H}}{\partial\mathcal{R}}\frac{\partial\mathcal{R}}{\partial g_{ab}} \\
&= -\mathcal{H}g^{ab} + 2\frac{\partial\mathcal{H}}{\partial K}K^{ab} + 4\frac{\partial\mathcal{H}}{\partial\mathcal{R}}R^{ab} && \text{(B.8a)} \\
&\stackrel{d=2}{=} -\mathcal{H}g^{ab} + 2\frac{\partial\mathcal{H}}{\partial K}K^{ab} + 2\frac{\partial\mathcal{H}}{\partial\mathcal{R}}\mathcal{R}g^{ab}, && \text{(B.8b)} \\
\mathcal{H}^{ab} &= \frac{\delta\mathcal{H}}{\delta K_{ab}} = \frac{\partial\mathcal{H}}{\partial K}g^{ab} + 2\frac{\partial\mathcal{H}}{\partial\mathcal{R}}(Kg^{ab} - K^{ab}). && \text{(B.8c)}
\end{aligned}
$$

Thus, we get with Eqn. (B.1)

$$
\begin{aligned}
\boldsymbol{f}^a = {}& \left(-\mathcal{H}g^{ab} + \frac{\partial\mathcal{H}}{\partial K}K^{ab} + \frac{\partial\mathcal{H}}{\partial\mathcal{R}}\mathcal{R}g^{ab}\right)\boldsymbol{e}_b \\
& - \left[\nabla^a\left(\frac{\partial\mathcal{H}}{\partial K}\right) + 2(Kg^{ab} - K^{ab})\nabla_b\left(\frac{\partial\mathcal{H}}{\partial\mathcal{R}}\right)\right]\boldsymbol{n}. && \text{(B.9)}
\end{aligned}
$$

As $\mathcal{H}$ is just a function of g_{ab} and K_{ab}, the tensors $\mathcal{G}^{abc}$ and $\mathcal{K}^{abc}$ are equal to zero. Let us discuss, in particular, the Einstein-Hilbert action $\mathcal{H} = \mathcal{R}$. From the general Eqns. (B.8) one obtains with Eqn. (B.7)

$$
\begin{aligned}
\mathcal{H}^{ab} &= 2(Kg^{ab} - K^{ab}), \quad \text{and} && \text{(B.10a)} \\
T^{ab} &= -\mathcal{R}g^{ab} + 4R^{ab} \stackrel{d=2}{=} \mathcal{R}g^{ab}, && \text{(B.10b)}
\end{aligned}
$$

which gives

$$
\boldsymbol{f}^a = 2(R^{ab} - \frac{1}{2}\mathcal{R}g^{ab})\boldsymbol{e}_b = 2G^{ab}\boldsymbol{e}_b, \tag{B.11}
$$

where G_{ab} is the Einstein tensor. Due to Eqn. (B.7), this tensor vanishes identically for a two-dimensional surface, which also renders the stress tensor zero.[3]

---

[2] In Sec. 3.4.1 it is shown that every Hamiltonian density which depends on intrinsic and extrinsic surface curvatures can be brought into this form.

[3] Note that this implies that the Euler-Lagrange derivative

$$
\mathcal{E}(\mathcal{R}) = \boldsymbol{n} \cdot \nabla_a \boldsymbol{f}^a = -2K^{ab}G_{ab},
$$

equals zero as well if the surface is two-dimensional. In higher dimensions, however, the stress tensor does not vanish and $\mathcal{E}(\mathcal{R}) \propto G_{ab}$ is a nontrivial result.

For the Hamiltonian density $\mathcal{H} = K^n$, one derives $\mathcal{H}^{ab} = nK^{n-1}g^{ab}$ and $T^{ab} = 2nK^{n-1}K^{ab} - K^n g^{ab}$. Thus, the stress tensor is given by

$$\boldsymbol{f}^a = (nK^{n-1}K^{ab} - K^n g^{ab})\boldsymbol{e}_b - n(\nabla^a K^{n-1})\boldsymbol{n} \ . \tag{B.12}$$

The case $n = 2$ is needed in Sec. 2.2. The corresponding stress tensor is exactly the same as for $\mathcal{H} = K_{ab}K^{ab}$. This can be shown by rewriting $K_{ab}K^{ab} = K^2 - \mathcal{R}$ with the help of the (doubly contracted) Gauss-Codazzi equation (A.50) and inserting it into Eqn. (B.9). Note, however, that the tensors T^{ab} and $\mathcal{H}^{ab}$ for K^2 and $K_{ab}K^{ab}$ are different (see also Table B.1).

B.2.2 Gradients of curvature

Consider the general Hamiltonian density $\mathcal{H} = \mathcal{H}(g_{ab}, K_{ab}, \nabla_a K_{bc})$. Now we need to keep in mind that $\mathcal{H}^{ab}$ and T^{ab} are functional derivatives. For $\mathcal{H}^{ab}$ we obtain

$$\mathcal{H}^{ab} = \frac{\delta\mathcal{H}}{\delta K_{ab}} = \frac{\partial\mathcal{H}}{\partial K_{ab}} - \nabla_c \mathcal{K}^{cab} \ , \tag{B.13}$$

where

$$\mathcal{K}^{cab} = \frac{\partial\mathcal{H}}{\partial\nabla_c K_{ab}} \ . \tag{B.14}$$

Note that the tensor $\mathcal{K}^{abc}$ does not vanish as before because now $\mathcal{H}$ depends on covariant derivatives of K_{ab}.

The determination of T^{ab} and $\mathcal{G}^{abc}$ is a little more difficult; to avoid errors, let us proceed cautiously and consider the variation of the Hamiltonian $H = \int \mathrm{d}A\,\mathcal{H}(g_{ab}, K_{ab}, \nabla_a K_{bc})$ with respect to the metric g_{ab} and identify T^{ab} and $\mathcal{G}^{abc}$ at the end of the calculation. The difficult part is the covariant differentiation, which acts on a *tensor field* and is thus dressed with additional Christoffel symbols (see page 168 in App. A). Since the latter depend on the metric and its first partial derivative, they will contribute to the variation:

$$\delta_g H = \int \mathrm{d}^2\xi \, \delta_g(\sqrt{g}\mathcal{H}) = \int \mathrm{d}A \, \left[\frac{\delta_g\sqrt{g}}{\sqrt{g}}\mathcal{H} + \frac{\partial\mathcal{H}}{\partial g_{ab}}\delta g_{ab} + \mathcal{K}^{cab}\delta_g(\nabla_c K_{ab})\right] \ . \tag{B.15}$$

The evaluation of the first term involves the reuse of Eqn. (B.4), while the last term calls for the Palatini identity (B.III) (see Technical Point B.2) [Wei72]. Using the latter, variation $\delta_g(\nabla_c K_{ab})$ can thus be rewritten as

$$\begin{aligned}
\delta_g(\nabla_c K_{ab}) &= \delta_g(\partial_c K_{ab} - K_{db}\Gamma_{ac}{}^d - K_{ad}\Gamma_{cb}{}^d) = -K_{db}\,\delta_g\Gamma_{ac}{}^d - K_{ad}\,\delta_g\Gamma_{cb}{}^d \\
&= -\frac{1}{2}\big[K_b^d\big(\nabla_a\delta g_{dc} + \nabla_c\delta g_{ad} - \nabla_d\delta g_{ca}\big) + \{a \leftrightarrow b\}\big] \ , \tag{B.16}
\end{aligned}$$

═══ **Technical Point B.2:** *The Palatini identity* ═══

The Palatini identity describes the change of the Christoffel symbols upon variation of the metric. It reads

$$\delta_g \Gamma_{ab}{}^c = \frac{1}{2} g^{cd} \big[\nabla_b \delta g_{da} + \nabla_a \delta g_{bd} - \nabla_d \delta g_{ab} \big] \ . \tag{B.III}$$

To proof it, let us consider the variation of the Christoffel symbol explicitly:

$$\delta_g \Gamma_{ab}{}^c \overset{(\text{A.16})}{=} \frac{1}{2} \bigg\{ \delta g^{cd} \Big[\partial_a g_{bd} + \partial_b g_{da} - \partial_d g_{ab} \Big] + g^{cd} \Big[\partial_a (\delta g_{bd}) + \partial_b (\delta g_{da}) - \partial_d (\delta g_{ab}) \Big] \bigg\} \ .$$

Using Eqn. (B.I) this can be rewritten as

$$\delta_g \Gamma_{ab}{}^c = -g^{ec} \Gamma_{ab}{}^f \delta g_{ef} + \frac{1}{2} g^{cd} \Big[\partial_a (\delta g_{bd}) + \partial_b (\delta g_{da}) - \partial_d (\delta g_{ab}) \Big] \ . \tag{B.IV}$$

If we at first specialize to *local tangent coordinates*, the Christoffel symbols vanish locally. This implies that the partial derivatives in the second term can be replaced by covariant ones. Furthermore, the first term in Eqn. (B.IV) vanishes. These two changes reproduce Eqn. (B.III), and we have thus shown it to hold in local tangent coordinates.

However, Eqn. (B.III) is a proper tensor equation: the right hand side is clearly a tensor and $\delta_g \Gamma_{ab}{}^c$ is a tensor as well: it is the *difference* between two Christoffel symbols, and thus the term in the transformation law which spoils the tensorial character cancels. Eqn. (B.III) therefore holds in *any* coordinate system, not just the local tangent coordinates in which it has been derived. *q.e.d.*

which gives, with $\mathcal{K}^{cab} = \mathcal{K}^{cba}$,

$$\begin{aligned} \mathcal{K}^{cab} \delta_g (\nabla_c K_{ab}) &= -\mathcal{K}^{cab} K_b^d \big(\nabla_a \delta g_{dc} + \nabla_c \delta g_{ad} - \nabla_d \delta g_{ca} \big) \\ &= -\big(\mathcal{K}^{bcd} K_d^a + \mathcal{K}^{cad} K_d^b - \mathcal{K}^{abd} K_d^c \big) \nabla_c \delta g_{ab} \ . \end{aligned} \tag{B.17}$$

The derivative of δg_{ab} is removed by a final partial integration. Collecting results, we find

$$\delta_g H \overset{(2.7\text{b})}{=} -\frac{1}{2} \int \mathrm{d}A \ T^{ab} \delta g_{ab} + \int \mathrm{d}A \ \nabla_c [\mathcal{G}^{cab} \delta g_{ab}] \ , \tag{B.18}$$

with

$$T^{ab} = -\mathcal{H} g^{ab} - 2 \frac{\partial \mathcal{H}}{\partial g_{ab}} + 2 \nabla_c \mathcal{G}^{cab} \ , \tag{B.19}$$

and[4]

$$\mathcal{G}^{cab} = -\left(\mathcal{K}^{acd}K_d^b + \mathcal{K}^{cad}K_d^b - \mathcal{K}^{abd}K_d^c\right) . \tag{B.20}$$

If we specialize to the Hamiltonian density $\mathcal{H} = \frac{1}{2}(\nabla_c K)(\nabla^c K) \equiv \frac{1}{2}(\nabla K)^2$, we obtain

$$\mathcal{K}^{cab} = \frac{\partial \mathcal{H}}{\partial \nabla_c K_{ab}} = (\nabla^c K)g^{ab} , \tag{B.21}$$

and consequently

$$\mathcal{H}^{ab} \overset{\text{(B.13)}}{=} -\nabla_c(g^{ab}\nabla^c K) = -g^{ab}\Delta K , \quad \text{and} \tag{B.22}$$

$$\mathcal{G}^{cab} \overset{\text{(B.20)}}{=} -(\nabla^c K)K^{ab} . \tag{B.23}$$

A short calculation gives

$$T^{ab} \overset{\text{(B.19)}}{=} (\nabla^a K)(\nabla^b K) - \frac{1}{2}g^{ab}(\nabla K)^2 - 2K^{ab}\Delta K . \tag{B.24}$$

Thus, for $\mathcal{H} = \frac{1}{2}(\nabla K)^2$ we get for $\boldsymbol{f}^a$ given by Eqn. (B.1) the remarkably compact expression,

$$\boldsymbol{f}^a = \left[(\nabla^a K)(\nabla^b K) - \frac{1}{2}g^{ab}(\nabla K)^2 - K^{ab}\Delta K\right]\boldsymbol{e}_b + \nabla^a\Delta K\,\boldsymbol{n} . \tag{B.25}$$

B.2.3 Vector field

As a final example let us consider Hamiltonians of the kind introduced in Sec. 1.2.2, which have internal vector degrees of freedom. With the symmetric tilt-strain tensor $M^{ab} = \frac{1}{2}(\nabla^a m^b + \nabla^b m^a)$ we can for instance look at the quadratic Hamiltonian density $\mathcal{H} = \frac{1}{2}(\nabla_a m^a)^2 = \frac{1}{2}M^2$, where m^a is the (contravariant) surface vector field and $M = g_{ab}M^{ab}$. This term is purely intrinsic, hence $\mathcal{H}^{ab} = 0$. Now the covariant differentiation acts on a *vector field* and is thus dressed with an additional Christoffel symbol. Analogous to the previous section it will contribute to the variation:

$$\begin{aligned}
\delta_g H &= \frac{1}{2}\int \mathrm{d}^2\xi\,\delta_g(\sqrt{g}M^2) \\
&= \frac{1}{2}\int \mathrm{d}A\left\{\frac{\delta_g\sqrt{g}}{\sqrt{g}}M^2 + \delta_g(\partial_a m^a + \Gamma_{ab}{}^a m^b)^2\right\} . \tag{B.26}
\end{aligned}$$

The first term is once more simplified via Eqn. (B.4), while the second term can be rewritten as

$$\begin{aligned}
\delta_g(\partial_a m^a + \Gamma_{ab}{}^a m^b)^2 &= 2Mm^b\delta_g\Gamma_{ab}{}^a \overset{\text{(B.III)}}{=} Mm^b g^{ad}(\nabla_b\delta g_{da} + \nabla_a\delta g_{bd} - \nabla_d\delta g_{ab}) \\
&= Mm^d g^{ab}(\nabla_d\delta g_{ab}) . \tag{B.27}
\end{aligned}$$

---

[4] Note that compared to Eqn. (B.17) indices a and b are exchanged in the first term. This is allowed because of the symmetry of δg_{ab}.

$\mathcal{H}$	T^{ab}	$\mathcal{H}^{ab}$	$\mathcal{K}^{abc}$	$\mathcal{G}^{abc}$
$\mathcal{H}(K, \mathcal{R})$	$-\mathcal{H}g^{ab} + 2\frac{\partial\mathcal{H}}{\partial K}K^{ab} + 2\frac{\partial\mathcal{H}}{\partial\mathcal{R}}\mathcal{R}g^{ab}$	$\frac{\partial\mathcal{H}}{\partial K}g^{ab} + 2\frac{\partial\mathcal{H}}{\partial\mathcal{R}} \cdot$ $\left(Kg^{ab} - K^{ab}\right)$	0	0
1	$-g^{ab}$	0	0	0
$\mathcal{R}$	$\mathcal{R}g^{ab}$	$2(Kg^{ab} - K^{ab})$	0	0
K^n	$2nK^{n-1}K^{ab} - K^n g^{ab}$	$nK^{n-1}g^{ab}$	0	0
$K_{ab}K^{ab}$	$-K_{cd}K^{cd}g^{ab} + 4K_c^a K^{bc}$	$2K^{ab}$	0	0
$\mathcal{H}(g_{ab}, K_{ab}, \nabla_a K_{bc})$	$-\mathcal{H}g^{ab} - 2\frac{\partial\mathcal{H}}{\partial g_{ab}} + 2\nabla_c\mathcal{G}^{cab}$	$\frac{\partial\mathcal{H}}{\partial K_{ab}} - \nabla_c\mathcal{K}^{cab}$	$\frac{\partial\mathcal{H}}{\partial\nabla_a K_{bc}}$	$-\left[(\mathcal{K}^{acd} + \mathcal{K}^{cad})K_d^b \right.$ $\left. -\mathcal{K}^{cbd}K_d^a\right]$
$\frac{1}{2}(\nabla K)^2 \equiv$ $\frac{1}{2}(\nabla_c K)(\nabla^c K)$	$(\nabla^a K)(\nabla^b K) - \frac{1}{2}g^{ab}(\nabla K)^2$ $-2K^{ab}\Delta K$	$-g^{ab}\Delta K$	$(\nabla^a K)g^{bc}$	$-(\nabla^a K)K^{bc}$
$\frac{1}{2}M^2 \equiv \frac{1}{2}(\nabla_a m^a)$	$\frac{1}{2}\left[M^2 + 2m^c\nabla_c M\right]g^{ab}$	0	0	$\frac{1}{2}Mm^a g^{bc}$
$M_{ab}M^{ab}$	$-M_{cd}M^{cd}g^{ab} + 2MM^{ab} + 2m^c\nabla_c M^{ab}$ $-(\nabla_c m^a)(\nabla^c m^b) + (\nabla^a m_c)(\nabla^b m^c)$	0	0	$m^a M^{bc}$
$\frac{1}{4}F_{ab}F^{ab}$	$\frac{1}{2}g^{ab}\left(\varepsilon_{cd}\nabla^c m^d\right)^2$	0	0	0

Table B.1: Tensors T^{ab}, $\mathcal{H}^{ab}$, $\mathcal{K}^{abc}$, and $\mathcal{G}^{abc}$ on a two-dimensional surface for several Hamiltonian densities.

The derivative of δg_{ab} can again be removed by a final partial integration. Collecting everything, we thus find

$$
\begin{aligned}
\delta_g H &= \frac{1}{2} \int \mathrm{d}A \left\{ \left[\frac{1}{2} M^2 - \nabla_d \big(m^d M \big) \right] g^{ab} \delta g_{ab} + \nabla_d \big(M m^d g^{ab} \delta g_{ab} \big) \right\} \\
&= -\frac{1}{2} \int \mathrm{d}A \left(\frac{1}{2} M^2 + m^d \nabla_d M \right) g^{ab} \delta g_{ab} + \int \mathrm{d}A \, \nabla_d \left(\frac{1}{2} M m^d g^{ab} \delta g_{ab} \right) \tag{B.28}
\end{aligned}
$$

Thus, the metric stress tensor is

$$
T^{ab} = \frac{1}{2} \Big[M^2 + 2 m^c \nabla_c M \Big] g^{ab} , \tag{B.29}
$$

and

$$
\mathcal{G}^{cab} = \frac{1}{2} M m^c g^{ab} . \tag{B.30}
$$

Notice that T^{ab} is directly proportional to the metric; its effect in the stress tensor will thus be to renormalize the surface tension.

The second quadratic invariant, $\mathcal{H} = M_{ab} M^{ab}$, does not provide any additional difficulties compared to $\frac{1}{2} M^2$, even though the calculation is a bit longer. One finds:

$$
\begin{aligned}
T^{ab} &= -M_{cd} M^{cd} g^{ab} + 2 M M^{ab} + 2 m^c \nabla_c M^{ab} \\
&\quad - (\nabla_c m^a)(\nabla^c m^b) + (\nabla^a m_c)(\nabla^b m^c) , \tag{B.31}
\end{aligned}
$$

and

$$
\mathcal{G}^{cab} = m^c M^{ab} . \tag{B.32}
$$

Finally, the third quadratic invariant $\mathcal{H} = \frac{1}{4} F_{ab} F^{ab}$ (with $F_{ab} = \nabla_a m_b - \nabla_b m_a = \partial_a m_b - \partial_b m_a$) can be treated rather easily by noting that F_{ab} and thus $\mathcal{H} = \frac{1}{4} g^{ac} g^{bd} F_{ab} F_{cd}$ are independent of the connection.[5] A short calculation then shows that

$$
T^{ab} = F^{ac} F^b{}_c - \frac{1}{4} g^{ab} F_{cd} F^{cd} . \tag{B.33}
$$

It should not come as a surprise that this has the same form as the energy-momentum tensor from electrodynamics [LL00]. In two dimensions it can be further simplified, since any antisymmetric tensor is then proportional to the epsilon-tensor: $F^{ab} = \frac{1}{2} \varepsilon^{ab} \varepsilon_{cd} F^{cd}$. Inserting this into Eqn. (B.33) and using the identity $\varepsilon^{ac} \varepsilon^b{}_c = g^{ab}$ (see Eqn. (A.14)), we find

$$
T^{ab} = \frac{1}{2} g^{ab} \big(\varepsilon_{cd} \nabla^c m^d \big)^2 , \tag{B.34}
$$

---

[5] This also implies that $\mathcal{G}^{cab}$ vanishes for that case as no covariant derivatives of δg_{ab} enter the variation.

showing that the stress is isotropic, just as in the case of the Hamiltonian $\mathcal{H} = \frac{1}{2}M^2$. It will thus only renormalize the surface tension and, in particular, not single out any specific new directions on the membrane.

In Table B.1 the results of this appendix for T^{ab}, $\mathcal{H}^{ab}$, $\mathcal{K}^{abc}$, and $\mathcal{G}^{abc}$ are summarized. In Chaps. 2 and 3 they are used to determine stress tensor, Euler-Lagrange equation and boundary conditions.

C Solutions of the membrane shape equation

In this appendix the shape equation for an up-down symmetric membrane (4.3)

$$-\kappa \Delta K + \frac{\kappa}{2} K (K^2 - 2 K_{ab} K^{ab}) + \sigma K = 0 \tag{C.1}$$

is solved for special cases.

C.1 Two cylinders on a membrane

For a translationally symmetric membrane Eqn. (C.1) reduces to

$$\lambda^2 \ddot{\psi} - \eta \sin \psi = 0 \ . \tag{C.2}$$

This equation can be solved for the free membrane sections of the two-cylinder case (see Sec. 5.2).[1] As was shown in Sec. 5.2.1, Eqn. (C.2) possesses a first integral with the proper integration constant:

$$\frac{\lambda^2}{2} \dot{\psi}^2 + \eta \cos \psi = 1 \ . \tag{C.3}$$

A separation of variables yields

$$\mathrm{d}s = \pm \frac{\lambda}{\sqrt{2(1 - \eta \cos \psi)}} \, \mathrm{d}\psi \ . \tag{C.4}$$

Due to the symmetry it is sufficient to consider only the left half of the membrane. While the outer sections are qualitatively identical for the symmetric and antisymmetric case, the inner sections differ. For each section Eqn. (C.4) can be integrated to determine s as a function of ψ which can be inverted to determine $\psi(s)$. A subsequent differentiation yields the curvature of the profile $K(s) = \pm \dot{\psi}(s)$.[2] Finally, the distances along $\boldsymbol{x}$ and $\boldsymbol{z}$ can be obtained from Eqns. (A.76):[2]

$$\Delta x(s) \;=\; \int_0^s \mathrm{d}s' \, \cos \psi(s') \overset{(C.3)}{=} \frac{1}{\eta} \int_0^s \mathrm{d}s' \, \left[1 - \frac{\lambda^2}{2} K^2(s') \right] \ , \tag{C.5a}$$

$$\Delta h(s) \;=\; \int_0^s \mathrm{d}s' \, \sin \psi(s') \overset{(C.2)}{=} \frac{\lambda^2}{\eta} \int_0^s \mathrm{d}s' \, \ddot{\psi}(s') = \pm \frac{\lambda^2}{\eta} [K(s) - K(0)] \ . \tag{C.5b}$$

---

[1] The calculations can also be found in a Mathematica file at [WWWc].
[2] The positive sign is valid for the inner section, the negative sign for the outer.
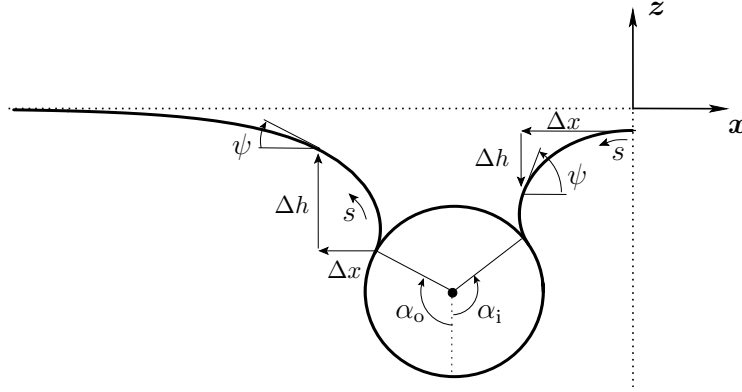
Figure C.1: Relevant parameters for the symmetric case. The arrows point in the positive direction of Δx, Δh, and s, respectively.

The sign of the resulting values for Δx and Δh depends on the direction of s (see Figs. C.1 and C.3 and footnote 10 in App. A.4.2).[3]
Eqn. (C.3) is a first-order differential equation involving one unknown constant η. Thus, two boundary conditions are required for each section.

C.1.1 Outer section

At infinity, ψ and its derivative $\dot{\psi}$ vanish. Inserting these conditions into Eqn. (C.3) yields $\eta = 1$ for the outer section. Without loss of generality we consider only positive values of ψ. The solution for negative angles can be obtained by reversing the sign of the function which corresponds to a reflection of the profile in the (x, y) plane.

At the contact point the profile leaves the cylinder at the fixed angle $\psi(0) = \alpha_{\mathrm{o}} \in [0, 2\pi]$ (see Fig. C.1). For increasing arc length s the angle ψ decreases. Thus, the sign in Eqn. (C.4) is negative and $s(\psi)$ can be obtained:

$$
\int_0^s \mathrm{d}s' = s(\psi) = -\int_{\alpha_{\mathrm{o}}}^{\psi} \frac{\lambda}{\sqrt{2(1 - \cos \psi')}} \mathrm{d}\psi' = -\int_{\alpha_{\mathrm{o}}}^{\psi} \frac{\lambda}{4 \tan\left(\frac{\psi'}{4}\right) \cos^2\left(\frac{\psi'}{4}\right)} \mathrm{d}\psi'
$$

$$
= -\lambda \left[\ln\left(\tan \frac{\psi'}{4} \right) \right]_{\alpha_{\mathrm{o}}}^{\psi} = -\lambda \ln\left[\cot\left(\frac{\alpha_{\mathrm{o}}}{4}\right) \tan\left(\frac{\psi}{4}\right) \right], \qquad (\mathrm{C.6})
$$

---

[3] Note that Eqn. (C.5b) is equivalent to the shape equation (2.64) of a (one-dimensional) fluid meniscus if we substitute $\lambda = \ell$ and $\eta = 1$. The physics of an Euler elasticum and a fluid meniscus can in fact be mapped onto each other (see also Technical Point 5.5 on page 131). Remarkably, in both cases it is the *curvature K* of the surface which fixes its height h even though the former is essentially a second derivative of h (compare Eqn. (A.81a)).
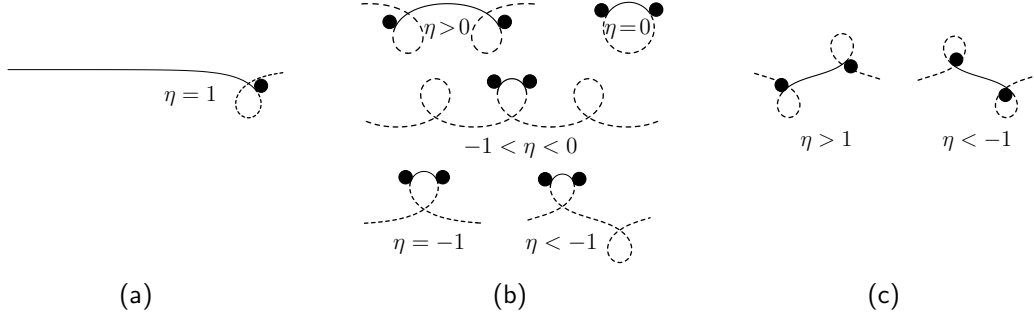
Figure C.2: Solutions of Eqn. (C.3) for the (a) outer section (b) inner section - symmetric case (c) inner section - antisymmetric case (*cf.* Fig. 5.8).

where we have exploited that $1 - \cos\psi = 2\sin^2\frac{\psi}{2}$ and $\sin\frac{\psi}{2} = 2\sin\left(\frac{\psi}{4}\right)\cos\left(\frac{\psi}{4}\right) = 2\tan\left(\frac{\psi}{4}\right)\cos^2\left(\frac{\psi}{4}\right)$. The inversion yields

$$\psi(s) = 4\arctan\left[\tan\left(\frac{\alpha_o}{4}\right)e^{-s/\lambda}\right]. \tag{C.7}$$

The curvature is given by

$$K(s) = -\dot\psi(s) = \frac{4e^{s/\lambda}\tan\frac{\alpha_o}{4}}{\lambda(e^{2s/\lambda} + \tan^2\frac{\alpha_o}{4})}, \tag{C.8}$$

and thus

$$K(0) = K_o = \frac{2}{\lambda}\sin\frac{\alpha_o}{2}. \tag{C.9}$$

Finally, $\Delta x(s)$ and $\Delta h(s)$ can be calculated:

$$\Delta x(s) \overset{(\text{C.5a})}{=} \int_0^s ds'\left[1 - \frac{\lambda^2}{2}K^2(s')\right] \overset{(\text{C.8})}{=} s + \frac{\lambda(1 - \cos\alpha_o)(1 - e^{2s/\lambda})}{(1 + e^{2s/\lambda}) - (1 - e^{2s/\lambda})\cos\frac{\alpha_o}{2}}, \tag{C.10}$$

and

$$\Delta h(s) \overset{(\text{C.5b})}{=} \lambda^2[K(0) - K(s)] \overset{(\text{C.8,C.9})}{=} 2\lambda\left(\sin\frac{\alpha_o}{2} - \frac{2e^{s/\lambda}\tan\frac{\alpha_o}{4}}{e^{2s/\lambda} + \tan^2\frac{\alpha_o}{4}}\right), \tag{C.11}$$

which yields

$$\lim_{s\to\infty}[\Delta h(s)] = \lambda^2 K(0) \overset{(\text{C.9})}{=} 2\lambda\sin\frac{\alpha_o}{2}. \tag{C.12}$$

as the vertical distance between contact point and asymptotic plane.[4]

---

[4] This is again nothing but the shape equation of a fluid meniscus (compare footnote 3).

C.1.2 Inner section

For the inner section, the arc length s is measured from the midplane. Due to this chosen orientation $K = +\dot\psi$ now. Again, only positive values of ψ are considered.

Symmetric case

In the symmetric case, $\psi(0)$ is equal to zero. From Eqn. (C.3) we thus obtain $\eta \leq 1$. This result is consistent with the fact that two cylinders on the same side of the membrane always repel (see Eqn. (5.12)): a scaled force of $\eta = 1$ is pulling to the left at the outer section which is only balanced partly by the scaled force acting to the right at the inner section (see also Sec. 5.2.3).

For $\eta = 1$, the cylinders are infinitely far apart and do not interact. If we omit this trivial case, five cases with different solutions for $\psi(s)$ must be considered separately. The sign of Eqn. (C.4) is positive in all of these cases as ψ increases for increasing s.

a) $0 < \eta < 1$**:**

The integration of Eqn. (C.4) yields

$$
\begin{aligned}
\int_0^s \mathrm{d}s' &= s(\psi) = \int_0^\psi \frac{\lambda}{\sqrt{2(1 - \eta \cos \psi')}} \mathrm{d}\psi' = \int_0^\psi \frac{\lambda}{\sqrt{2[1 + \eta \cos (\psi' - \pi)]}} \mathrm{d}\psi' \\
&= \int_0^\psi \frac{\lambda}{\sqrt{2[1 + \eta(1 - 2 \sin^2 \frac{\psi'-\pi}{2})]}} \mathrm{d}\psi' = \int_0^\psi \frac{\lambda}{\sqrt{2[(1 + \eta) - 2\eta \sin^2 \frac{\psi'-\pi}{2}]}} \mathrm{d}\psi' \\
&= \frac{\lambda}{\sqrt{2(1 + \eta)}} \int_0^\psi \frac{1}{\sqrt{1 - \frac{2\eta}{1+\eta} \sin^2 \frac{\psi'-\pi}{2}}} \mathrm{d}\psi' \; .
\end{aligned} \tag{C.13}
$$

For all of the following it proves handy to define the parameter

$$
m := \frac{2|\eta|}{1 + |\eta|} \; , \tag{C.14}
$$

with $m < 1$ for $0 < \eta < 1$. If we insert m into Eqn. (C.13) and substitute $\theta' = \frac{\psi'-\pi}{2}$, we obtain

$$
s(\psi) = \frac{2\lambda}{\sqrt{2(1 + \eta)}} \int_{-\frac{\pi}{2}}^{\frac{\psi-\pi}{2}} \frac{1}{\sqrt{1 - m \sin^2 \theta'}} \mathrm{d}\theta' = \lambda \sqrt{\frac{m}{\eta}} \left(\mathcal{F}\left[\!\!\left[\frac{\psi - \pi}{2}, m \right]\!\!\right] + \mathcal{F}\left[\!\!\left[\frac{\pi}{2}, m \right]\!\!\right] \right) , \tag{C.15}
$$

where $\mathcal{F}[\![\varphi, m]\!]$ is the elliptic integral of the first kind (see Table C.1). Note that $\mathcal{F}[\![\pi/2, m]\!] = \mathcal{K}[\![m]\!]$, where $\mathcal{K}[\![m]\!]$ is the complete elliptic integral of the first kind

[AS70]. The integral can be inverted:

$$\frac{s}{\lambda}\sqrt{\frac{\eta}{m}} - \mathcal{K}[\![m]\!] = \mathcal{F}\left[\!\left[\frac{\psi-\pi}{2}, m\right]\!\right] \quad\Leftrightarrow\quad \mathrm{am}\left[\!\left[\frac{s}{\lambda}\sqrt{\frac{\eta}{m}} - \mathcal{K}[\![m]\!], m\right]\!\right] = \frac{\psi-\pi}{2}$$

$$\Leftrightarrow\quad \psi(s) = \pi + 2\,\mathrm{am}\left[\!\left[\frac{s}{\lambda}\sqrt{\frac{\eta}{m}} - \mathcal{K}[\![m]\!], m\right]\!\right] , \tag{C.16}$$

where $\mathrm{am}[\![t,m]\!]$ is the Jacobi amplitude (see Table C.1 and Ref. [AS70]). A differentiation with respect to s yields the curvature

$$K(s) = +\dot\psi(s) = \frac{2}{\lambda}\sqrt{\frac{\eta}{m}}\,\mathrm{dn}\left[\!\left[\frac{s}{\lambda}\sqrt{\frac{\eta}{m}} - \mathcal{K}[\![m]\!], m\right]\!\right] , \tag{C.17}$$

with $\mathrm{dn}[\![t,m]\!] = \sqrt{1 - m\,\mathrm{sn}^2[\![t,m]\!]}$ and $\mathrm{sn}[\![t,m]\!] = \sin\left(\mathrm{am}[\![t,m]\!]\right)$ (see again Table C.1).

By inserting Eqn. (C.17) into Eqn. (C.5a) we obtain

$$\begin{aligned}
\Delta x(s) &= \frac{1}{\eta}\int_0^s \mathrm{d}s'\left[1 - \frac{\lambda^2}{2}\left(\frac{2}{\lambda}\sqrt{\frac{\eta}{m}}\,\mathrm{dn}\left[\!\left[\frac{s}{\lambda}\sqrt{\frac{\eta}{m}} - \mathcal{K}[\![m]\!], m\right]\!\right]\right)^2\right] \\
&= \frac{s}{\eta} - \frac{2}{m}\int_0^s \mathrm{d}s'\,\mathrm{dn}^2\left[\!\left[\frac{s}{\lambda}\sqrt{\frac{\eta}{m}} - \mathcal{K}[\![m]\!], m\right]\!\right] \\
&= \frac{s}{\eta} - \frac{2\lambda}{\sqrt{\eta\,m}}\left[\mathcal{E}\left[\!\left[\mathrm{am}\left[\!\left[\frac{s'}{\lambda}\sqrt{\frac{\eta}{m}} - \mathcal{K}[\![m]\!], m\right]\!\right], m\right]\!\right]\right]_0^s \\
&\overset{\text{(C.IIb,C.IVa)}}{=} \frac{s}{\eta} - \frac{2\lambda}{\sqrt{\eta\,m}}\left(\mathcal{E}\left[\!\left[\mathrm{am}\left[\!\left[\frac{s}{\lambda}\sqrt{\frac{\eta}{m}} - \mathcal{K}[\![m]\!], m\right]\!\right], m\right]\!\right] + \mathcal{E}[\![k]\!]\right) , \tag{C.18}
\end{aligned}$$

where $\mathcal{E}[\![\varphi, m]\!]$ is the elliptic integral of the second kind and $\mathcal{E}[\![\pi/2, m]\!] = \mathcal{E}[\![m]\!]$ its complete version (see Table C.1).

Inserting Eqn. (C.17) into Eqn. (C.5b) yields,

$$\begin{aligned}
\Delta h(s) &= \frac{\lambda^2}{\eta}\left(\frac{2}{\lambda}\sqrt{\frac{\eta}{m}}\,\mathrm{dn}\left[\!\left[\frac{s}{\lambda}\sqrt{\frac{\eta}{m}} - \mathcal{K}[\![m]\!], m\right]\!\right] - \frac{2}{\lambda}\sqrt{\frac{\eta}{m}}\,\mathrm{dn}\left[\!\left[- \mathcal{K}[\![m]\!], m\right]\!\right]\right) \\
&\overset{\text{(C.IVc)}}{=} \frac{2\lambda}{\sqrt{\eta\,m}}\left(\mathrm{dn}\left[\!\left[\frac{s}{\lambda}\sqrt{\frac{\eta}{m}} - \mathcal{K}[\![m]\!], m\right]\!\right] - \sqrt{1-m}\right) . \tag{C.19}
\end{aligned}$$

b) $\eta = 0$**:**

From Eqn. (C.4) follows

$$\dot\psi = \frac{\sqrt{2}}{\lambda} \Rightarrow \psi(s) = \frac{\sqrt{2}}{\lambda}s . \tag{C.20}$$

elliptic integral of the first kind	$$\mathcal{F}[\![\varphi, m]\!] \quad = \quad \int_0^\varphi \frac{1}{\sqrt{1 - m \sin^2 \theta}} \, \mathrm{d}\theta$$
complete elliptic integral of the first kind	$$\mathcal{K}[\![m]\!] \quad = \quad \mathcal{F}\left[\!\left[\frac{\pi}{2}, m\right]\!\right]$$
elliptic integral of the second kind	$$\mathcal{E}[\![\varphi, m]\!] \quad = \quad \int_0^\varphi \sqrt{1 - m \sin^2 \theta} \, \mathrm{d}\theta$$
complete elliptic integral of the second kind	$$\mathcal{E}[\![m]\!] \quad = \quad \mathcal{E}\left[\!\left[\frac{\pi}{2}, m\right]\!\right]$$
Jacobi amplitude	$$\mathrm{am}[\![\mathcal{F}[\![\varphi, m]\!], m]\!] = \varphi$$
Jacobi elliptic function sn	$$\mathrm{sn}[\![t, m]\!] \quad = \quad \sin\left(\mathrm{am}[\![t, m]\!]\right)$$
Jacobi elliptic function cn	$$\mathrm{cn}[\![t, m]\!] \quad = \quad \cos\left(\mathrm{am}[\![t, m]\!]\right)$$
Delta amplitude	$$\mathrm{dn}[\![t, m]\!] \quad = \quad \sqrt{1 - m \, \mathrm{sn}^2[\![t, m]\!]}$$

$$\mathcal{F}[\![\varphi, m]\!] = m^{-1/2} \mathcal{F}[\![\alpha, m^{-1}]\!] \,, \quad \text{where } \sin \alpha = m^{1/2} \sin \varphi \,. \qquad \text{(C.I)}$$

$$\mathcal{F}[\![-\varphi, m]\!] = -\mathcal{F}[\![\varphi, m]\!] \,, \qquad \text{(C.IIa)} \qquad \mathcal{E}[\![-\varphi, m]\!] = -\mathcal{E}[\![\varphi, m]\!] \,. \qquad \text{(C.IIb)}$$

$$\begin{aligned} \mathrm{am}[\![0, m]\!] &= 0 \,, \quad \text{(C.IIIa)} & \mathrm{am}[\![-\mathcal{K}[\![m]\!], m]\!] &= -\pi/2 \,, \quad \text{(C.IVa)} \\ \mathrm{cn}[\![0, m]\!] &= 1 \,, \quad \text{(C.IIIb)} & \mathrm{cn}[\![-\mathcal{K}[\![m]\!], m]\!] &= 0 \,, \quad \text{(C.IVb)} \\ \mathrm{dn}[\![0, m]\!] &= 1 \,. \quad \text{(C.IIIc)} & \mathrm{dn}[\![-\mathcal{K}[\![m]\!], m]\!] &= \sqrt{1 - m} \,. \quad \text{(C.IVc)} \end{aligned}$$

Table C.1: Elliptic integrals and elliptic functions (upper part) and a few identities between them (lower part). The parameters φ, m, and t are real numbers with $m \sin^2 \theta < 1 \; \forall \theta \in [0, \varphi]$ (see also Ref. [AS70]).

The solution is a circular arc of curvature $K = \sqrt{2}/\lambda$. The distances Δx and Δh can be calculated directly:

$$\Delta x(s) = \int_0^s \mathrm{d}s' \, \cos\left(\frac{\sqrt{2}}{\lambda} s'\right) = \frac{\lambda}{\sqrt{2}} \sin\left(\frac{\sqrt{2}}{\lambda} s\right), \tag{C.21}$$

and

$$\Delta h(s) = \int_0^s \mathrm{d}s' \, \sin\left(\frac{\sqrt{2}}{\lambda} s'\right) = -\frac{\lambda}{\sqrt{2}}\left[\cos\left(\frac{\sqrt{2}}{\lambda} s\right) - 1\right] = \lambda\sqrt{2} \sin^2\left(\frac{s}{\lambda\sqrt{2}}\right). \tag{C.22}$$

c) $-1 < \eta < 0$:

For negative values of η the integrated Eqn. (C.4) can be simplified in the following way

$$\int_0^s \mathrm{d}s' = s(\psi) = \int_0^\psi \frac{\lambda}{\sqrt{2(1 + |\eta|\cos\psi')}}\mathrm{d}\psi' = \int_0^\psi \frac{\lambda}{\sqrt{2[1 + |\eta|(1 - 2\sin^2\frac{\psi'}{2})]}}\mathrm{d}\psi'$$

$$= \frac{\lambda}{\sqrt{2(1 + |\eta|)}} \int_0^\psi \frac{1}{\sqrt{1 - m\sin^2\frac{\psi'}{2}}}\mathrm{d}\psi', \tag{C.23}$$

where we used $m \overset{(C.14)}{=} \frac{2|\eta|}{1+|\eta|} < 1$ again. The substitution $\theta' = \frac{\psi'}{2}$ yields:

$$s(\psi) = \frac{2\lambda}{\sqrt{2(1 + |\eta|)}} \int_0^{\frac{\psi}{2}} \frac{1}{\sqrt{1 - m\sin^2\theta'}}\mathrm{d}\theta' \overset{m\leq 1}{=} \lambda\sqrt{\frac{m}{|\eta|}}\mathcal{F}\left[\!\left[\frac{\psi}{2}, m\right]\!\right], \tag{C.24}$$

which can be inverted easily:

$$\psi(s) = 2\,\mathrm{am}\left[\!\left[\frac{s}{\lambda}\sqrt{\frac{|\eta|}{m}}, m\right]\!\right]. \tag{C.25}$$

The curvature is given by

$$K(s) = \frac{2}{\lambda}\sqrt{\frac{|\eta|}{m}}\,\mathrm{dn}\left[\!\left[\frac{s}{\lambda}\sqrt{\frac{|\eta|}{m}}, m\right]\!\right]. \tag{C.26}$$

To obtain $\Delta x(s)$ and $\Delta h(s)$, we insert $K(s)$ into Eqns. (C.5) again

$$\Delta x(s) \overset{(C.26)}{=} \frac{1}{\eta}\int_0^s \mathrm{d}s' \left[1 - \frac{\lambda^2}{2}\left(\frac{2}{\lambda}\sqrt{\frac{|\eta|}{m}}\,\mathrm{dn}\left[\!\left[\frac{s}{\lambda}\sqrt{\frac{|\eta|}{m}}, m\right]\!\right]\right)^2\right]$$

$$= -\frac{s}{|\eta|} + \frac{2}{m}\int_0^s \mathrm{d}s' \, \mathrm{dn}^2\left[\!\left[\frac{s}{\lambda}\sqrt{\frac{|\eta|}{m}}, m\right]\!\right]$$

$$\overset{(C.IIIa)}{=} -\frac{s}{|\eta|} + \frac{2\lambda}{\sqrt{|\eta|\,m}}\mathcal{E}\left[\!\left[\mathrm{am}\left[\!\left[\frac{s}{\lambda}\sqrt{\frac{|\eta|}{m}}, m\right]\!\right], m\right]\!\right], \tag{C.27}$$

and

$$\Delta h(s) \overset{\text{(C.26)}}{=} \frac{\lambda^2}{\eta}\left(\frac{2}{\lambda}\sqrt{\frac{|\eta|}{m}}\,\text{dn}\left[\!\left[\frac{s}{\lambda}\sqrt{\frac{|\eta|}{m}},m\right]\!\right] - \frac{2}{\lambda}\sqrt{\frac{|\eta|}{m}}\right)$$

$$\overset{\text{(C.IIIc)}}{=} \frac{2\lambda}{\sqrt{|\eta|\,m}}\left(1 - \text{dn}\left[\!\left[\frac{s}{\lambda}\sqrt{\frac{|\eta|}{m}},m\right]\!\right]\right). \tag{C.28}$$

d) $\eta = -1$:

For the case of $\eta = -1$, integration of Eqn. (C.4) yields

$$\int_0^s \mathrm{d}s' = s(\psi) = \int_0^\psi \frac{\lambda}{\sqrt{2(1+\cos\psi')}}\mathrm{d}\psi' = \int_0^\psi \frac{\lambda}{2\cos\frac{\psi'}{2}}\mathrm{d}\psi'$$

$$= \int_0^\psi \frac{\lambda}{2(\cos^2\frac{\psi'}{4} - \sin^2\frac{\psi'}{4})}\mathrm{d}\psi' = \lambda\left[\ln\left(\frac{\cos\frac{\psi'}{4} + \sin\frac{\psi'}{4}}{\cos\frac{\psi'}{4} - \sin\frac{\psi'}{4}}\right)\right]_0^\psi$$

$$= -\lambda\ln\left(\frac{2}{1+\tan\frac{\psi}{4}} - 1\right). \tag{C.29}$$

Thus, the angle is given by

$$\psi(s) = 4\arctan\left[\tanh\left(\frac{s}{2\lambda}\right)\right], \tag{C.30}$$

where $0 < \psi < \pi$. The corresponding profile can also be obtained by reflecting the solution of $\eta = 1$ in the (x, y) plane (see Fig. C.2 (a) and (b)). Note, however, that different parts of the loop have to be considered for each of the two cases. Differentiating Eqn. (C.30) yields the curvature

$$K(s) = \frac{4}{1 + \tanh^2\left(\frac{s}{2\lambda}\right)}\frac{1}{\cosh^2\left(\frac{s}{2\lambda}\right)}\frac{1}{2\lambda} = \frac{2}{\lambda\cosh\left(\frac{s}{\lambda}\right)}. \tag{C.31}$$

Now, $\Delta x(s)$ and $\Delta h(s)$ can be calculated using Eqns. (C.5) once more:

$$\Delta x(s) \overset{\text{(C.31)}}{=} -s + \frac{\lambda^2}{2}\int_0^s \mathrm{d}s'\frac{4}{\lambda^2\cosh^2\left(\frac{s}{\lambda}\right)} = -s + 2\lambda\tanh\left(s/\lambda\right), \tag{C.32}$$

and

$$\Delta h(s) \overset{\text{(C.31)}}{=} 2\lambda\left[1 - \frac{1}{\cosh\left(\frac{s}{\lambda}\right)}\right]. \tag{C.33}$$

e) $\eta < -1$**:**

The final case for a symmetric cylinder configuration is $\eta < -1$. Exactly as in paragraph c), the arc length can be written as

$$\int_0^s \mathrm{d}s' = s(\psi) = \int_0^\psi \frac{\lambda}{\sqrt{2(1+|\eta|\cos\psi')}}\mathrm{d}\psi' = \frac{2\lambda}{\sqrt{2(1+|\eta|)}} \int_0^{\frac{\psi}{2}} \frac{1}{\sqrt{1-m\sin^2\theta'}}\mathrm{d}\theta' \ . \tag{C.34}$$

The parameter m is greater than 1 now. According to Eqn. (C.I), however, we can write $\mathcal{F}[\![\varphi, m]\!] = m^{-1/2}\mathcal{F}[\![\alpha, m^{-1}]\!]$ with $\sin\alpha = m^{1/2}\sin\varphi$ (see also Ref. [AS70]). With $\varphi = \psi/2$ we get

$$s(\psi) = \lambda\sqrt{\frac{m}{|\eta|}}\frac{1}{\sqrt{m}}\mathcal{F}[\![\alpha, m^{-1}]\!] = \lambda\sqrt{\frac{1}{|\eta|}}\mathcal{F}[\![\alpha, m^{-1}]\!] \ , \tag{C.35}$$

and thus

$$\alpha = \mathrm{am}\left[\!\!\left[\frac{s}{\lambda}\sqrt{|\eta|}, m^{-1}\right]\!\!\right] \ . \tag{C.36}$$

We finally obtain

$$\sin\alpha = m^{1/2}\sin\frac{\psi}{2} = \mathrm{sn}\left[\!\!\left[\frac{s}{\lambda}\sqrt{|\eta|}, m^{-1}\right]\!\!\right]$$

$$\Leftrightarrow \quad m\sin^2\frac{\psi}{2} = \mathrm{sn}^2\left[\!\!\left[\frac{s}{\lambda}\sqrt{|\eta|}, m^{-1}\right]\!\!\right]$$

$$\Leftrightarrow \quad \frac{m}{2}(1-\cos\psi) = \mathrm{sn}^2\left[\!\!\left[\frac{s}{\lambda}\sqrt{|\eta|}, m^{-1}\right]\!\!\right]$$

$$\Leftrightarrow \quad \cos\psi = 1 - \frac{2}{m}\mathrm{sn}^2\left[\!\!\left[\frac{s}{\lambda}\sqrt{|\eta|}, m^{-1}\right]\!\!\right] \ . \tag{C.37}$$

The angle ψ is positive for $0 \leq s \leq \frac{2\lambda}{\sqrt{|\eta|}}\mathcal{K}[\![m^{-1}]\!]$. Thus, for that interval,

$$\psi(s) = \arccos\left(1 - \frac{2}{m}\mathrm{sn}^2\left[\!\!\left[\frac{s}{\lambda}\sqrt{|\eta|}, m^{-1}\right]\!\!\right]\right) \ , \tag{C.38}$$

where $[-1, 1] \ni x \mapsto \arccos(x) \in [0, \pi]$.

With $\mathrm{cn}[\![t, m]\!] = \cos\left(\mathrm{am}[\![t, m]\!]\right)$ and $\mathrm{sn}^2[\![t, m]\!] + \mathrm{cn}^2[\![t, m]\!] = 1$ we obtain for the

curvature[5]

$$
\begin{aligned}
K(s) \quad &\overset{(5.50)}{=} \quad \lambda^{-1}\sqrt{2(1+|\eta|\cos\psi)} \\
&\overset{(C.37)}{=} \quad \lambda^{-1}\sqrt{2\Big[1+|\eta|\Big(1-\frac{2}{m}\operatorname{sn}^2\Big[\!\!\Big[\frac{s}{\lambda}\sqrt{|\eta|},m^{-1}\Big]\!\!\Big]\Big)\Big]} \\
&= \quad \lambda^{-1}\sqrt{2\Big(1+|\eta|-\frac{2|\eta|}{m}+\frac{2|\eta|}{m}\operatorname{cn}^2\Big[\!\!\Big[\frac{s}{\lambda}\sqrt{|\eta|},m^{-1}\Big]\!\!\Big]\Big)} \\
&= \quad \frac{2}{\lambda}\sqrt{\frac{|\eta|}{m}}\operatorname{cn}\Big[\!\!\Big[\frac{s}{\lambda}\sqrt{|\eta|},m^{-1}\Big]\!\!\Big]\,, &(C.39)
\end{aligned}
$$

where we exploited that $|\eta|\overset{(C.14)}{=}\frac{m}{2-m}$ in the last step.
The distance Δx is given by

$$
\begin{aligned}
\Delta x(s) \quad &= \quad \int_0^s \mathrm{d}s'\cos\psi(s')\overset{(C.37)}{=}\int_0^s\mathrm{d}s'\Big(1-\frac{2}{m}\operatorname{sn}^2\Big[\!\!\Big[\frac{s'}{\lambda}\sqrt{|\eta|},m^{-1}\Big]\!\!\Big]\Big) \\
&= \quad s-\frac{2\lambda}{\sqrt{|\eta|}}\Big[-\mathcal{E}\Big[\!\!\Big[\operatorname{am}\Big[\!\!\Big[\frac{s'}{\lambda}\sqrt{|\eta|},m^{-1}\Big]\!\!\Big],m^{-1}\Big]\!\!\Big]+\frac{s'}{\lambda}\sqrt{|\eta|}\Big]_0^s \\
&\overset{(C.\mathrm{IIIa})}{=} \quad -s+\frac{2\lambda}{\sqrt{|\eta|}}\mathcal{E}\Big[\!\!\Big[\operatorname{am}\Big[\!\!\Big[\frac{s}{\lambda}\sqrt{|\eta|},m^{-1}\Big]\!\!\Big],m^{-1}\Big]\!\!\Big]\,. &(C.40)
\end{aligned}
$$

To determine the height Δh, we insert the curvature (C.39) into Eqn. (C.5b) and use Eqn. (C.IIIb)

$$
\Delta h(s)=-\frac{\lambda^2}{|\eta|}\Big(\frac{2}{\lambda}\sqrt{\frac{|\eta|}{m}}\operatorname{cn}\Big[\!\!\Big[\frac{s}{\lambda}\sqrt{|\eta|},m^{-1}\Big]\!\!\Big]-1\Big)=\frac{2\lambda}{\sqrt{|\eta|\,m}}\Big(1-\operatorname{cn}\Big[\!\!\Big[\frac{s}{\lambda}\sqrt{|\eta|},m^{-1}\Big]\!\!\Big]\Big)\,,
$$
$$
(C.41)
$$

Antisymmetric case

In the antisymmetric case, the curvature at the midline vanishes, which implies that $\dot\psi=0$ and

$$
\cos\psi_{\mathrm{mid}}\overset{(C.3)}{=}\frac{1}{\eta}\,, \qquad (C.42)
$$

where $\psi(0):=\psi_{\mathrm{mid}}$. Thus, $|\eta|>1$, and we have to consider different cases again. For $\psi_{\mathrm{mid}}=0$ or $\psi_{\mathrm{mid}}=180°$ the profile is flat which corresponds to the solution with the two cylinders infinitely apart. If $0<\psi_{\mathrm{mid}}<90°$, η is greater than 1, whereas it is lower than -1 if $90°<\psi_{\mathrm{mid}}<180°$.

---

[5] Note that although ψ is just given for a finite interval of the arc length, the following expressions for K, Δx, and Δh are correct for all $s/\lambda\in\mathbb{R}$.

a) $\eta > 1$:

According to Eqn. (C.3), $\cos\psi$ has to decrease for increasing s. Consequently, $\dot{\psi} > 0$, and

$$\int_0^s \mathrm{d}s' = s(\psi) = \int_{\psi_{\mathrm{mid}}}^{\psi} \frac{\lambda}{\sqrt{2(1-\eta\cos\psi')}}\mathrm{d}\psi' = \frac{\sqrt{2}\lambda}{\sqrt{(1+\eta)}} \int_{\frac{\psi_{\mathrm{mid}}-\pi}{2}}^{\frac{\psi-\pi}{2}} \frac{1}{\sqrt{1-m\sin^2\theta'}}\mathrm{d}\theta' .$$
(C.43)

The parameter m is again greater than 1. With Eqn. (C.I), however, we can rewrite the arc length as

$$s(\psi) = \lambda\sqrt{\frac{m}{\eta}}\left(\frac{1}{\sqrt{m}}\mathcal{F}\big[\![\theta, m^{-1}]\!\big] - \frac{1}{\sqrt{m}}\mathcal{F}\big[\![\theta_{\mathrm{mid}}, m^{-1}]\!\big]\right) ,$$
(C.44)

where $\sin\theta = m^{1/2}\sin\left(\frac{\psi-\pi}{2}\right)$ and $\sin\theta_{\mathrm{mid}} = m^{1/2}\sin\left(\frac{\psi_{\mathrm{mid}}-\pi}{2}\right)$. Eqn. (C.44) can be converted to

$$\theta = \mathrm{am}\left[\!\!\left[\frac{s}{\lambda}\sqrt{\eta} + \mathcal{F}\big[\![\theta_{\mathrm{mid}}, m^{-1}]\!\big], m^{-1}\right]\!\!\right]$$

$$\Leftrightarrow \quad \sin\theta = m^{1/2}\sin\left(\frac{\psi-\pi}{2}\right) = \mathrm{sn}\left[\!\!\left[\frac{s}{\lambda}\sqrt{\eta} + \mathcal{F}\big[\![\theta_{\mathrm{mid}}, m^{-1}]\!\big], m^{-1}\right]\!\!\right]$$

$$\Leftrightarrow \quad m\sin^2\left(\frac{\psi-\pi}{2}\right) = \mathrm{sn}^2\left[\!\!\left[\frac{s}{\lambda}\sqrt{\eta} + \mathcal{F}\big[\![\theta_{\mathrm{mid}}, m^{-1}]\!\big], m^{-1}\right]\!\!\right]$$

$$\Leftrightarrow \quad \frac{m}{2}[1 - \underbrace{\cos(\psi-\pi)}_{=-\cos(\psi)}] = \mathrm{sn}^2\left[\!\!\left[\frac{s}{\lambda}\sqrt{\eta} + \mathcal{F}\big[\![\theta_{\mathrm{mid}}, m^{-1}]\!\big], m^{-1}\right]\!\!\right]$$

$$\Leftrightarrow \quad \cos\psi = \frac{2}{m}\mathrm{sn}^2\left[\!\!\left[\frac{s}{\lambda}\sqrt{\eta} + \mathcal{F}\big[\![\theta_{\mathrm{mid}}, m^{-1}]\!\big], m^{-1}\right]\!\!\right] - 1 .$$
(C.45)

From the condition that $\dot{\psi}(0) = 0$ we obtain a value for θ_{mid}. With Eqn. (C.3) follows:

$$\cos\psi_{\mathrm{mid}} = \frac{1}{\eta} \stackrel{(s=0)}{=} \frac{2}{m}\mathrm{sn}^2\left[\!\!\left[\mathcal{F}\big[\![\theta_{\mathrm{mid}}, m^{-1}]\!\big], m^{-1}\right]\!\!\right] - 1 = \frac{2}{m}\sin^2(\theta_{\mathrm{mid}}) - 1$$

$$\Leftrightarrow \quad \frac{m}{2}\left(1 + \frac{1}{\eta}\right) = \sin^2(\theta_{\mathrm{mid}}) \Leftrightarrow 1 = \sin^2(\theta_{\mathrm{mid}}) \Rightarrow \theta_{\mathrm{mid}} = \pm(2n+1)\frac{\pi}{2} , \text{(C.46)}$$

where $n \in \mathbb{N}$. With $m > 1$ and $\psi_{\mathrm{mid}} \in \{0, \pi\}$, $\sin\theta_{\mathrm{mid}} = m^{1/2}\sin\left(\frac{\psi_{\mathrm{mid}}-\pi}{2}\right)$ has to be negative. We choose $\theta_{\mathrm{mid}} = -\frac{\pi}{2}$. Thus,

$$\cos\psi = \frac{2}{m}\mathrm{sn}^2\left[\!\!\left[\frac{s}{\lambda}\sqrt{\eta} - \mathcal{K}\big[\![m^{-1}]\!\big], m^{-1}\right]\!\!\right] - 1 ,$$
(C.47)

and, for $-\frac{\lambda}{\sqrt{|\eta|}}\mathcal{K}[\![m^{-1}]\!] \le s \le \frac{\lambda}{\sqrt{|\eta|}}\mathcal{K}[\![m^{-1}]\!]$,

$$\psi(s) = \arccos\left(\frac{2}{m}\mathrm{sn}^2\left[\!\!\left[\frac{s}{\lambda}\sqrt{\eta} - \mathcal{K}\big[\![m^{-1}]\!\big], m^{-1}\right]\!\!\right] - 1\right) .$$
(C.48)

The curvature can be obtained in total analogy to Eqn. (C.39) (see paragraph e) in the previous section)

$$
\begin{aligned}
K(s) \;\overset{(5.50)}{=}\;& \lambda^{-1}\sqrt{2(1-\eta\cos\psi)} \\
\overset{(C.47)}{=}\;& \lambda^{-1}\sqrt{2\left[1+\eta\left(1-\frac{2}{m}\,\mathrm{sn}^2\left[\!\!\left[\frac{s}{\lambda}\sqrt{\eta}-\mathcal{K}\left[\!\!\left[m^{-1}\right]\!\!\right],m^{-1}\right]\!\!\right]\right)\right]} \\
=\;& \frac{2}{\lambda}\sqrt{\frac{\eta}{m}}\,\mathrm{cn}\left[\!\!\left[\frac{s}{\lambda}\sqrt{\eta}-\mathcal{K}\left[\!\!\left[m^{-1}\right]\!\!\right],m^{-1}\right]\!\!\right] > 0 \text{ for } s>0\,. \qquad (C.49)
\end{aligned}
$$

The distance Δx is given by

$$
\begin{aligned}
\Delta x(s) \;=\;& \int_0^s \mathrm{d}s'\,\cos\psi(s') \overset{(C.47)}{=} \int_0^s \mathrm{d}s'\left(\frac{2}{m}\,\mathrm{sn}^2\left[\!\!\left[\frac{s'}{\lambda}\sqrt{\eta}-\mathcal{K}\left[\!\!\left[m^{-1}\right]\!\!\right],m^{-1}\right]\!\!\right]-1\right) \\
=\;& -s+\frac{2\lambda}{\sqrt{\eta}}\left[-\mathcal{E}\left[\!\!\left[\mathrm{am}\left[\!\!\left[\frac{s'}{\lambda}\sqrt{\eta}-\mathcal{K}\left[\!\!\left[m^{-1}\right]\!\!\right],m^{-1}\right]\!\!\right],m^{-1}\right]\!\!\right]\right. \\
& \left.+\frac{s'}{\lambda}\sqrt{\eta}-\mathcal{K}\left[\!\!\left[m^{-1}\right]\!\!\right]\right]_0^s \\
=\;& s-\frac{2\lambda}{\sqrt{\eta}}\left(\mathcal{E}\left[\!\!\left[\mathrm{am}\left[\!\!\left[\frac{s}{\lambda}\sqrt{\eta}-\mathcal{K}\left[\!\!\left[m^{-1}\right]\!\!\right],m^{-1}\right]\!\!\right],m^{-1}\right]\!\!\right]+\mathcal{E}\left[\!\!\left[m^{-1}\right]\!\!\right]\right)\,, \quad (C.50)
\end{aligned}
$$

where Eqns. (C.IIb) and (C.IVa) were inserted in the last step. The height Δh can be calculated with the help of Eqn. (C.5b)

$$
\Delta h(s) \overset{(C.IVb,C.49)}{=} \frac{2\lambda}{\sqrt{\eta\,m}}\,\mathrm{cn}\left[\!\!\left[\frac{s}{\lambda}\sqrt{\eta}-\mathcal{K}\left[\!\!\left[m^{-1}\right]\!\!\right],m^{-1}\right]\!\!\right]\,. \qquad (C.51)
$$

b) $\eta < -1$**:**

Now, $\cos\psi$ has to increase with increasing s because η is negative (see Eqn. (C.3)). Thus, $\dot\psi < 0$. One can rewrite Eqn. (C.3) a bit to benefit from the calculations that were already done:

$$
\frac{\lambda^2}{2}\dot\psi^2+\eta\cos\psi=1 \Leftrightarrow \frac{\lambda^2}{2}\dot\psi^2-|\eta|\cos\psi=1 \Leftrightarrow \frac{\lambda^2}{2}\dot\psi^2+|\eta|\cos(\pi-\psi)=1\,. \quad (C.52)
$$

From the previous paragraph we know that the solution of the equation on the right-hand side is given by:

$$
\begin{aligned}
\pi-\psi \;=\;& \arccos\left(\frac{2}{m}\,\mathrm{sn}^2\left[\!\!\left[\frac{s}{\lambda}\sqrt{|\eta|}-\mathcal{K}\left[\!\!\left[m^{-1}\right]\!\!\right],m^{-1}\right]\!\!\right]-1\right) \\
\Leftrightarrow \psi(s) \;=\;& \pi-\arccos\left(\frac{2}{m}\,\mathrm{sn}^2\left[\!\!\left[\frac{s}{\lambda}\sqrt{|\eta|}-\mathcal{K}\left[\!\!\left[m^{-1}\right]\!\!\right],m^{-1}\right]\!\!\right]-1\right) \\
=\;& \arccos\left(1-\frac{2}{m}\,\mathrm{sn}^2\left[\!\!\left[\frac{s}{\lambda}\sqrt{|\eta|}-\mathcal{K}\left[\!\!\left[m^{-1}\right]\!\!\right],m^{-1}\right]\!\!\right]\right)\,, \qquad (C.53)
\end{aligned}
$$
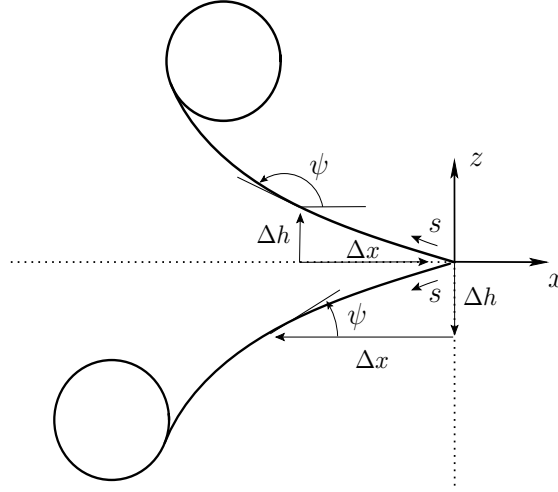
Figure C.3: Relevant parameters for the inner section in the antisymmetric case. The arrows point in the positive direction of Δx, Δh, and s, respectively.

if $-\frac{\lambda}{\sqrt{|\eta|}}\mathcal{K}[\![m^{-1}]\!] \leq s \leq \frac{\lambda}{\sqrt{|\eta|}}\mathcal{K}[\![m^{-1}]\!]$.

Note that we have to check that $\dot{\psi} < 0$ which is indeed the case here. Analogous to Eqn. (C.39), we obtain for the curvature

$$K(s) = -\frac{2}{\lambda}\sqrt{\frac{|\eta|}{m}}\operatorname{cn}\left[\!\!\left[\frac{s}{\lambda}\sqrt{|\eta|} - \mathcal{K}\left[\!\left[m^{-1}\right]\!\right], m^{-1}\right]\!\!\right] < 0 \text{ for } s > 0 \,. \tag{C.54}$$

Finally, we calculate Δx and Δh again. With $\cos\psi = -\cos[\pi - \psi]$,

$$
\begin{aligned}
\Delta x(s) &= \int_0^s \mathrm{d}s' \, \cos\psi(s') = -\int_0^s \mathrm{d}s' \, \cos[\pi - \psi(s')] \\
&= -\int_0^s \mathrm{d}s' \left(\frac{2}{m}\operatorname{sn}^2\left[\!\!\left[\frac{s'}{\lambda}\sqrt{|\eta|} - \mathcal{K}\left[\!\left[m^{-1}\right]\!\right], m^{-1}\right]\!\!\right] - 1\right) \\
&\overset{(C.50)}{=} -s + \frac{2\lambda}{\sqrt{|\eta|}}\left(\mathcal{E}\left[\!\!\left[\operatorname{am}\left[\!\!\left[\frac{s}{\lambda}\sqrt{|\eta|} - \mathcal{K}\left[\!\left[m^{-1}\right]\!\right], m^{-1}\right]\!\!\right], m^{-1}\right]\!\!\right] + \mathcal{E}\left[\!\left[m^{-1}\right]\!\right]\right), \quad (C.55)
\end{aligned}
$$

and with the help of Eqn. (C.5b)

$$
\begin{aligned}
\Delta h(s) &= \int_0^s \mathrm{d}s' \, \sin\psi(s') = \frac{\lambda^2}{\eta}[K(s) - K(0)] \\
&\overset{(C.51)}{=} \frac{2\lambda}{\sqrt{|\eta|}\,m}\operatorname{cn}\left[\!\!\left[\frac{s}{\lambda}\sqrt{|\eta|} - \mathcal{K}\left[\!\left[m^{-1}\right]\!\right], m^{-1}\right]\!\!\right]. \tag{C.56}
\end{aligned}
$$

If we compare the two equations (C.55) and (C.56) to the corresponding results of the previous paragraph a), it becomes obvious that the shape for $-|\eta|$ can simply be obtained by reflecting the shape for $|\eta|$ about the x axis (see also Fig. C.3).

C.2 The nanodrum in small gradient approximation

The shape equation (C.1) for the axially symmetric nanodrum in small gradient approximation reads:

$$\boldsymbol{\nabla}^2\big(\boldsymbol{\nabla}^2 - \lambda^{-2}\big)h = 0 \; . \tag{C.57}$$

Its solution is given by

$$h(\rho) = h_1 + h_2 \ln(\rho/\lambda) + h_3 \, \mathrm{I}_0(\rho/\lambda) + h_4 \, \mathrm{K}_0(\rho/\lambda) \; , \tag{C.58}$$

where the constants $h_1, \ldots, h_4$ can be determined from the appropriate boundary conditions (4.8) (see page 86). From $h(R_{\mathrm{pore}}) = 0$ one directly obtains:

$$h_1 = -h_2 \ln(R_{\mathrm{pore}}/\lambda) - h_3 \, \mathrm{I}_0(R_{\mathrm{pore}}/\lambda) - h_4 \, \mathrm{K}_0(R_{\mathrm{pore}}/\lambda) \; . \tag{C.59}$$

Using the relations (4.I) for the derivatives of the Bessel functions $\mathrm{I}_0(\rho)$ and $\mathrm{K}_0(\rho)$, the derivative of the height function can be written as:

$$h'(\rho) = \frac{h_2}{\rho} + \frac{h_3}{\lambda} \, \mathrm{I}_1(\rho/\lambda) - \frac{h_4}{\lambda} \, \mathrm{K}_1(\rho/\lambda) \; . \tag{C.60}$$

Thus, the boundary conditions (4.8b) yield

$$
\begin{aligned}
h_2 &= -\frac{R_{\mathrm{pore}}}{\lambda} \left[h_3 \, \mathrm{I}_1(R_{\mathrm{pore}}/\lambda) - h_4 \, \mathrm{K}_1(R_{\mathrm{pore}}/\lambda) \right] \; , \quad \text{and} \\
h_3 &= \frac{c^2 \lambda + h_4 R_{\mathrm{tip}} \left[c \, \mathrm{K}_1(c/\lambda) - R_{\mathrm{pore}} \, \mathrm{K}_1(R_{\mathrm{pore}}/\lambda) \right]}{R_{\mathrm{tip}} \left[c \, \mathrm{I}_1(c/\lambda) - R_{\mathrm{pore}} \, \mathrm{I}_1(R_{\mathrm{pore}}/\lambda) \right]} \; .
\end{aligned} \tag{C.61}
$$

The constant h_4 can be obtained with the help of the second boundary condition in Eqn. (4.8a). It is given by N/D, where

$$
\begin{aligned}
N &= \lambda \Big\{ 2\lambda c^2 \big[\mathrm{I}_0(\tilde{R}_{\mathrm{pore}}/\lambda) - \mathrm{I}_0(c/\lambda) \big] + (c^2 - 2h_0 R_{\mathrm{tip}}) c \, \mathrm{I}_1(c/\lambda) \\
&\qquad + R_{\mathrm{pore}} \, \mathrm{I}_1(R_{\mathrm{pore}}/\lambda) \big[2 \ln(c/R_{\mathrm{pore}}) c^2 - c^2 + 2h_0 R_{\mathrm{tip}} \big] \Big\} \; , \quad \text{and} \\
D &= 2R_{\mathrm{tip}} \Big\{ \lambda \big[2\lambda - c \, \mathrm{I}_0(R_{\mathrm{pore}}/\lambda) \, \mathrm{K}_1(c/\lambda) - R_{\mathrm{pore}} \, \mathrm{I}_0(c/\lambda) \, \mathrm{K}_1(R_{\mathrm{pore}}/\lambda) \big] \\
&\qquad - R_{\mathrm{pore}} \, \mathrm{I}_1(R_{\mathrm{pore}}/\lambda) \big[\lambda \, \mathrm{K}_0(c/\lambda) + c \, \mathrm{K}_1(c/\lambda) \ln(c/R_{\mathrm{pore}}) \big] \\
&\qquad - c \, \mathrm{I}_1(c/\lambda) \big[\lambda \, \mathrm{K}_0(R_{\mathrm{pore}}/\lambda) - R_{\mathrm{pore}} \, \mathrm{K}_1(R_{\mathrm{pore}}/\lambda) \ln(c/R_{\mathrm{pore}}) \big] \Big\} \; . \tag{C.62}
\end{aligned}
$$

Combining this result with the expressions for the other constants yields the height function in terms of the contact point c. The latter has to be determined numerically using the remaining boundary condition (4.8c). The solution of the profile can then be inserted into Eqn. (4.V) to determine the force.[6]

---

[6] These calculations can be found in two Mathematica files at [WWWd] and [WWWe].

List of Tables

List of Figures

List of Technical Points

Bibliography

[ACCG02]   G. Arreaga, R. Capovilla, C. Chryssomalakos, and J. Guven. Area-constrained planar elastica. *Phys. Rev. E*, 65(3): 031801, March 2002.

[AEBD⁺96]   H. Aranda-Espinoza, A. Berman, N. Dan, P. Pincus, and S. Safran. Interaction Between Inclusions Embedded in Membranes. *Biophys. J.*, 71(2): pp. 648–656, August 1996.

[AF05]   A. Alessandrini and P. Facci. Afm: a versatile tool in biophysics. *Meas. Sci. Technol.*, 16(6): pp. R65–R92, June 2005.

[AJL⁺02]   B. Alberts, A. Johnson, J. Lewis, M. Raff, K. Roberts, and P. Walter. *Molecular Biology of the Cell*. Garland Publishing, New York, NY, fourth edition, 2002.

[Ant06]   B. Antonny. Membrane deformation by protein coats. *Curr. Opin. Struct. Biol.*, 18(4): 386–394, August 2006.

[Arf85]   G. Arfken. *Mathematical Methods for Physicists*. Academic Press, Orlando, FL, third edition, 1985.

[AS70]   M. Abramowitz and I. A. Stegun, editors. *Handbook of Mathematical Functions*. Dover, New York, NY, ninth edition, 1970.

[AT86]   M. P. Allen and D. J. Tildesley. *Computer Simulations of Liquids*. Oxford University Press, Oxford, U.K., reprint edition, 1986.

[BBR02]   P. Biscari, F. Bisi, and R. Rosso. Curvature effects on membrane-mediated interactions of inclusions. *J. Math. Biol.*, 45: pp. 37–56, 2002.

[BCK05]   H.-J. Butt, B. Cappella, and M. Kappl. Force measurements with the atomic force microscope: Technique, interpretation and applications. *Surf. Sci. Rep.*, 59(1–6): pp. 1–152, October 2005.

[BF03]   D. Bartolo and J.-B. Fournier. Elastic interaction between "hard" or "soft" pointwise inclusions on biological membranes. *Eur. Phys. J. E*, 11: pp. 141–146, 2003.

[BHW03]   T. Baumgart, S. T. Hess, and W. W. Webb. Imaging coexisting fluid domains in biomembrane models coupling curvature and line tension. *Nature*, 425(6960): pp. 821–824, October 2003.

[BKIM03]   K. Bohinc, V. Kralj-Iglič, and S. May. Interaction between two cylindrical inclusions in a symmetric lipid bilayer. *J. Chem. Phys.*, 119(14): pp. 7435–7444, October 2003.

[BL75]   F. Brochard and J. F. Lennon. Frequency spektrum of flicker phenomenon in erythrocytes. *J. Phys.–Paris*, 36(11): pp. 1035–1047, 1975.

[BL97]   D. A. Brown and E. London. Structure of Detergent-Resistant Membrane Domains: Does Phase Separation Occur in Biological Membranes? *Biophys. Res. Commun.*, 240(1): pp. 1–7, November 1997.

[BL98]   D. A. Brown and E. London. Functions of lipid rafts in biological membranes. *Annu. Rev. Cell Dev. Biol.*, 14: pp. 111–136, November 1998.

[Bou99]   A. A. Boulbitch. Equations of heterophase equilibrium of a biomembrane. *Arch. Appl. Mech.*, 69(2): pp. 83–93, March 1999.

[BV06]   P. D. Blood and G. A. Voth. Direct observation of bin/amphiphysin/ rvs (bar) domain-induced membrane curvature by means of molecular dynamics simulations. *Proc. Natl. Acad. Sci. USA*, 103(41): pp. 15068–15072, October 2006.

[Cal85]   H. B. Callen. *Thermodynamics and an Introduction to Thermostatistics.* John Wiley & Sons, New York, NY, second edition, 1985.

[Car76]   M. P. Do Carmo. *Differential Geometry of Curves and Surfaces.* Prentice Hall, Upper Saddle River, NJ, 1976.

[CD05]   I. R. Cooke and M. Deserno. Solvent-free model for self-assembling fluid bilayer membranes: Stabilization of the fluid phase based on broad attractive tail potentials. *J. Chem. Phys.*, 123(22): 224710, December 2005.

[CD06]   I. Cooke and M. Deserno. Coupling between Lipid Shape and Membrane Curvature. *Biophys. J.*, 91(2): pp. 487–495, July 2006.

[CDBN05]   D. Cuvelier, I. Derényi, P. Bassereau, and P. Nassoy. Coalescence of Membrane Tethers: Experiments, Theory, and Applications. *Biophys. J.*, 88(4): pp. 2714–2726, April 2005.

[CG02a]   R. Capovilla and J. Guven. Geometry of lipid vesicle adhesion. *Phys. Rev. E*, 66: 041604, 2002.

[CG02b]   R. Capovilla and J. Guven. Stresses in lipid membranes. *J. Phys. A: Math. Gen.*, 35: pp. 6233–6247, 2002.

[CG04]   R. Capovilla and J. Guven. Stress and geometry of lipid vesicles. *J. Phys.: Condens. Matter*, 16(22): S2187–S2191, 2004.

[CGH+96]   R. M. Corless, G. H. Gonnet, D. E. G. Hare, D. J. Jeffrey, and D. E. Knuth. On the Lambert W function. *Adv. Comput. Math.*, 5(1): pp. 329–359, December 1996.

[CGS02]   R. Capovilla, J. Guven, and J. A. Santiago. Lipid membranes with an edge. *Phys. Rev. E*, 66(2): 021607, August 2002.

[CGS03]   R. Capovilla, J. Guven, and J. A. Santiago. Deformations of the geometry of lipid vesicles. *J. Phys. A: Math. Gen.*, 36: pp. 6281–6295, 2003.

[CKD05]   I. R. Cooke, K. Kremer, and M. Deserno. Tunable generic model for fluid bilayer membranes. *Phys. Rev. E*, 72(1): 011506, July 2005.

[CM93]   P. C. Cross and K. L. Mercer. *Cell and Tissue Ultrastructure: A Functional Perspective*. W. H. Freeman and Company, New York, NY, second edition, 1993.

[CVG07]   P. Castro-Villarreal and J. Guven. Axially symmetric membranes with polar tethers. *J. Phys. A: Math. Theor.*, 40(17): pp. 4273–4283, April 2007.

[DB03]   M. Deserno and T. Bickel. Wrapping of a spherical colloid by a fluid membrane. *Europhys. Lett.*, 62(5): pp. 767–773, 2003.

[DBSŽ03]   J. Derganc, B. Božič, Saša Svetina, and Boštjan Žekš. Equilibrium shapes of erythrocytes in rouleau formation. *Biophys. J.*, 84(3): pp. 1486–1492, March 2003.

[DBV+01]   C. Dietrich, L. A. Bagatolli, Z. N. Volovyk, N. L. Thompson, M. Levi, K. Jacobson, and E. Gratton. Lipid Rafts Reconstituted in Model Membranes. *Biophys. J.*, 80(3): pp. 1417–1428, March 2001.

[Del41]   C. Delaunay. Sur la surface de révolution dont la courbure moyenne est constante. *J. Math. Pures Appl.*, 6: pp. 309–315, 1841.

[Des04a]   M. Deserno. Elastic deformation of a fluid membrane upon colloid binding. *Phys. Rev. E*, 69: 031903, 2004.

[Des04b]   M. Deserno. When do fluid membranes engulf sticky colloids? *J. Phys.: Condens. Matter*, 16: pp. 2061–2070, 2004.

[DFG98]   P. G. Dommersnes, J.-B. Fournier, and P. Galatola. Long-range elastic forces between membrane inclusions in spherical vesicles. *Europhys. Lett.*, 42(2): pp. 233–238, 1998.

[dGBWQ03]   P.-G. de Gennes, F. Brochard-Wyart, and D. Quéré. *Capillarity and Wetting Phenomena*. Springer-Verlag, Berlin, Germany, 2003.

[DH01]   M. Deserno and C. Holm. Cell model and Poisson-Boltzmann theory: A brief introduction. In C. Holm, P. Kékicheff, and R. Podgornik, editors, *Electrostatic Effects in Soft Matter and Biophysics*, volume 46 of *NATO Science Series: II. Mathematics, Physics and Chemistry*. Kluwer Academic Publishers, Dordrecht, The Netherlands, 2001.

[DJP02]   I. Derényi, F. Jülicher, and J. Prost. Formation and Interaction of Membrane Tubes. *Phys. Rev. Lett.*, 88(23): 238101, June 2002.

[DL91]   F. David and S. Leibler. Vanishing tension of fluctuating membranes. *J. Phys. II France*, 1(8): pp. 959–976, August 1991.

[DOD06]   A. Domínguez, M. Oettel, and S. Dietrich. Force balance of particles trapped at fluid interfaces. *arXiv:cond-mat/0611329 v1*, November 2006.

[DS95]   J. Dai and M. P. Sheetz. Mechanical Properties of Neuronal Growth Cone Membranes Studied by Tether Formation with Laser Optical Tweezers. *Biophys. J.*, 68(3): pp. 988–996, March 1995.

[DS99]   J. Dai and M. P. Sheetz. Membrane Tether Formation from Blebbing Cells. *Biophys. J.*, 77(6): pp. 3363–3370, December 1999.

[EHLR03]   E. Evans, V. Heinrich, F. Ludwig, and W. Rawicz. Dynamic Tension Spectroscopy and Strength of Biomembranes. *Biophys. J.*, 85(4): pp. 2342–2350, October 2003.

[ER90]   E. Evans and W. Rawicz. Entropy-Driven Tension and Bending Elasticity in Condensed-Fluid Membranes. *Phys. Rev. Lett.*, 64(17): pp. 2094–2097, April 1990.

[FG02]   J.-B. Fournier and P. Galatola. Anisotropic capillary interactions and jamming of colloidal particles trapped at a liquid-fluid interface. *Phys. Rev. E*, 65: 031601, 2002.

[FIM06]   M. Fošnarič, A. Iglič, and S. May. Influence of rigid inclusions on the bending elasticity of a lipid membrane. *Phys. Rev. E*, 74(5): 051503, November 2006.

[FMM+89]   J. F. Faucon, M. D. Mitov, P. Meleard, I. Bivas, and P. Bothorel. Bending elasticity and thermal fluctuations of lipid-membranes–theoretical and experimental requirements. *J. Phys.–Paris*, 50(17): pp. 2389–2414, September 1989.

[Fou99]   J.-B. Fournier. Microscopic membrane elasticity and interactions among membrane inclusions: interplay between the shape, dilation, tilt and tilt-difference modes. *Eur. Phys. J. B*, 11(2): pp. 261–272, September 1999.

[Fou07]   J.-B. Fournier. On the stress and torque tensor in fluid membranes. *Soft Matter*, 3(7): pp. 883–888, July 2007.

[Fra03]   T. Frankel. *The Geometry of Physics*. Cambridge University Press, Cambridge, U.K., second edition, 2003.

[FS02]   D. Frenkel and B. Smit. *Understanding Molecular Simulation–From Algorithms to Applications*. Academic Press, London, U.K. - San Diego, CA, second edition, 2002.

[GBM+03]   E. Gottwein, J. Bodem, B. Müller, A. Schmechel, H. Zentgraf, and H.-G. Kräusslich. The Mason-Pfizer Virus PPPY and PSAP Motifs Both Contribute to Virus Release. *J. Virol.*, 77(17): pp. 9474–9485, September 2003.

[GBP93]   M. Goulian, R. Bruinsma, and P. Pincus. Long-Range Forces in Heterogeneous Fluid Membranes. *Europhys. Lett.*, 22(2): pp. 145–150, 1993. See also: Erratum in *Europhys. Lett.*, 23(2): p. 155, 1993.

[GG25]   M. D. Gorter and F. Grendel. On bimolecular layers of lipoids on the chromocytes of the blood. *J. Exp. Med.*, 41(4): pp. 439–443, 1925.

[GG01]   W. T. Góźdź and G. Gompper. Shape transformations of two-component membranes under weak tension. *Europhys. Lett.*, 55(4): pp. 587–593, August 2001.

[GH96]   R. Goetz and W. Helfrich. The Egg Carton: Theory of a Periodic Superstructure of Some Lipid Membranes. *J. Phys. II France*, 6: pp. 215–223, February 1996.

[GH99]   D. Goulding and J.-P. Hansen. Attraction between like-charged colloidal particles induced by a surface: A density functional analysis. *Europhys. J.*, 46(3): pp. 407–413, May 1999.

[GK96]   J. Gould and W. Keeton. *Biological Science*. W. W. Norton and Co., New York, NY, sixth edition, 1996.

[GKD+04] G. Gompper, U. B. Kaupp, J. K. G. Dhont, D. Richter, and R. G. Winkler, editors. *Physics meets Biology*, volume 19 of *Matter and Materials*. Forschungszentrum Jülich GmbH, Jülich, Germany, 2004.

[GS71]   W. A. Gifford and L. E. Scriven. On the attraction of floating particles. *Chem. Eng. Sci.*, 26: pp. 287–297, 1971.

[Guv04]   J. Guven. Membrane geometry with auxiliary variables and quadratic constraints. *J. Phys. A: Math. Gen.*, 37: L313–L319, 2004.

[Guv06]   J. Guven. Laplace pressure as a surface stress in fluid vesicles. *J. Phys. A: Math. Gen.*, 39(14): pp. 3771–3785, 2006.

[Han06]   J. F. Hancock. Lipid rafts: contentious only from simplistic standpoints. *Nat. Rev. Mol. Cell Bio.*, 7(6): pp. 456–462, June 2006.

[HD06]   V. A. Harmandaris and M. Deserno. A novel method for measuring the bending rigidity of model lipid membranes by simulating tethers. *J. Chem. Phys.*, 125(20): 204905, November 2006.

[Hel73]   W. Helfrich. Elastic Properties of Lipid Bilayers: Theory and Possible Experiments. *Z. Naturforsch.*, 28 c: pp. 693–703, 1973.

[HK00]   M. Hamm and M. M. Kozlov. Elastic energy of tilt and bending of fluid membranes. *Eur. Phys. J. E*, 3(4): pp. 323–335, December 2000.

[HP88]   W. Helfrich and J. Prost. Intrinsic bending force in anisotropic membranes made of chiral molecules. *Phys. Rev. A*, 38(6): pp. 3065–3068, September 1988.

[HSDS96]   R. M. Hochmuth, J.-Y. Shao, J. Dai, and M. P. Sheetz. Deformation and Flow of Membrane into Tether Extracted from Neuronal Growth Cones. *Biophys. J.*, 70(1): pp. 358–369, January 1996.

[HW04]   S. R. Heidemann and D. Wirtz. Towards a regional approach to cell mechanics. *Trends Cell Biol.*, 14(4): 160–166, April 2004.

[Ill07]   G. Illya. Personal communication, 2007.

[Ise92]   C. Isenberg. *The science of soap films and soap bubbles.* Dover, Mineola, NY, 1992.

[Isr92]   J. N. Israelachvili. *Intermolecular and Surface Forces.* Academic Press, London, U.K. - San Diego, CA, second edition, 1992.

[JL96]   F. Jülicher and R. Lipowsky. Shape transformation of vesicles with intramembrane domains. *Phys. Rev. E*, 53(3): pp. 2670–2683, March 1996.

[JNOF00]   A. Janshoff, M. Neitzert, Y. Oberdörfer, and H. Fuchs. Force Spectroscopy of Molecular Systems—Single Molecule Spectroscopy of Polymers and Biomolecules. *Angew. Chem. Int. Ed.*, 39(18): pp. 3212–3237, September 2000.

[JS94]   F. Jülicher and U. Seifert. Shape equations for axisymmetric vesicles: A clarification. *Phys. Rev. E*, 49(5): pp. 4728–4731, 1994.

[KC98]   R. Koynova and M. Caffrey. Phases and phase transitions of the phosphatidylcholines. *BBA-Biomembranes*, 1376(1): pp. 91–145, June 1998.

[KCD+05]   G. Koster, A. Cacciuto, I. Derényi, D. Frenkel, and M. Dogterom. Force Barriers for Membrane Tube Formation. *Phys. Rev. Lett.*, 94(6): 068101, February 2005.

[Kil98]   J. A. Killian. Hydrophobic mismatch between proteins and lipids in membranes. *BBA-Biomembranes*, 1376(3): pp. 401–416, November 1998.

[Kir59]   G. Kirchhoff. Über das Gleichgewicht und die Bewegung eines unendlich dünnen elastischen Stabes. *J. Reine Angew. Math. (Crelle)*, 56: pp. 285–313, 1859.

[KNO98]   K. S. Kim, J. Neu, and G. Oster. Curvature-Mediated Interactions Between Membrane Proteins. *Biophys. J.*, 75: pp. 2274–2291, November 1998.

[Kos04]   K. D. Kosta. Single-cell elastography: Probing for disease with the atomic force microscope. *Dis. Markers*, 19(2–3): pp. 139–154, 2004.

[Koz06]   M. M. Kozlov. Membrane shape equations. *J. Phys.: Condens. Matter*, 18(28): S1177–S1190, July 2006.

[Koz07]   M. M. Kozlov. Bending over to attract. *Nature*, 447(7143): pp. 387–389, May 2007.

[KPDN95]   P. A. Kralchevsky, V. N. Paunov, N. D. Denkov, and K. Nagayama. Stresses in Lipid Membranes and Interactions between Inclusions. *J. Chem. Soc. Faraday Trans.*, 91(19): pp. 3415–3432, 1995.

[Kre91]   E. Kreyszig. *Differential geometry.* Dover, Mineola, NY, 1991.

[KRS99]   I. Koltover, J. O. Rädler, and C. R. Safinya. Membrane Mediated Attraction and Ordered Aggregation of Colloidal Particles Bound to Giant Phospholipid Vesicles. *Phys. Rev. Lett.*, 82(9): pp. 1991–1994, 1999.

[Kul04]   I. M. Kulić. *Statistical Mechanics of Protein Complexed and Condensed DNA.* Ph.D. thesis, Johannes Gutenberg-Universität Mainz, May 2004.

[KZK04]   Y. Kozlovsky, J. Zimmerberg, and M. M. Kozlov. Orientation and Interaction of Oblique Cylindrical Inclusions Embedded in a Lipid Monolayer: A Theoretical Model for Viral Fusion Peptides. *Biophys. J.*, 87(2): pp. 999–1012, August 2004.

[LAMH06]   H. J. Limbach, A. Arnold, B. A. Mann, and C. Holm. ESPResSo— an extensible simulation package for reseach on soft matter systems. *Comput. Phys. Commun.*, 174(9): pp. 704–727, May 2006.

[LBM+04]   H. Lodish, A. Berk, P. Matsudaira, C. A. Kaiser, M. Krieger, M. P. Scott, S. L. Zipursky, and J. Darnell. *Molecular Cell Biology.* W. H. Freeman and Co., New York, NY, fifth edition, 2004.

[Lea01]   A. R. Leach. *Molecular modelling: principles and applications.* Pearson Education Limited, Harlow, U.K., second edition, 2001.

[LFL01]   P. Lenz, W. Fenzl, and R. Lipowsky. Wetting of ring-shaped surface domains. *Europhys. Lett.*, 53(5): pp. 618–624, 2001.

[LH92]   E. J. Luna and A. L. Hitt. Cytoskeleton–Plasma Membrane Interactions. *Science*, 258(5084): pp. 955–964, November 1992.

[LL76]   L. D. Landau and E. M. Lifshitz. *Mechanics.* Butterworth-Heinemann, Oxford, U.K., third edition, 1976.

[LL86]   L. D. Landau and E. M. Lifshitz. *Theory of Elasticity*. Butterworth-Heinemann, Oxford, U.K., third edition, 1986.

[LL87]   L. D. Landau and E. M. Lifshitz. *Fluid Mechanics*. Butterworth-Heinemann, Oxford, U.K., second edition, 1987.

[LL00]   L. D. Landau and E. M. Lifshitz. *The Classical Theory of Fields*. Butterworth-Heinemann, Oxford, U.K., fourth edition, 2000.

[LLW01]   C.-H. Lee, W.-C. Lin, and J. Wang. All-optical measurements of the bending rigidity of lipid-vesicle membranes across structural phase transitions. *Phys. Rev. E*, 64(2): 020901, August 2001.

[LM06]   M. A. Lomholt and L. Miao. Descriptions of membrane mechanics from microscopic and effective two-dimensional perspectives. *J. Phys. A: Math. Gen.*, 39(33): pp. 10323–10354, 2006.

[LS95]   R. Lipowsky and E. Sackmann, editors. *Structure and Dynamics of Membranes - From Cells to Vesicles*, volume 1A of *Handbook of Biological Physics*. Elsevier Science B.V., Amsterdam, The Netherlands, 1995.

[Mar01]   M. Marsh, editor. *Endocytosis, Frontiers in Molecular Biology*. Oxford University Press, Oxford, U.K., 2001.

[May00]   S. May. Protein-induced bilayer deformations: the lipid tilt degree of freedom. *Eur. Biophys. J.*, 29(1): pp. 17–28, February 2000.

[MBS99]   S. May and A. Ben-Shaul. Molecular Theory of Lipid-Protein Interaction and the L_α-$H_\parallel$ Transition. *Biophys. J.*, 76(2): pp. 751–767, February 1999.

[MFR$^+$91] L. Miao, B. Fourcade, M. Rao, M. Wortis, and R. K. P. Zia. Equilibrium budding and vesiculation in the curvature model of fluid lipid vesicles. *Phys. Rev. A*, 43(12): pp. 6843–6856, June 1991.

[MG05]   H. T. McMahon and J. L. Gallop. Membrane curvature and mechanisms of dynamic cell membrane remodelling. *Nature*, 438(7068): pp. 590–596, December 2005.

[MH01]   C. E. Morris and U. Homann. Cell Surface Area Regulation and Membrane Tension. *J. Membrane. Biol.*, 179: pp. 79–102, 2001.

[ML91]   F. C. MacKintosh and T. C. Lubensky. Orientational Order, Topology, and Vesicle Shapes. *Phys. Rev. Lett.*, 67(9): pp. 1169–1172, August 1991.

Bibliography

[ML93]   F. C. MacKintosh and T. C. Lubensky. Theory of "Ripple" Phases of Lipid Bilayers. *Phys. Rev. Lett.*, 71(10): pp. 1565–1568, August 1993.

[MM02]   V. I. Marchenko and C. Misbah. Elastic interaction of point defects on biological membranes. *Eur. Phys. J. E*, 8: pp. 477–484, 2002.

[MSdM02]   N. Maeda, T. J. Senden, and J.-M. di Meglio. Micromanipulation of phospholipid bilayers by atomic force microscopy. *BBA-Biomembranes*, 1564(1): pp. 165–172, August 2002.

[Mül04]   M. M. Müller. Theoretical examinations of interface mediated interactions between colloidal particles. Diploma thesis, Johannes Gutenberg-Universität Mainz, December 2004.

[Mun03]   S. Munro. Lipid Rafts: Elusive or Illusive? *Cell*, 115(4): pp. 377–388, November 2003.

[NG99]   M. Nizette and A. Goriely. Towards a classification of euler-kirchhoff filaments. *J. Math. Phys.*, 40(6): pp. 2830–2866, June 1999.

[NGA98]   C. Nielsen, M. Goulian, and O. S. Andersen. Energetics of Inclusion-Induced Bilayer Deformations. *Biophys. J.*, 74(4): pp. 1966–1983, April 1998.

[Nic49]   M. M. Nicolson. The interaction between floating particles. *Proc. Cambridge Philos. Soc.*, 45: pp. 288–295, 1949.

[Nic05]   B. Nichols. Without a raft. *Nature*, 436(7051): pp. 638–639, August 2005.

[NP92]   P. Nelson and T. Powers. Rigid Chiral Membranes. *Phys. Rev. Lett.*, 69(23): pp. 3409–3412, December 1992.

[NP93]   P. Nelson and T. Powers. Renormalization of chiral couplings in tilted bilayer membranes. *J. Phys. II France*, 3(10): pp. 1535–1569, October 1993.

[NPW04]   D. Nelson, T. Piran, and S. Weinberg, editors. *Statistical Mechanics of Membranes and Surfaces*, volume 5 of *Jerusalem Winter School for Theoretical Physics*. World Scientific, River Edge, NJ, second edition, 2004.

[NS03]   A. V. Nguyen and H. J. Schulz, editors. *Colloidal Science of Flotation*, volume 118 of *Surfactant Science Series*. Marcel Dekker, New York, NY, 2003.

226

[PHG02]   T. R. Powers, G. Huber, and R. E. Goldstein. Fluid-membrane teth-
           ers: Minimal surfaces and elastic boundary layers. *Phys. Rev. E*,
           65(4): 041901, March 2002.

[PTVF92]   W. H. Press, S. A. Teukolsky, W. T. Vetterling, and B. P. Flan-
           nery, editors. *Numerical Recipes in C*. Cambridge University Press,
           Cambridge, U.K., second edition, 1992.

[Rad02]   M. Radmacher. Measuring the elastic properties of living cells by the
           atomic force microscope. *Methods Cell Biol.*, 68: pp. 67–90, 2002.

[Rey07]   B. J. Reynwar. Personal communication, 2007.

[RIH+07]   B. J. Reynwar, G. Illya, V. A. Harmandaris, M. M. Müller, K. Kre-
           mer, and M. Deserno. Aggregation and vesiculation of membrane
           proteins by curvature-mediated interactions. *Nature*, 447(7143):
           pp. 461–464, May 2007.

[Rob97]   M. S. Robinson. Coats and vesicle budding. *Trends Cell Biol.*, 7(3):
           99–102, March 1997.

[ROM+00]   W. Rawicz, K. C. Olbrich, T. McIntosh, D. Needham, and E. Evans.
           Effect of Chain Length and Unsaturation on Elasticity of Lipid Bi-
           layers. *Biophys. J.*, 79(1): pp. 328–339, July 2000.

[RSS89]   W. N. Russel, D. A. Saville, and W. R. Schowalter. *Colloidal Dis-
           persions*. Cambridge University Press, Cambridge, U.K., 1989.

[RW02]   J. S. Rowlinson and B. Widom. *Molecular Theory of Capillarity*.
           Dover, Mineola, NY, 2002.

[SBL91]   U. Seifert, K. Berndl, and R. Lipowsky. Shape transformation of vesi-
           cles: Phase diagram for spontaneous-curvature and bilayer-coupling
           models. *Phys. Rev. A*, 44(2): pp. 1182–1202, July 1991.

[SDJ00]   D. Stamou, C. Duschl, and D. Johannsmann. Long-range attraction
           between colloidal spheres at the air-water interface: The consequence
           of an irregular meniscus. *Phys. Rev. E*, 62: pp. 5263–5272, 2000.

[Sei95]   U. Seifert. Self-Consistent Theory of Bound Vesicles. *Phys. Rev.
           Lett.*, 74(25): pp. 5060–5063, June 1995.

[Sei97]   U. Seifert. Configurations of fluid membranes and vesicles. *Adv.
           Phys.*, 46(1): pp. 13–137, January-February 1997.

[SI97]   K. Simons and E. Ikonen. Functional rafts in cell membranes. *Nature*, 387: pp. 569–572, June 1997.

[SIH+06]   S. Semrau, T. Idema, L. Holtzer, T. Schmidt, and C. Storm. Accurate determination of elastic parameters for multi-component membranes. *arXiv:cond-mat/0612554*, December 2006.

[SL90]   U. Seifert and R. Lipowsky. Adhesion of vesicles. *Phys. Rev. A*, 42(8): pp. 4768–4771, 1990.

[SL95]   U. Seifert and R. Lipowsky. Morphology of vesicles. In R. Lipowsky and E. Sackmann, editors, *Structure and Dynamics of Membranes - From Cells to Vesicles*, volume 1A of *Handbook of Biological Physics*. Elsevier Science B.V., Amsterdam, The Netherlands, 1995.

[SMD+06]   S. Steltenkamp, M. M. Müller, M. Deserno, C. Hennesthal, C. Steinem, and A. Janshoff. Mechanical Properties of Pore-Spanning Lipid Bilayers Probed by Atomic Force Microscopy. *Biophys. J.*, 91(1): pp. 217–226, July 2006.

[Spi76]   M. Spivak. *A Comprehensive Introduction to Differential Geometry*. Publish or Perish, Boston, MA, second edition, 1976.

[SSN96]   U. Seifert, J. Shillcock, and P. Nelson. Role of Bilayer Tilt Difference in Equilibrium Membrane Shapes. *Phys. Rev. Lett.*, 77(26): pp. 5237–5240, December 1996.

[SSS03]   A.-S. Smith, E. Sackmann, and U. Seifert. Effects of a pulling force on the shape of a bound vesicle. *Europhys. Lett.*, 64(2): pp. 281–287, October 2003.

[SSS04]   A.-S. Smith, E. Sackmann, and U. Seifert. Pulling Tethers from Adhered Vesicles. *Phys. Rev. Lett.*, 92(20): 208101, May 2004.

[Ste06a]   S. Steltenkamp. *Mechanische Eigenschaften von freitragenden artifiziellen und nativen Membranen*. Ph.D. thesis, Johannes Gutenberg-Universität Mainz, April 2006.

[Ste06b]   S. Steltenkamp. Personal communication, 2006.

[SŽ89]   S. Svetina and B. Žekš. Membrane bending energy and shape determination of phospholipid vesicles and red blood cells. *Eur. Biophys. J.*, 17(2): pp. 101–111, June 1989.

[Tan91]   C. Tanford. *The Hydrophobic Effect: Formation of Micelles and Biological Membranes.* Krieger Publishing Company, Malabar, FL, second edition, 1991.

[TJI98]   H. A. Thieringer, P. G. Jones, and M. Inouye. Cold shock and adaptation. *Bioessays*, 20(1): pp. 49–57, January 1998.

[TOY03]   Z. C. Tu and Z. C. Ou-Yang. Lipid membranes with free edges. *Phys. Rev. E*, 68(6): 061915, December 2003.

[VK05]   S. L. Veatch and S. L. Keller. Miscibility Phase Diagrams of Giant Vesicles Containing Sphingomyelin. *Phys. Rev. Lett.*, 94(14): 148101, April 2005.

[VM04]   D. Vella and L. Mahadevan. The 'Cheerios effect'. *arXiv:cond-mat/0411688*, November 2004.

[VM05]   D. Vella and L. Mahadevan. The "Cheerios effect". *Am. J. Phys.*, 73(9): pp. 817–825, September 2005.

[Wei72]   S. Weinberg. *Gravitation and Cosmology.* Wiley, New York, NY, first edition, 1972.

[Wei03]   T. R. Weikl. Indirect interactions of membrane-adsorbed cylinders. *Eur. Phys. J. E*, 12: pp. 265–273, 2003.

[Wen86]   H. C. Wente. Counterexample to a conjecture of H. Hopf. *Pac. J. Math.*, 121(1): pp. 193–243, January 1986.

[WKH98]   T. R. Weikl, M. M. Kozlov, and W. Helfrich. Interaction of conical membrane inclusions: Effect of lateral tension. *Phys. Rev. E*, 57(6): pp. 6988–6995, 1998.

[WWWa]   http://www.espresso.mpg.de.

[WWWb]   http://www.nature.com/nature/journal/v447/n7143/suppinfo/nature05840.html.

[WWWc]   http://www.geomnat.com/phd/twocylinders.nb.

[WWWd]   http://www.geomnat.com/phd/nanodrum_linearized_shape.nb.

[WWWe]   http://www.geomnat.com/phd/nanodrum_linearized_force.nb.

[ZcH89]   O.-Y. Zhong-can and W. Helfrich. Bending energy of vesicle membranes: General expressions for the first, second, and third variation of the shape energy and applications to spheres and cylinders. *Phys. Rev. A*, 39(10): pp. 5280–5288, May 1989.

[ZK06]   J. Zimmerberg and M. M. Kozlov. How proteins produce cellular membrane curvature. *Nat. Rev. Mol. Cell Bio.*, 7(1): pp. 9–19, January 2006.